2-2009

Supercritical Fluid Deposition Of Thin Metal Films: Kinetics, Mechanics And Applications

Christos Fotios Karanikas
University of Massachusetts - Amherst

SUPERCRITICAL FLUID DEPOSITION OF THIN METAL FILMS: KINETICS, MECHANICS AND APPLICATIONS

A Dissertation Presented
by

CHRISTOS FOTIOS KARANIKAS

Submitted to the Graduate School of the
University of Massachusetts Amherst in partial fulfillment
of the requirements for the degree of

DOCTOR OF PHILOSOPHY

February 2009

CHEMICAL ENGINEERING

SUPERCRITICAL FLUID DEPOSITION OF THIN METAL FILMS: KINETICS, MECHANICS AND APPLICATION

A Dissertation Presented
by

CHRISTOS FOTIOS KARANIKAS

Approved as to style and content by:

_____
James J. Watkins, Chair

_____
E. Bryan Coughlin, Member

_____
Dimitrios Maroudas, Member

_____
Triantafillos J. Mountziaris, Member

_____
Triantafillos J. Mountziaris, Department Head
Chemical Engineering

DEDICATION

To Irene.

ACKNOWLEDGMENTS

I would like to give many thanks to my advisor, Professor James J. Watkins. His guidance, support, friendship and challenges have helped me to grow both professionally and personally. His trust and tremendous patience allowed me to have a very successful graduate school experience. I would also like to thank my committee members, Professor Dimitrios Maroudas, Professor Triantafillos J. Mountziaris and Professor E. Bryan Coughlin. Your support, advice, suggestions and time are greatly appreciated.

I want to thank all of my friends in the Watkins group, both past and present, for their friendship and advice. I thank Zong for being a wonderful mentor that took the time to show me the ropes when I was just getting started. I thank Tim for being a great friend. I thank Scott, Ephrem, Shan, Ajay, Vikram, Siva, Adam, Mike, Eric and Nick for great discussions and support. I thank Eun Young for being a friend and feel happy leaving some of the ongoing research in her hands. I thank Chris, Curran, Todd and Dan for not only making the lab a fantastic place to work in but for being some of the best friends I have ever had the pleasure of knowing. They all made my graduate school experience one I will never forget.

I want to give my sincerest thanks to all of the staff in the Chemical Engineering and the Polymer Science and Engineering Department who helped me in every aspect of my research. I thank Joe and Gary for always helping me when I was in a time pinch and needed something machined. I thank Jack, Sekar and Lou not only for training me on the XPS, XRD and SEM and providing me with guidance on analyzing data but also for being good friends.

I want to thank all of my friends at UMass and give special thanks to Kham, Nancy, Karl, Jared and Bernie for being great roommates as well as wonderful friends over the past few years. Special thanks go to Hossein for being a great workout partner and amazing friend. I also thank the entire UMass Tae Kwon Do team for being a fun group to go and wind down with after a long, hard day at work.

To my parents, Athanasios and Agnes, I want to thank you for all the love and support I could have ever needed. I would also like to thank my brothers Dino, Pete and Tony as well as my nephew and niece, Julian and Mia. My entire family was my source of motivation. Finally, to my girlfriend, Irene, whose love, support and sacrifices are immeasurable, I could have never finished if it were not for you.

ABSTRACT

SUPERCRITICAL FLUID DEPOSITION OF THIN METAL FILMS:
KINETICS, MECHANICS AND APPLICATION

February 2009

CHRISTOS FOTIOS KARANIKAS, B.S., UNIVERSITY OF PITTSBURGH

Ph.D., UNIVERSITY OF MASSACHUSETTS AMHERST

Directed by: Professor James J. Watkins

In order to meet the demands of the continuous scaling of electronic devices, new technologies have been developed over the years. As we approach the newest levels of miniaturization, current technologies, such as physical vapor deposition and chemical vapor deposition, are reaching a limitation in their ability to successfully fabricate nano sized electronic devices.

Supercritical fluid deposition (SFD) is a demonstrated technology that provides excellent step coverage for the deposition of metals and metal oxides within narrow, high aspect ratio features. This technique shows the potential to satisfy the demands of integrated circuit miniaturization while maintaining a cost effective process needed to keep the technology competitive. In order to complement SFD technology heuristics for scale-up, an understanding of the deposition mechanism and kinetics and resolution of integration issues such as interfacial film adhesion must be resolved.

It is critical to have a fundamental understanding of the chemistry behind the reaction process in supercritical fluid deposition. For this purpose, a detailed kinetic study of the deposition of ruthenium from bis(2,2,6,6-tetramethyl-3,5-heptanedionato) (1,5-cyclooctadiene) ruthenium(II) is carried out so that growth rate orders and a

mechanism can be established. These predictive kinetic results provide the means to control the reaction which allows for overall optimization of the process.

Reliability is of the utmost importance for fabricated devices since they must withstand harsh steps in the fabrication process as well as perform and last under standard and extreme usage conditions. One issue of reliability is assessed by addressing the adhesion of the metallization layers deposited by SFD. A quantitative determination of the interfacial adhesion energy of as deposited and pretreated copper metallization layers from SFD onto barrier layers is used to determine the potential for integration of these films for industry standards.

Extension of the basics of SFD by performing co-deposition of multiple compounds, layer-by-layer deposition for device fabrication and integration with other unique technologies for novel applications demonstrates the ability of this technique to satisfy a wide range of commercial applications and be used as the basis for new technologies. Co-depositions of Ce/Pt, Co/Pt, Ba/Ti and Nd/Ni for the fabrication of functional direct methanol fuel cell electrodes, magnetic alloys for media storage applications, high k dielectric films for alternative energy storage devices and alternative materials for solid oxide fuel cell cathodes, respectively, are performed. Layer-by-layer deposition with masking is used to fabricate nanometer scale capacitors. Finally, plasma spray technology is combined with the rapid expansion of supercritical solvents technique to form a novel, patent pending, process that is used to fabricate next generation photovoltaic cells.

TABLE OF CONTENTS

LIST OF TABLES

LIST OF FIGURES

CHAPTER 1

INTRODUCTION

1.1 Overview

The goal of the research presented in this dissertation is to help advance supercritical fluid deposition technology from its current state of being a demonstrated laboratory technology, to a point where it is a viable manufacturing option for the miniaturization of integrated circuits in industry. The challenges that must be overcome in order to meet this goal include scale-up and reliability testing.

Scale-up is necessary in order to convert a bench top result into a practical application for industrial use. To do this, it is critical to have a fundamental understanding of the chemistry behind the reaction process in supercritical fluid deposition. For this purpose, a detailed kinetic study of the deposition is carried out such that growth rate orders and a mechanism can be established. This will help enable control over the reaction by promoting predictive kinetic results and will also allow for an overall optimization of the process.

Reliability is of the utmost importance for fabricated devices if they are to withstand the upcoming harsh steps in the fabrication process as well as perform and last under standard and extreme usage conditions. The challenge of reliability is accessed by addressing the adhesion of the metallization layers deposited by SFD. A quantitative determination of the interfacial adhesion energy of as deposited and pretreated metallization layers from SFD onto barrier layers is used to determine the reliability of these films for industry standards.

Application of SFD technology to a variety of commercially oriented applications is important in order to show the techniques versatility. Extension of the basics of SFD by performing co-deposition of multiple compounds, layer-by-layer deposition for device fabrication and integration with other unique technologies for novel applications demonstrates the ability of this technique to satisfy a wide range of commercial applications and be used as the basis for new technologies.

In this first chapter, conventional deposition techniques are discussed. Supercritical fluid deposition is then discussed in detail and compared to the conventional deposition techniques. An overview of the common instruments used for post experimental analysis is discussed with a description of the settings used for most data collection.

Chapter 2 details the experiments involved with the kinetic study used to satisfy the first challenge of scale-up. This chapter discusses the kinetics of ruthenium thin film deposition by supercritical fluids using bis(2,2,6,6-tetramethyl-heptane-3,5-dionato)(1,5-cyclooctadiene) ruthenium(II), $Ru(tmhd)_2cod$, as the precursor. Reaction rate orders are determined and a Langmuir – Hinshelwood deposition mechanism is proposed.

Chapter 3 is a detailed discussion based on the experiments used to satisfy the challenge of reliability. The chapter discusses the mechanics study used to quantify the interfacial adhesion of poly(acrylic acid) modified and unmodified copper thin films deposited on TaN capped silicon wafers by the hydrogen assisted reduction of bis(2,2,7-trimethyloctane-3,5-dionato) copper in supercritical carbon dioxide.

Chapter 4 and Chapter 5 are examples of applications in which SFD technology is used to mimic, better or create new applications that have commercial interest.

Chapter 4 focuses on a wide variety of applications that benefit from the use of SFD. The co-deposition of cobalt and platinum onto TaN capped silicon wafers using bis(cyclopentadienyls) cobalt (II), $CoCp_2$, as the cobalt source and dimethyl(1,5-cyclooctadiene) platinum (II), $Pt(Me)_2cod$, as the platinum source is demonstrated. The catalytically enhanced deposition of ceria and platinum from tetrakis(2,2,6,6-tetramethyl-3,5-heptanedionato) cerium (IV), $Ce(tmhd)_4$, and $Pt(Me)_2cod$, respectively, is reported. Attempts at the modification of a process used to fabricate $BaTiO_3$ powders is undertaken in order to fabricate high k dielectric films from barium isopropoxide (Baip) and titanium isopropoxide (Ttip). Simultaneous deposition of nickel and neodymium films are deposited by the hydrogen assisted reduction of tris(2,2,6,6-tetramethyl-3,5-heptanedionato) neodymium (III), $Nd(tmhd)_3$, and bis(2,2,6,6-tetramethyl-3,5-heptanedionato) nickel (II), $Ni(tmhd)_2$, via SFD for solid oxide fuel cell cathodes. Finally, the deposition of mutli-layer stacks of $Ru/TiO_2/Ru$ and $Ru/HfO_2/Ru$ from $Ru(tmhd)_2cod$, di(isopropoxide)bis(2,2,6,6-tetramethyl-3,5-heptanedionato) titanium (IV), $Ti(tmhd)_2(iPr)_2$ and tetra(2,2,6,6-tetramethyl-3,5-heptanedionato)hafnium, $Hf(tmhd)_4$.is performed in order to fabricate capacitor devices on the nano scale.

Chapter 5 focuses on the union of two unique technologies, plasma spray and rapid expansion of supercritical solutions, to create a new technology called plasma-enhanced rapid expansion of supercritical solvents, labeled PRESS. Highly dendritic columnar structures are deposited using Ttip PRESS. Samples have an ideal structure for high surface area electron carriers in photovoltaic cells.

Chapter 6 is a summary of all the conclusions of this dissertation as well a discussion on the suggested future works.

1.2 Motivation

In the world of microelectronics, miniaturization is a key issue.[1] In 1965, co-founder and former CEO of Intel, Gordon Moore, authored an article predicting the growth of transistors on integrated circuits.[2] Moore's Law states that the number of transistors on a microprocessor die would double every 18 months. The prediction held true for many years after which it deviated slightly. The current trend shows the number of transistors on a die doubling approximately every 24 months, Figure 1.1.[3]

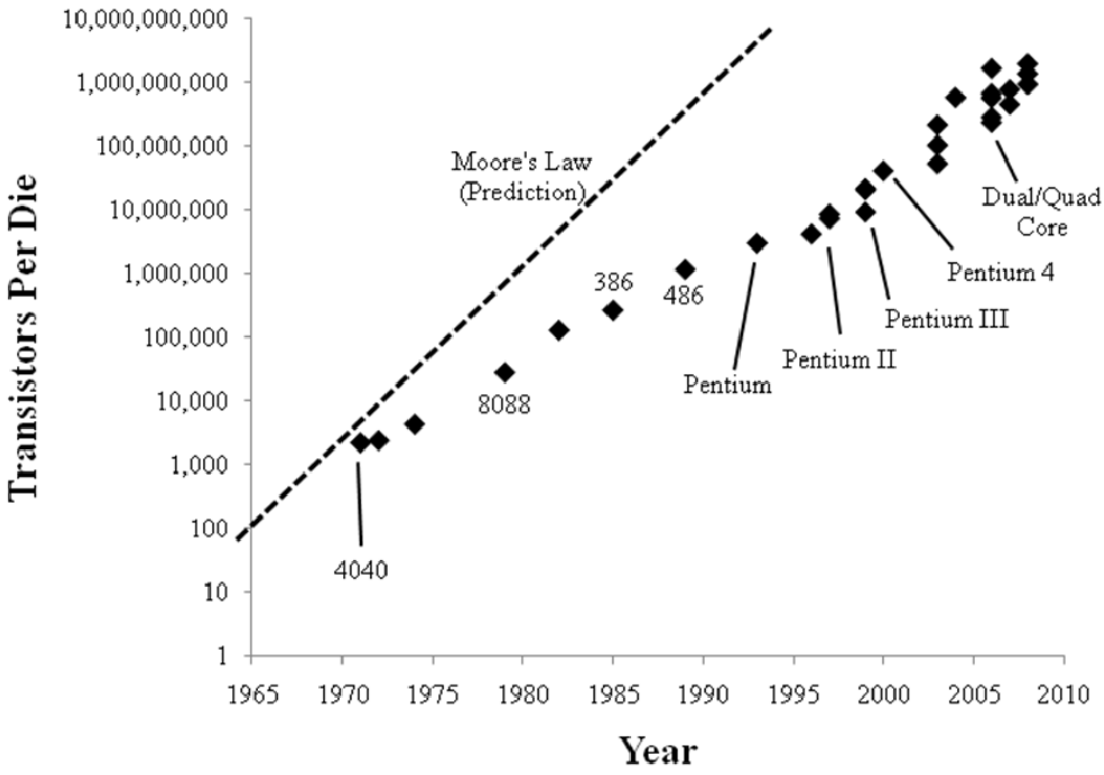

Figure 1.1: Moore's Law states that the number of transistors per die will double every 18 months. The actual doubling has held relatively close to this prediction being every 24 months.

In order to meet the demands of miniaturizing electronic devices, new technologies have been developed over the years. As we approach the newest levels of miniaturization, such as the 45 and 32 nm nodes, current technologies are reaching a

limitation in their abilities to successfully fabricate the nano sized electronic devices. The inability of conventional top-down device fabrication to satisfy the miniaturization of integrated circuits is forcing industry to a new method of fabrication called bottom-up fabrication. However, the majority of electronic devices are still fabricated using the top-down method.

Conventional deposition technique such as physical vapor deposition (PVD), atomic layer deposition (ALD) and chemical vapor deposition (CVD) suffer from a few critical flaws that prevent them from meeting the needs of miniaturization in top-down fabrication. The primary limitations of these techniques are the efficiency, both speed and cost, at which films can be deposited, the ability to deposit conformal films in high aspect ratio features and the adhesion of the deposited films to the integrated circuits for post processing steps.

Supercritical fluid deposition is a demonstrated technology that has overcome the limitations of these conventional techniques. This technique shows unique potential to satisfy all the demands of integrated circuit miniaturization while maintaining a cost effective process needed to keep the technology competitive.

1.3 Conventional Deposition Techniques

The most common conventional deposition techniques are electroplating, electroless plating, PVD, ALD and CVD. Electro and Electroless plating are liquid phase techniques while PVD, ALD and CVD are gas phase techniques.

1.3.1 Electroplating

Electroplating is a process that uses a liquid solution to transport metal ions from an anode to a cathode. The item to be plated is attached to the anode of a direct current source, typically a battery, while the metal source is connected to the anode. Both the anode and cathode are placed into a solution which promotes the flow of electricity, usually done by adding metal salts to the solution. When the current source is switched on, the metal attached to the anode is oxidized to form cations which in turn associate with the anions in solution. They are then reduced, and therefore plated, on the cathode. This process can be used to deposit films that are very conformal. However, this process produces a large amount of waste and also requires that the anode and cathode are conductive. For non conductive materials, it is necessary to deposit a seed layer in order to make the material conductive. This, however, becomes problematic for interconnect structures as conformal seed layers are necessary. Given the complex geometry, which results in challenging seed layer depositions and an extra step in the fabrication process of electronics, it is desirable to seek other options that can alleviate these issues.

1.3.2 Electroless Plating

Similar in nature to the electroplating process, this process produces the same result, plating of an object, however without the use of a current source. This process typically requires the use of toxic reducing agents in the aqueous solution, resulting in large amounts of hazardous waste. Additionally, a conductive seed layer is required for this autocatalytic process if the item to be coated is not conductive.

With both electroplating and electroless plating, high precursor concentrations can be achieved due to the liquid phase of the system. However, slow mass transport in the fluid phase and large volumes of waste water and byproducts negatively impact these processes.

1.3.3 Physical Vapor Deposition

Physical Vapor Deposition (PVD) is a process that uses thermodynamic or mechanical means to produce a solid thin film, typically in a low-pressure environment. Evaporation is the oldest technique for the physical deposition of thin films, such as Au and Al. Metals, such as these, are heated to the point of vaporization and then evaporate and form a thin film covering the substrate of interest. This technique is performed under vacuum, which allows the composition of the material being deposited to be controlled. The mean free path of the deposited molecule is typically on the order of 10 m. This means that the molecules do not interact with background gases and collide with the substrate in a linear path from the target. This only allows for a line of sight deposition, also known as shadowing, which limits its use to planar substrates and low aspect ratio structures. In addition, creating thick films is problematic due to the limited size of targets as constrained by the limitations imposed by heat transfer of the heating filaments. Regardless, this uses the target in one of the most efficient methods for deposition.

Sputtering, a more popular PVD technique, occurs when a target is bombarded with energetic ions, typically Ar^+. The atoms at the surface of the target are dislodged and then transported to the substrate, where the deposition occurs. The heat generated by this process can cause substrate temperatures of nearly 900 °C, which can cause

redistribution of doped molecules. In addition, argon atoms are typically incorporated into the deposited film. This process is also a line of sight deposition which causes shadowing in high aspect ratio features. The shadowing causes uneven film formation and eventually seals off the tops of deep trenches and vias.

The advantage of PVD is the deposition of alloys which is as simple as making the target the same composition as the film desired. This process can also be used in the reverse manner, called sputter etching. This is used to clean substrates prior to film deposition.

Electron beam deposition is similar to evaporation; however, instead of increasing the temperature of the target with a filament, the temperature of the target is increased by an electron beam with energy up to 15 keV. This allows for the evaporation of the target and then deposits a thin film on the surface of the substrate. This method suffers from the same disadvantages that evaporation and sputtering have, line of sight deposition. Inconsistent target depths, due to target evaporation, also cause uneven deposition rates. This is offset by the ability for high through put processing due to controllable deposition rates up to the order of 10 mm/min.

1.3.4 Chemical Vapor Deposition

Chemical vapor deposition (CVD) is the process by which the thermal decomposition or reaction of gaseous compounds forms a thin film on the surface of a substrate. This process deposits the desired material directly from the gas phase onto the substrate. CVD is performed at a pressure which results in the mean free path of the deposited material being relatively small, resulting in a non line of sight deposition. Due

to the high temperatures (150 – 2200 ºC) required for this process in addition to the non line of sight process, exceptional step coverage can be achieved, in principle, for even the most complex geometries.[4] However, due to precursor solubility limitations, this is not the case. The precursor solubility in the CVD process is limited by precursor vapor pressure, which ultimately results in lower solubility as compared to liquid phase deposition techniques. Due to this, precursors are being synthesized to increase the vapor pressure to alleviate this concentration issue for CVD. However, the use of complex ligand systems increases the contamination of the interface of the deposited film during deposition leading to another drawback of CVD, poor film adhesion. Additionally, the high temperature process limits the substrates able to withstand the deposition process as well as causing mechanical stress build up in the film which leads to device failure. Regardless of its setbacks, CVD is a widely accepted technique and used in a multi-billion dollar per year industry.

It is important to mention the specific are of CVD used for metal deposition which is closely related to the topics discussed in this dissertation, called metalorganic chemical vapor deposition, MOCVD. MOCVD is a process where the metal atom is bound to an organic compound which increases the solubility in the gas phase and which promotes the thermal decomposition of the organometallic compound and thus the deposition of the metal. This process is used for a wide range of metals including, but not limited to, Mo, Ta, Ti, W, Ru, Cu, Pt, Pd and many more.[5-11]

1.3.5 Atomic Layer Deposition

Atomic layer deposition (ALD) is similar to CVD in that it is a gas phase deposition process but at very low concentrations and is repeated numerous times. It requires alternating precursor gas exposure for self-limited reactions to form films. However, the films deposited have precise composition, conformal coverage, exceptionally high interfacial adhesion and thickness control on the angstrom level. ALD, although a candidate for conformal films with precise composition control, is only an effective solution at thicknesses of 10 nm or less due to the amount of time required to deposit the films. For thicker films, significantly longer processing times are required, thus making it unsuitable for industrial integration.

1.4 Supercritical Fluid Deposition

Supercritical fluid deposition (SFD) is a hybrid process that combines both vapor and liquid phase deposition characteristics in order to reduce organometallic compounds with hydrogen or other reducing agents in the presence of a supercritical fluid as the solvent, typically carbon dioxide. Vapor phase depositions are limited by precursor solubility. For instance, the CVD process is limited by the vapor pressure of the precursor.[12] However, in the liquid phase, like electroless plating, the concentration of precursor can be quite high. SFD uses a supercritical fluid as the solvent and enables a solubility which is orders of magnitude higher than CVD. To date, many metals have been deposited from the SFD process, some of which include: Au, Cu, Co, Ni, Ir, Rh, Ru, Pd, Pt.[13-30]

Supercritical fluids are sometimes referred to as gas-liquid phase hybrid and employ properties of both phases. The supercritical region can be found above the critical point which is at the end of the two phase line between the gas and liquid regions[31], Figure 1.2.

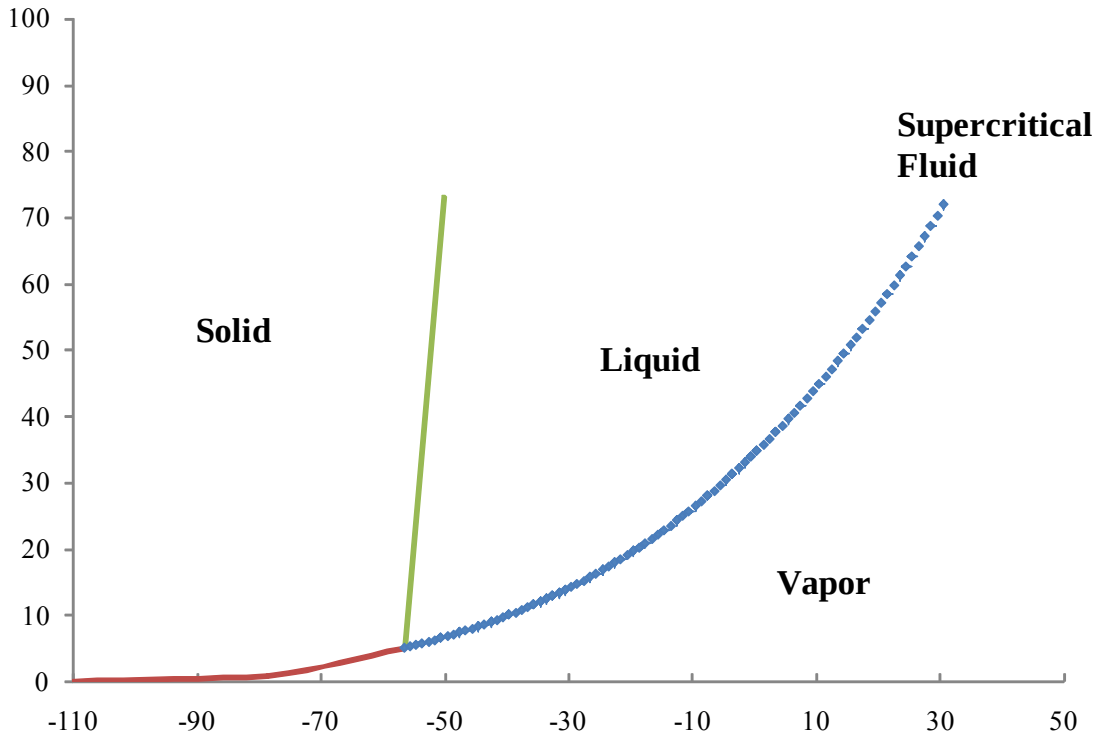

Figure 1.2: Phase diagram of carbon dioxide which includes the supercritical region.

Supercritical fluids behave like gases in that they have favorable transport properties. These include low viscosity, which allows for fast mass transport within the reactor, and zero surface tension[32], Figure 1.3, which allows for deposition in confined geometries.

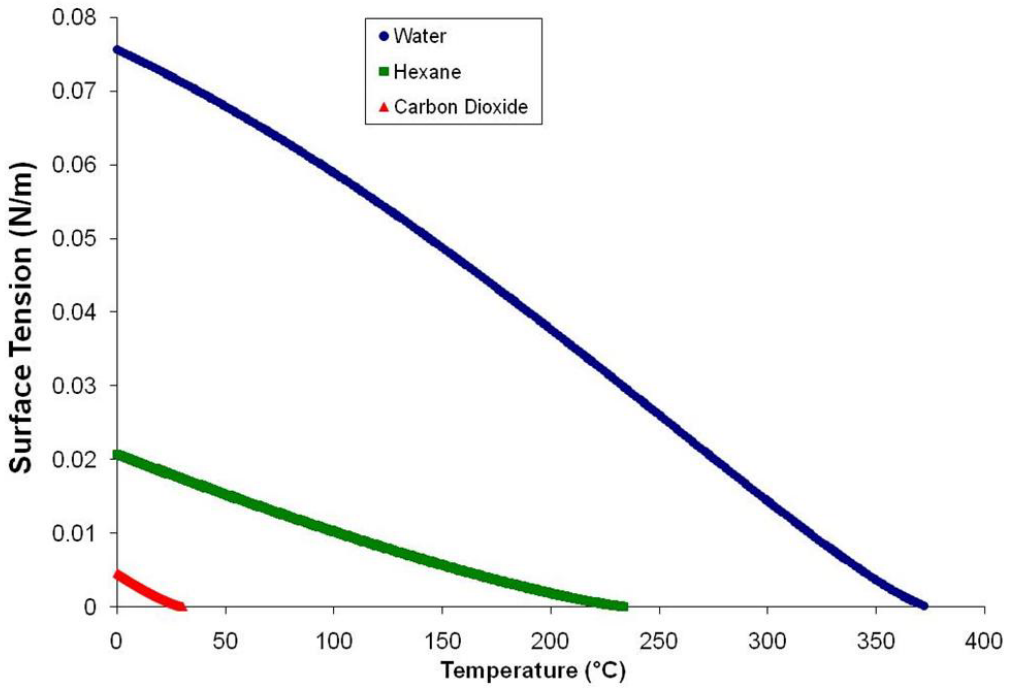

Figure 1.3: Surface tension of various solvents as a function of temperature.

The choice of supercritical carbon dioxide as a solvent for the SFD system is the result of many considerations. It has an easily attainable critical point as well as zero surface tension at its critical point and above. It also has a highly tunable density[32], Figure 1.4, which allows for much higher precursor concentrations than are possible with CVD. This is an enabling feature of SFD that changes the deposition from a mass transfer limited regime to a reaction rate limited regime. This means that the reaction can proceed at the same speed across the entire surface of the substrate, resulting in conformal film growth at relatively fast growth rates. Carbon dioxide is non toxic, inert and very cheap.[33] For all of these reasons, carbon dioxide is the solvent of choice for the SFD process.

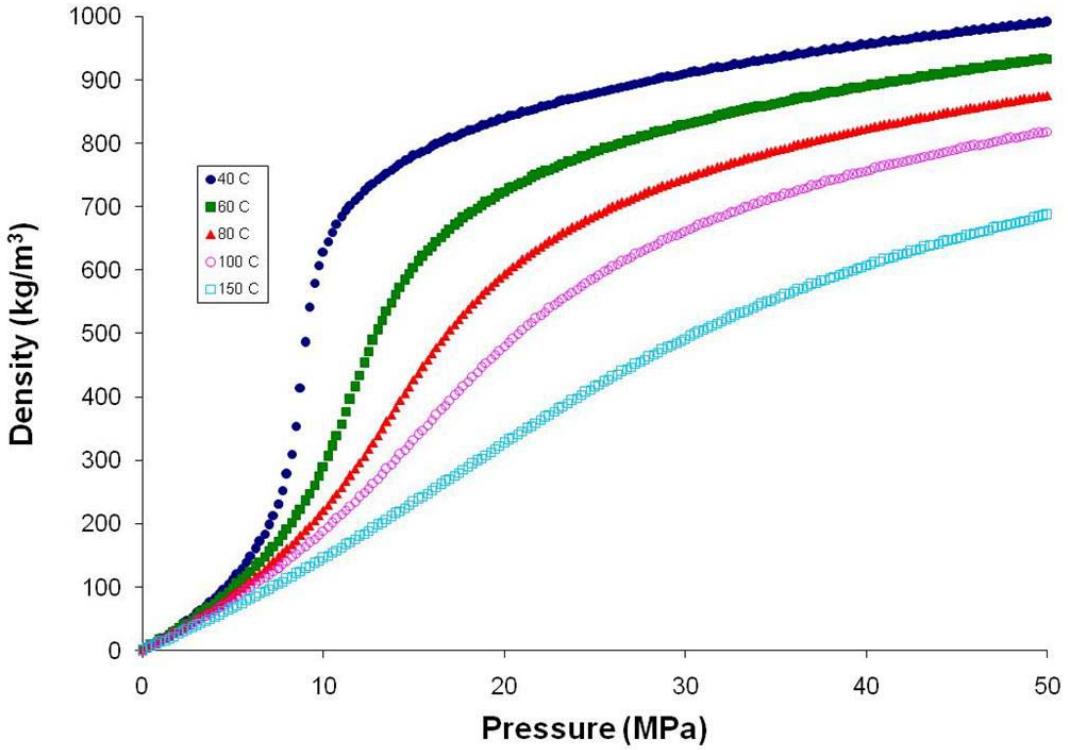

Figure 1.4: Density plot as a function of pressure for carbon dioxide at temperatures between 40 ºC – 150 ºC.

1.5 Instruments and Techniques

1.5.1 Scanning Electron Microscope

Imaging at the nano scale is done using a Semi – In – Lens Field Emission – Scanning Electron Microscope (JEOL USA Inc. and JEOL LTD.), model JSM-6320FXV. The software used to operate the instrument and handle images is the JEOL Orion software package, version 1.72.01. Typical SEM settings are: probe beam current = 3 – 5 μA, accelerator voltage = 5 or 10 kV, emissions = 8 μA. The working distance is set to either 2 or 3 mm, depending on sample.

Both Au and Pt coatings are used to increase conductance and thereby increasing image resolution. Au coatings are applied using a Cressington Sputter Coater 108, model 6002, (Ted Pella, Inc.). Typically, the current is set to 35 mA and is coated for 45

seconds. Pt coatings are applied using a High Resolution Ion Beam Coater, model 681, (GATAN Inc.). Beam energy is set to 9 keV and results in a growth of 1 nm/min.

1.5.2 Atomic Force Microscope

Atomic force microscopy (AFM) is carried out using a Dimension 3100 atomic force microscope (Digital Instruments, a subsidiary of Veeco Instruments, Inc.). The AFM is interfaced with a NanoScope IIIa controller. Both tapping and contact modes are used. The software used is Nanoscope (R) IIIa, version 5.12r3. The tips used for the microscope are Veeco, model RTESPW, 1 – 10 Ω-cm N doped Si. Tip specifications: T = 3.5 – 4.5 μm, L = 115 – 135 μm, W = 30 – 40 μm, f° = 312 – 342 kHz and k = 20 – 80 N/m.

1.5.3 X-ray Photoelectron Spectroscopy

A Quantum 2000 Scanning ESCA Microprobe (Physical Electronics USA) is used to perform X-ray photoelectron spectroscopy (XPS) using a monochromatic Al Kα X-ray source (1486.6 eV) and is equipped with an Ar^+ ion-sputtering gun. Typical x-ray settings used are 15 kV, 25 W, with 100 μm beam size. The take off angle is 45° and the ion gun sputtering settings are 500 V, 700 nA, and a 0.5 x 0.5 mm square crater. XPS raw data is analyzed using Multipak, version 6.1A (Physical Electronics USA).

1.5.4 Nuclear Magnetic Resonance

Species are analyzed using nuclear magnetic resonance in order to determine unknown species as well as confirming results. An Advance spectrometer (Bruker Instruments) is used with a Bruker 400 Ultrashield Magnet. Interfacing with the

instrument is done by using the NMR Suite, version 3.5 patch level 6 (Bruker Biospin GmbH). Collection of data and processing is done with XWIN-NMR, version 3.5 (Bruker Biospin GmbH) and post experimental analysis is done with XWIN-Plot Editor, version 3.5-pl2 (Bruker Biospin GmbH) and MestReC, version 4.8.6.0 (MestReLab Research).

1.5.5 X-ray Diffraction

The crystalline structure of samples is analyzed using a Phillips X'Pert PW 3040 with a Cu Kα radiation source. Films are analyzed using X'Pert Highscore and Viewer.

1.5.6 Ultraviolet-Visible Spectroscopy

An Agilent 8453 Spectrophotometer (Agilent Technologies) is used to perform ultraviolet and visible spectroscopy of samples. A standard deuterium lamp and tungsten lamp are calibrated and used as received from Agilent Technologies. Samples are analyzed in a standard optical glass cuvette (3.0 mL total volume, 10 mm pathlength and 10 mm pathwidth) and seated in a standard cell holder. The instrument is interfaced with an HP Vectra VLi 8SF (Hewlett Packard) system. Raw data is analyzed using Agilent UV-visible Chemstation software (Agilent Technologies), version A.08.03 [71].

1.6 References

(1) International Technology Roadmap for Semiconductors, http://www.itrs.net/, **2007**

(2) G. E. Moore, *Electronics* **1965**, *38*, 114-117.

(3) Moore's Law, www.intel.com, **2008**

(4) T. T. Kodas, *The Chemistry of Metal CVD*, John Wiley & Sons Ltd, **1994**.

(5) R.-s. Chen, Y.-s. Huang, Y.-l. Chen, Y. Chi, *Thin Solid Films* **2002**, *413*, 85-91.

(6) F. Frohlich, D. Machajdik, V. Cambel, J. Fedor, A. Pisch, J. Lindner, *Journal of Physics IV France* **2001**, *11*, Pr3-325 - Pr323-332.

(7) J. Goswami, W. Noh, S. K. Dey, *Chemical Vapor Deposition* **2005**, *11*, 94-98.

(8) P. Hones, F. Levy, T. Gerfin, M. Gratzel, *Chemical Vapor Deposition* **2000**, *6*, 193-198.

(9) D.-H. Kim, R. H. Wentorf, W. N. Gill, *Journal of the Electrochemical Society* **1993**, *140*, 3267-3272.

(10) A. Schneider, N. Popovska, F. Holzmann, H. Gerhard, C. Topf, U. Zenneck, *Chemical Vapor Deposition* **2005**, *11*, 99-105.

(11) F. Papadatos, S. Consiglio, S. Skordas, E. T. Eisenbraun, A. E. Kaloyeros, J. Peck, D. Thompson, C. Hoover, *Journal of Materials Research* **2004**, *19*, 2947-2955.

(12) R. Koelliker, G. Bor, *Inorganic Chemistry* **1991**, *30*, 2236-2237.

(13) J. M. Blackburn, A. Cabanas, D. P. Long, J. J. Watkins, *Abstracts of Papers of the American Chemical Society* **2002**, *223*, U663-U664.

(14) J. M. Blackburn, D. P. Long, A. Cabanas, J. J. Watkins, *Science* **2001**, *294*, 141-145.

(15) J. M. Blackburn, D. P. Long, J. J. Watkins, *Chemistry of Materials* **2000**, *12*, 2625-2631.

(16) A. Cabanas, J. M. Blackburn, J. J. Watkins, *Microelectronic Engineering* **2002**, *64*, 53-61.

(17) A. Cabanas, D. P. Long, J. J. Watkins, *Chemistry of Materials* **2004**, *16*, 2028-2033.

(18) A. Cabanas, X. Shan, J. J. Watkins, *Chemistry of Materials* **2003**, *15*, 2910-2916.

(19) E. T. Hunde, J. J. Watkins, *Chemistry of Materials* **2004**, *16*, 498-503.

(20) E. Kondoh, *Japanease Journal of Applied Physics* **2005**, *44*, 5799-5802.

(21) E. Kondoh, K. Shigama, *Thin Solid Films* **2005**, *491*, 228-234.

(22) D. P. Long, J. M. Blackburn, J. J. Watkins, *Advanced Materials* **2000**, *12*, 913-915.

(23) A. O'Neil, J. J. Watkins, *Chemistry of Materials* **2006**, *18*, 5652-5658.

(24) X. Shan, J. J. Watkins, *Thin Solid Films* **2006**, *496*, 412-416.

(25) H. Wakayama, N. Setoyama, *Advanced Materials* **2003**, *15*, 742-745.

(26) J. J. Watkins, J. M. Blackburn, T. J. McCarthy, *Chemistry of Materials* **1999**, *11*, 213-215.

(27) Y. Zong, J. J. Watkins, *Chemistry of Materials* **2005**, *17*, 560-565.

(28) E. Kondoh, *Japanease Journal of Applied Physics* **2004**, *43*, 3928-3933.

(29) N. E. Fernandes, S. M. Fisher, J. C. Poshusta, D. G. Vlachos, M. Tsapatsis, J. J. Watkins, *Chemistry of Materials* **2001**, *13*, 2023-2031.

(30) Y. Zhang, D. Kang, M. Aindow, C. Erkey, *Journal of Physical Chemistry B* **2005**, *109*, 2617-2624.

(31) M. A. McHugh, V. J. Krukonis, *Supercritical Fluid Extraction Practice and Principles*, Butterworth-Heinemann, **1994**.

(32) Nist Chemistry Web Book, http://webbook.nist.gov/chemistry/, **2008**

(33) A. O'Neil, J. J. Watkins, *Green Chemistry* **2004**, *6*, 363-368.

CHAPTER 2

DEPOSITION KINETICS OF BIS(2,2,6,6-TETRAMETHYL-HEPTANE-3,5-DIONATO)(1,5-CYCLOOCTADIENE)RUTHENIUM(II)

2.1 Introduction

The preparation of nanostructured elements for future generations of microelectronic and optoelectronic devices will require the deposition of high purity, conformal, metal thin films within narrow (<100 nm) and/or high aspect ratio (>10) features. For example, microprocessors are predicted to operate at the 45 nm node as early as 2010.[1] Ruthenium's characteristic properties (ρ = 7.2 $\mu\Omega$-cm at 25 °C, 6.5 on Moh's scale, T_m = 2427 °C and equivalent oxide thickness (EOT) of less than one) make this an ideal candidate for complementary metal-oxide semiconductor (CMOS) gates. In addition, ruthenium characteristics make it a viable option for dynamic (DRAM) and nonvolatile ferroelectric (FeRAM) random access memory electrodes.[2, 3] Additional applications include conductive diffusion barrier layers for copper interconnects in semiconductors.

Ruthenium has typically been deposited by physical vapor deposition (PVD), chemical vapor deposition (CVD) or atomic layer deposition (ALD) using a wide range or precursors.[4-28] Line of sight limitations for most PVD techniques present difficulties when conformal deposition within high aspect ratio features is needed. ALD yields excellent step coverage, but sub-monolayer deposition thickness per reaction cycle presents deposition rate challenges for films beyond a few nanometers in thickness. Ruthenium films deposited via CVD can contain high levels of impurities due to ligand

decomposition products. CVD environments are also typically oxidizing, which can lead to high levels of oxygen contamination in the film or in the seed layer, like Ta.[29] In addition, due to precursor vapor pressure limitations, conversion is typically less than 10 % and the CVD process is mass transfer limited.[30, 31] Thus the deposition of conformal films in high aspect ratio features via CVD remains a challenge.

Recently, excellent step coverage for the deposition of conformal ruthenium films deposited within complex geometries using supercritical fluid deposition (SFD) under reducing conditions was reported. In that study, the hydrogen assisted reduction organoruthenium complexes, including triruthenium dodecacarbonyl ($Ru_3(CO)_{12}$), tris(2,2,6,6-tetramethyl-heptane-3,5-dionato)ruthenium ($Ru(tmhd)_3$), and bis(2,2,6,6-tetramethyl heptane-3,5-dionato)(1,5 cyclooctadiene) ruthenium ($Ru(tmhd)_2cod$) yielded highly reflective thin films with resistivities as low as 22 μΩ cm for a 33 nm thick film and excellent step coverage of high purity films was achieved within 200 nm x 300 nm trenches on patterned tantalum-coated surfaces and within 2 μm x 30 μm and 300 nm x 1.2 μm via structures on etched silicon substrates[32] SFD is a hybrid approach to reactive metal deposition that combines the advantages of solution-based processes, namely high precursor concentration and the elimination of precursor volatility constraints, with those of a vapor phase techniques, namely favorable transport properties and the absence of surface tension. High fluid phase precursor concentrations are important because they can yield conformal coverage if deposition kinetics can shifted to into regimes of surface reaction rate control. To date, a number of metal films have been deposited using SFD, which include Cu, Au, Ag, Pt, Pd, Ni, Rh, Ru, Co, Ir and alloys.[32-46] While the utility of SFD, especially for conformal films, is established, there are few kinetic studies of the

process and thus confirmation that SFD provides access to growth kinetics that are zero order in precursor concentration. Recently, Zong, et al., reported the kinetics and reaction mechanism of copper SFD via the hydrogen assisted reduction of bis(2,2,7-trimethyloctane-3,5-dionato)copper(II), $Cu(tmod)_2$, and proposed a Langmuir-Hinshelwood rate expression for the reaction.[46] This was the first time the kinetics of an SFD process was studied. Cu SFD using this precursor was found to be mechanistically similar to the CVD process and was modeled accordingly. However, Zong found that unlike in CVD, the high precursor concentration accessible in SFD yielded surface reaction rate limited, zero-order deposition kinetics with respect to precursor over broad ranges of precursor concentrations. Here is presented a comprehensive study of ruthenium SFD kinetics via the hydrogen assisted reduction of bis(2,2,6,6-tetramethyl-heptane-3,5-dionato)(1,5-cyclooctadiene)ruthenium(II), $Ru(tmhd)_2cod$ and find similar results for access to zero order deposition rates at elevated precursor concentrations that are presumably surface-reaction rate limited.

2.2 Experimental

2.2.1 Equipment

2.2.1.1 Differential Kinetics Cold Wall Batch Reactor

The kinetics study is performed in a differential kinetics cold wall batch reactor, Figure 2.1, comprised of two opposed 316 stainless steel flanges sealed with a 2-236 buna-N o-ring. A cylindrical (r = 10 mm) aluminum stage heated by three 1” long, 120 V, 100 W cartridge heaters (Omega Engineering, Inc., Stamford, CT) is used to quickly attain the desired reaction temperature. The wall of the stainless steel reactor is heated

using four 3” long, 120 V, 170 W cartridge heaters and is maintained at a lower temperature than the reaction stage in order to induce selective deposition to the higher temperature sample stage. The reaction is performed in a batch process and precursor conversion never exceeds 15 % conversion, which allows for use of the differential method of rate analysis for the kinetics study.

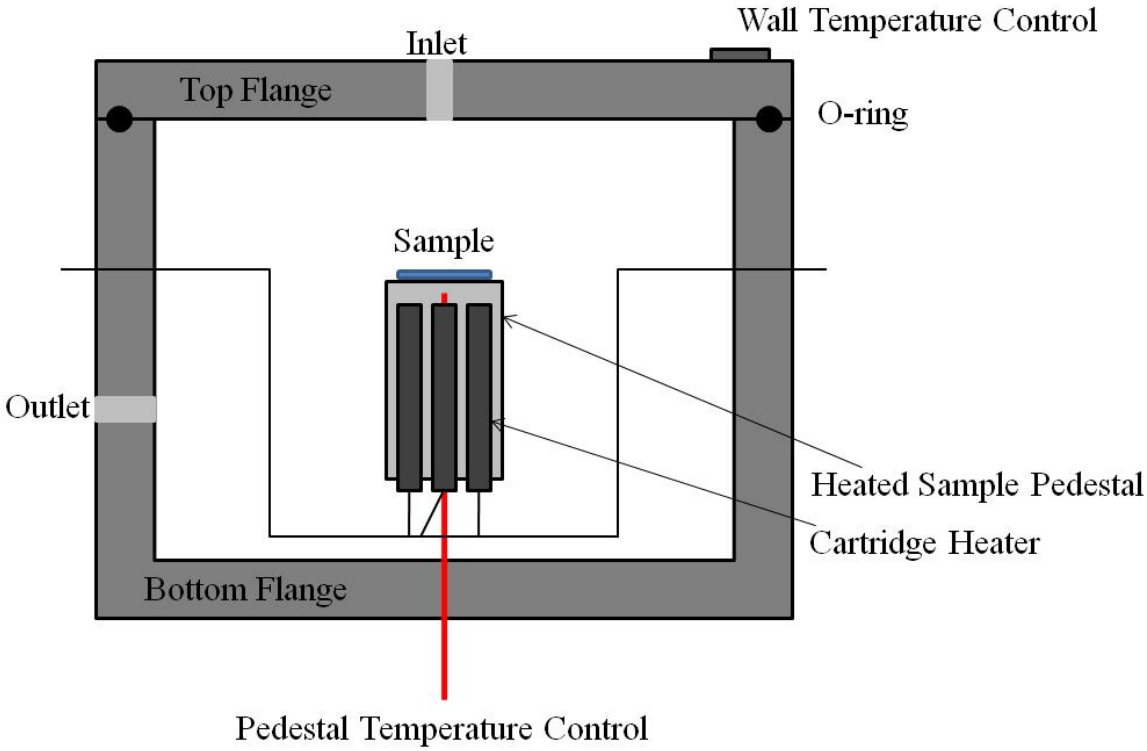

Figure 2.1: Custom built 316 stainless steel differential kinetics cold wall batch reactor with aluminum sample stage.

2.2.1.2 HPLC Sample Loop

A microelectronic actuated, six-loop, multi position, high pressure, UW type configuration Valco Valve (Vici Valco Instruments Company Inc., Houston, TX), Figure 2.2, made of Nitronic 60 is used to collect samples *in situ*. The UW type rotor used for multi positioning is made of Valcon E which allows for the high temperature, high pressure sampling. Sample loops sizes range from 0.2 mL to 10 mL. The entire system

is encased in a high temperature resistant box to maintain a consistent temperature. The valve is heated with a ring type aluminum block heated with a cartridge heater (Omega Engineering Inc., Stamford, CT).

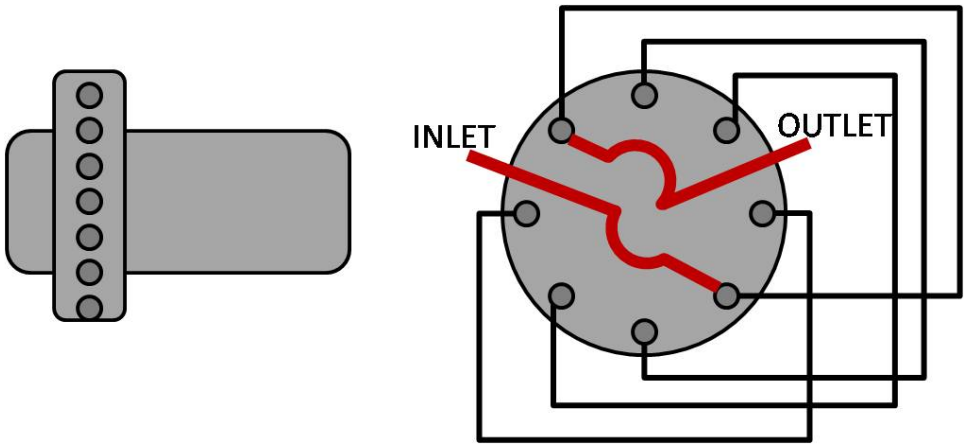

Figure 2.2: Microelectronic actuated, six-loop, multi position, high pressure, UW type configuration valco valve for experimental sampling loop system (left) schematic view (right) internal view with sample loops attached.

2.2.1.3 CO_2/Water Burette System

During the reaction, small samples of known volume are collected via the previously mentioned HPLC sample loop system so that further analysis by UV visible spectroscopy can be used to confirm precursor concentration. The temperature of the samples in the reactor are typically around 150 – 200 ºC. Samples are collected from the reactor to an HPLC sample loop over 5 seconds. The sample loops are maintained at 70 ºC. Calculations for concentration are based on the 70 ºC sample loop temperature. To confirm sufficient time is allowed for the high temperature samples collected from the reactor to equilibrate to the new temperature of the HPLC loop, a water burette system is incorporated into the sampling system. A controlled expansion of the high pressure sample to atmospheric pressure into the water filled burette allows for the back calculation of the temperature of the collected sample. It is found that the temperature of

the collected sample reaches the temperature of the HPLC sample loop in the 5 seconds used to collect the sample thereby confirming that 5 seconds is a sufficient amount of time to collect a single sample.

2.2.2 Materials

Bis(2,2,6,6-tetramethyl-3,5-heptanedionato)(1,5-cyclooctadiene)ruthenium(II), 99 %, (99.9 % Ru), $Ru(tmhd)_2cod$, [329735-79-7], Figure 2.3, is obtained from Strem Chemicals, Inc. (Newburyport, MA) and is ground using a mortar and pestle and used without any further purification. Approximately 98 % pure n-heptane [142-82-5] (Fisher Scientific, Pittsburgh, PA) is used as received without any further purification. Coleman grade (99.99 %) carbon dioxide, ultra high purity (99.999 %) hydrogen and prepurified grade (99.998 %) nitrogen are used as received (Merriam Graves Corp, Charlestown, NH). A buna-N o-ring, size 2-236, is used for the high pressure and high temperature reactor seal (Marco Rubber and Plastic Products, Inc., North Andover, MA). Films are deposited on silicon (crystal orientation <100>, 500 nm thermally grown oxide, 1-100 micro-ohm centimeter, 750 micron total thickness) (Novellus, San Jose, CA).

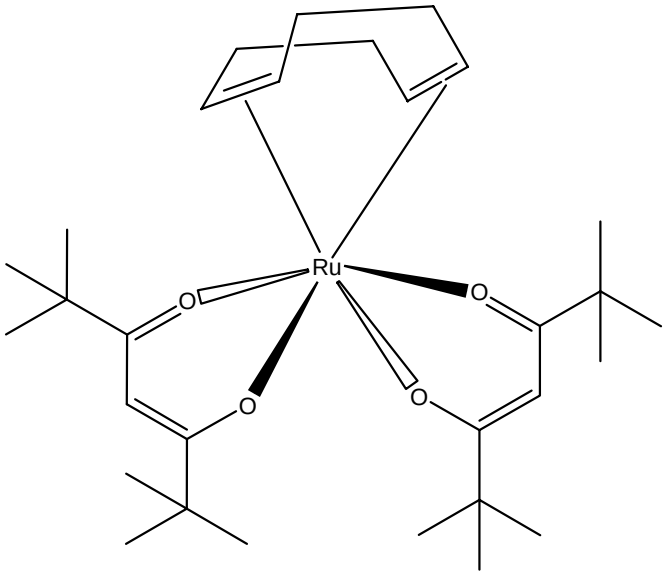

Figure 2.3: Ruthenium precursor, *bis*(2,2,6,6-tetramethyl-heptane-3,5-dionato)(1,5-cyclooctadiene)ruthenium(II), Ru(tmhd)$_2$cod, used for supercritical fluid deposition kinetics study.

2.2.3 Procedure

For a typical reaction, a 12 mm by 12 mm silicon <100> wafer, with a 500 nm thermally grown oxide layer, is mounted to the aluminum heated stage and secured with two clips. A known amount of precursor is loaded into the vessel. The vessel is then sealed and placed behind protective polycarbonate housing. Then, using a constant flow of nitrogen, the reaction vessel is purged continuously over a 15 minute period. The reactor wall is then heated to the desired temperature and allowed to equilibrate (t = 60 min.). Carbon dioxide is introduced into the reactor using a computer-controlled syringe pump (Teledyne Isco, Inc., Lincoln, NE), which enables precise volume measurement of the added CO_2. A suitable amount of time is allowed for complete dissolution of precursor[47] (t = 60 min.), Figure 2.4, in the convection dominated flow[48] of the supercritical CO_2 in the reactor. Figure 2.4 shows dissolution time of Ru(tmhd)$_2$cod precursor into carbon dioxide at 75, 100, 125 ºC. Precursor is loaded into the reactor and

samples are taken at at known times and the concentration is calculated via UV-Visible spectroscopy. Equilibrium is reached when the concentration pleataus.

For byproduct dependence reactions, the byproduct is loaded into an HPLC sample loop and then a known volume of byproduct is injected into the reactor. Next, hydrogen is loaded into the system using a manifold of known volume (70 mL). The moles of hydrogen injected are then calculated by pressure drop using the ideal gas law. The aluminum stage is then quickly heated (~ 15 s.) to the desired reaction temperature and maintained for 3 minutes. The heated stage is then allowed to cool down (~ 15 s.) while fresh CO_2 is used to flush multiple reactor volumes through the system to remove reaction byproducts and unreacted precursor. The effluent is passed through an activated carbon bed and silicon oil bubbler before being vented to the atmosphere. During the reaction, small gas phase samples of known volume are collected using HPLC sample loops. Samples were decompressed and the precursor is recovered in a known volume of n-heptane and the resulting solutions are analyzed using UV visible spectroscopy (257 nm and 305 nm, Figure 2.5) in order to determine precursor concentrations (Figure 2.6 shows the standard curve for $Ru(tmhd)_2cod$ in n-heptane where the extinction coefficients for the Beer-Lambert law are 18.71 L/g for the primary absorbance of 257 nm and 9.69 L/g for the secondary absorbance of 305 nm) in the fluid phase and confirm conversions of less than 15 %. A differential method of rate analysis is used to analyze the data and propose a reaction mechanism as well as determine the reaction rate orders for the growth rate. The method of excess is used to account for multiple reactants.

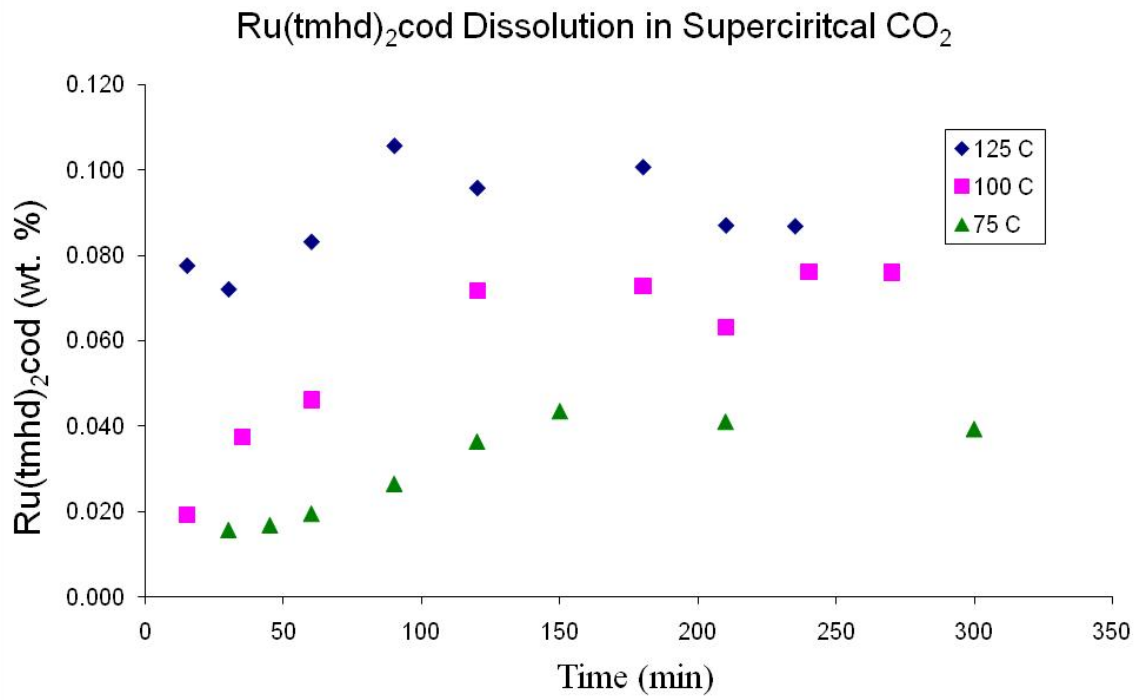

Figure 2.4: Dissolution time of solid Ru(tmhd)$_2$cod precursor into carbon dioxide at 75, 100, 125 ºC.

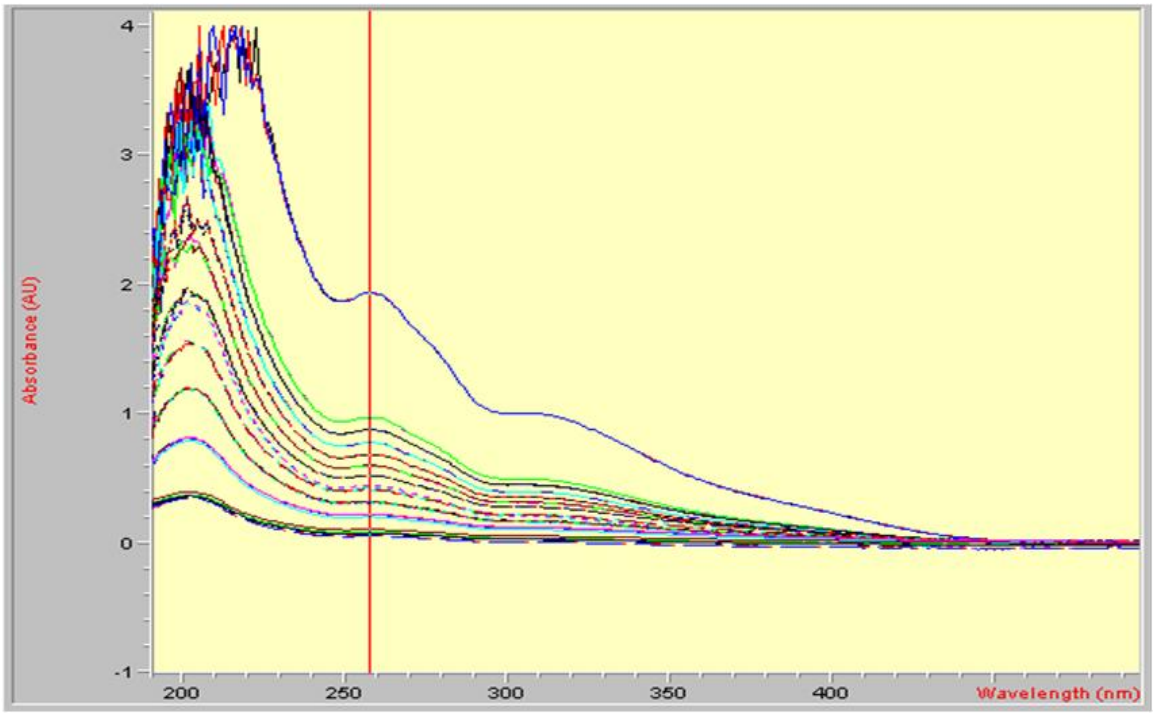

Figure 2.5: Absorbance of Ru(tmhd)$_2$cod in n-heptane over the concentration range of 0.005 – 0.105 mg/mL. Red line is showing primary identification absorbance peak of 257 nm. Secondary identification absorbance peak of 305 nm also used.

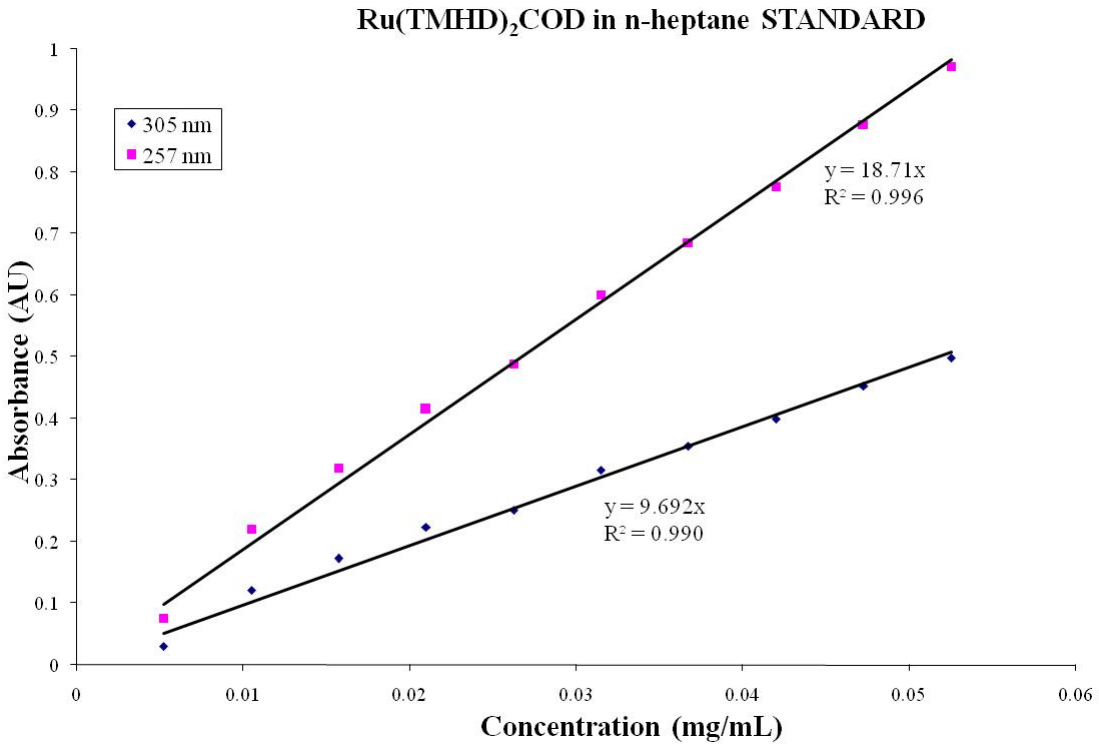

Figure 2.6: Standard curve for concentration of Ru(tmhd)$_2$cod in n-heptane for UV absorbance of 257 nm (primary) and 305 nm (secondary). Extinction coefficients of the Beer-Lamber law for the primary and secondary absorbances are 18.71 L/g and 9.69 L/g, respectively.

The deposited films are characterized in order to obtain their thickness, purity, sheet resistance and roughness. Thickness measurements are performed using a Sloan Dektak[3] Surface Profiler. Growth rates are then calculated by dividing film thickness by reaction time. Film purity is determined by x-ray photoelectron spectroscopy (XPS). The film's sheet resistance is measured with a Jandel four-point probe and Keithley 2000 multimeter. Atomic force microscopy (AFM) is carried out in both tapping and contact mode to gather height and phase data.

2.3 Results and Discussion

2.3.1 Film Quality

High quality ruthenium films are deposited in this study. The purity of the films is determined using x-ray photoelectron spectroscopy (XPS). Figure 2.7 shows an XPS sputter depth profile of an 83 nm thick ruthenium film deposited by the hydrogen assisted reduction of $Ru(tmhd)_2cod$ from a 0.09 wt. % solution of precursor in CO_2 at a stage temperature of 260 ºC in the presence of excess hydrogen. No significant contamination is observed throughout the bulk of the film. Although carbon concentration is not determined directly from the C1s peak due to overlapping of its orbital energy position with that of the Ru 3d orbital, it is possible to determine if carbon impurities are present. The peak separation between the Ru $3d_{3/2}$ and $3d_{5/2}$ peak is known to be 4.2 eV in pure Ruthenium. [49-53] Additionally, the peak height ratio is known to be approximately 1.5. Convolution of the Ru peaks with the C1s peaks would be expected to alter these relationships. Figure 2.8 shows an XPS survey spectrum with enlarged, Figure 2.9, Ru 3d binding energy fingerprint region. The observed results reflect these expectations indicating a high purity ruthenium film.

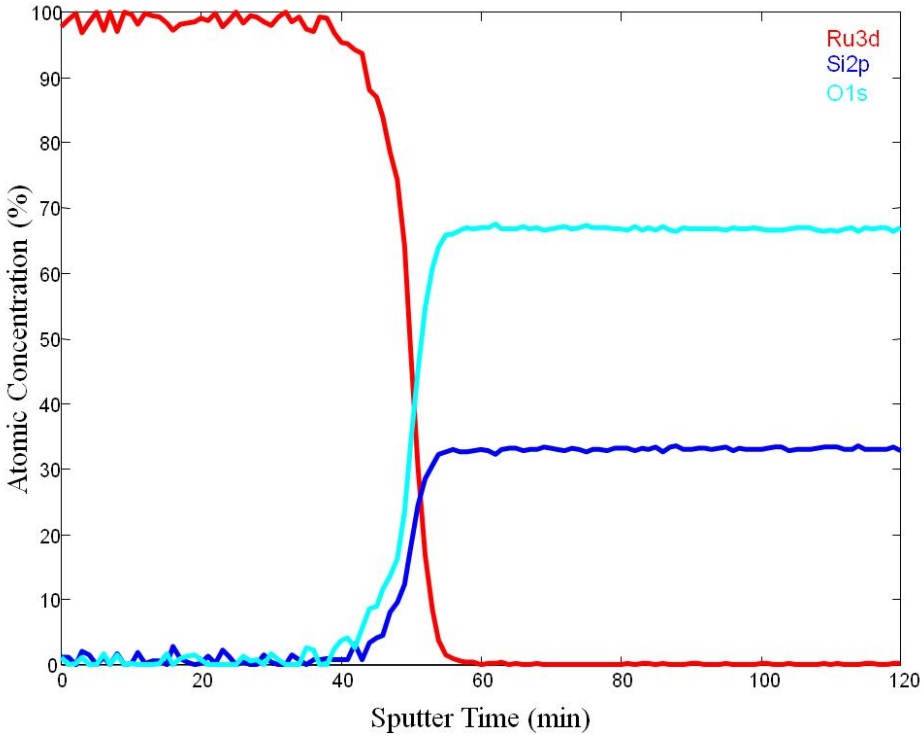

Figure 2.7: X-ray photoelectron spectroscopy sputter depth profile of a highly conformal, 83 nm thick ruthenium film deposited by SFD. Reaction conditions: 260 °C, 172 bar, 0.09 wt. % $Ru(tmhd)_2cod$, 0.3 wt. % hydrogen, 3 minute heating.

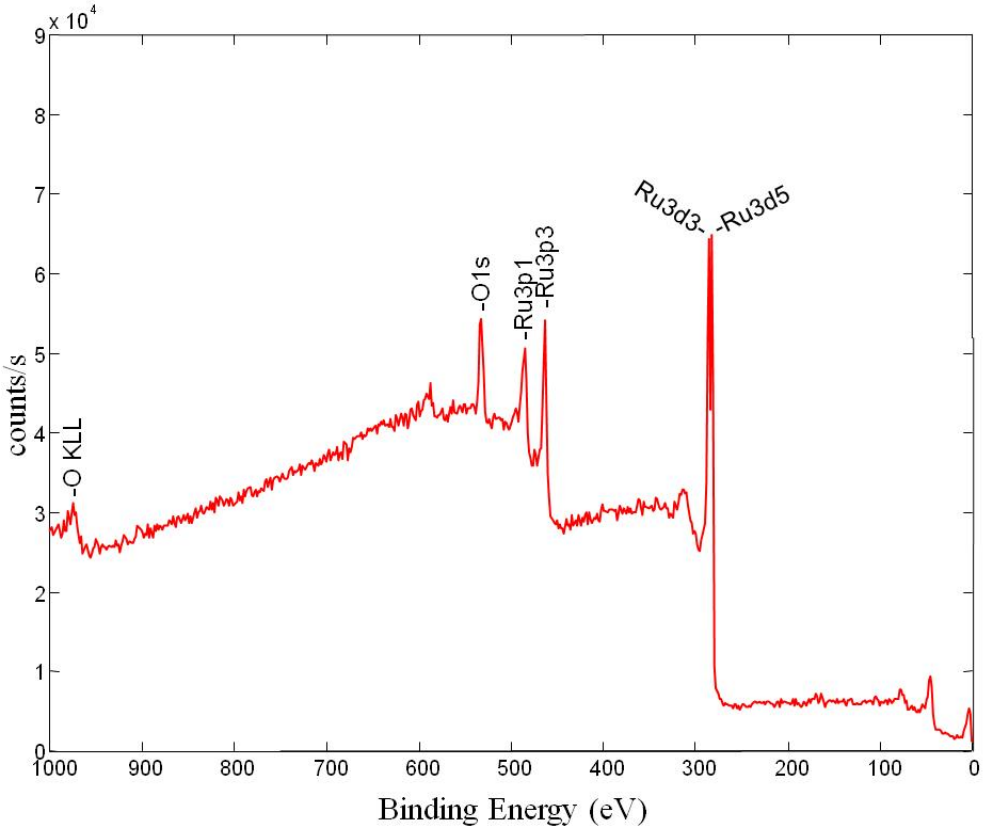

Figure 2.8: X-ray photoelectron spectroscopy survey scan of a highly conformal, 83 nm thick ruthenium film deposited by SFD. Reaction conditions: 260 °C, 172 bar, 0.09 wt. % $Ru(tmhd)_2cod$, 0.3 wt. % hydrogen, 3 minute heating.

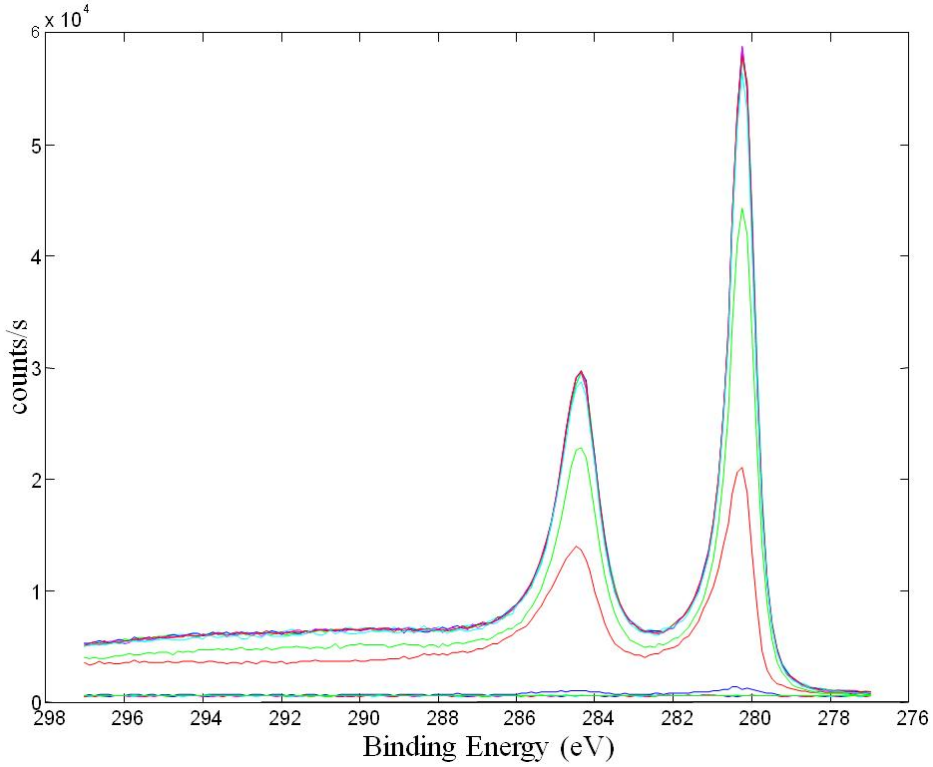

Figure 2.9: X-ray photoelectron spectroscopy ruthenium 3d orbital binding energy region of a highly conformal, 83 nm thick ruthenium film deposited by SFD. Reaction conditions: 260 °C, 172 bar, 0.09 wt. % $Ru(tmhd)_2cod$, 0.3 wt. % hydrogen, 3 minute heating.

Resistivity measurements are consistent with high film purity. Sheet resistance is calculated from film resistivity and thickness measurements and is determined to be approximately 20 μΩ-cm. While the measured resistance is greater than that of bulk Ru (7.6 μΩ -cm), this is expected due to the thin nature of the film and grain boundary effects. Had significant levels of carbon contamination been present, sheet resistance values would be expected to be much higher.

A cross sectional field emission scanning electron microscopy, FESEM, is shown in Figure 2.10 (top down) and Figure 2.11 (cross section). Figure 2.12 is a height image from atomic force microscopy, AFM, analysis. The SEM image indicates that continuous ruthenium films are deposited on the planar silicon substrates, while AFM data indicates

a mean surface roughness of 1 nm. Examples of excellent step coverage in high aspect ratios using this deposition chemistry under similar conditions can be found in a previous report.[32]

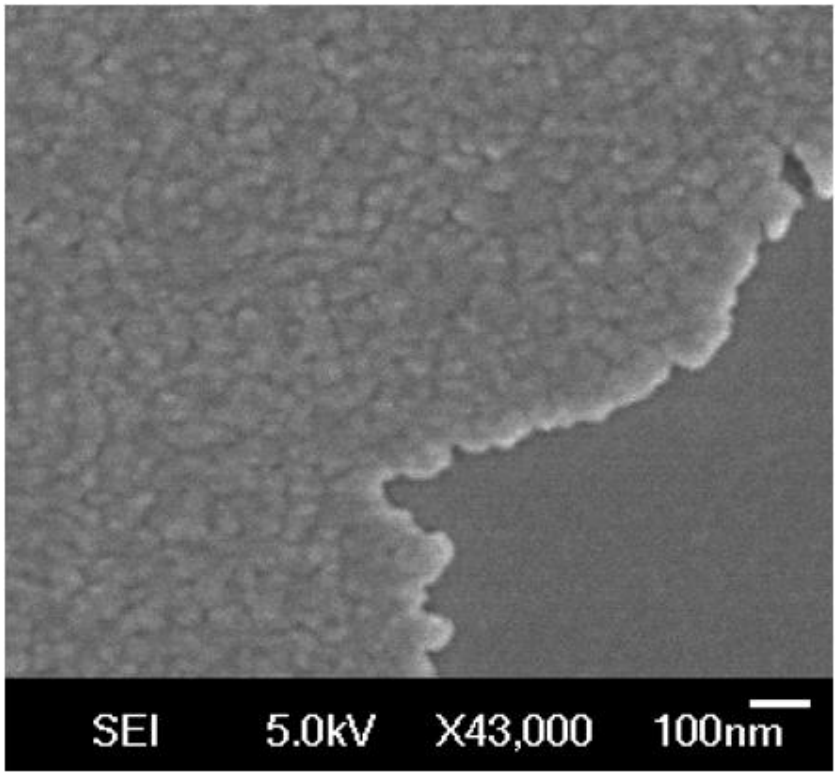

Figure 2.10: Field-Emission Scanning Electron Microscope top-down image of a 35 nm thick ruthenium film deposited by SFD. Reaction conditions: 310 °C, 90 bar, 0.15 wt. % $Ru(tmhd)_2cod$, 0.6 wt. % hydrogen, 5 minute heating.

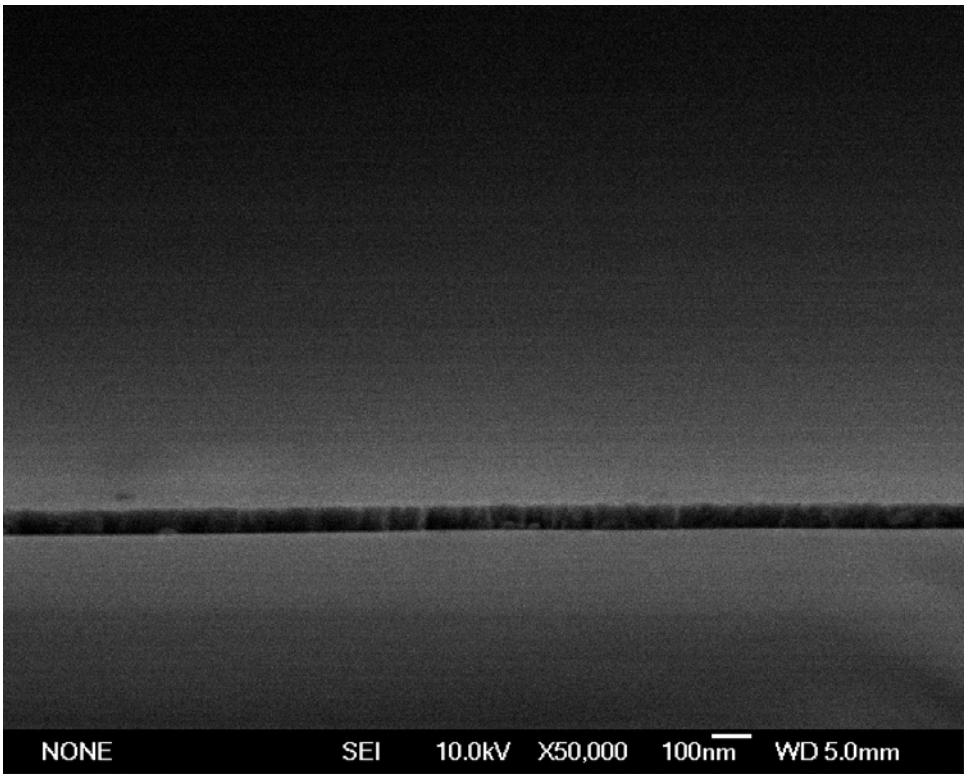

Figure 2.11: Field Emission Scanning Electron Microscope cross section image of a 77 nm thick ruthenium film deposited by SFD. Reaction conditions: 260 °C, 145 bar, 0.09 wt. % Ru(tmhd)$_2$cod, 0.3 wt. % hydrogen, 3 minute heating.

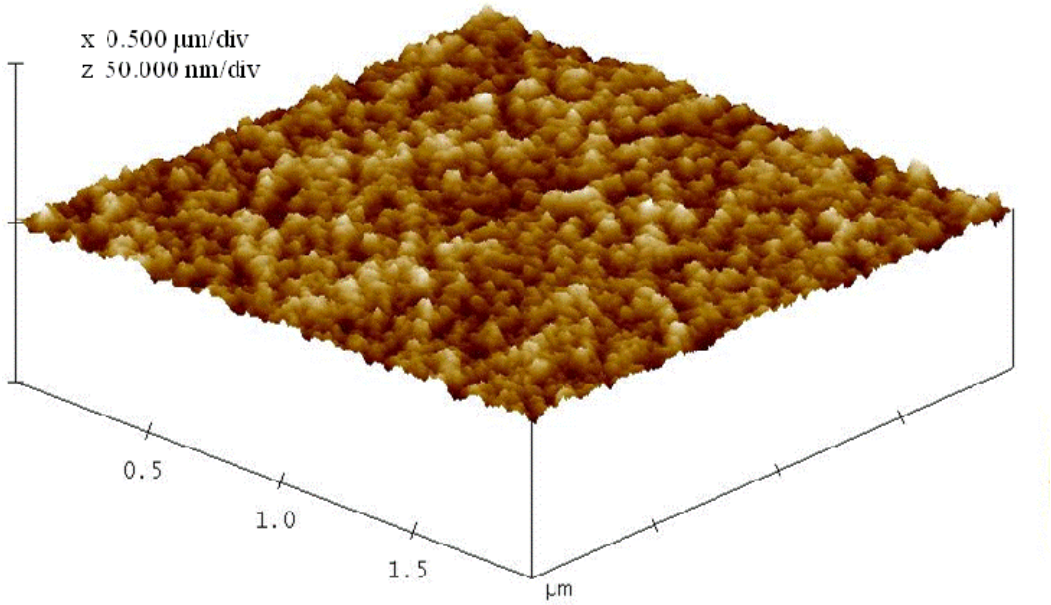

Figure 2.12: Atomic Force Microscopy height data indicating mean surface roughness of 1nm. Reaction conditions: 260 °C, 145 bar, 0.09 wt. % Ru(tmhd)$_2$cod, 0.3 wt. % hydrogen, 3 minute heating

2.3.2 Kinetics

2.3.2.1 Temperature Dependence

The Arrhenius equation is used to determine the activation energy for the SFD of ruthenium films deposited by the hydrogen assisted reduction of $Ru(tmhd)_2cod$. The temperature dependence of growth rate is studied over the range of 240 °C to 280 °C in 10 °C steps (Figure 2.13). The experiments are performed at a constant reaction pressure of 172 bar, a precursor concentration of 0.07 wt. % and hydrogen concentration of 0.3 wt. %. The apparent activation energy is found to be 45.3 kJ/mol.

In other kinetic studies of interest, Papadatos, et al., found the activation energy for $Ru(tmhd)_2cod$ deposition on SiO_2 to be 41.3 kJ/mol using a metal organic CVD (MOCVD) process between 400 – 450 ºC, 1 torr and oxygen and hydrogen as the reactive gases.[54] The same group also found the activation energy for bis(ethylcyclopentadienyl)ruthenium, $Ru(EtCp)_2$, on SiO_2 to be 43 kJ/mol using MOCVD between 320 – 360 ºC, 0.3 torr and oxygen as the reactive gas.[55] Dey, et al., found that the oxygen-assisted pyrolysis of $Ru(tmhd)_2cod$ for the deposition of ruthenium on amorphous HfO_2, has an activation energy of 136 kJ/mol using a liquid source MOCVD process between 250 – 290 ºC.[56]

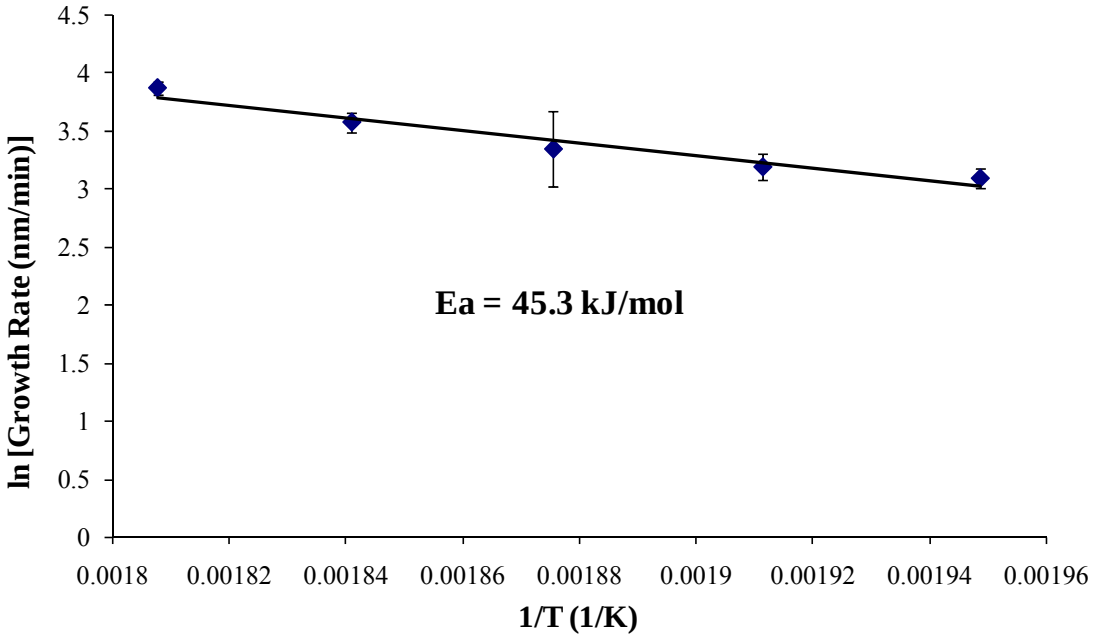

Figure 2.13: Temperature dependence of $Ru(tmhd)_2cod$ by the Arrhenius law for the supercritical fluid deposition of ruthenium thin films from carbon dioxide. Reaction conditions: 240 °C to 280 °C in 10 °C steps, 172 bar, 0.07 wt. % $Ru(tmhd)_2cod$, 0.3 wt. % hydrogen, 3 minutes heating. Apparent activation energy is 45.3 kJ/mol.

2.3.2.2 Precursor Concentration Dependence

The growth rate dependence on precursor concentration is studied at a constant temperature of 260 °C and 280 °C (Figure 2.14). The initial reaction pressure for all reactions is 172 bar. Hydrogen concentration is also held constant for all reactions at 0.3 wt. %. At low precursor concentrations, less than 0.06 wt. %, the growth rate dependence on precursor concentration is first order. Above precursor concentrations of 0.06 wt. %, there was no increase in the growth rate with concentration, indicating zero order dependence. The zero order kinetics of the growth rate with respect to precursor concentration is an enabling feature of SFD that yields conformal film deposition over a

broad process window. The observed zero order kinetics suggests that the rate determining step for this deposition is either the surface reaction or the desorption of byproducts from the active catalytic surface sites.

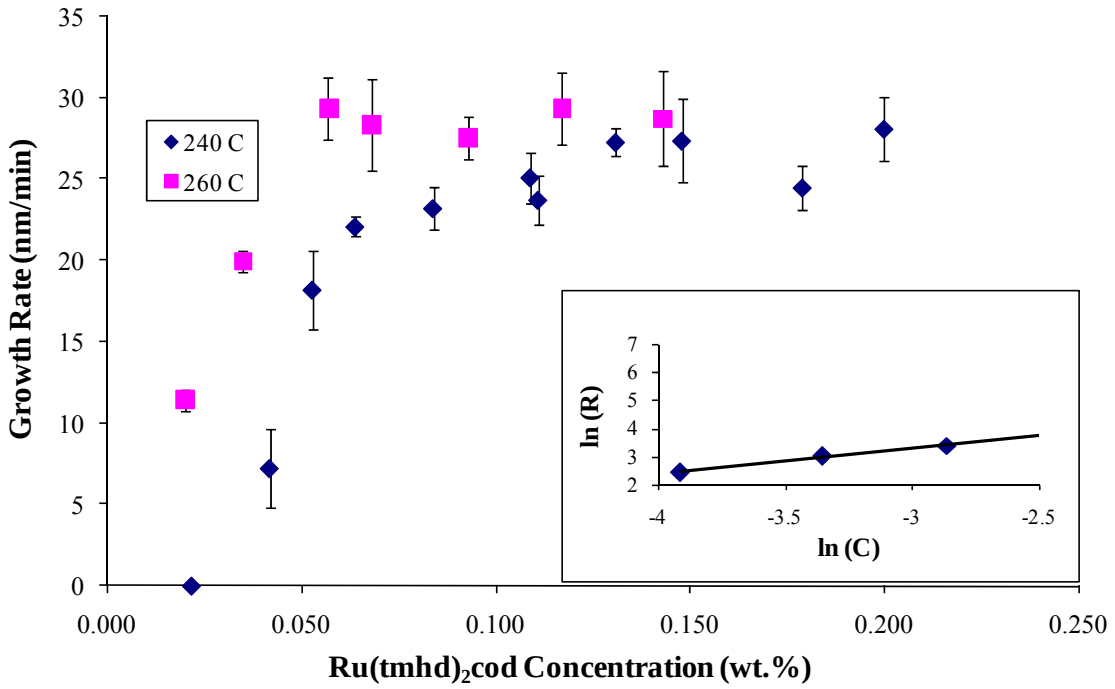

Figure 2.14: Growth rate dependence upon $Ru(tmhd)_2cod$ concentration. Reaction conditions: 260 °C and 280 °C, 172 bar, 0.3 wt. % hydrogen, 3 minutes heating. Using differential kinetics (inset), zero order kinetics is observed at high precursor concentration and first order kinetics at lower precursor concentration.

2.3.2.3 Pressure Dependence

Increasing pressure during SFD increases the density of supercritical carbon dioxide thereby improving its solvent strength. Increases in solvent strength in turn promotes desorption of the precursor decomposition products, which are soluble in the fluid. The effect of pressure (solvent density) on the growth rate may therefore provide

insight into the rate controlling step. If the desorption of precursor is promoted, more surface sites should become available

The results of the study of pressure dependence are shown in Figure 2.15. The temperature is held constant at 260 °C and the hydrogen concentration is held constant at 0.3 wt. % while the pressure is varied between 135 bar and 200 bar. For the entire range of pressures that is studied, it is found that the reaction pressure has no effect on the growth rate of the ruthenium film. The growth rate remains constant at about 27 nm/min. This result suggested that over the range of solvent strengths accessible, density mediated enhancements in the desorption of precursor decomposition products from the active surface sites did not affect the rate of film growth.

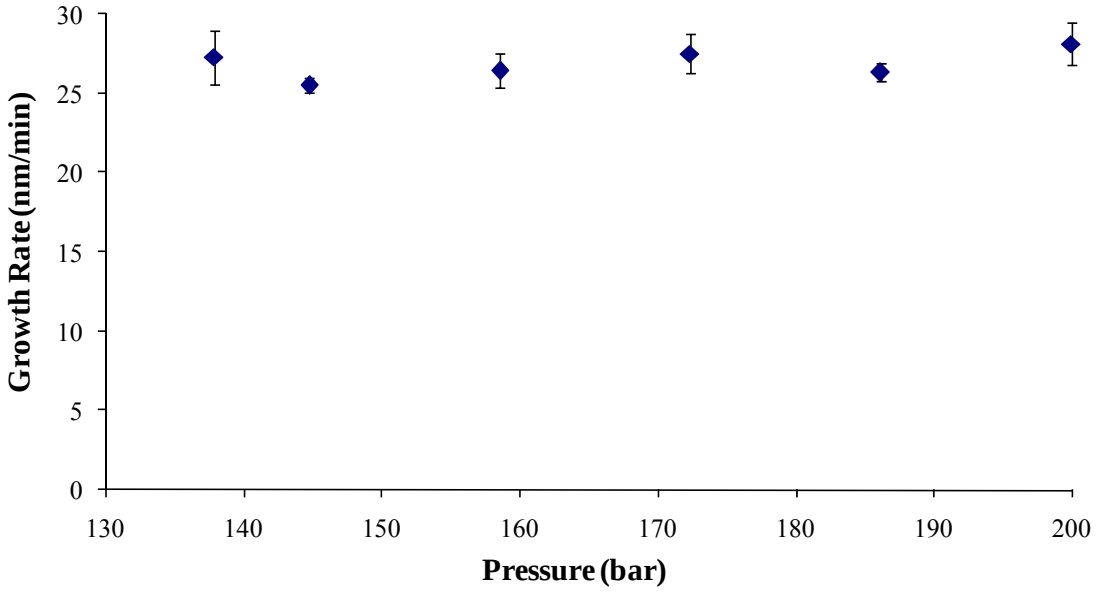

Figure 2.15: Growth rate dependence upon reaction pressure. Reaction conditions: 260 °C, 135 bar to 200 bar, 0.09 wt. % $Ru(tmhd)_2cod$, 0.3 wt. % hydrogen, 3 minutes heating. Pressure does not influence growth rate over the range of 135 bar to 200 bar.

2.3.2.4 Hydrogen Concentration Dependence

The effect of hydrogen concentration on the growth rate of ruthenium films is studied. The data are shown in Figure 2.16. The study is performed at a constant reaction temperature of 260 °C for 3 minutes, 172 bar and $Ru(tmhd)_2cod$ at a loading of 0.09 wt. %. At concentrations above 0.26 wt. % growth rate of the ruthenium film is independent of hydrogen concentration. It is noted that at hydrogen concentrations of 0.4 wt. % and above, the films delaminate due to increased stress in the film, Figure 2.17. At concentrations below 0.26 wt. %, the film growth rate increases with increasing hydrogen concentration. The effect of hydrogen was 2nd order with respect to ruthenium film growth rate. At concentrations of 0.1 wt. % and below, there is no deposition which is attributed to parasitic consumption of the hydrogen, possibly due to deposition on the exposed areas of the heated stage during the time that the substrate was reaching reactive conditions for film deposition.

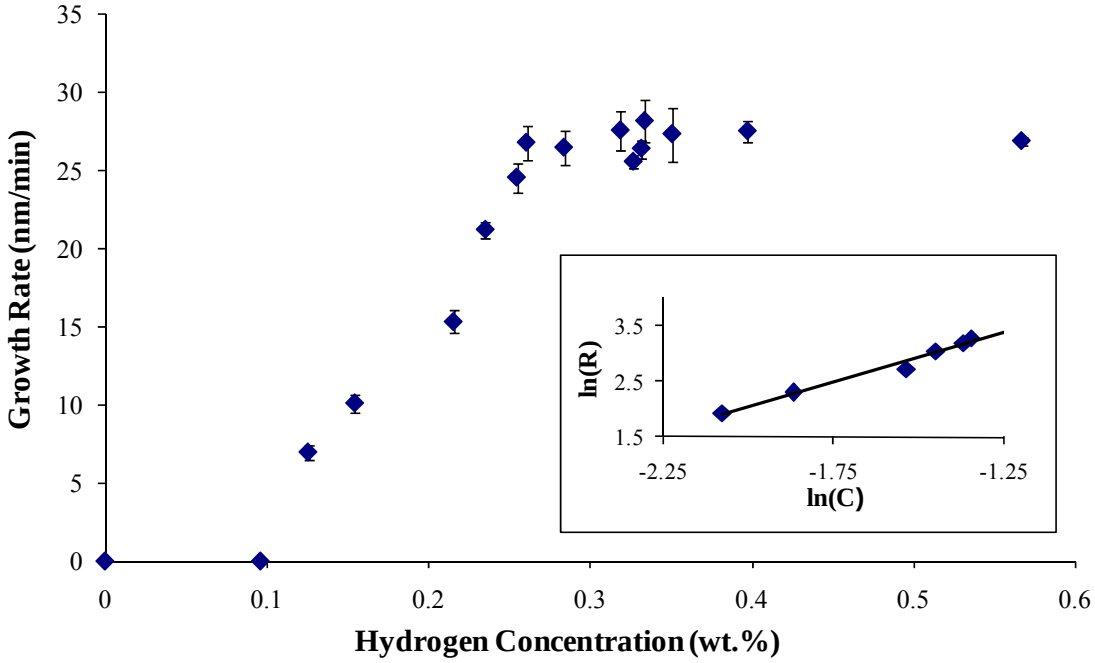

Figure 2.16: Growth rate dependence upon hydrogen concentration. Reaction conditions: 260 °C, 0.09 wt. % $Ru(tmhd)_2cod$, 0 wt. % - 0.6 wt. % hydrogen, 3 minutes heating. Using differential kinetics (inset), zero order kinetics is observed at high hydrogen concentration and 2nd order kinetics at lower concentrations. Parasitic deposition is noted at 0.1 wt. % hydrogen and lower.

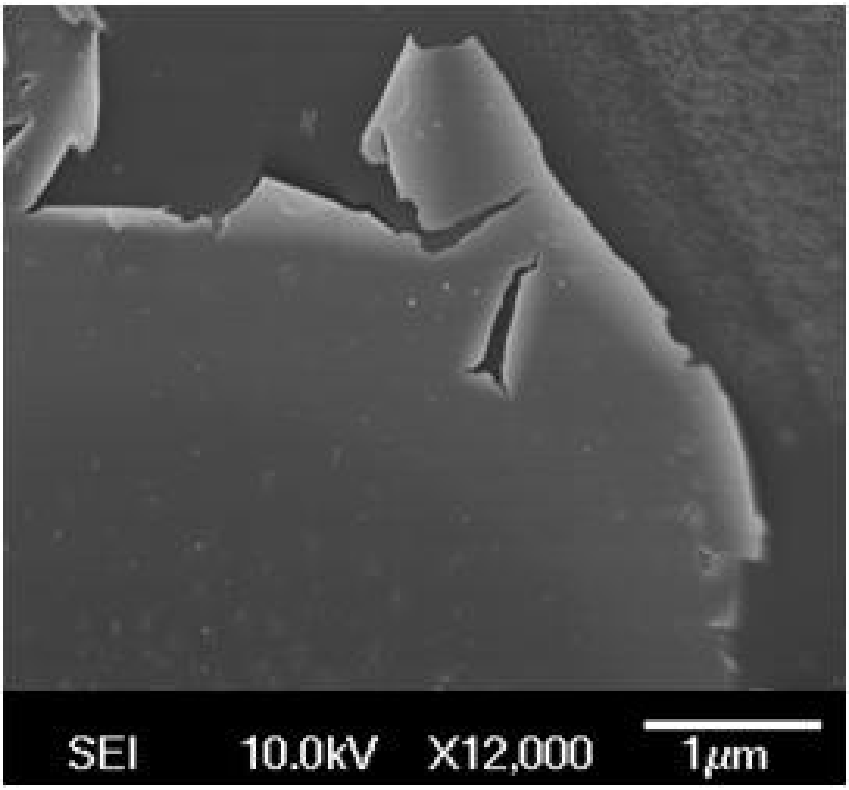

Figure 2.17: Example of a foiled ruthenium film due to increased stress in the film. Reaction conditions: 260 °C, 172 bar, 0.09 wt. % $Ru(tmhd)_2cod$, 0.6 wt. % hydrogen, 3 minutes heating.

2.3.2.5 Byproduct Concentration Dependence

The reaction decomposition products, 1,5-cyclooctadiene (cod), cyclooctane (cot), and 2,2,6,6-tetramethyl-heptane-3,5-dionato (tmhd), are studied to determine their effects on the growth rate. Each byproduct is tested independently of the others over specified ranges. The reactions are carried out at a constant reaction temperature of 260 °C for 3 minutes, 172 bar, 0.9 wt. % $Ru(tmhd)_2cod$, 0.3 wt. % hydrogen. Plots of the data are shown for tmhd, cod and cot in Figure 2.18, Figure 2.19 and Figure 2.20, respectively.

Tmhd and cod concentrations are varied from 0 wt. % to 0.9 wt. % and plots of the data show a negative effect on the growth rate of the films. The differential method of rate analysis was used to determine the reaction order from the inset plot. The slope of

the lines indicates that the growth rate has a negative ½ order dependence for each of the byproducts separately. There are two possibilities to account for this result. Byproduct competition for hydrogen, in order to hydrogenate ligand decomposition products, may have consumed the available hydrogen in the system. However, given that the amount of hydrogen in the reactor is in excess of 1000 times the necessary amount for complete reduction of all loaded precursor, it is not likely the reason. It is proposed that the ligands are occupying the surface active sites thereby reducing the probability for a successful surface reaction.

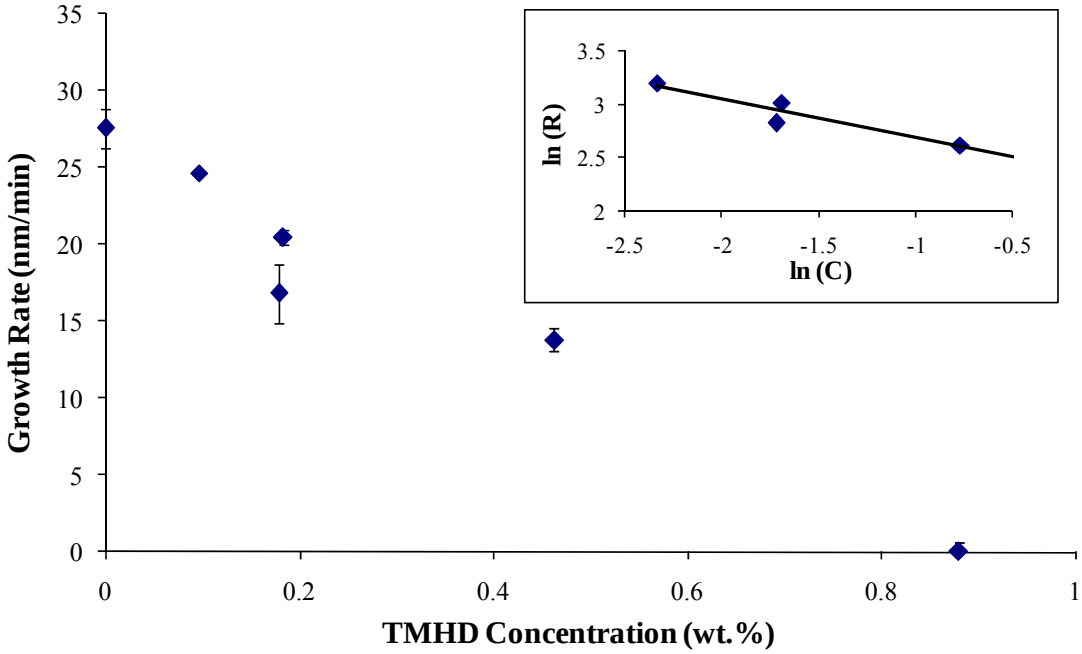

Figure 2.18: Growth rate dependence upon tmhd concentration. Reaction conditions: 260 °C, 0.09 wt. % $Ru(tmhd)_2cod$, 0.3 wt. % hydrogen, 3 minutes heating. Using differential kinetics (inset), negative first order kinetics is observed with addition of tmhd from concentrations between 0 wt. % - 0.9 wt. %.

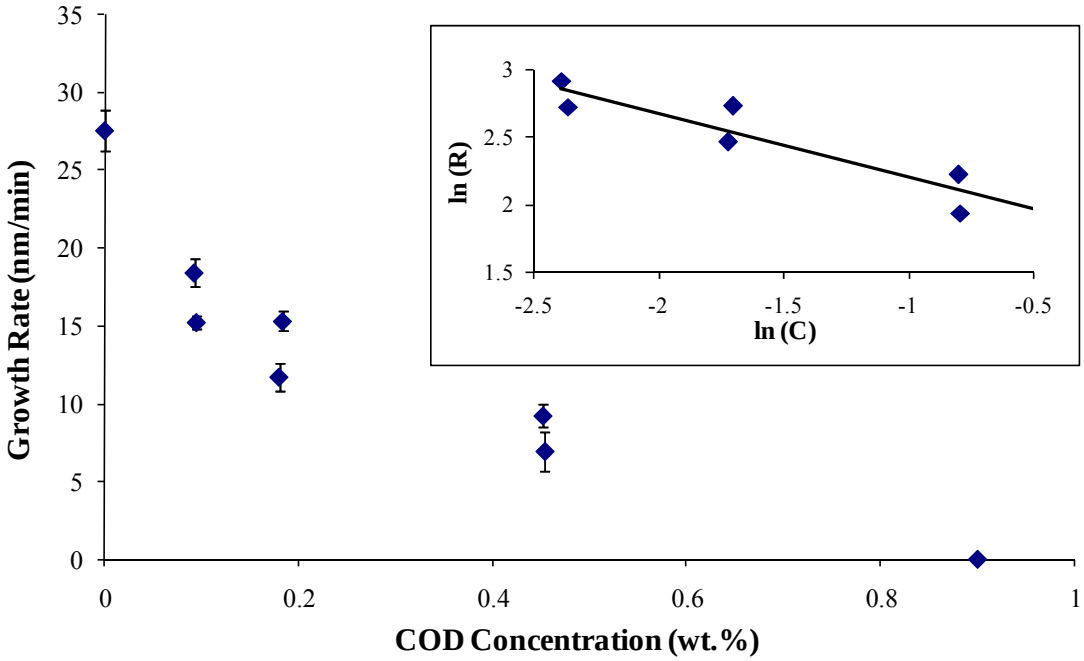

Figure 2.19: Growth rate dependence upon cod concentration. Reaction conditions: 260 °C, 0.09 wt. % Ru(tmhd)$_2$cod, 0.3 wt. % hydrogen, 3 minutes heating. Using differential kinetics (inset), negative first order kinetics is observed with addition of cod from concentrations between 0 wt. % - 0.9 wt. %.

Cot concentration is varied from 0 wt. % to 0.8 wt. %. The data indicate a slight negative trend, however, after differential kinetics analysis, it is a negligible effect. The zero order effect that cot has on growth rate is attributed to its low affinity for absorption to the surface after being formed from hydrogenation of cod and cyclooctene, coe.

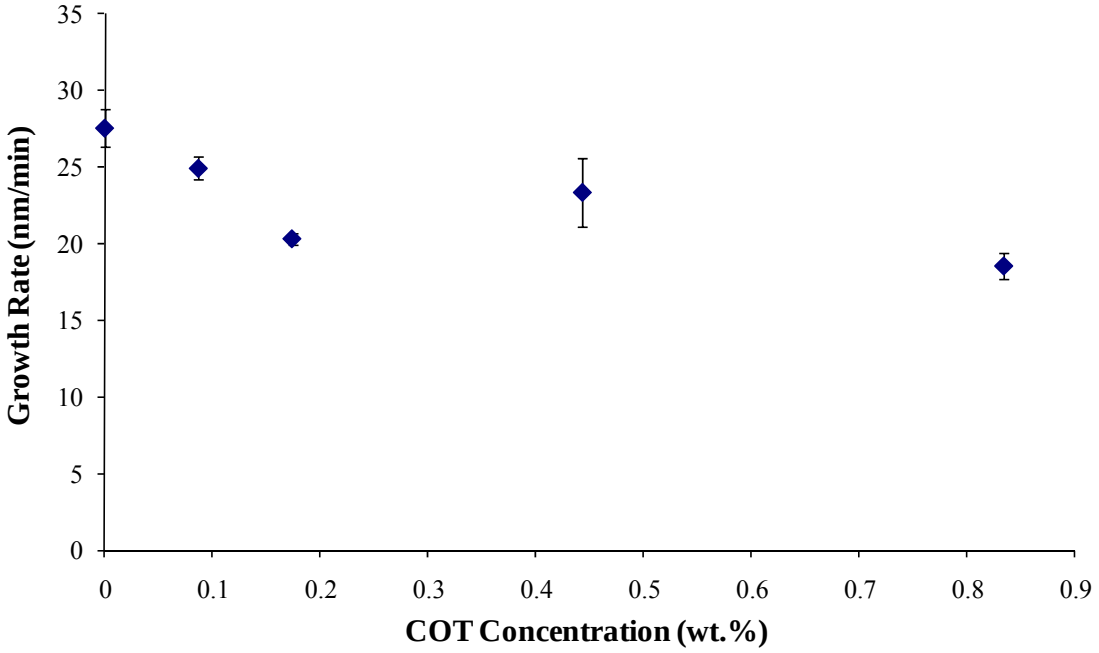

Figure 2.20: Growth rate dependence upon cot concentration. Reaction conditions: 260 °C, 0.09 wt. % Ru(tmhd)$_2$cod, 0.3 wt. % hydrogen, 3 minutes heating. Cot has a weak negative effect on growth rates between 0 wt. % - 0.9 wt. %.

2.3.3 Equilibrium and Mechanism

In 1995, Hampdensmith and Kodas[30, 31] described the CVD of metal films as an eight step process. From experimental findings, it is believed that this is very similar to what is occurring in the SFD process. It is then advantageous to then use this overview of the CVD process as a starting point for developing the kinetics behind the deposition of ruthenium films from supercritical fluids.

In a kinetic study performed by Dey, et al.[56] in 2003, a low pressure, horizontal MOCVD hot wall reactor was used to study the deposition of ruthenium from the oxygen-assisted pyrolysis of Ru(tmhd)$_2$cod by liquid-source MOCVD. The depositions were conducted on $HfO_2/SiO_2/Si$ substrates between temperatures of 250 – 320 °C. The

activation energy was found to be 136 kJ/mol for the surface reaction limited regime which occurred between 250 – 290 °C and below. As temperature increased past 290 °C, the surface reaction limited regime for growth gave way to the mass transfer limited regime as growth rate became independent of temperature.

In 2002, Papadatos, et al.,[54] performed ruthenium depositions from $Ru(tmhd)_2cod$ on SiO_2/Si using MOCVD and PACVD. Data on growth rates indicate an activation energy of 59.4 kJ/mol and 41.3 kJ/mol for PACVD and MOCVD, respectively. Again, in 2004, Papadatos, et al.[55] reported ruthenium depositions from $Ru(EtCp)_2$ on SiO_2/Si using MOCVD. The activation energy was found to be 43 kJ/mol.

Similarly, ruthenium and various other metals can be deposited from supercritical carbon dioxide ($SCCO_2$) for device fabrication on both planar and patterned substrates. The process is initiated with the addition of a reducing agent, specifically, hydrogen. Due to $SCCO_2$ miscibility with hydrogen and the absence of surface tension, infiltration into complex features is possible. With its ability to readily dissolve many precursors due to its liquid like density, it is possible to deposit highly conformal films in very complex geometries at rates much faster than can be realized with techniques such as CVD and ALD. Film contamination, as a result of reaction byproducts, is eliminated since byproducts are readily desorbed from the surface due to their high solubility in the $SCCO_2$. However, to date, only one attempt has been made to describe the kinetics underlying this deposition mechanism.

In 2005, Zong, et al.[46] investigated the hydrogen assisted reduction of bis-(2,2,7-trimethyloctane-3,5dionato)copper(II) in supercritical carbon dioxide via the use of a temperature controlled cold wall reactor with resistive substrate heating. The activation

energy was found to be 51.9 kJ/mol and a Langmuir – Hinshelwood rate expression was used to represent the data. It was found that growth rate was zero order with respect to pressure, precursor concentration and hydrogen concentration. However, at low concentrations of either precursor or hydrogen, half order dependence was noted. All byproducts studied indicated a negative effect on growth rate as concentration was increased. It was proposed that the rate determining step was the surface reaction.

The deposition of ruthenium from $Ru(tmhd)_2cod$, although analogous in process to the deposition of copper from $Cu(tmod)_2$, is much more complicated mechanistically due to the addition of a cyclooctadiene ligand and its behavior in $SCCO_2$.

Cod has been shown to enhance solubility of precursors in $SCCO_2$ because it can shield the positive electrical charge of various metal centers.[47] However, as the reaction proceeds and the cod concentration increases, a negative effect on growth rate is observed due to its competition for hydrogen in order to reduce to its monoene and its competition for surface active sites, thereby reducing the number of available sites to allow the desired reaction to continue.

A number of studies have been carried out in order to better understand the hydrogenation of cod. It was observed that 1,5 cod is isomerized to the conjugated diene, 1,3 cod, due to the lower energy state.[57] The conjugated diene then more quickly hydrogenated to coe. Additionally, the presence of cod and its ability to more readily adsorb to the surface hindered the following hydrogenation of coe to cot. It was found that the activation energy for the reduction of cod to coe over a $Pd/\alpha\text{-}Al_2O_3$ catalyst was 74 kJ/mol while the activation energy was 98 kJ/mol for coe to cot.[58] Haas and Gaube[59] reported that the hydrogenation of cod occurs 6 times faster than the hydrogenation of

coe. These findings indicated a first order hydrogenation with respect to cod at low concentrations and a much lower rate at higher concentrations of cod due to the competition for surface sites, resulting in low hydrogen surface concentrations at higher cod concentrations.

Based upon previous CVD and SFD studies as well as observed experimental results, the following reaction sequence is proposed for the deposition of ruthenium from $Ru(tmhd)_2cod$ in $SCCO_2$.

$Ru(tmhd)_2cod + 2^* \leftrightarrow Ru\ tmhd\ cod^* + tmhd^*$ Equation 01

$Ru\ tmhd\ cod^* + * \leftrightarrow Ru\ cod^* + tmhd^*$ Equation 02

$Ru\ tmhd\ cod^* + * \leftrightarrow Ru\ tmhd^* + cod^*$ Equation 03

$Ru(tmhd)_2cod + 2^* \leftrightarrow Ru\ (tmhd)_2^* + cod^*$ Equation 04

$Ru\ (tmhd)_2^* + * \leftrightarrow Ru\ tmhd^* + tmhd^*$ Equation 05

$H_2 + 2^{**} \leftrightarrow 2H^{**}$ Equation 06

$2H^{**} + cod^* \leftrightarrow coe^* + 2^{**}$ Equation 07

$2H^{**} + coe^* \leftrightarrow cot^* + 2^{**}$ Equation 08

$cod^* \leftrightarrow * + cod_{(g)}$ Equation 09

$coe^* \leftrightarrow * + coe_{(g)}$ Equation 10

$cot^* \leftrightarrow * + cot_{(g)}$ Equation 11

$Ru\ tmhd^* \leftrightarrow Ru_{(s)} + tmhd^*$ Equation 12

$Ru\ cod^* \leftrightarrow Ru_{(s)} + cod^*$ Equation 13

$H^{**} + tmhd^* \rightarrow (tmhd)H^* + **$ Equation 14

$(tmhd)H^* \leftrightarrow * + (tmhd)H_{(g)}$ Equation 15

* and ** represent different surface active sites available for chemisorptions. Equation 01 – 05 is the precursor adsorption to the first surface active site and ligand dissociation from the chelated metal center to the surface while equation 06 is the adsorption and dissociation of atomic hydrogen to molecular hydrogen on the second surface active site. Equation 07 – 11 is the conversion of cod to cot and their subsequent desorption. Equation 12 and 13 are film creation. Equation 14 is the rate determining step which is the surface reaction in which bound hydrogen protonates bound ligand. Equation 15 is the desorption of hydrogenated ligand back into the $SCCO_2$. A graphical representation of the proposed mechanism is shown in Figure 2.21.

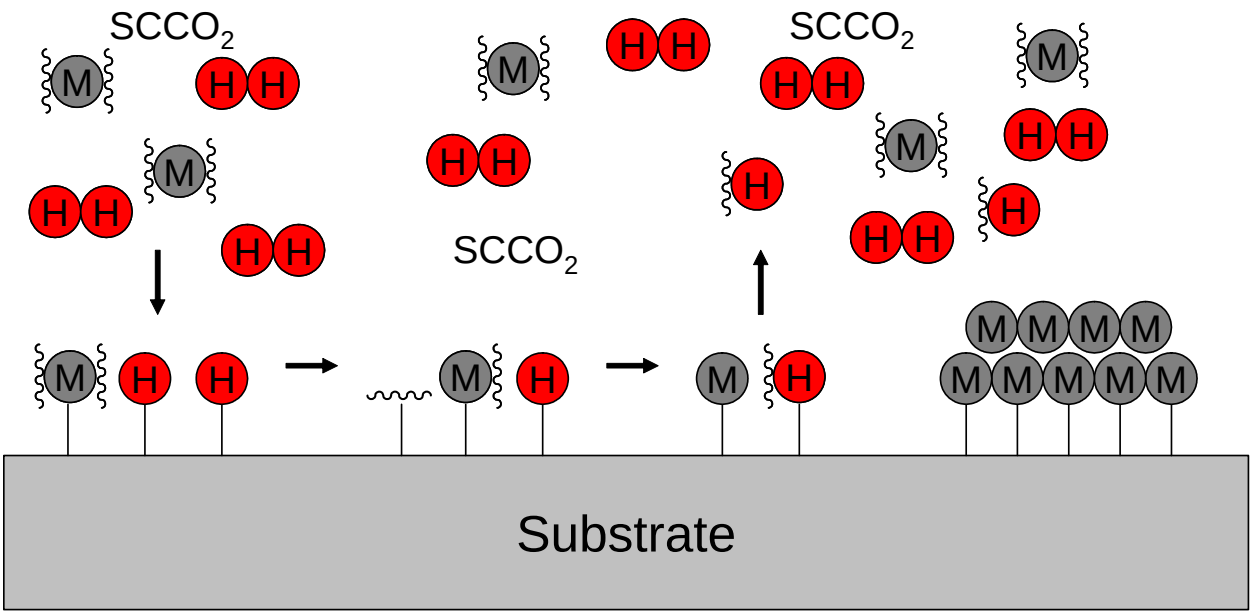

Figure 2.21: Schematic of the proposed mechanism for the deposition of ruthenium via the hydrogen assisted reduction of bis(2,2,6,6-tetramethyl-heptane-3,5-dionato)(1,5-cyclooctadiene)ruthenium(II) in supercritical carbon dioxide via the supercritical fluid deposition process.

2.4 Conclusions

The kinetics of ruthenium film deposition by supercritical fluid deposition using bis(2,2,6,6-tetramethyl-heptane-3,5-dionato)(1,5-cyclooctadiene)ruthenium(II) as the

precursor is studied. Reaction rate orders are determined as well as proposing a Langmuir – Hinshelwood deposition mechanism. It is found that the apparent activation energy is 45.3 kJ/mol over the temperature range of 240 °C to 280 °C. The dependence of precursor concentration on growth rate is found to be first order for concentrations less than 0.06 wt. % and zero order for concentrations higher than 0.06 wt. %. Zero order deposition kinetics is an enabling feature of SFD that provides conformal film deposition in high aspect ratio and topographically complex features. It is also determined that reaction pressure has no effect on the growth rate over a large process window of 135 bar to 200 bar. Hydrogen concentration is studied and found to have a 2nd order effect on growth rate for concentrations less than 0.26 wt. % and a zero order effect on concentrations above that. Precursor decomposition products (tmhd, cod and cot) are studied. Tmhd and cod are shown to have a negative 1st order effect on film growth which is attributed to their competition for surface active sites thereby decreasing the probability of a successful surface reaction. Cot shows negligible negative effects on growth rate which is attributed to cot having no affinity for the surface. The surface reaction is found to be rate determining.

2.5 References

(1) International Technology Roadmap for Semiconductors, http://www.itrs.net/, **2007**

(2) R. Chan, T. N. Arunagiri, Y. Zhang, O. Chyan, R. M. Wallace, M. J. Kim, T. Q. Hurd, *Electrochemical and Solid-State Letters* **2004**, *7*, G154-G157.

(3) C. Cheng, T. Arunagiri, O. Chyan, *American Journal of Undergraduate Research* **2003**, *2*, 11-18.

(4) T. Aoyama, K. Eguchi, *Japanease Journal of Applied Physics* **1999**, *38*, L1134-L1136.

(5) T. Aoyama, M. Kiyotoshi, S. Yamazaki, K. Eguchi, *Japanease Journal of Applied Physics* **1999**, *38*, 2194-2199.

(6) A. D. Berry, D. K. Brown, R. Kaplan, E. J. Cukauskas, *Journal of Vacuum Science and Technology A: Vacuum, Surfaces, and Films* **1986**, *4*, 215-218.

(7) E. P. Boyd, D. R. Ketchum, B. Deng, S. G. Shore, *Chemistry of Materials* **1997**, *9*, 1154-1158.

(8) Y. Chi, F. J. Lee, C.-S. Liu, *USA Patent U.S. Patent 6,303,809*, **2001**.

(9) J. N. Crosby, R. S. Hanley, *United States Patent U.S. Patent 4,250,210*, **1981**.

(10) X. Jin, C. P. Wade, X. Tao, E. Pao, Y. Wang, J. Zhao, *USA Patent U.S. Patent 6,479,100*, **2002**.

(11) M. Kadoshima, T. Nabatame, M. Hiratani, Y. Nakamura, *Japanease Journal of Applied Physics* **2002**, *41*, L347-L350.

(12) J. J. Kim, D. H. Jung, M. S. Kim, S. H. Kim, D. Y. Yoon, *Thin Solid Films* **2002**, *409*, 28-32.

(13) Y.-H. Lai, Y.-L. Chen, Y. Chi, C.-S. Liu, A. J. Carty, S.-M. Peng, G.-H. Lee, *Journal of Materials Chemistry* **2003**, *13*, 1999-2006.

(14) M. Lashdaf, T. Hatanpaa, A. O. I. Krause, J. Lahtinen, M. Lindblad, M. Tiitta, *Applied Catalysis A: General* **2003**, *241*, 51-63.

(15) D.-J. Lee, S.-W. Kang, S.-W. Rhee, *Thin Solid Films* **2002**, *413*, 237-242.

(16) F.-J. Lee, Y. Chi, C.-S. Liu, P.-F. Hsu, T.-Y. Chou, S.-M. Peng, G.-H. Lee, *Chemical Vapor Deposition* **2001**, *7*, 99-101.

(17) J.-H. Lee, J.-Y. Kim, S.-W. Rhee, D. Yang, D.-H. Kim, C.-H. Yang, Y.-K. Han, C.-J. Hwang, *Journal of Vacuum Science and Technology A: Vacuum, Surfaces, and Films* **2000**, *18*, 2400-2403.

(18) J. M. Lee, J. C. Shin, C. S. Hwang, H. J. Kim, *Journal of Vacuum Science and Technology A: Vacuum, Surfaces, and Films* **1998**, *16*, 2768-2771.

(19) S.-H. Lee, J.-K. Chun, J.-J. Hur, J.-S. Lee, G.-H. Rue, Y.-H. Bae, S.-H. Hahm, Y.-H. Lee, H.-H. Lee, *IEEE Electron Device Letters* **2000**, *21*, 261-263.

(20) Y. Matsui, M. Hiratani, T. Nabatame, Y. Shimamoto, S. Kimura, *Electrochemical and Solid-State Letters* **2001**, *4*, C9-C12.

(21) Y. Matsui, M. Hiratani, T. Nabatame, Y. Shimamoto, S. Kimura, *Electrochemical and Solid-State Letters* **2002**, *5*, C18-C21.

(22) T. Nabatame, M. Hiratani, M. Kadoshima, Y. Shimamoto, *Japanease Journal of Applied Physics* **2000**, *39*, L1188-L1190.

(23) S.-E. Park, H.-M. Kim, K.-B. Kim, S.-H. Min, *Journal of the Electrochemical Society* **2000**, *147*, 203-209.

(24) Y. Senzaki, W. L. Gladfelter, F. B. McCormick, *Chemistry of Materials* **1993**, *5*, 1715-1721.

(25) Y. Senzaki, F. B. McCormick, W. L. Gladfelter, *Chemistry of Materials* **1992**, *4*, 747-749.

(26) D. E. Trent, B. Paris, H. H. Krause, *Inorganic Chemistry* **1964**, *3*, 1057-1058.

(27) C. P. Wade, E. Pao, Y. Wang, J. Zhao, *USA Patent 6,440,495*, **2002**.

(28) Q. Wang, J. G. Ekerdt, D. Gay, Y.-M. Sun, J. M. White, *Applied Physics Letters* **2004**, *84*, 1380-1382.

(29) L. Chen, N. Magtoto, B. Ekstrom, J. Kelber, *Thin Solid Films* **2000**, *376*, 115-123.

(30) M. J. Hampden-Smith, T. T. Kodas, *Chemical Vapor Deposition* **1995**, *1*, 8-23.

(31) M. J. Hampden-Smith, T. T. Kodas, *Chemical Vapor Deposition* **1995**, *1*, 39-48.

(32) A. O'Neil, J. J. Watkins, *Chemistry of Materials* **2006**, *18*, 5652-5658.

(33) J. M. Blackburn, A. Cabanas, D. P. Long, J. J. Watkins, *Abstracts of Papers of the American Chemical Society* **2002**, *223*, U663-U664.

(34) J. M. Blackburn, D. P. Long, A. Cabanas, J. J. Watkins, *Science* **2001**, *294*, 141-145.

(35) J. M. Blackburn, D. P. Long, J. J. Watkins, *Chemistry of Materials* **2000**, *12*, 2625-2631.

(36) A. Cabanas, J. M. Blackburn, J. J. Watkins, *Microelectronic Engineering* **2002**, *64*, 53-61.

(37) A. Cabanas, D. P. Long, J. J. Watkins, *Chemistry of Materials* **2004**, *16*, 2028-2033.

(38) A. Cabanas, X. Shan, J. J. Watkins, *Chemistry of Materials* **2003**, *15*, 2910-2916.

(39) N. E. Fernandes, S. M. Fisher, J. C. Poshusta, D. G. Vlachos, M. Tsapatsis, J. J. Watkins, *Chemistry of Materials* **2001**, *13*, 2023-2031.

(40) E. T. Hunde, J. J. Watkins, *Chemistry of Materials* **2004**, *16*, 498-503.

(41) E. Kondoh, *Japanese Journal of Applied Physics* **2004**, *43*, 3928-3933.

(42) E. Kondoh, *Japanese Journal of Applied Physics* **2005**, *44*, 5799-5802.

(43) E. Kondoh, K. Shigama, *Thin Solid Films* **2005**, *491*, 228-234.

(44) D. P. Long, J. M. Blackburn, J. J. Watkins, *Advanced Materials* **2000**, *12*, 913-915.

(45) J. J. Watkins, J. M. Blackburn, T. J. McCarthy, *Chemistry of Materials* **1999**, *11*, 213-215.

(46) Y. Zong, J. J. Watkins, *Chemistry of Materials* **2005**, *17*, 560-565.

(47) O. Aschenbrenner, S. Kemper, N. Dahmena, K. Schaber, E. Dinjus, *The Journal of Superciritcal Fluids* **2007**, *41*, 179-186.

(48) X. Shan, D. P. Schmidt, J. J. Watkins, *The Journal of Supercritical Fluids* **2007**, *40*, 84-92.

(49) Y. Baer, P. F. Heden, J. Hedman, M. Klasson, C. Nordling, K. Siegbahn, *Physica Scripta* **1970**, *1*, 55-65.

(50) G. B. Fisher, N. E. Erikson, T. E. Madey, J. John T. Yates, *Surface Sciences* **1977**, *65*, 210-228.

(51) B. Folkesson, *Acta Chemica Scandinavica* **1973**, *27*, 287-302.

(52) K. S. Kim, N. Winograd, *Journal of Catalysis* **1974**, *35*, 66-72.

(53) R. Nyholm, N. Martensson, *Journal of Physics C: Solid State Physics* **1980**, *13*, L279-L284.

(54) F. Papadatos, S. Skordas, Z. Patel, S. Consiglio, E. Eisenbraun, "Chemical Vapor Deposition of Ru and RuO2 for Gate Eelectrode Applications", presented at *Material Research Society*, **2002**.

(55) F. Papadatos, S. Consiglio, S. Skordas, E. T. Eisenbraun, A. E. Kaloyeros, J. Peck, D. Thompson, C. Hoover, *Journal of Materials Research* **2004**, *19*, 2947-2955.

(56) S. K. Dey, J. Goswami, A. Das, W. Cao, M. Floyd, R. Carpenter, *Journal of Applied Physics* **2003**, *94*, 774-777.

(57) M. Di-Serio, V. Valato, A. Dimiccoli, L. Maffucci, P. Iengo, E. Santacesaria, *Catalysis Today* **2001**, *66*, 403-410.

(58) A. Schmidt, R. Schomacker, *Ind. Eng. Chem. Res.* **2007**, *46*, 1677-1681.

(59) T. Haas, J. Gaube, *Chemical Engineering and Technology* **1989**, *12*, 45-53.

CHAPTER 3

THIN FILM ADHESION AND FOUR-POINT BEND FRACTURE MECHANICS

3.1 Introduction

In the semiconductor industry, copper is currently the industry standard material used for interconnects in advanced integrated circuits (IC). Originally, aluminum was used because it is cheap and easy to pattern. However, as dimensions were reduced, lower resistances were needed for interconnect material to compensate for reduced current. Additionally, aluminum has a lower electromigration resistance and an increased surface roughness as compared to copper, both of which are problematic for ICs. This made for a quick transition to copper since the ICs in production have deep sub-micron features which greatly benefited from higher electromigration resistance and lower electrical resistance. The introduction of copper itself, however, is not without complication as it has a high diffusivity in semiconductors, like Si, which ultimately degrades and destroys the IC. This necessitates the use of a barrier layer, typically TaN. Copper is also easily oxidized and does not self-passivate thereby limiting further oxidization. Finally, the adhesion of copper is poor to most other materials, most importantly, TaN. This presents a reliability issue for ICs that must be addressed through the use of interfacial adhesion enhancement methods if the copper interconnects are to withstand chemical mechanical planarization (CMP) used in the dual damascene process.

The production of copper interconnects for IC is a two step process. Initially, the deposition of a Cu seed layer by sputtering, a common type of physical vapor deposition (PVD), is performed. Next, electrochemical deposition is used to perform a bottom-up

fill of the interconnect trench. Due to PVD being a line of sight technique, it is difficult to sputter conformal and defect free copper seed layers in trenches as device dimensions are reduced below the 32 nm node. Subsequent electrochemical filling of these features can create voids that cause high resistance and open circuits.

While the two step PVD seed layer – electrochemical fill process has been adapted to meet the demands of current interconnect dimensions, there are serious concerns that this approach will fail to do so in the future. Consequently, an alternative solution is needed. Other deposition techniques include atomic layer deposition (ALD), chemical vapor deposition (CVD) and supercritical fluid deposition (SFD). Although CVD can in principle be used to deposit conformal copper, it fails to do so in high aspect ratio feature. Additionally, it suffers from both inefficient consumption of the precursor and poor adhesion.[1, 2] Low precursor conversion is attributed to low precursor concentrations, which is a function of the low precursor vapor pressure. Poor adhesion is attributed to contamination of the interface between the trench (barrier layer) and the deposited copper. Contamination is from precursor byproducts of the reaction, typically the ligand, and from oxidation of the barrier layer.[1-4] ALD is a CVD variant using alternating precursor gas exposure for self-limited reactions to form films with precise composition, conformal coverage, exceptionally high interfacial adhesion and thickness control on the angstrom level. ALD, although a candidate for conformal films with precise composition control, is only a time effective solution at sub-monolayer thicknesses requiring significantly longer processing times for thicker films, thus making it unsuitable for industrial integration. Additionally, ALD provides no solution for the important Cu/Ta/TaN seed/barrier layer formation used for ICs.[5-9] SFD presents a unique

solution for the single step, rapid and conformal deposition of films in high aspect ratio features with near complete precursor conversion. Unfortunately, films deposited with this method still have weak adhesion from oxidation at the barrier during deposition. It is the focus of this study to outline current progress in increasing interfacial adhesion of copper to barrier layers, of which SFD specific solutions have been identified, and to explore quantitative methods of analyzing this increased adhesion. This enhances the likelihood that a single step process for the efficient and conformal filling of Cu into Ta/TaN for seed/barrier systems of high aspect ratios can seamlessly be integrated into the microelectronics industry.

There are a variety of reasons why poor adhesion is experienced with deposited films. As mentioned previously, the reaction chemistry used has a significant effect on the adhesion of deposited films. With methods like CVD and SFD, which use reduction chemistry, significant contamination can occur at the interface, which reduces adhesion. The precursors used in SFD and CVD typically have a hydrocarbon or fluorine based ligand that is chelated to a metal core. The purpose being that the ligand increases the solubility of the metal in whichever medium used.[10-12] The reduction reaction reduces the ligands and leaves behind the metal center for deposition[1, 2], typically modeled after Langmuir – Hinshelwood kinetics. However, the reduced ligands are trapped at the interface and reduce the number of sites for bonding, thereby decreasing adhesion.

Additional causes of poor adhesion include process defects and oxidation at the interface. Process defects, typically gaps and cracks formed by stress, greatly reduce adhesion. Oxidation is an important aspect of adhesion that is usually overlooked. By directly addressing the oxidation at the interface, it is possible to increase the number of

sites with which the deposited film can bond with the previous layer. Copper is easily oxidized in the presence of oxygen in very small quantities. Therefore, for the reduction of precursors for copper deposition, it is advantageous to work in an inert atmosphere. In SFD, a high density CO_2 atmosphere is used which drastically reduces the potential for copper oxidation thereby giving way to greater adhesion.

There are multiple approaches that have been used toward the end goal of increasing adhesion between copper and its barrier layer. Self-assembled molecular nanolayers (MNLs) have been employed in order to increase adhesion from the angle of improving interfacial bonding. 3-mercapto-propyl-tri-methyoxy-silane (MPTMS) MNLs have been used for PVD deposited Cu/SiO_2 interfaces resulting in a threefold increase in adhesion.[13-15] Mutli-layers of vinyl silane monomers were cross-linked to form C-Si films which increase adhesion.[16, 17] Poly(dimethylsiloxane) was used to cold weld gold contacts together at ambient conditions.[18] Unfortunately, these MNLs have low stability at temperatures exceeding 400 ºC due to desorption or degradation. Ramanath et al. recently reported the use of the same MPTMS's previously reported, however with the improvement of stability at temperatures exceeding the MNL's desorption temperature.[19] Additional methods for increasing adhesion by improving interfacial bonding include the alloying of other metals, such as aluminum, magnesium and ruthenium to copper.[20-27] Even though these alloyed metals show two- and threefold increases in adhesion, they are currently not used in industry.

Taking advantage of the relatively inert environment of supercritical carbon dioxide used during SFD, Zong et al. reported the use of ultrathin layers of poly(acrylic acid) (PAA)on diffusion barrier layers of TiN, Ta and TaN to dramatically increase the

adhesion of copper films to these barrier layers by preventing interfacial oxidation through the hydrogen assisted reduction of bis(2,2,7-trimethyloctane-3,5-dionato) copper.[28] The pretreatment of the silicon substrates with PAA was performed by either spin coating of PAA or vapor phase exposure of PAA. Additionally, it was suggested that this method be extended to more complex substrates by the adsorption of acrylic acid to the substrate and subsequent thermal or UV polymerization to PAA to achieve the same pretreatment effect. Post copper deposition XPS indicated that there was no PAA layer at the copper/barrier interface, which indicates that the PAA layer was completely sacrificial at the reaction conditions used. The increased adhesion was attributed to the reduction of oxides at the interface due to the presence and subsequent degradation of the PAA layer at the interface.

Within the microelectronics industry, there exists a need for a standard quantitative method of measuring adhesion. It will then be possible to fully understand the mechanisms of adhesion, which will make it possible to fully exploit the potential of thin films for this critical application. Due to this need, a wide range of measurements have been developed. However, the majority of these (scribed tape test, scratch test, peel test and many others[29-36]) are qualitative since they only allow for visual comparison for quality control purposes. Therefore, the results of these numerous tests make it impossible to compare material properties outside of individual tests. If tests are more quantitative, then a direct comparison of critical energies can be made and understanding the energy dissipative mechanisms of interfacial adhesion would be possible.

Typical tests including micro indentation, the pull-off test, the blister test, the edge-delamination test and the four-point bend test are all quantitative measurements.[37-42]

Unfortunately, the majority of these are designed for macro scale films. A few, however, can be extended to thin film adhesion; of these, some still suffer further from difficult sample preparation methods. However, over the recent years, four-point bend has emerged as the industry standard method of quantitatively measuring thin film adhesion.[43-54] The four-point bending method is the method of choice not necessarily because sample preparation is easier, but because the experimental data is relatively easier to interpret. This is primarily because of two reasons, the first being that the method is based on established fracture mechanics, and the second being that the film is bonded to one substrate in the crack wake and consequently the residual stress in the film is not relieved to contribute to the crack driving force (energy release rate).

3.2 Experimental

3.2.1 Equipment

3.2.1.1 Cold Wall Reactor

The deposition of copper is carried out in a cold wall reactor, Figure 1. The reactor consists of two opposed 316 stainless steel flanges sealed with a 2-236 Buna-N o-ring. The internal volume of the reactor is approximately 70 cm^3. A custom designed 2.3” diameter aluminum sample stage, Appendix B, with 450 W coiled resistive heater (Belilove Company Engineers, Hayward, CA) is installed at the bottom of the reactor with a high pressure sealing split gland fitting (Conax Buffalo Corp, Buffalo, NY). The wall of the stainless steel reactor is heated using four 3” long, 120 V, 170 W cartridge heaters and is maintained at a lower temperature than the reaction stage in order to induce selective deposition to the higher temperature sample stage. The heated sample stage and

reactor wall are controlled and heated separately using custom built temperature controllers consisting of a solid state relay (Omega Engineering Inc, Stamford, CT) and microprocessor-based temperature controller, model CN76000 (Omega Engineering Inc, Stamford, CT) encased in an aluminum enclosure.

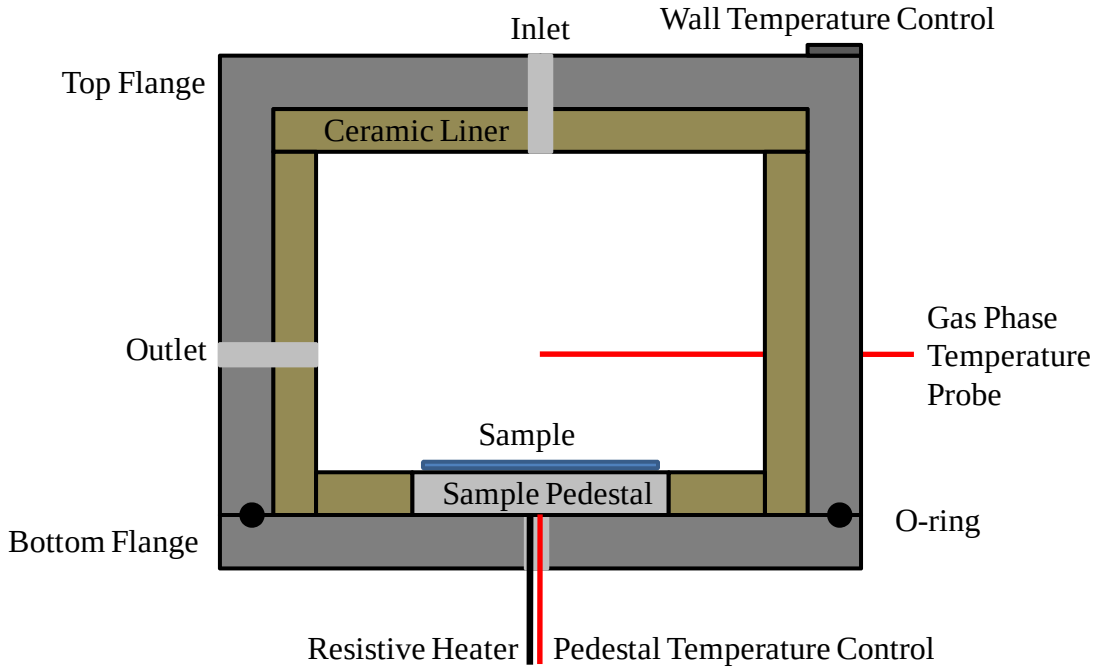

Figure 3.1: Custom built 316 stainless steel cold wall reactor with resistive heated aluminum sample stage.

3.2.1.2 Dicing Saw

A high speed dicing saw, model ADA-321, (DISCO, Tokyo, Japan) is used to dice wafers as well as create the notch to within 50um of the intended interface in samples prior to testing. A dicing speed as low as 0.3mm/s is used to achieve a sufficiently smooth finish.

3.2.1.3 Four-point Bend Setup

The samples were tested using a custom built four-point bending mechanical test system[54], which works in displacement controlled mode with the loading continuously measured with a high-sensitivity load cell. The system also features high rigidity as well as an integration of a closed environmental cell to finely control both the relative humidity and temperature inside the cell.

3.2.2 Materials

Bis(2,2,7-trimethyloctane-3,5-dionato) copper, $Cu(tmod)_2$, is used as received without any further purification (Epichem, Inc., Allentown, PA), Figure 2. Poly(acrylic acid), PAA, [9003-01-4] (25 % solution in water, M_w ~ 90k) is diluted and used for spin coating (Polysciences, Inc., Warrington, PA). Acrylic acid [79-10-7] is used as received without further purification (Sigma-Aldrich Co., St. Louis, MO). EPO-TEK 353ND is used as received (Epoxy Technology, Billerica, MA). Approximately 98 % pure n-heptane [142-82-5] (Fisher Scientific, Pittsburgh, PA) is used as received without any further purification. Coleman grade (99.99 %) carbon dioxide and ultra high purity (99.999 %) hydrogen are used as received (Merriam Graves Corp, Charlestown, NH). A buna-N o-ring, size 2-236, is used for the high pressure and high temperature reactor seal (Marco Rubber and Plastic Products, Inc., North Andover, MA). Films are deposited on silicon wafers with 30 nm TaN deposited by CVD (crystal orientation <100>, 300 Å TaN by CVD, 1-100 micro-ohm centimeter, 750 micron total thickness). A silicon wafer (crystal orientation <100>, 500 nm thermally grown oxide, 1-100 micro-ohm centimeter,

750 micron total thickness) (Novellus, San Jose, CA) is used for the dummy side support of the sample stack.

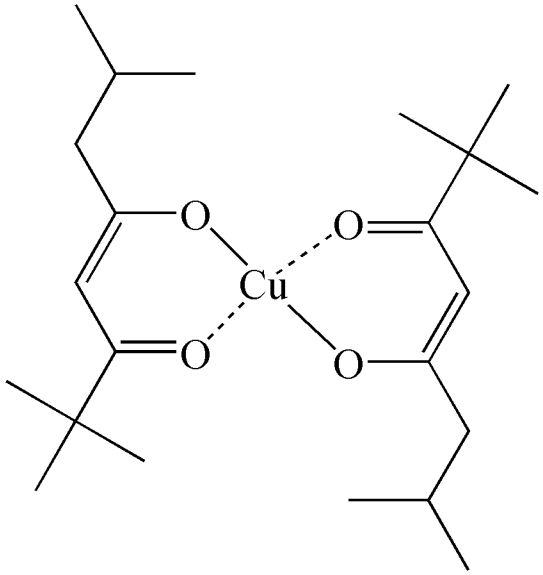

Figure 3.2: Chemical structure of bis(2,2,7-trimethyloctane-3,5-dionato) copper, $Cu(tmod)_2$.

3.2.3 Procedure

3.2.3.1 Poly(acrylic acid) Pretreatment

Poly(acrylic acid), PAA, is spun at 4000 rpm onto the TaN coated substrates from a 1 % solution of PAA in water to form a 15 nm thick layer. Data for PAA film thickness versus spin seed at various PAA/water concentrations was previously determined.[55] Film thickness was confirmed with variable angle spectroscopic ellipsometry, VASE.

3.2.3.2 Supercritical Fluid Deposition of Copper

The supercritical fluid deposition of copper onto PAA treated and untreated substrates is performed in the cold wall reactor mentioned in the previous section. The reaction is performed in a batch process and precursor conversion is near complete for

each deposition. For a typical reaction, a 35 mm by 45 mm silicon <100> wafer with 30 nm TaN deposited by CVD is mounted to the aluminum stage and secured with two clips. An amount of solid $Cu(tmod)_2$ precursor is loaded into the reactor so that zero order kinetics are attained and conformal deposition is achieved. Typically, precursor loading is approximately between 0.2 – 0.9 wt. %. The vessel is then sealed and placed behind protective polycarbonate housing. Then, using a constant flow of nitrogen, the reaction vessel is purged continuously over a 15 minute period. Simultaneously, the reactor wall is heated to the desired temperature (T = 60 ºC) and reaches equilibrium within 10 min. Supercritical carbon dioxide (P = 103 bar, T = 60 ºC) is then introduced into the reactor using the computer controlled syringe pump, which enables precise volume measurement of the added CO_2. A suitable amount of time is allowed for the complete dissolution of precursor in the convection dominated flow of the supercritical CO_2 in the reactor (1 hr.). Next, using a pressure drop, hydrogen is loaded into the reactor via a manifold of known volume (70 mL) and higher pressure. The moles of hydrogen injected are then calculated by pressure drop using the ideal gas law. Typically, hydrogen concentration is approximately 0.5 wt. % which is at least 100 times in excess of what is needed for complete conversion of the precursor. The aluminum stage is quickly heated (~1 min.) to the desired reaction temperature (270 – 285 ºC) and maintained at this temperature for a known amount of time. The heated stage is allowed to cool down (~5 min.) while fresh CO_2 is used to flush multiple reactor volumes though the system to remove reaction byproducts and unreacted precursor. The effluent is passed through an activated carbon bed and silicone oil bubbler before being vented to the atmosphere. During select reactions, small gas phase samples of known volume are collected using HPLC sample

loops. The samples are decompressed and the precursor is recovered in a known volume of n-heptane. The resulting solutions are analyzed using UV-visible spectroscopy in order to determine precursor concentration in the fluid phase at various points in the reaction. This is used to confirm near complete conversion of precursor.

The deposited films are characterized in order to obtain their thickness and purity. Thickness measurements are made with the profilometer while purity is confirmed via XPS.

3.2.3.3 Sample Preparation

EPO-TEK 353ND epoxy is used to bond the copper deposited silicon substrate to a dummy silicon substrate similar to the substrate used for copper deposition. The epoxy is spun on at 7500 rpms for 45 s. and then cured at 140 ºC at 8 kPa for 40 min. resulting in an epoxy layer thickness of approximately 5 microns. The sample stacks are diced into 45 mm (L) * 4.5 mm (W) * 0.73 mm (h) samples using a high-speed dicing saw. Finally, a notch is machined into the sample stack to within approximately 50 microns of the interface. The final sample stack for untreated and PAA pretreated films is shown in Figure 3 and 4, respectively.

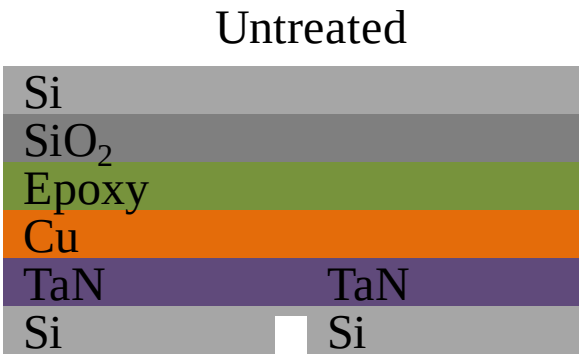

Figure 3.3: Experimental sample stack for mechanical adhesion testing of copper deposited film on unmodified TaN capped substrates. Si, SiO_2, Epoxy, TaN thicknesses are approximately 700-750 μm, 500 nm, 5 μm and 30 nm, respectively. Cu thickness varies according to Table 3.1.

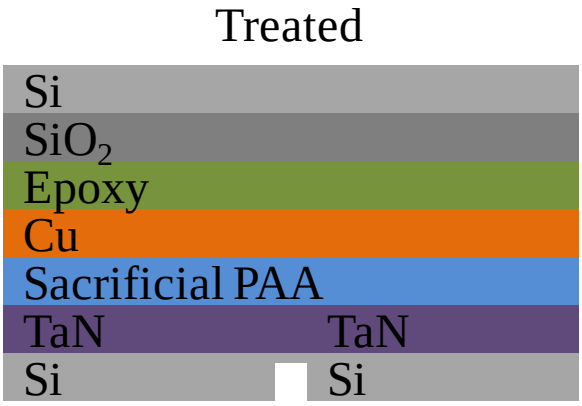

Figure 3.4: Experimental sample stack for mechanical adhesion testing of copper deposited film on poly(acrylic acid) modified TaN capped substrates. PAA thickness approximately 15 nm.

3.2.3.4 Mechanical Testing

The delamination experiments to determine the adhesion energy of the Cu/TaN interface are performed using the four-point bending technique, Figure 5. All samples are tested at 21 ± 0.3 ºC in an environmental cell with N_2 flow, relative humidity below 10 %, immediately after the samples are cured. Before formal testing, a three-hour stabilizing period is allowed to achieve thermal equilibrium and minimize thermal fluctuation during test. The default loading rate, crosshead speed, is 0.1 μm/s. Four-point

bend geometry is S = 20 mm and L = 8 mm. 4 samples are tested at each condition for statistical information. The energy release rate *G* to drive the crack along the Cu/TaN interface under these conditions is taken to be the adhesion energy of the interface, with *G* calculated using the following, [47]

$$G = \frac{21P^2L^2\left(1-\nu^2\right)}{16Eb^2h^3},$$

where *P* is the steady load taken as the average value over the plateau region in the load-displacement curve after the major load drop, *b* is the width and *h* is the half thickness of the sample. *E* = 168.9 GPa and *v* = 0.064 are the Young's modulus and Poisson's ratio of Si as appropriate for the crystallographic orientation of the samples.

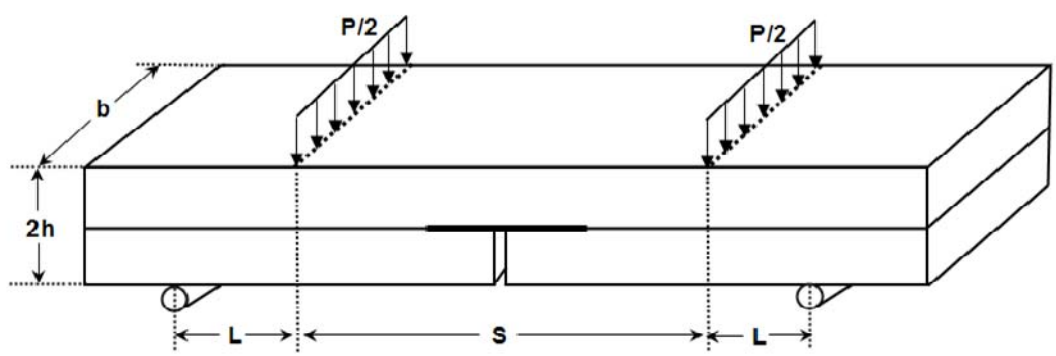

Figure 3.5: Schematic and force diagram for four point bend technique.

3.3 Results

Copper films are deposited by the hydrogen assisted reduction of $Cu(tmod)_2$ in supercritical carbon dioxide on TaN barriers. The barrier layers are treated with PAA, a known interfacial adhesion enhancer for copper deposited by SFD, prior to deposition.

Four-point bend fracture mechanics are then used to quantify the interfacial adhesion energy of the Cu/TaN interface, Table 3.1.

The copper SFD reaction temperature is between 270 – 285 ºC for all depositions. Precursor concentration is between 0.2 – 0.9 wt. % and hydrogen concentration is approximately 0.5 wt. % for all depositions. The hydrogen concentration is always in excess of 100 times the necessary amount needed for complete conversion of the loaded $Cu(tmod)_2$. X-ray photoelectron spectroscopy (XPS) is used to confirm crack propagation at the interface of interest.

Table 3.1: Table of adhesion energy for untreated and poly(acrylic acid) treated samples.

Sample group		Cu thickness (nm)	Cu/TaN adhesion energy (J/m^2)	Variation (J/m^2)
Untreated	A-1	68	0.55	0.25
	A-2	97	1.40	0.37
	A-3	126	0.56	0.05
	A-4	131	1.56	0.20
	A-5	180	0.50	0.03
Treated	B-1	130	>5.3*	N/A
	B-2	172	3.36	0.57
	B-3	190	4.69	0.20
	B-4	192	>5.3*	N/A
	B-5	266	5.32	0.92
* Pre-crack failed to grow into interface				

Untreated sample stacks have a copper thickness range of 68 – 180 nm. PAA pretreated stacks have a copper thickness range of 130 – 266 nm. It is observed that the growth rate of copper is faster on PAA pretreated samples as compared to samples that did not have a pretreatment for equivalent reaction conditions.

A typical load versus displacement curve for an untreated and PAA pretreated stack is shown in Figure 6 and Figure 7, respectively. The steady state load is determined

after the major load drop. Finally, the average interfacial adhesion energy of the Cu/TaN interface is calculated[47] and is found to be approximately 1 J/m^2 for untreated stacks and approximately 5 J/m^2 for PAA pretreated stacks, Figure 8.

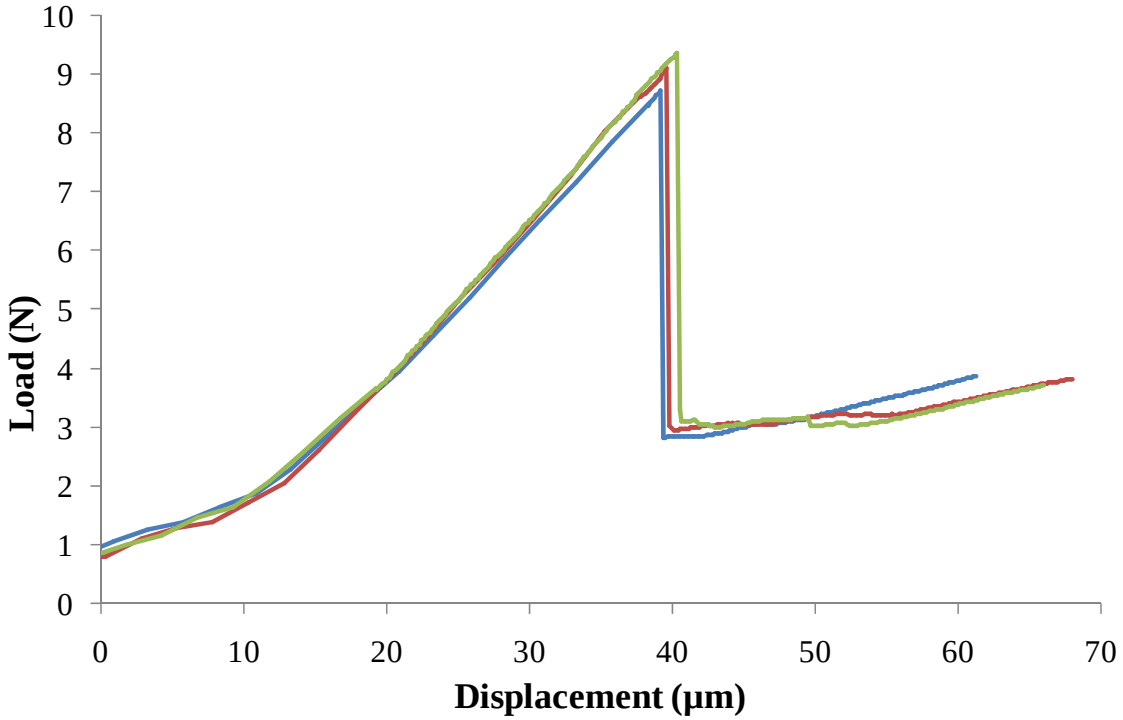

Figure 3.6: Load versus displacement plot for sample A-5, unmodified surface.

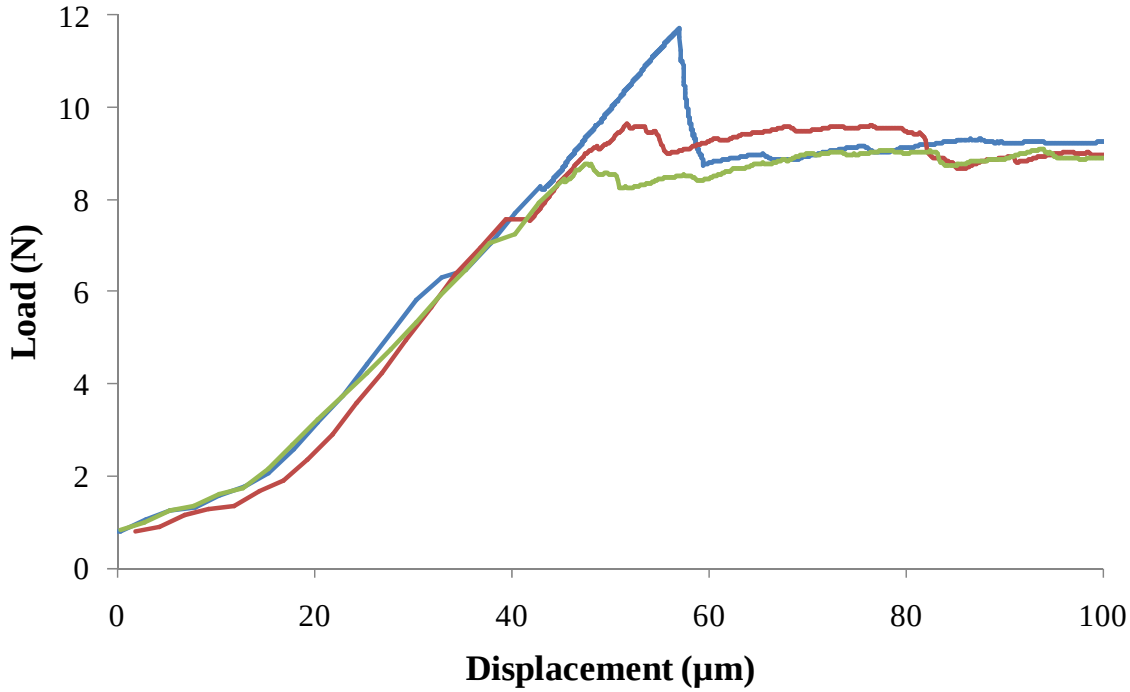

Figure 3.7: Load versus displacement plot for sample B-3, poly(acrylic acid) modified surface.

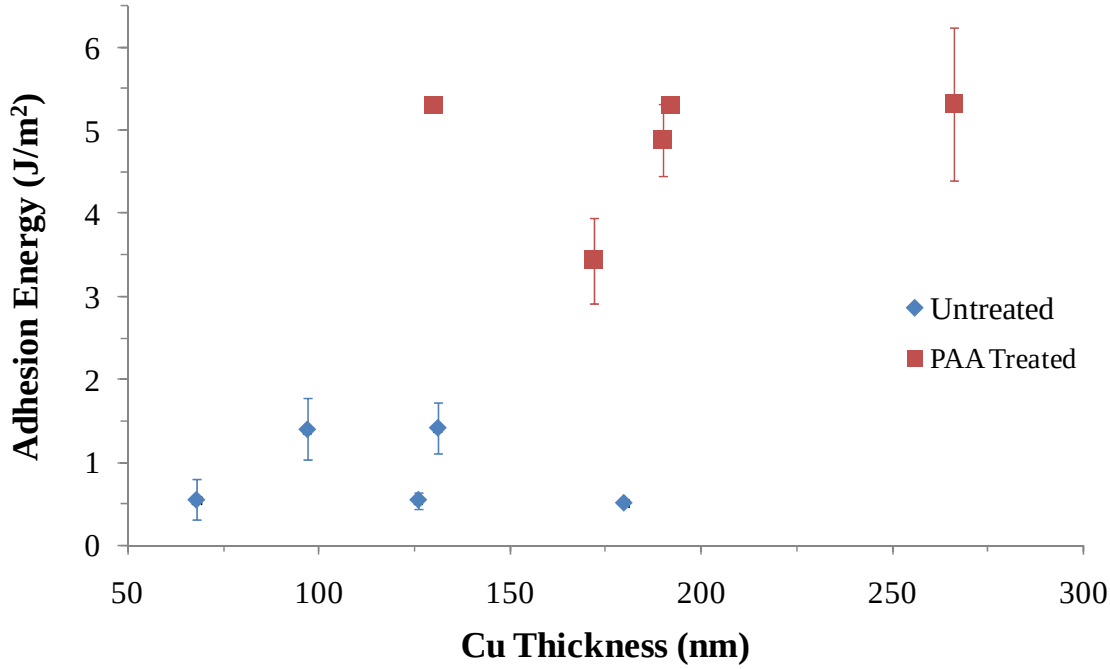

Figure 3.8: Statistical data for adhesion energy versus thickness of the deposited copper film for both treated and untreated substrates.

Visual inspection of the deposition side, graphical representation in Figure 9, of the substrate shows a copper free surface. XPS is used to confirm these results, Figure 10. No trace of the copper $2p_{1/2}$ and $2p_{3/2}$ signature XPS peaks is observed. Visual inspection of the dummy side shows a shiny copper film. XPS survey scan and sputter depth profiling of this side, Figure 12, immediately shows a high purity copper film eventually moving into a high carbon count region. The results do not differ for all samples, regardless of it being untreated or PAA pretreated, which confirms the sacrificial nature of the PAA at the reaction conditions used.

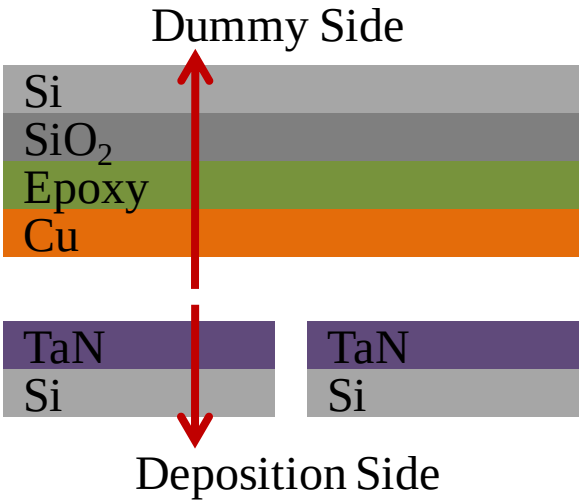

Figure 3.9: Representation of the post mechanical tested sample stack with directionality indication of XPS for sputter depth profiling.

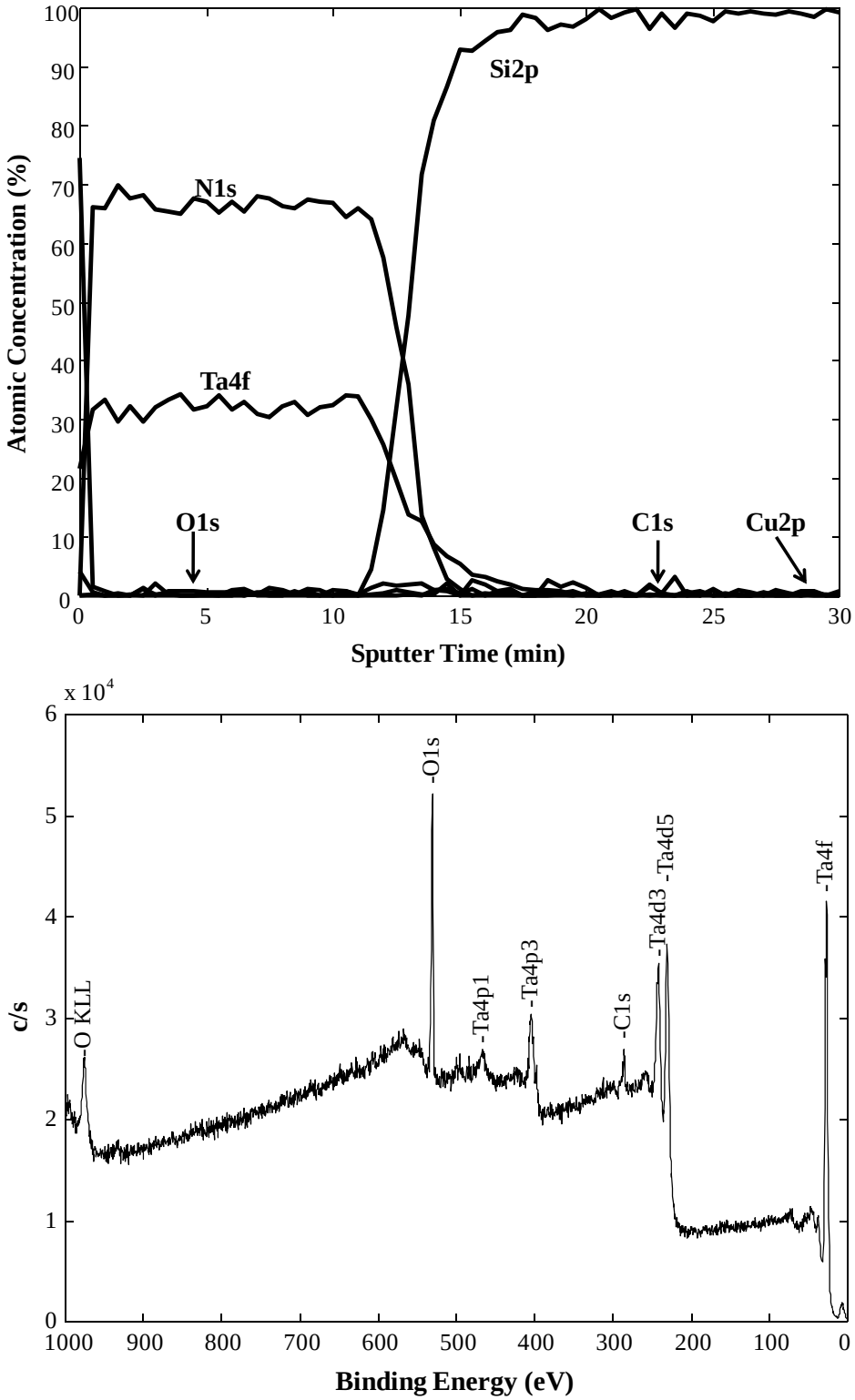

Figure 3.10: XPS sputter depth profile (top) and survey scan (bottom) of sample A-5, deposition side. No Cu layer is detected prior to the TaN region which confirms that the crack propagated at the desired interface.

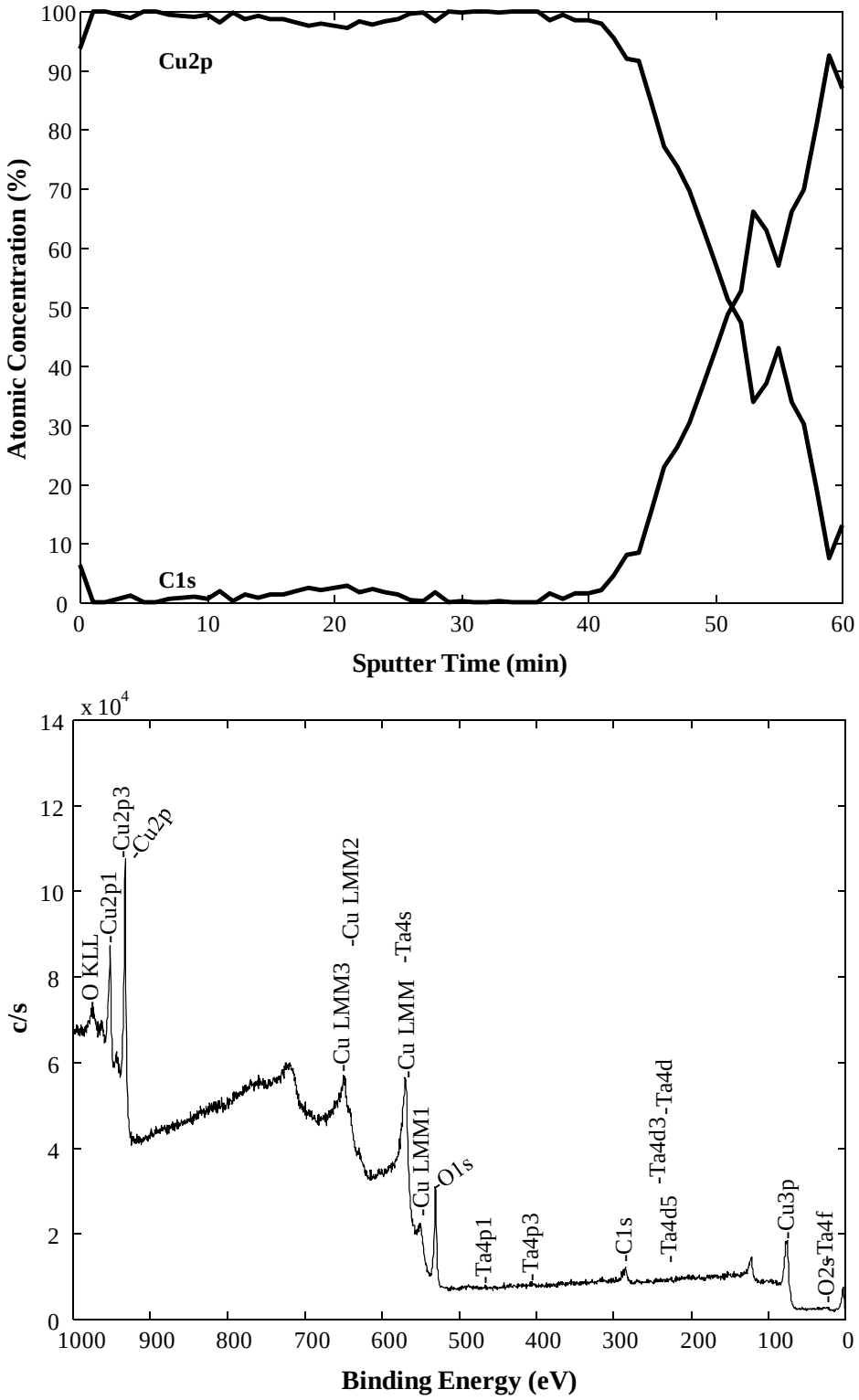

Figure 3.11: XPS sputter depth profile (top) and survey scan (bottom) of sample B-5, dummy side. The lack of presence by the TaN layer prior to the copper rich region confirms propagation of the crack at the desired interface.

3.4 Discussion

PAA is used at the Cu/TaN interface to maintain an oxide and contamination free interface during SFD deposition of copper. PAA, at the reaction conditions used, will degrade and is ultimately sacrificial, as seen in the XPS sputter depth profiles in Figure 10 and 11. Along with its decomposition products, PAA, a weak acid (p*K*a = 4.28), acts as an etching agent to clean the surface of any oxides or ligand contamination that are formed or left behind during the reduction reaction. A comparison of the adhesion energy of untreated stacks vs PAA pretreated stacks indicates that there is a 5 fold increase in adhesion energy of the Cu/TaN interface when pretreated with a 15 nm thick layer of spun on PAA from a 1 % PAA in water solution. This increase in adhesion energy allows copper deposited by SFD to meet industry standards. Interfaces with an adhesion energy of less than 5 J/m^2 exhibit delamination or cracking during chemical mechanical polishing (CMP) and for this reason, 5 J/m^2 is the adhesion energy required in the semiconductor industry.[49]

It is important to note that in Figure 10 and 11, there is a slight carbon count at the beginning of each sputter depth profile for one cycle; this is attributed to contamination from the air after mechanical testing and not the presence of the PAA layer.

Although film thickness is known to affect adhesion energy as a result of plasticity in the film, this is only common for relatively thicker films than studied here. Sensitivity for changes in energy is a function of, in this case, the load cell used. There is no obvious trend in adhesion energy as a function of film thickness in either the untreated or PAA pretreated stacks.

During mechanical testing, the load-versus-displacement curves show a common trend with a major load drop, which is consistent with four-point bend tests. This load drop occurs as the precut notch initiates the interfacial crack. More often than not, the initiation of interfacial crack is asymmetric and the crack will propagate down one side of the sample initially. If the sample does not break, the energy will be enough to begin a crack that propagates down the other side of the sample. This is evident when a second major energy drop occurs, which corresponds to the crack propagating into the other side of the sample. As the crack propagates, the load begins with a plateau regime during which the energy release rate remains constant. The crack arrests as it approaches the inner loading pins, manifested as a steady increase of load without further crack extension.

A broken sample, in which the crack does not propagate into the interface but instead the entire stack immediately fails indicates superior adhesion, as the crack always chooses a path with minimum energy dissipation. If the intended interface is sufficiently tough, it is energetically more favorable to propagate through the film then bulk silicon substrate, than along the tough interface.

An increase in the growth rate is observed for copper deposited on substrates that are pretreated with PAA versus those that are not pretreated. It is proposed that the increase in growth rate for PAA pretreated copper films is due to the higher number of available surface sites for reaction during the deposition. This is due to the etching and cleaning of oxides and contaminants by the PAA as it degrades.

3.5 Conclusions

A fivefold increase in adhesion is observed for PAA pretreated Cu/TaN interfaces in which the copper films are deposited by the hydrogen assisted reduction of bis(2,2,7-trimethyloctane-3,5-dionato) copper in supercritical carbon dioxide. The pretreatment of PAA is done via spin coating and the remaining 15 nm layer at the interface becomes sacrificial at the reaction conditions used, leaving behind no trace of the PAA. The resulting average interfacial adhesion energy is 5 J/m^2, which meets adhesion standards in the semiconductor industry. The adhesion measurements are performed with a custom built four-point bend fracture mechanics testing system. Film thickness is found to have no affect on the adhesion energy. Finally, the growth rate of copper during deposition is higher on surfaces pretreated with PAA due to the increased availability of surface sites for the reduction reactions.

3.6 References

(1) M. J. Hampden-Smith, T. T. Kodas, *Chemical Vapor Deposition* **1995**, *1*, 8-23.

(2) M. J. Hampden-Smith, T. T. Kodas, *Chemical Vapor Deposition* **1995**, *1*, 39-48.

(3) S. Voss, S. Gandikota, L. Y. Chen, R. Tao, D. Cong, A. Duboust, N. Yoshida, S. Ramaswami, *Microelectronic Engineering* **2000**, *50*, 501-508.

(4) S. Gandikota, S. Voss, R. Tao, A. Duboust, D. Cong, L. Y. Chen, S. Ramaswami, D. Carl, *Microelectronic Engineering* **2000**, *50*, 547-553.

(5) H. Kim, *Journal of Vacuum Science & Technology B* **2003**, *21*, 2231-2261.

(6) A. Furuya, M. Tagami, K. Shiba, K. Kikuta, Y. Hayashi, *Ieee Transactions on Electron Devices* **2002**, *49*, 733-738.

(7) J. S. Park, M. J. Lee, C. S. Lee, S. W. Kang, *Electrochemical and Solid State Letters* **2001**, *4*, C17-C19.

(8) S. M. Rossnagel, A. Sherman, F. Turner, *Journal of Vacuum Science & Technology B* **2000**, *18*, 2016-2020.

(9) R. Fix, R. G. Gordon, D. M. Hoffman, *Chemistry of Materials* **1993**, *5*, 614-619.

(10) O. Aschenbrenner, S. Kemper, N. Dahmena, K. Schaber, E. Dinjus, *The Journal of Superciritcal Fluids* **2007**, *41*, 179-186.

(11) A. F. Lagalante, B. N. Hansen, T. J. Bruno, R. E. Sievers, *Inorg. Chem.* **1995**, *34*, 5781-5785.

(12) N. G. Smart, T. Carleson, T. Kast, A. A. Clifford, M. D. Burford, C. M. Wai, *Talanta* **1997**, *44*, 137-150.

(13) P. G. Ganesan, J. Gamba, A. Ellis, R. S. Kane, G. Ramanath, *Applied Physics Letters* **2003**, *83*, 3302-3304.

(14) A. Krishnamoorthy, K. Chanda, S. P. Murarka, G. Ramanath, J. G. Ryan, *Applied Physics Letters* **2001**, *78*, 2467-2469.

(15) G. Ramanath, G. Cui, P. G. Ganesan, X. Guo, A. V. Ellis, M. Stukowski, K. Vijayamohanan, P. Doppelt, M. Lane, *Applied Physics Letters* **2003**, *83*, 383-385.

(16) J. Tong, D. Martini, N. Magtoto, M. Pritchett, J. Kelber, *Applied Surface Science* **2002**, *187*, 253-260.

(17) L. Chen, J. A. Kelber, *Journal of Vacuum Science & Technology a-Vacuum Surfaces and Films* **1999**, *17*, 1968-1973.

(18) G. S. Ferguson, M. K. Chaudhury, G. B. Sigal, G. M. Whitesides, *Science* **1991**, *253*, 776-778.

(19) D. D. Gandhi, M. Lane, Y. Zhou, A. P. Singh, S. Nayak, U. Tisch, M. Eizenberg, G. Ramanath, *Nature* **2007**, *447*, 299-U292.

(20) S. M. Yi, K. H. Jang, J. U. An, S. S. Hwang, Y. C. Joo, *Microelectronics Reliability* **2008**, *48*, 744-748.

(21) T. G. Woo, I. S. Park, H. W. Lee, M. H. Lee, E. K. Park, Y. K. Hwang, K. W. Seol, *Journal of the Korean Institute of Metals and Materials* **2007**, *45*, 423-428.

(22) S. M. Yi, J. U. An, S. S. Hwang, J. R. Yim, Y. H. Huh, Y. B. Park, Y. C. Joo, *Thin Solid Films* **2008**, *516*, 2325-2330.

(23) T. S. de Felipe, S. P. Murarka, S. Bedell, W. A. Lanford, *Thin Solid Films* **1998**, *335*, 49-53.

(24) W. A. Lanford, P. J. Ding, W. Wang, S. Hymes, S. P. Murarka, *Materials Chemistry and Physics* **1995**, *41*, 192-198.

(25) J. J. Toomey, S. Hymes, S. P. Murarka, *Applied Physics Letters* **1995**, *66*, 2074-2076.

(26) P. J. Ding, W. A. Lanford, S. Hymes, S. P. Murarka, *Journal of Applied Physics* **1994**, *75*, 3627-3631.

(27) P. J. Ding, W. A. Lanford, S. Hymes, S. P. Murarka, *Applied Physics Letters* **1994**, *64*, 2897-2899.

(28) Y. Zong, X. Shan, J. J. Watkins, *Langmuir* **2004**, *20*, 9210-9216.

(29) ASTM Standard D3359 - 08, 2003, "Standard Test Methods for Measuring Adhesion by Tape Test," ASTM International, West Conshohocken, PA, www.astm.org.

(30) P. R. Chalker, S. J. Bull, D. S. Rickerby, *Materials Science and Engineering a-Structural Materials Properties Microstructure and Processing* **1991**, *140*, 583-592.

(31) K. L. Mittal, *Electrocomponent Science and Technology* **1976**, *3*, 21-42.

(32) H. K. Pulker, A. J. Perry, *Surface Technology* **1981**, *14*, 25-39.

(33) J. Sekler, P. A. Steinmann, H. E. Hintermann, *Surface & Coatings Technology* **1988**, *36*, 519-529.

(34) P. A. Steinmann, H. E. Hintermann, *Journal of the Electrochemical Society* **1988**, *135*, C358-C358.

(35) P. A. Steinmann, H. E. Hintermann, *Journal of Vacuum Science & Technology a-Vacuum Surfaces and Films* **1989**, *7*, 2267-2272.

(36) P. A. Steinmann, Y. Tardy, H. E. Hintermann, *Thin Solid Films* **1987**, *154*, 333-349.

(37) W. W. Gerberich, D. E. Kramer, N. I. Tymiak, A. A. Volinsky, D. F. Bahr, M. D. Kriese, *Acta Materialia* **1999**, *47*, 4115-4123.

(38) J. J. Kim, J. H. Jeong, K. R. Lee, D. Kwon, *Thin Solid Films* **2003**, *441*, 172-179.

(39) T. Kitamura, H. Hirakata, T. Itsuji, *Engineering Fracture Mechanics* **2003**, *70*, 2089-2101.

(40) M. D. Kriese, W. W. Gerberich, N. R. Moody, *Journal of Materials Research* **1999**, *14*, 3007-3018.

(41) M. D. Kriese, W. W. Gerberich, N. R. Moody, *Journal of Materials Research* **1999**, *14*, 3019-3026.

(42) L. Magagnin, R. Maboudian, C. Carraro, *Thin Solid Films* **2003**, *434*, 100-105.

(43) P. G. Charalambides, J. Lund, A. G. Evans, R. M. McMeeking, *Journal of Applied Mechanics* **1989**, *56*, 77-82.

(44) R. H. Dauskardt, M. Lane, Q. Ma, N. Krishna, *Engineering Fracture Mechanics* **1998**, *61*, 141-162.

(45) S. J. Howard, Y. C. Tsui, T. W. Clyne, *Acta Metallurgica et Materialia* **1994**, *42*, 2823-2836.

(46) M. P. Hughey, D. J. Morris, R. F. Cook, S. P. Bozeman, B. L. Kelly, S. L. N. Chakravarty, D. P. Harkens, L. C. Stearns, *Engineering Fracture Mechanics* **2004**, *71*, 245-261.

(47) Q. Ma, *Journal of Materials Research* **1997**, *12*, 840-845.

(48) S. Roham, K. Hardikar, P. Woytowitz, *Journal of Materials Research* **2004**, *19*, 3019-3027.

(49) T. Scherban, B. Sun, J. Blaine, C. Block, B. Jin, E. Andideh, "Interfacial Adhesion of Copper-Low k Interconnects", presented at *Interconnect Technology Conference, 2001. Proceedings of the IEEE 2001 International*, Burlingame, CA, **2001**.

(50) Y. C. Tsui, S. J. Howard, T. W. Clyne, *Acta Metallurgica et Materialia* **1994**, *42*, 2837-2844.

(51) H. Li, D. B. Farmer, R. G. Gordon, Y. Lin, J. Vlassak, *Journal of the Electrochemical Society* **2007**, *154*, D642-D647.

(52) Z. Li, R. G. Gordon, D. B. Farmer, Y. Lin, J. J. Vlassak, *Electrochemical and Solid State Letters* **2005**, *8*, G182-G185.

(53) T. Y. Tsui, A. J. McKerrow, J. J. Vlassak, *Journal of Materials Research* **2005**, *20*, 2266-2273.

(54) J. J. Vlassak, Y. Lin, T. Y. Tsui, *Materials Science and Engineering A* **2005**, *391*, 159-174.

(55) Y. Zong, in *Chemical Engineering*, Vol. Ph.D., University of Massachusetts - Amherst, **2004**.

CHAPTER 4

APPLICATIONS OF SUPERCRITICAL FLUID DEPOSITION

4.1 Introduction

The use of SFD to deposit a wide variety of highly conformal thin films in high aspect ratio features is demonstrated. However, beyond the ability to deposit single component metals and metal oxides exists the opportunity for more complex applications. The simultaneous deposition of multiple components allows one to form both dispersed multi-elemental films as well as alloys with precise composition control in a single step. Multiple single component depositions allow high purity stacks to be fabricated which is the basis for top-down fabrication in the microelectronics industry. The goal of this chapter is to outline particular areas of interest utilizing the previously mentioned techniques to fabricate devices and build components for a wide variety of applications ranging from nano-sized capacitors to alternative materials for both fuel cell electrodes and energy storage devices.

4.2 Co-depositions and Alloys

4.2.1 Cobalt/Platinum

In the area of magnetic recording and storage, the recording media is of paramount importance and is the focus of much research. The media itself can be classified into two types, longitudinal and perpendicular recording media. In longitudinal recording media, information is stored magnetically across the horizontal axis of the media while in perpendicular recording magnetically stores information vertically.

Perpendicular recording is less area intensive then longitudinal and is the primary method for recording and storing data because of this. Another aspect of recording media that is important is the type of material that is used. There are soft and hard materials. Soft materials are named such due to their low coercivity (ability to be demagnetized) and are typically implemented in shielding applications. Hard materials have a high coercivity and are called permanent magnets due to the relatively high energy needed to demagnetize them. Recording media is in the form of thin magnetic layers of hard materials able to be used for perpendicular writing. A few of the hard materials used for magnetic recording media include: CoPt, CoPd, CoC, CoNi, CoFe, CoP and FePt.[1]

In the pursuit of high density recording media (magneto-optical recording[2] and perpendicular magnetic recording[3, 4]) as well as hard magnetic components in microelectro-mechanical systems[5] (MEMS), CoPt alloys have prevailed as being one of the best possible choices.[6-11] This is due to a variety of reasons. Co itself also has uniaxial symmetry, meaning that it has a single optical axis which enables light to pass through unhindered, making it an ideal candidate for digital media storage. The alloying of Pt to Co also increases the magnetocrystalline anisotropy of the Co. CoPt particles have a small grain size which is fundamental in having small recording bits.[12-14] Additionally, CoPt has high coercivity and acceptable remanence, which are necessary magnetic properties.[15, 16] CoPt films are ideal as layers and alloys for "ultra high density" magnetic recording media due to their high magnetic anisotropy, high coercivity, chemical stability and resistance to corrosion.[17-19]

4.2.1.1 Experimental

4.2.1.1.1 Equipment

4.2.1.1.1.1 Cold Wall Reactor

The cold wall reactor used is previously described in detail in chapter 3.

4.2.1.1.1.2 Hot Wall Reactor

Hot wall reactors are also used for the deposition of Co and Pt. A hot wall reactor varies from the previously mentioned cold wall reactor in that the entire vessel is heated and no selective deposition is obtained. The reactor used is a 25 mL, 17-4PH stainless steel Thar vessel (TharTech/TharSFC, Pittsburgh, PA) which is a "finger-tight" sealing, high pressure reactor, Figure 4.1. The reactor utilizes a polyimide cup with spring as the sealing mechanism. Under pressure, the spring is energized and pushes on the inside and outside lips of the polyimide cup which in turn forms a seal with the finger-tightened cap and the inside wall of the reactor.

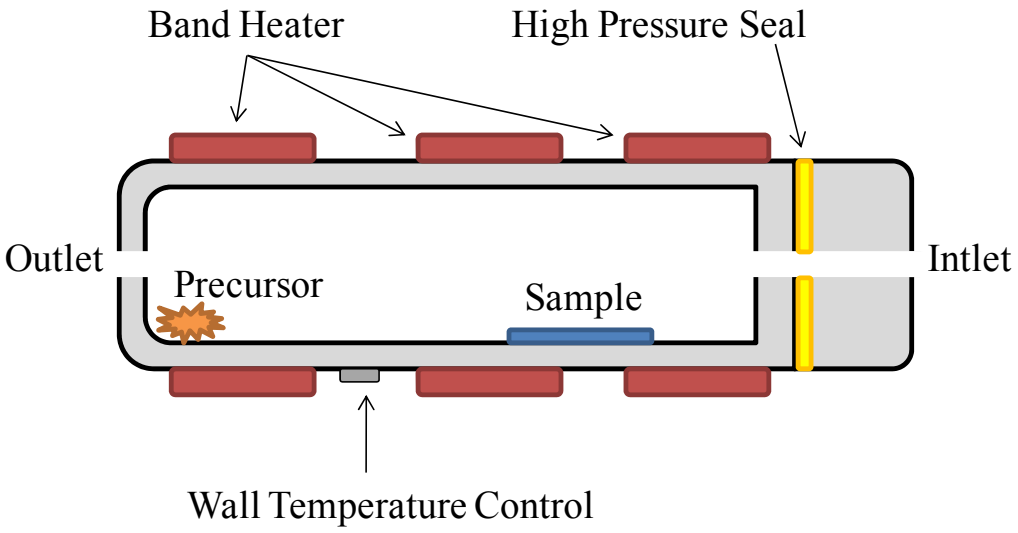

Figure 4.1: Schematic of hot wall reaction vessel.

4.2.1.1.2 Materials

Tris(2,2,6,6-tetramethyl-3,5-heptanedionato)cobalt (III), 99 % (99.9+ % - Co), $Co(tmhd)_3$, [14877-41-9], bis(cyclopentadienyls)cobalt (II), 98 %, cobaltocene, $CoCp_2$, [1277-43-6], and dimethyl(1,5-cyclooctadiene)platinum (II), 99 %, $Pt(Me)_2cod$, [12266-92-1] are used as received without any further purification (Strem Chemicals, Inc., Newburyport, MA), Figure 4.2. Coleman grade (99.99 %) carbon dioxide, ultra high purity (99.999 %) hydrogen and prepurified grade (99.998 %) nitrogen are used as received (Merriam Graves Corp, Charlestown, NH). A buna-N o-ring, size 2-236, is used for the high pressure and high temperature cold wall reactor seal (Marco Rubber and Plastic Products, Inc., North Andover, MA). A thin (0.001") 3.25" by 3.25" polyamide Kapton film is cut to size and used for lining the inside of the hot wall reactors (McMaster-Carr, Atlanta, GA). Films are deposited on silicon wafers with 30 nm TaN deposited by CVD(crystal orientation <100>, 300 Å TaN by CVD, 1-100 micro-ohm centimeter, 750 micron total thickness) and silicon wafers without TaN(Novellus, San Jose, CA).

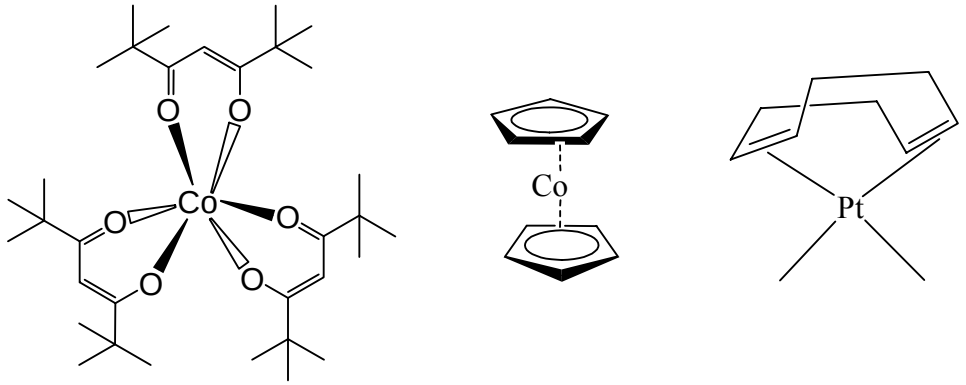

Figure 4.2: Chemical structure of tris(2,2,6,6-tetramethyl-3,5-heptanedionato)cobalt (III), $Co(tmhd)_3$, bis(cyclopentadienyls)cobalt (II), $CoCp_2$, and dimethyl(1,5-cyclooctadiene)platinum (II), $Pt(Me)_2cod$.

4.2.1.1.3 Procedure

Both hot and cold wall reactors are used to experiment with different precursor systems and pressure and temperature ranges.

For a typical reaction in the cold wall reactor, a 25 mm by 19 mm silicon <100> wafer with 30 nm TaN layer on top, is mounted to the aluminum heated stage and secured with clips. A known amount of precursor is loaded into the vessel. Reaction conditions are listed in Table 4.1. The vessel is sealed and placed behind protective polycarbonate housing. Then, using a constant flow of nitrogen, the reaction vessel is purged continuously over a 30 minute period. The reactor wall and stage are then heated to the desired preheating temperature and allowed to equilibrate (t = 60 min.). Carbon dioxide is introduced into the reactor using a computer-controlled syringe pump (Teledyne Isco, Inc., Lincoln, NE), which enables precise volume measurement of the added CO_2. The reactor sits at this condition for a set time (t = 60 min.) to allow for dissolution of the precursor into the CO_2. Next, hydrogen is loaded into the system using a manifold of known volume (70 mL). The aluminum stage is then quickly heated (~ 15 s.) to the desired reaction temperature and maintained for a set time. The heated stage is then allowed to cool down (~ 15 s.) while fresh CO_2 is used to flush multiple reactor volumes through the system to remove reaction byproducts and unreacted precursor. The effluent is passed through an activated carbon bed and silicon oil bubbler before being vented to the atmosphere.

For a typical reaction in the hot wall reactor, a thin (0.001”) 3.25” by 3.25” polyamide (Kapton) film is used to line the inside of the reactor. A 25 mm by 19 mm silicon <100> wafer with 30 nm TaN layer on top, is then placed into the long tubular

reactor. A known amount of precursor is loaded into the vessel. Reaction conditions are listed in Table 4.1. The vessel is sealed and placed behind protective polycarbonate housing. Then, using a constant flow of nitrogen, the reaction vessel is purged continuously over a 10 minute period. The reactor is then heated to the desired preheating temperature and allowed to equilibrate (t = 10 min.). Carbon dioxide is introduced into the reactor.. The reactor sits at this condition for a set time (t = 60 min.) to allow for dissolution of the precursor into the CO_2. Next, hydrogen is loaded into the system using a manifold of known volume (70 mL). The system is maintained at these conditions for a set time. The reactor is then allowed to cool down while fresh CO_2 is used to flush multiple reactor volumes through the system to remove reaction byproducts and unreacted precursor. The effluent is passed through an activated carbon bed and silicon oil bubbler before being vented to the atmosphere.

The deposited films are characterized in order to obtain their purity, crystallinity and composition. Film purity and composition is determined by XPS (Co^{20-25}, Pt^{25-36}). Crystallinity is determined by XRD.

4.2.1.2 Results and Discussion

Results for the co-deposition of cobalt and platinum from various precursors are presented. Both a cold wall and a hot wall reactor are used for the depositions. The temperature ranges used for the hot wall reactor and the cold wall reactor are 40 ºC to 150 ºC and 60 ºC to 300 ºC. $Pt(Me)_2cod$ is the only platinum precursor used while $CoCp_2$ and $Co(tmhd)_3$ are both used as the cobalt source. $Pt(Me)_2cod$ concentration is varied between 0.2 wt. % and 0.5 wt. %. $CoCp_2$ concentration is varied between 0.2 wt. % and

0.5 wt. %. $Co(tmhd)_3$ concentration is varied between 0.2 wt. % and 0.4 wt. %. Hydrogen concentration is typically maintained between 0.4 and 0.5 wt. %.

Co-deposition of cobalt and platinum is successful with $CoCp_2$ as the cobalt source in the hot wall reactor at both 150 ºC and 60 ºC. Figure 4.3 and Figure 4.4 are XPS sputter depth profiles and survey scans of Co/Pt deposited at 150 ºC and 60 ºC, respectively. Figure 4.5 is a top down FE-SEM image showing the Co/Pt film deposited at 150 ºC. The film is primarily platinum with traces of cobalt throughout. Using the cold wall reactor, Co/Pt films are either not obtained or only a Pt film is deposited. The lack of cobalt or a film being deposited is likely a result of the parasitic nature of the deposition that is typically encountered in the cold wall reactor. This is due to the heat ramping which occurs to the underside and side of the heated sample stage as well as platinum's ability to deposit at very low temperatures to the entire interior of the reactor. Switching to the $Co(tmhd)_3$ precursor as the cobalt source, no significant deposition is obtained when using the cold wall reactor. The hot wall reactor yields high purity platinum films with only a trace of cobalt being detected. Figure 4.6 is an image of the platinum film deposited on the polyamide liner for the hot wall reactor. Figure 4.7 and Figure 4.8 are the XRD and XPS sputter depth profile and survey scan of the platinum film. Again, the difference between no deposition in the cold wall reactor and platinum deposition in the hot wall reactor is attributed to the slight parasitic nature of the deposition to the heated stage as well as to the walls of the reactor. Additionally, when using $CoCp_2$ as the cobalt source as opposed to $Co(tmhd)_3$, it is noted that cobalt is deposited in trace amounts via XPS. The lack of cobalt from $Co(tmhd)_3$ is proposed to be a result of the ability for the tmhd ligand to etch the surface of the film during deposition.

Given that the cobalt concentration is so low, it is likely that the tmhd etched away the cobalt that is deposited.

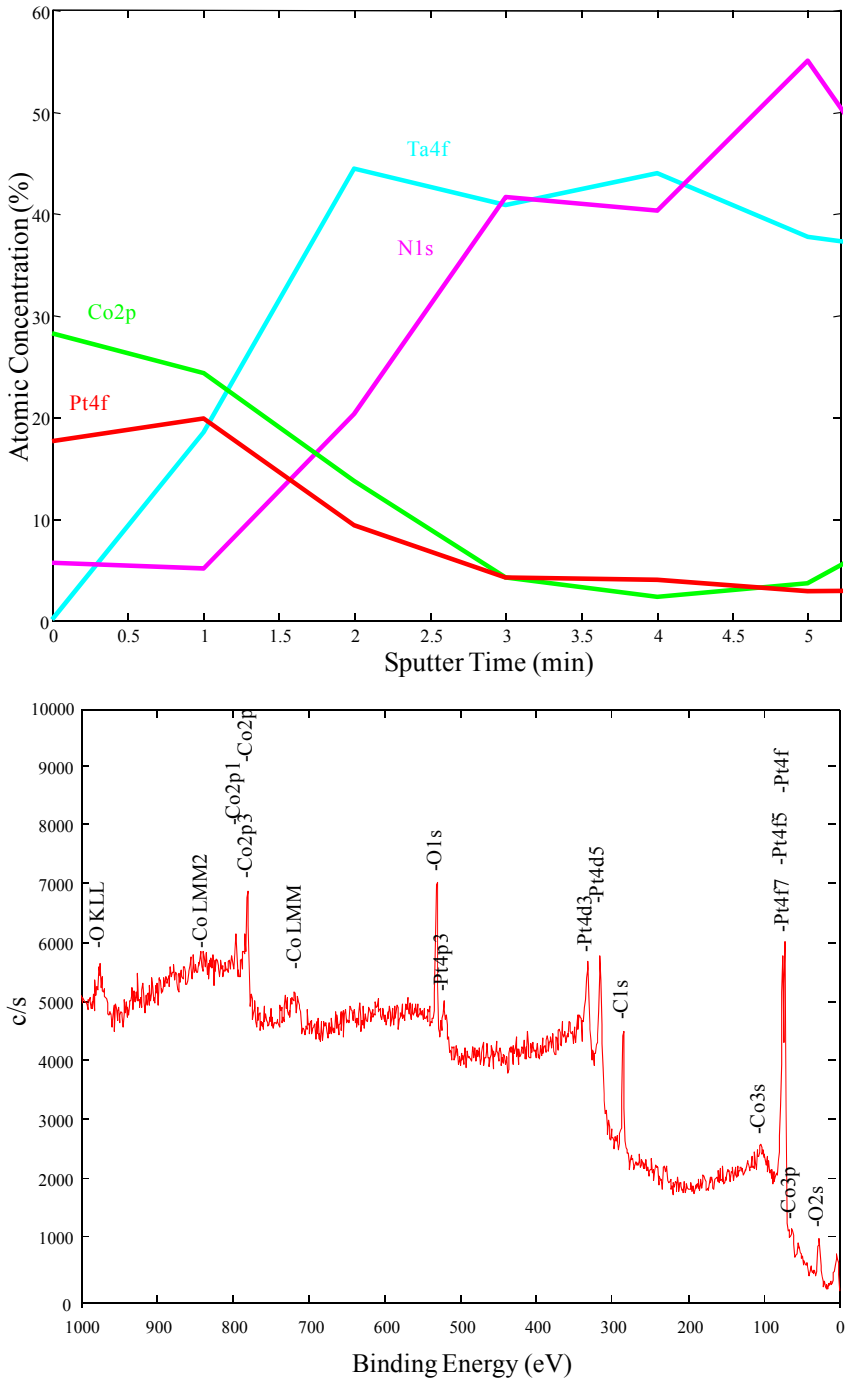

Figure 4.3: XPS sputter depth profile (top) and survey scan (bottom) showing a relatively constant ratio of Co:Pt throughout the bulk of the film for sample CoPt1 which is an SFD co-deposition of Co and Pt deposited at 150 ºC in a hot wall reaction vessel.

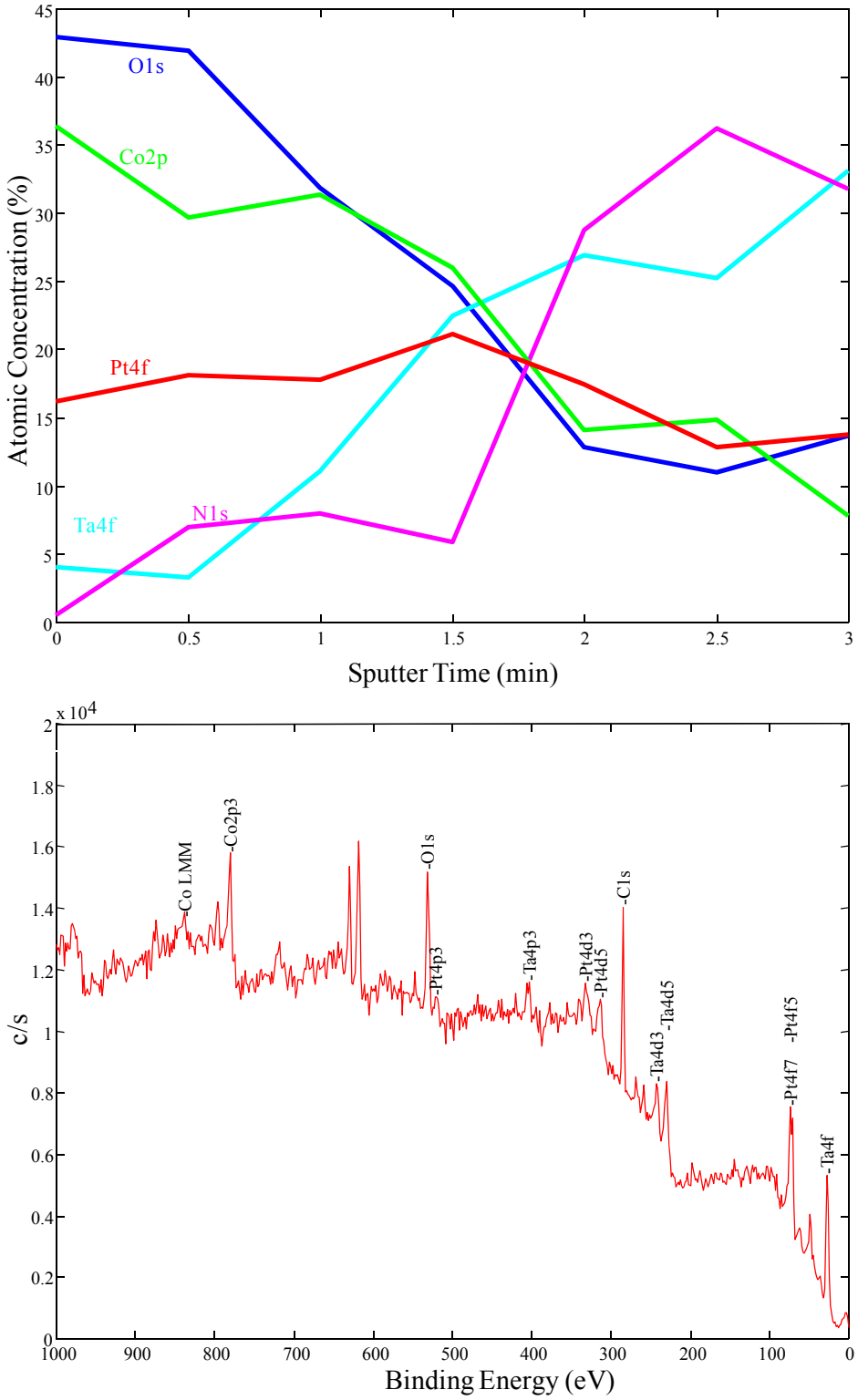

Figure 4.4: XPS sputter depth profile (top) and survey scan (bottom) showing a 2:1 ratio of Co:Pt for sample CoPt14 which is an SFD co-deposition of Co and Pt deposited at 60 ºC in a hot wall reaction vessel.

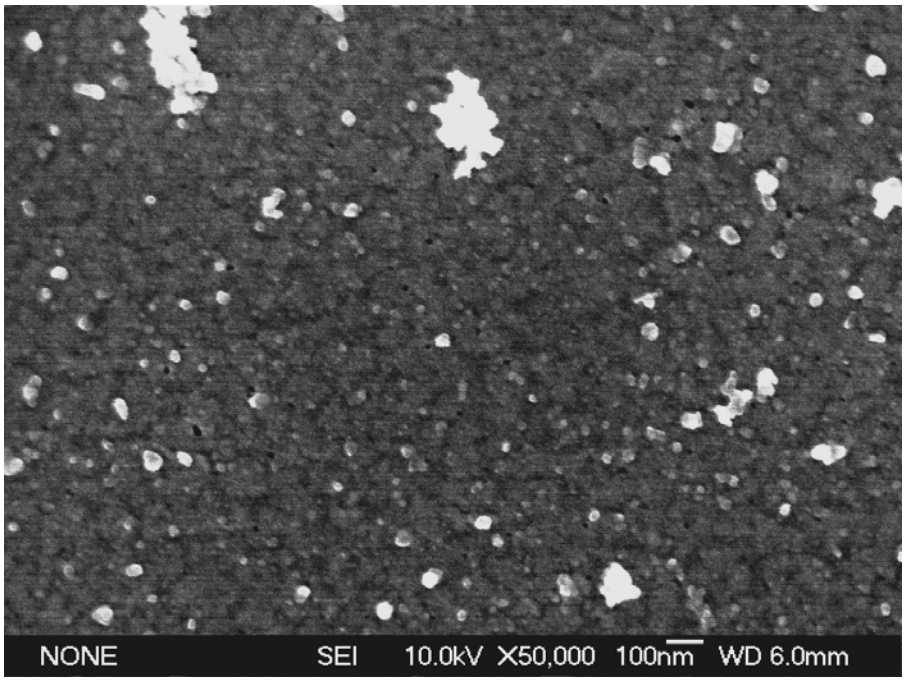

Figure 4.5: Top-down FE-SEM of sample CoPt2 showing a uniform coating of Co and Pt on the surface. Deposited via SFD in a hot wall reaction vessel at 150 ºC.

Figure 4.6: Polyamide hot wall reaction vessel liner used during experiment CoPt11. The film seen is a pure Pt flim deposited at 60 ºC via SFD.

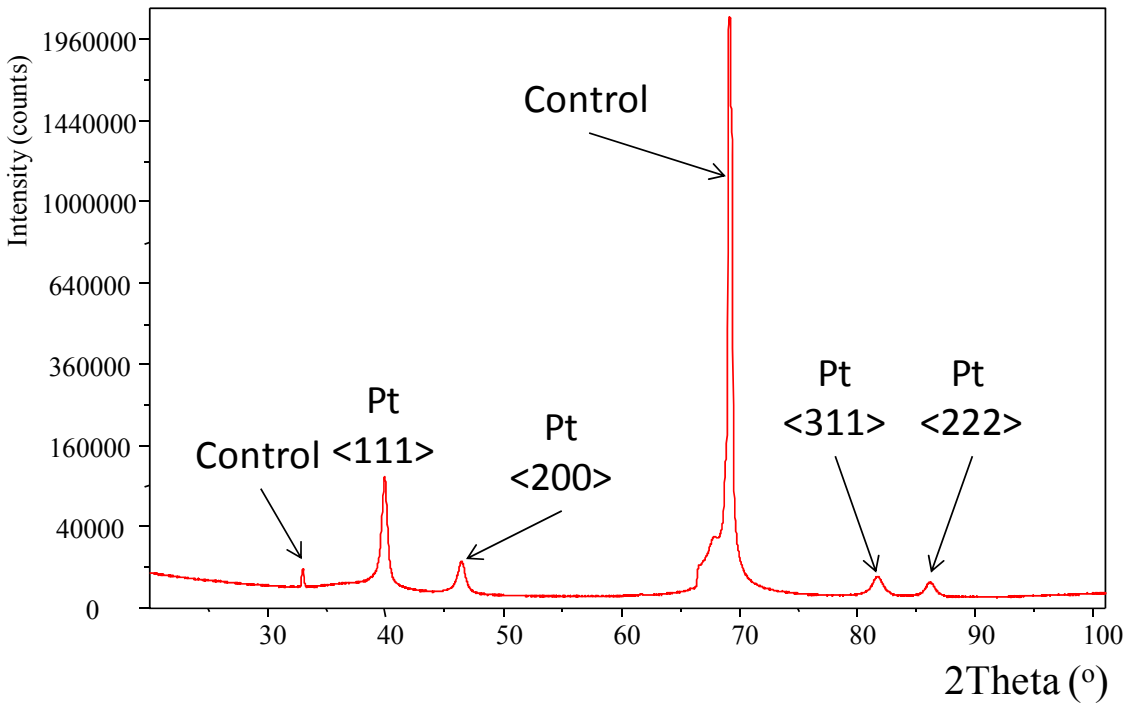

Figure 4.7: XRD of sample CoPt11 showing a polycrystalline platinum film. Deposited in a hot wall reaction vessel via SFD at 60 ºC.

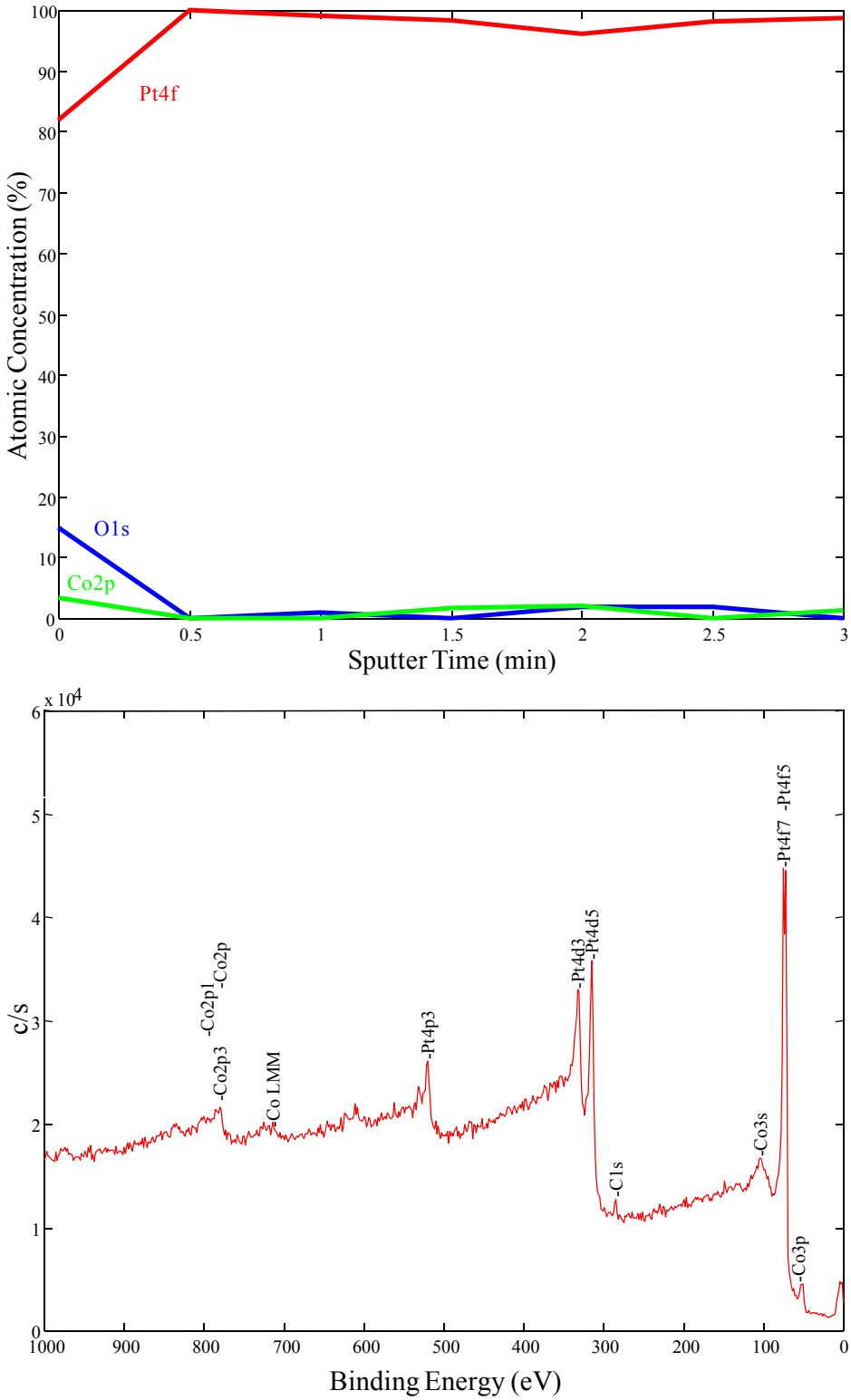

Figure 4.8: XPS sputter depth profile (top) and survey scan (bottom) of sample CoPt11 showing a pure platinum film with little surface contamination and no contamination through the bulk of the film. Deposited in a hot wall reaction vessel via SFD at 60 ºC.

Table 4.1: Table of reaction conditions for experiments CoPt1 – CoPt15.

		Precursors				Hydorgen	Reaction T
Sample	Reactor	Pt	wt. %	Co	wt. %	wt. %	ºC
CoPt1	Hot Wall	$Pt(Me)_2cod$	0.407	$CoCp_2$	0.458	0.515	150
CoPt2	Hot Wall	$Pt(Me)_2cod$	0.544	$CoCp_2$	0.519	0.854	150
CoPt3	Cold Wall	$Pt(Me)_2cod$	0.301	$CoCp_2$	0.303	0.259	250
CoPt4	Cold Wall	$Pt(Me)_2cod$	0.311	$CoCp_2$	0.280	0.402	250
CoPt5	Cold Wall	$Pt(Me)_2cod$	0.250	$CoCp_2$	0.250	0.488	250
CoPt6	Cold Wall	$Pt(Me)_2cod$	0.194	$CoCp_2$	0.247	0.403	300
CoPt7	Cold Wall	$Pt(Me)_2cod$	0.216	$Co(tmhd)_3$	0.392	0.345	300
CoPt8	Cold Wall	$Pt(Me)_2cod$	0.213	$Co(tmhd)_3$	0.389	0.288	75
CoPt9	Cold Wall	$Pt(Me)_2cod$	0.085	$Co(tmhd)_3$	0.156	0.432	60
CoPt10	Hot Wall	$Pt(Me)_2cod$	0.128	$Co(tmhd)_3$	0.237	0.483	40
CoPt11	Hot Wall	$Pt(Me)_2cod$	0.207	$Co(tmhd)_3$	0.378	0.439	60
CoPt12	Hot Wall	$Pt(Me)_2cod$	0.065	$Co(tmhd)_3$	0.375	0.483	60
CoPt13	Hot Wall	$Pt(Me)_2cod$	0.072	$Co(tmhd)_3$	0.389	0.439	60
CoPt14	Hot Wall	$Pt(Me)_2cod$	0.451	$CoCp_2$	0.256	0.438	60
CoPt15	Hot Wall	$Pt(Me)_2cod$	0.293	$CoCp_2$	0.163	0.527	60

4.2.1.3 Conclusions

Cobalt and platinum are successfully co-deposited onto TaN capped silicon wafers using $CoCp_2$ as the cobalt source and $Pt(Me)_2cod$ as the platinum source in a hot wall reactor at both 60 ºC and 150 ºC. Platinum only deposition or no deposition in the cold wall reactor is attributed to parasitic deposition to the heated sample stage and wall. The tmhd ligand in $Co(tmhd)_3$ is etching the cobalt during deposition resulting in high purity platinum films being deposited. Finally, XRD is used to analyze the crystal structure of the deposited film and alloying of the cobalt and platinum is not observed.

4.2.2 Ceria/Platinum

Direct methanol fuel cells (DMFCs) are a type of fuel cell that allows for the direct oxidation of methanol to carbon dioxide and reduction of oxygen to water. Although methanol has a greater energy density than hydrogen, DMFCs are limited by current membrane technology in attaining their true power density. However, they have the ability to store tremendous amounts of energy, thus making them ideal as alternative energy storage devices. The oxidation of methanol to carbon dioxide occurs at the anode and is shown in Equation 4.1. The reduction of oxygen to water occurs at the cathode and is shown in Equation 4.2. The overall reaction is shown in equation 4.3.[37-39]

$$CH_3OH + H_2O \rightarrow CO_2 + 6H^+ + 6e^- \qquad \text{Equation 4.1}$$

$$3/2\ O_2 + 6H^+ + 6e^- \rightarrow 3H_2O \qquad \text{Equation 4.2}$$

$$CH_3OH + 3/2\ O_2 \rightarrow CO_2 + 2H_2O \qquad \text{Equation 4.3}$$

CO is a known intermediate in these reactions and will adsorb to the catalyst, typically platinum, used for the fuel cell electrodes. The CO reduces the active surface area of the catalyst which slowly reduces the performance of the fuel cell.[40] In an attempt to alleviate this problem, researchers are attempting to identify materials that can be dispersed in the catalyst that will oxidize the CO instead of allowing the CO to poison the catalyst. On such material identified is ceria, a metal oxide, which can quickly switch back and forth between the +3 and +4 oxidation state, and therefore acts as an oxygen buffer.[41] This helps the CO oxidize to CO_2 and reduces the catalyst poisoning. Due to this, the development of a platinum and ceria matrix for the electrode in DMFCs is gaining a lot of interest in research.[42] Given the ability to individually deposit both

ceria[43] and platinum[44] from SFD, it is advantageous to combine the individual processes and develop a method for deposition of CeO_X/Pt matrices for DMFC electrodes.

4.2.2.1 Experimental

4.2.2.1.1 Equipment

4.2.2.1.1.1 Reactors

The cold wall reactor used is previously described in detail in chapter 3. The hot wall reactor used is the Thar vessel described earlier in this chapter.

4.2.2.1.2 Materials

Tetrakis(2,2,6,6-tetramethyl-3,5-heptanedionato)cerium (IV), 97 % (99.9 % Ce), $Ce(tmhd)_4$, [18960-54-8] and dimethyl(1,5-cyclooctadiene)platinum (II), 99 %, Me_2Pt-cod, [12266-92-1] are used as received without any further purification (Strem Chemicals, Inc., Newburyport, MA), Figure 4.9. Coleman grade (99.99 %) carbon dioxide, ultra high purity (99.999 %) hydrogen and prepurified grade (99.998 %) nitrogen are used as received (Merriam Graves Corp, Charlestown, NH). A buna-N o-ring, size 2-236, is used for the high pressure and high temperature cold wall reactor seal (Marco Rubber and Plastic Products, Inc., North Andover, MA). A thin (0.001") 3.25" by 3.25" polyamide Kapton film is cut to size and used for lining the inside of the hot wall reactors (McMaster-Carr, Atlanta, GA). Films are deposited on silicon wafers with 30 nm TaN deposited by CVD(crystal orientation <100>, 300 Å TaN by CVD, 1-100 micro-ohm centimeter, 750 micron total thickness) and carbon glass and carbon substrates which are prepared at the University of Puerto Rico – Rio Piedras campus, Cabrera group.

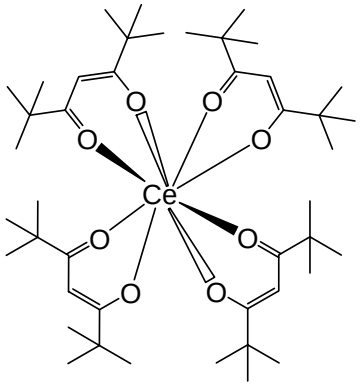

Figure 4.9: Chemical structure of Tetrakis(2,2,6,6-tetramethyl-3,5-heptanedionato)cerium (IV), Ce(tmhd)$_4$.

4.2.2.1.3 Procedure

Both hot and cold wall reactors are used to experiment with different precursor systems and pressure and temperature ranges.

For a typical reaction in the cold wall reactor, the substrate is mounted to the aluminum heated stage and secured with clips. A known amount of precursor is loaded into the vessel. Reaction conditions are listed in Table 4.2. The vessel is sealed and placed behind protective polycarbonate housing. Then, using a constant flow of nitrogen, the reaction vessel is purged continuously over a 30 minute period. The reactor wall and stage are then heated to the desired preheating temperature (typically 60 ºC) and allowed to equilibrate (t = 60 min.). Carbon dioxide is introduced into the reactor using a computer-controlled syringe pump. The reactor is then heated to a higher temperature (typically 150 ºC) to induce quicker dissolution of precursor into the CO_2 (t = 60 min.). The reactor is then cooled down to the original preheating temperature (t = 60 min.). Next, hydrogen is loaded into the system using a manifold of known volume (70 mL). The aluminum stage is then quickly heated (~ 15 s.) to the desired reaction temperature (typically 300 ºC) and maintained for a set time. The heated stage is then allowed to cool

down (~ 15 s.) while fresh CO_2 is used to flush multiple reactor volumes through the system to remove reaction byproducts and unreacted precursor. The effluent is passed through an activated carbon bed and silicon oil bubbler before being vented to the atmosphere.

For a typical reaction in the hot wall reactor, a thin (0.001") 3.25" by 3.25" polyamide (Kapton) film is used to line the inside of the reactor. A 25 mm by 19 mm silicon carbon glass, carbon substrate or TaN capped Si is then placed into the long tubular reactor. A known amount of precursor is loaded into the vessel. Reaction conditions are listed in Table 4.2. The vessel is sealed and placed behind protective polycarbonate housing. Then, using a constant flow of nitrogen, the reaction vessel is purged continuously over a 10 minute period. The reactor is then heated to the desired preheating temperature and allowed to equilibrate (t = 10 min.). Carbon dioxide is introduced into the reactor. The reactor is then heated to a higher temperature to induce quicker dissolution of precursor into the CO_2 (t = 60 min.). The reactor is then cooled down to the original preheating temperature (t = 60 min.). Next, hydrogen is loaded into the system using a manifold of known volume (70 mL). The system is maintained at these conditions for a set time. The reactor is then allowed to cool down while fresh CO_2 is used to flush multiple reactor volumes through the system to remove reaction byproducts and unreacted precursor. The effluent is passed through an activated carbon bed and silicon oil bubbler before being vented to the atmosphere.

The deposited films are characterized in order to obtain their purity, crystallinity and composition. Film purity and composition is determined by XPS (Ce^{45-54}, Pt^{25-36}). Crystallinity is determined by XRD.

4.2.2.2 Results and Discussion

Results for the co-deposition of ceria (cerium oxide, CeO_x) and platinum from $Ce(tmhd)_4$ and $Pt(Me)_2cod$ are presented. Both a cold wall and a hot wall reactor are used to conduct these experiments. For initial film deposition, TaN capped Si wafers are used as the deposition substrate, labeled TaN in Table 4.2. Experiments are performed in the hot wall reactor at a temperature of 60 ºC. The hot wall vessel is heated to 150 ºC prior to the deposition so that precursor can dissolve quicker into the supercritical carbon dioxide. The reactor is allowed to cool back to 60 ºC before the reaction is initiated with hydrogen. An FE-SEM image of a Ce/Pt co-deposited film is shown in Figure 4.10. Figure 4.11 is an XPS sputter depth profile showing a 1:1::Ce:Pt ratio at the surface. XRD further confirms the presence of Ce and Pt and also indicates the crystallinity of the Ce to be Ce_2O_3, <102> and <212>, and <200> for the platinum, Figure 4.12. The 2*theta values for Pt and Ce_2O_3 are very similar and therefore peak determination is based on peak intensity values. This observation is consistent with XPS results.

Table 4.2: Table of reaction conditions for each deposition, including subsequent depositions on the same sample, for samples TaN 01 – TaN 13 and samples C01 – C18.

	Deposition 1					Deposition 2				
Sample	Reactor	$Ce(tmhd)_4$	$Pt(Me)_2cod$	Ce:Pt::1:X	H_2	Reactor	$Ce(tmhd)_4$	$Pt(Me)_2cod$	Ce:Pt::1:X	H_2
		wt. %	wt. %	molar ratio	wt. %		wt. %	wt. %	molar ratio	wt. %
TaN 01	Hot	0.654	0.241	1.035	0.685					
TaN 02	Hot	0.616	0.266	0.883	0.855					
TaN 03	Hot	0.637	0.244	0.994	0.430					
TaN 04	Hot	0.613	0.268	0.874	0.771					
TaN 05	Hot	0.064	1.471	0.017	0.596					
TaN 06	Hot	0.639	0.277	0.880	0.000					
TaN 07	Hot	0.640	0.290	0.843	0.000					
TaN 08	Hot	0.639	0.231	1.057	0.856					
TaN 09	Hot	0.643	0.216	1.134	0.515					
TaN 10	Hot	1.271	0.217	2.231	0.512					
TaN 11	Hot	0.326	0.218	0.569	0.517					
TaN 12	Hot	0.000	0.229	N/A	0.604	Hot	0.649	0.000	N/A	0.000
TaN 13	Hot	0.645	0.225	1.093	0.515					
C 01	Hot	0.646	0.221	1.115	0.515					
C 02	Hot	0.646	0.227	1.087	0.344					
C 03	Cold	0.162	0.058	1.073	0.454					
C 06	Hot	0.652	0.240	1.038	0.855					
C 07	Cold	0.286	0.000	N/A	0.000	Hot	0.652	0.240	1.038	0.855
C 08	Hot	0.000	0.241	N/A	0.604	Hot	0.629	0.221	1.086	0.686
C 09	Cold	0.163	0.000	N/A	0.000	Hot	0.635	0.234	1.035	0.515
C 10	Hot	0.000	0.232	N/A	0.604	Cold	0.163	0.000	N/A	0.000
C 11	Hot	0.341	0.221	0.589	0.431					
C 12	Hot	1.287	0.221	2.218	0.427					
C 13	Hot	0.000	0.244	N/A	0.604					
C 14	Hot	0.000	0.242	N/A	0.518					
C 15	Hot	0.000	0.242	N/A	0.518	Hot	0.000	0.223	N/A	1.032
C 16	Cold	0.157	0.000	N/A	0.000	Cold	0.167	0.062	1.029	0.238
C 17	Hot	0.000	0.244	N/A	0.432					
C 18	Hot	0.000	0.223	N/A	1.032	Cold	0.157	0.000	N/A	0.000

	Deposition 3					Deposition 4				
Sample	Reactor	$Ce(tmhd)_4$	$Pt(Me)_2cod$	Ce:Pt::1:X	H_2	Reactor	$Ce(tmhd)_4$	$Pt(Me)_2cod$	Ce:Pt::1:X	H_2
		wt. %	wt. %	molar ratio	wt. %		wt. %	wt. %	molar ratio	wt. %
C 10	Hot	0.000	0.227	N/A	1.032	Cold	0.158	0.000	N/A	0.000
C 18	Hot	0.000	0.244	N/A	0.432	Cold	0.155	0.000	N/A	0.000

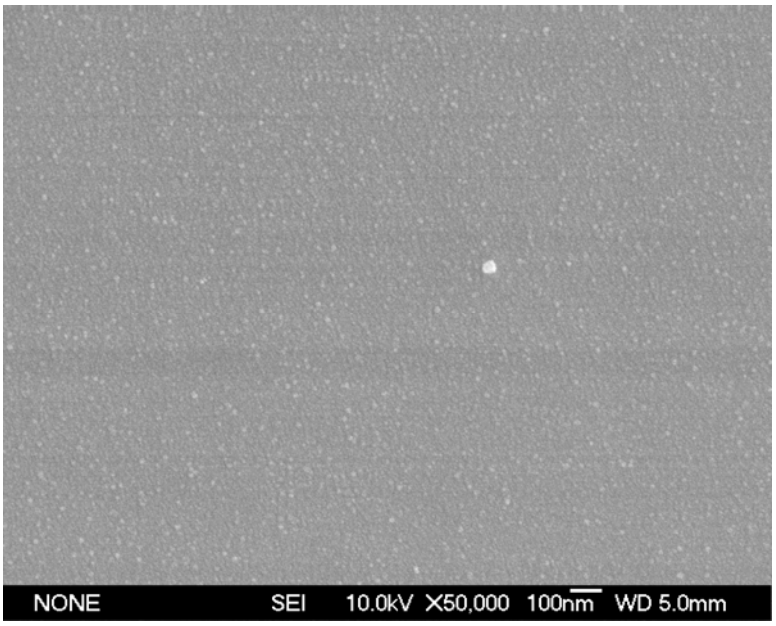

Figure 4.10: Top-down FE-SEM of sample TaN08 showing a conformal coating of Ce and Pt on the TaN capped substrate. Deposited via SFD in a hot wall reaction vessel at 150 ºC.

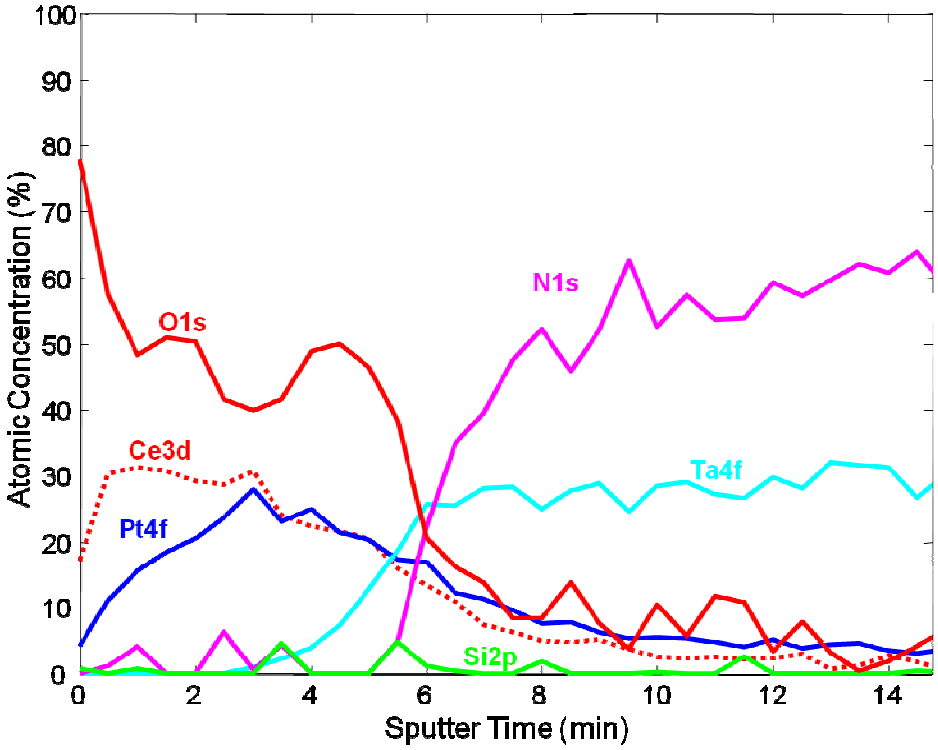

Figure 4.11: XPS sputter depth profile of sample TaN11 showing a 1:1::Ce:Pt ratio at the surface of the TaN surface. Deposited in a hot wall reaction vessel via SFD at 150 ºC.

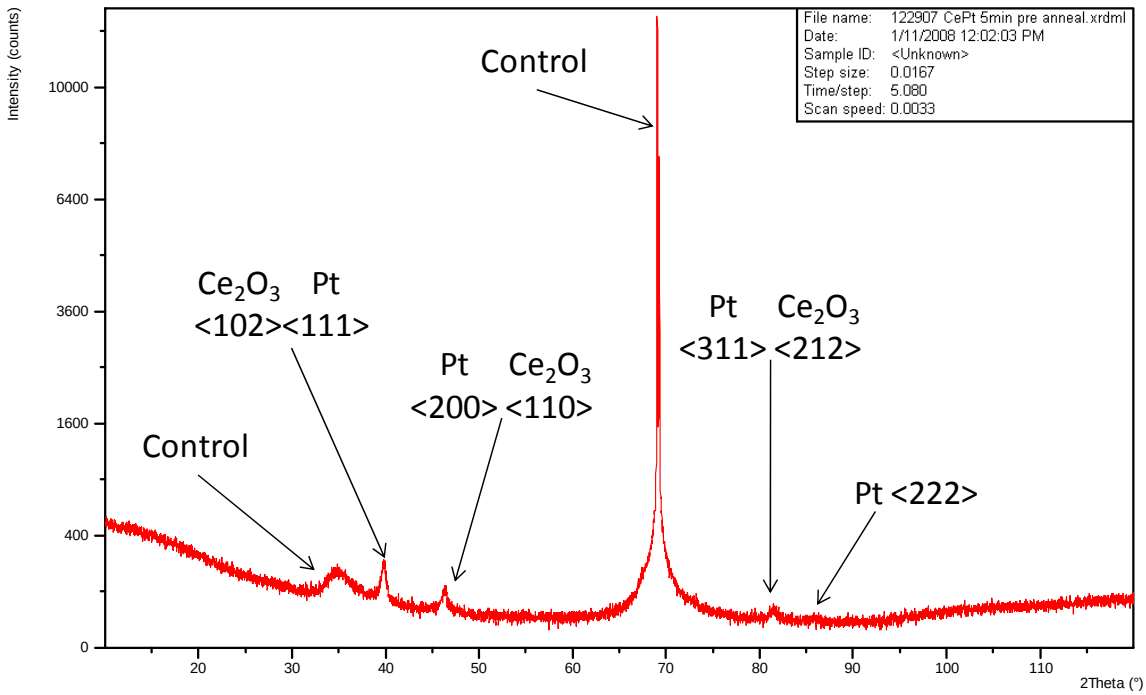

Figure 4.12: XRD pattern that confirms the presence of Ce and Pt on sample TaN11. The Ce peaks correspond to Ce_2O_3, <102> and <212> while the platinum peaks correspond to <200>. Ce and Pt deposited in a hot wall reaction vessel via SFD at 150 ºC.

An interesting result is the deposition of ceria at the reduced temperature of 60 ºC as opposed to the typical deposition temperature of 300 ºC.[43] It is proposed that the platinum is acting as a catalyst which is enhancing the deposition of the ceria to the surface. In a similar finding, Puddephatt et al. reports the use of palladium catalysts to reduce the CVD deposition temperature of cerium oxide from various $Ce(CF_3COCHCOCF_3)$, $Ce(hfac)_3$, compounds from 450 ºC to 250 ºC.[49] He also reports the catalyst-enhanced CVD of yttrium oxide from $Y(tmhd)_3$ at temperatures as low as 315 ºC from temperatures as high as 500 ºC.[55]

Having successfully deposited CeO_x and Pt simultaneously in a dispersed matrix on TaN capped Si, applications were identified that would benefit from this process. A collaboration with the Cabrera group at the University of Puerto Rico- Rio Piedras campus (UPR) was initiated in an attempt to fabricate alternative DMFC electrodes. The

ceria and platinum need to be dispersed into a carbon glass or carbon film so that the DMFC electrode can be fabricated and function properly. For this reason, the substrates used for deposition are now the carbon matrices provided by UPR, labeled C1 – C12 in Table 4.2.

CeO_x/Pt co-depositions are carried out in a similar fashion to the previous depositions. FE-SEM, XPS and XRD are used to characterize the deposited films. A low magnification SEM image, Figure 4.13, shows a uniform CeO_x/Pt film deposited on the carbon matrix. A higher magnification, Figure 4.14, reveals CeO_x/Pt particles, whose sizes range between 100 – 500 nm, dispersed on top of the carbon matrix. An XPS sputter depth profile, Figure 4.15 (bottom), not only further confirms that the ceria (top left) and platinum (top right) are dispersed across the surface, but dispersed throughout the thickness of the carbon substrate. XRD, Figure 4.16, indicates that platinum is polycrystalline and the ceria is in the $^{+}3$ state (Ce_2O_3).

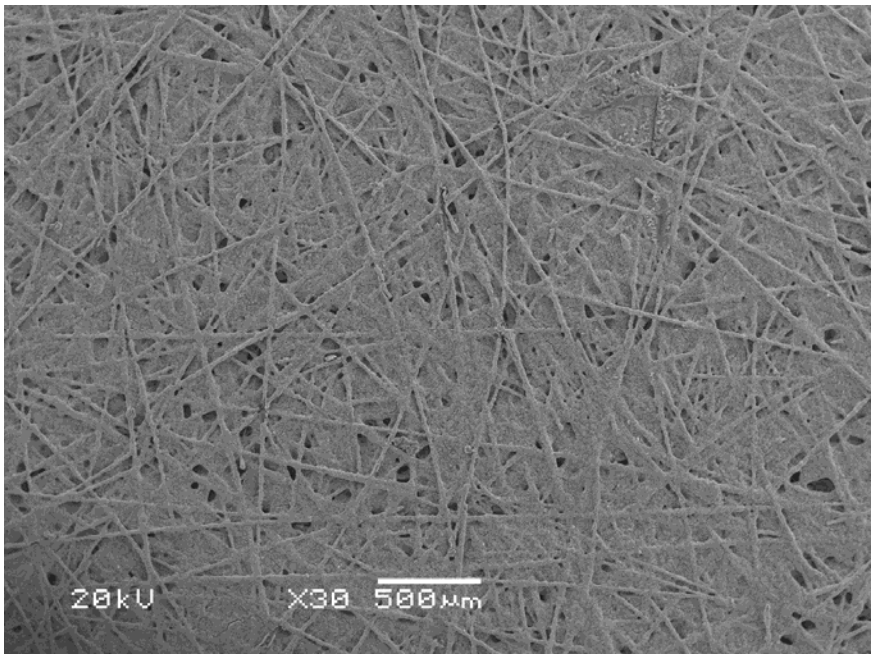

Figure 4.13: FE-SEM image at low magnification showing Ce/Pt deposited on a carbon matrix, sample C08. Ce/Pt deposited via two separate SFD reactions. The first reaction is a deposition with platinum precursor only in a hot wall reaction vessel at 150 ºC. The second is deposition of both Ce and Pt precursors in a hot wall reaction vessel at 150 ºC.

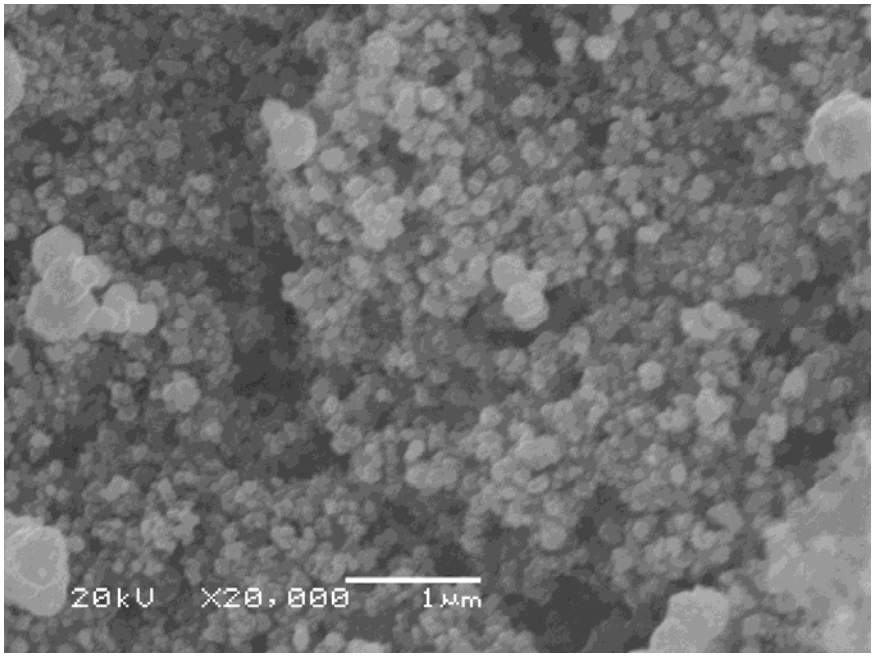

Figure 4.14: FE-SEM image showing Ce/Pt deposited on a carbon matrix, sample C08. Particle sizes range from 100 – 500 nm. Ce/Pt deposited via two separate SFD reactions. The first reaction is a deposition with platinum precursor only in a hot wall reaction vessel at 150 ºC. The second is deposition with both Ce and Pt precursors in a hot wall reaction vessel at 150 ºC.

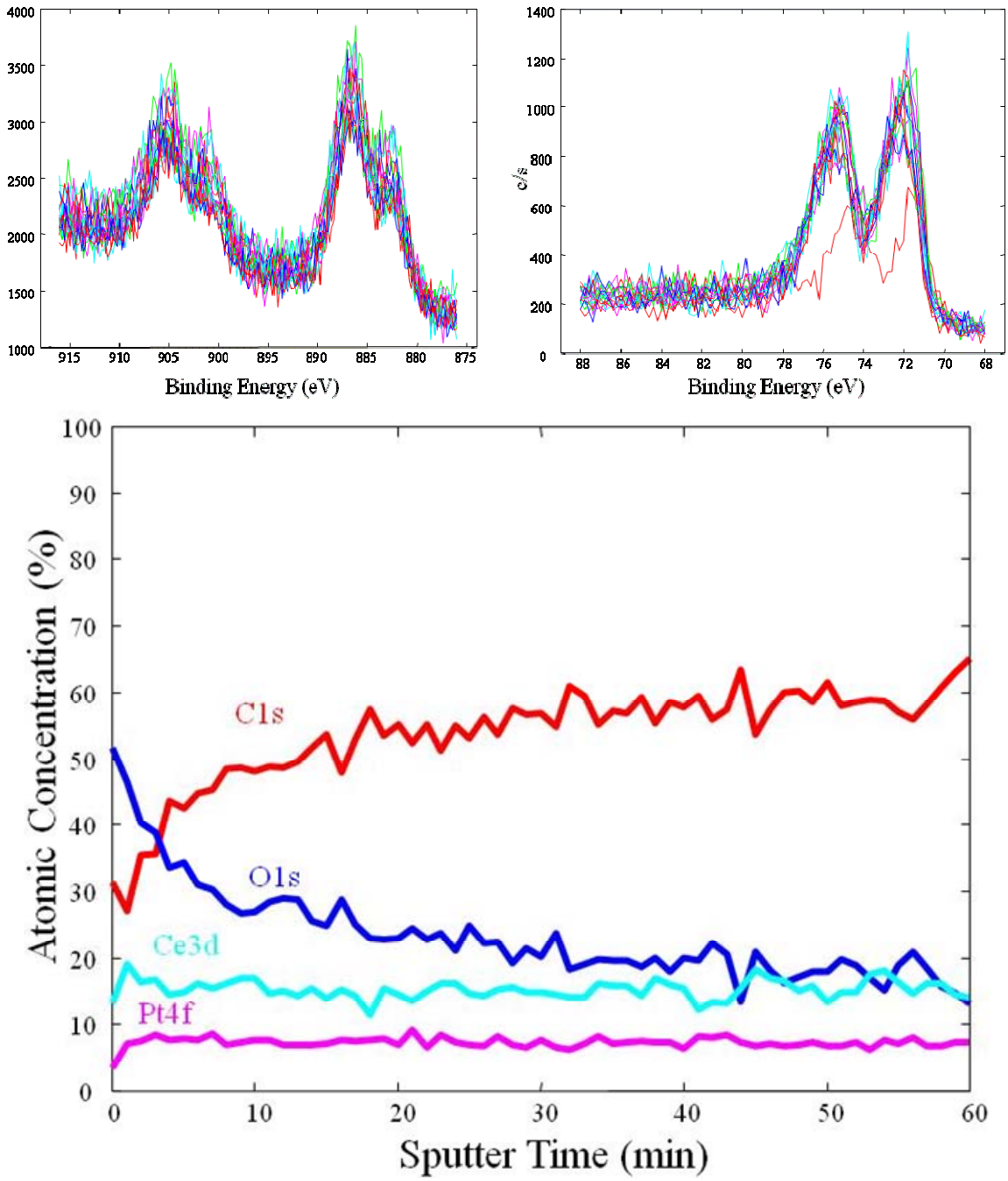

Figure 4.15: XPS spectra of the Ce 3d finger print region (top left) and Pt 4f finger print region (top right) confirming the presence of both Ce and Pt in sample C09. XPS sputter depth profile (bottom) showing that the Ce and Pt are dispersed throughout the entire thickness of the carbon substrate. Ce/Pt deposited via two separate SFD reactions. The first reaction is a deposition of ceria only in a cold wall reaction vessel at 300 ºC. The second is deposition of both Ce and Pt in a hot wall reaction vessel at 150 ºC.

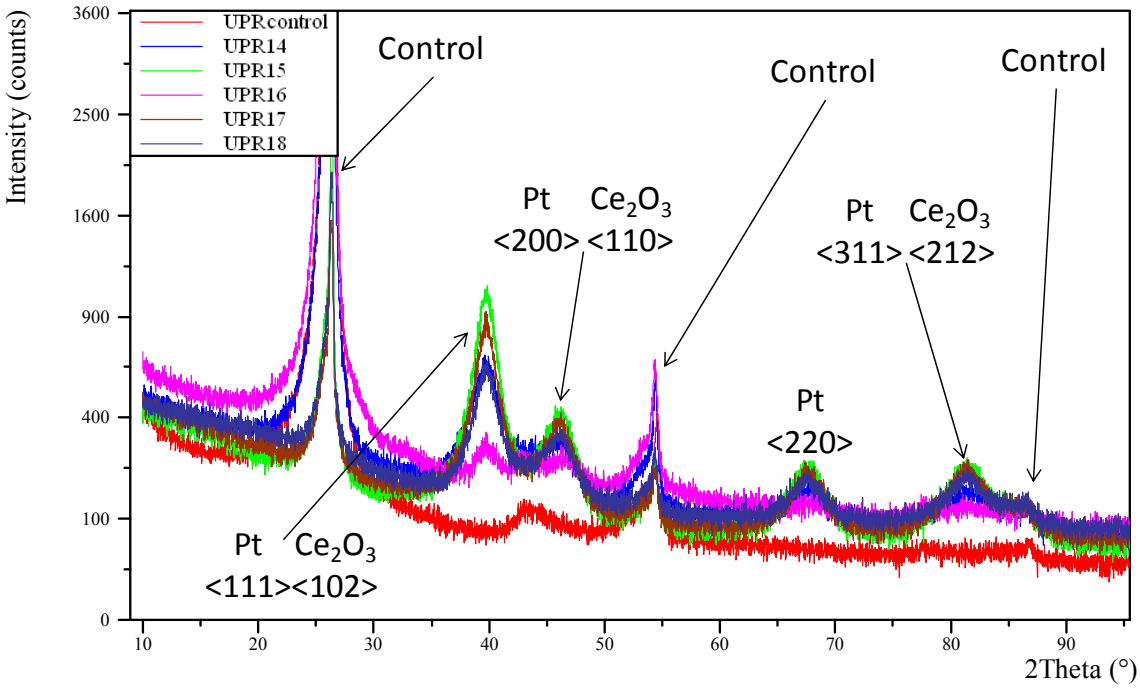

Figure 4.16: XRD comparison of samples C14 – C18. All samples show polycrystalline platinum peaks and indicate that ceria is also polycrystalline in the $^{+}3$ state (Ce_2O_3).

The samples are then sent to UPR for electrochemical measurements. The electrical testing results of sulfuric acid cyclic voltammetry and methanol oxidation are used to evaluate which process of ceria and platinum deposition yielded the optimum catalytic activity are reported in Table 4.3. A result of "partial" indicates that there is an observable activity, however it is negligible. These "partial" results correspond to films from single depositions. It is found that subsequent depositions of Pt and Ce yielded the optimum films due to the greatest catalytic activity. It is therefore proposed that the multiple depositions allow for higher concentration of catalytic material to be deposited, thereby increasing the catalytic activity of the electrode.

Table 4.3: Qualitative results of electrical testing to determine catalytic activity of samples C03, C06 – C12.

	Catalytic Activity	
Sample	Sulfuric Acid	Methanol Oxidation
C 03	N	N
C 06	N	N
C 07	Partial	Y
C 08	Y	Y
C 09	Y	Y
C 10	Y	Y
C 11	Partial	Y
C 12	Y	Partial

4.2.2.3 Conclusions

A low temperature process for the co-deposition of polycrystalline ceria ($^{+}3$ state) and polycrystalline platinum from $Ce(tmhd)_4$ and $Pt(Me)_2cod$ is discovered. It is proposed that the platinum is catalytically enhancing the deposition of ceria at temperatures as low at 60 ºC as opposed to typical SFD ceria films deposited at 300 ºC. This co-deposition process is extended towards the application of methanol oxidation fuel cell electrodes. Electrical testing indicates that layer by layer deposition of Pt and Ce yield the highest amount of catalytic activity in the fabricated electrodes.

4.2.3 Barium Titanate

There exists a need for better energy storage devices given the rise in increasingly power intensive microelectronics devices. Batteries based off of standard lithium ion chemistry have high efficiencies of roughly 80 %. However, the power density is very low, requiring large bulky batteries to power cell phones and laptop computers for short periods of time before a recharge is needed. Additionally, the recharge time for batteries is on the order of hours, which for most electronics renders them unusable while recharging. The total number of recharge cycles is also limited to roughly 1000, limiting most rechargeable lithium ion batteries to a daily usage lifetime of 3 years. An alternative to liquid lithium ion chemistry based batteries is the use of solid ceramics, having a high dielectric constant (k). These solid state alternative energy devices have increased power density and recharge times with as many as 10^6 recharge cycles.

One such solid state ceramic, alternative energy, high k dielectric material is barium strontium titanate ($Ba_{1-x}Sr_xTiO_3$, BST).[56, 57] $BaTiO_3$, BT, was originally studied because it exhibits ferroelectric behavior.[58] It has high dielectric permittivity, good thermal stability and a Curie temperature of 120 ºC, which makes it an ideal candidate for multi layer ceramic capacitors (MLCCs).[59] It was found that with the addition of strontium to the BT material, the Curie temperature could be controllably lowered to room temperature.[60-62] The ability to have a room temperature Curie temperature, in conjunction with sub 100 nm particle size, opens up the possibility for a wide range of applications: tunable resonators, filters, phase-shifters, variable-powder dividers and variable-frequency oscillators.[63, 64] Unfortunately, the techniques (sol-gel[65-67],

precipitation[68-70], hydrothermal[64, 71-74] and mechanochemical[75]) for fabricating BST powders suffer from a variety of problems, some of which are the need for multiple complex steps, temperatures over 1300 ºC needed for processing, large particle size distributions[76-78] and secondary phases are formed, such as Ba_2TiO_4 and $Ba_6Ti_{17}O_{10}$.

Current areas of research are focused on simplifying the BT and BST synthesis process. In 1999, Bocquet et al. reported the semi-continuous process for the formation of BT powders using a solvothermal reaction and supercritical treatment.[79] This was quickly followed by the first fully continuous synthesis of BT[80] and BST[81] powders by Aymonier et al. in 2005 and 2006, respectively. It is now of interest to extend this single step continuous synthesis of BT and BST material to the deposition of films in order to pursue thin ceramic film applications. For example, a nano sized capacitors that will have orders of magnitude higher energy density than current capacitors used in the microelectronics industry.

4.2.3.1 Experimental

4.2.3.1.1 Equipment

4.2.3.1.1.1 Reactor

The cold wall reactor used is previously described in detail in chapter 3. The aluminum stage was replaced with a stainless steel stage in order to prevent aluminum oxide formation in the highly corrosive H_2O/EtOH environment.

4.2.3.1.2 Materials

Barium isopropoxide, Baip, [24363-37-9] and titanium (IV) isopropoxide, 98 %, Ttip, [546-68-9] are used as received without any further purification (Strem Chemicals, Inc., Newburyport, MA), Figure 4.17. Prepurified grade (99.998 %) nitrogen is used as received (Merriam Graves Corp, Charlestown, NH). A viton o-ring, size 2-236, is used for the high pressure and high temperature cold wall reactor seal (Marco Rubber and Plastic Products, Inc., North Andover, MA). Films are deposited on silicon (crystal orientation <100>, 500 nm thermally grown oxide, 1-100 micro-ohm centimeter, 750 micron total thickness) (Novellus, San Jose, CA).

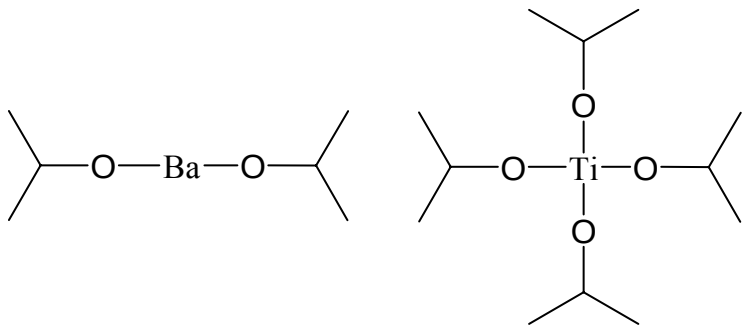

Figure 4.17: Chemical structure of barium isopropoxide, Baip, and titanium (IV) isopropoxide, Ttip.

4.2.3.1.3 Procedure

The procedure used here is adopted from Aymonier et al. for powder formation and modified to adapt to the cold wall reactor system for film formation. The solvent system used is an H_2O/EtOH mixture. EtOH is used since the selected precursors are stabilized in the solution. H_2O plays a critical role in the crystallization of high purity $BaTiO_3$. The thermodynamic phase behavior of EtOH[82-86] and H_20/EtOH[87-98] is found in the literature.

4.2.3.1.3.1 Precursor Synthesis

Reaction conditions are listed in Table 4.4. In an N_2 glove box, a known mass Baip is added to a known volume of EtOH. Ttip is then added drop wise to the solution. Solution should be clear, if precipitate is seen, Baip may have degraded due to presence of oxygen. The beaker is sealed and stirred for 2 to 3 hours.

4.2.3.1.3.2 Film Deposition

For a typical reaction, a 2" <100> silicon wafer is mounted to the stainless steel heated stage and secured with clips. The vessel is sealed and placed behind protective polycarbonate housing. Then, using a constant flow of nitrogen, the reaction vessel is purged continuously over a 30 minute period. The precursor solution that finished mixing is now collected into a large syringe. The precursor solution is injected into the reactor. A known volume of H_2O is injected into the reactor and nitrogen is used to quickly purge the inlet and outlet of the reactor. The valves through which the precursor solution and H_2O were injected are now sealed. The system is heated to 150 ºC and maintained for 30 min (to induce film formation and to improve stoichiometry). The system is heated to 250 ºC and maintained for 30 min (EtOH decomposes via dehydration). Ideally, the system would be heated to 380 ºC and maintained for 30 minutes to allow crystallization. However, due to reactor limitations, the system is heated to 290 ºC and maintained for 30 minutes. The system is cooled overnight and opened the next day.

The deposited films are characterized with XPS (Ba[99, 100], Sr[100] and Ti[22, 25, 101-104]) in order to obtain their purity and composition.

4.2.3.2 Results and Discussion

Experiments are carried out in order to deposit films of $BaTiO_3$ from supercritical water and ethanol mixtures onto silicon substrates. Ethanol is used in order to dissolve both precursors prior to reaction so that $BaTiO_3$ is formed and not barium carbonate, which is favored when reacting the components individually. The first step in this reaction process is the precursor synthesis. It is important to note that the Baip is very air sensitive, showing color change instantly in the presence of air. The precursor synthesis is by far the most important step and significant attention is required to properly synthesize the precursor solution. The precursor solution is stable for approximately 3 hours after synthesis and therefore must be made prior to each experiment. A new stainless steel heated stage is used for the reactions since the aluminum readily oxidizes to aluminum oxide in the presence of water at the reaction temperatures.

For all reactions, the Ba to Ti molar ratio is always 1 to 1. The temperatures used during the reaction are 150 ºC, 250 ºC and 290 ºC. The first temperature, 150 ºC, is used to obtain an appropriate stoichiometry for the film and to induce film formation. The temperature is taken to 250 ºC, which is used to dehydrate the EtOH and supply more water to the system. For powder formation, the final temperature used is 380 ºC which results in high purity, polycrystalline BT powders without barium carbonate formation. However, as previously mentioned, the physical limitations of the reactor prevented this and a final temperature of 290 ºC is used.

Water is a critical key to the crystallization of BT and without it, $BaCO_3$ is formed. The optimum water to molecular titanium ratio is found to be 1536.[80] This ratio is used for experiment BT1 through BT3. For experiments BT4 through BT6, the water

ratio is adjusted in order to determine its effects on BT film formation. Propoxide concentration is changed from the optimum value in powder formation to 0.01 in experiment BT2 to determine its effect on BT film formation. Experiment BT2 and BT3 serve as the control experiments.

Experiments BT1 through BT6 did not yield BT films. Changing both the water concentration and the propxide concentration did not have any effect on the ability to deposit BT films. XPS confirms the presence of Ba, and no Ti, in all experiments, Figure 4.18, however the atomic concentration is below 1 %. Additionally, from the detection of both carbon and oxygen, as detected by XPS, Figure 4.19, both at the surface and throughout the bulk of the film, it is concluded that a trace amount of $BaCO_3$ is formed throughout the film.

Table 4.4: Table of reaction conditions for samples BT1 – BT6.

	Baip	Ttip	H_2O	EtOH	Propoxide Concentration	H_2O/Ti
Experiment	wt. %	wt. %	wt. %	wt. %	mol/(L EtOH)	mol ratio
BT1	0.138	0.152	14.837	84.872	0.03	1536
BT2	0.052	0.056	5.452	94.441	0.01	1536
BT3	0.052	0.056	5.452	94.441	0.01	1536
BT4	0.053	0.057	3.570	96.321	0.01	1000
BT5	0.054	0.058	1.907	97.981	0.01	500
BT6	0.055	0.059	0.478	99.408	0.01	100

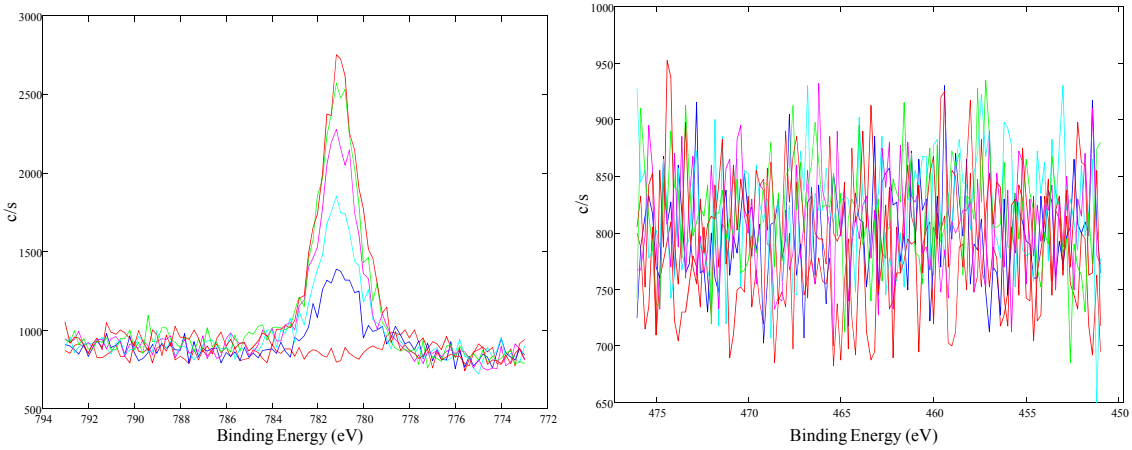

Figure 4.18: XPS spectra of Ba 3d (left) and Ti 2p (right) finger print regions of sample BT5. Ba is present, however Ti is not. Deposited from supercritical H_2O/EtOH at 290 ºC with a 0.01 M propoxide concentration and a H_2O/Ti molar ratio of 500.

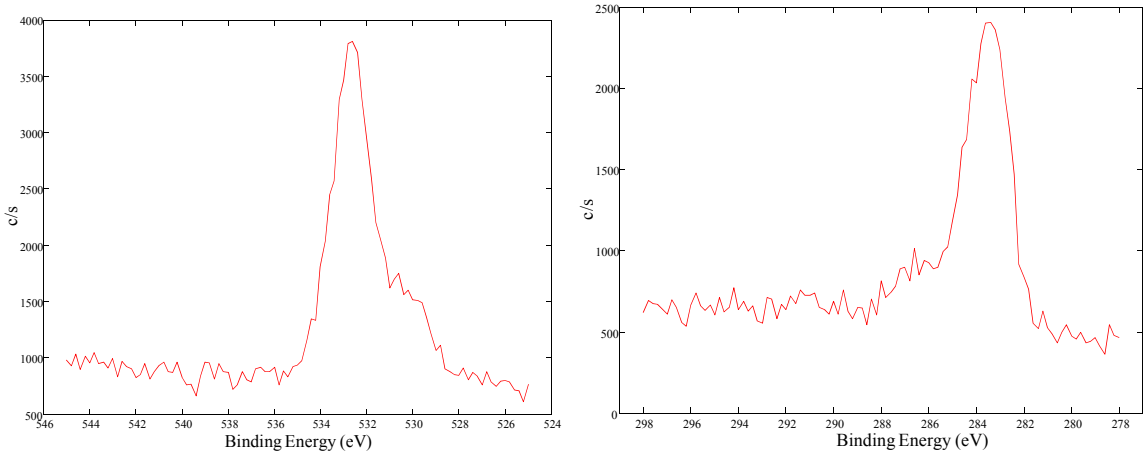

Figure 4.19: XPS spectra of O 1s (left) and C 1s (right) finger print regions of sample BT6. Both C and O are present in high concentration confirming the formation of $BaCO_3$. Deposited from supercritical H_2O/EtOH at 290 ºC with a 0.01 M propoxide concentration and a H_2O/Ti molar ratio of 100.

4.2.3.3 Conclusions

The method for single step synthesis of $BaTiO_3$ powders is modified to attempt $BaTiO_3$ film deposition from supercritical ethanol/water solutions. Two studies are performed in order to analyze their ability to induce $BaTiO_3$ film formation in this new process. Both the water ratio, which controls $BaTiO_3$ crystallinity, and the propoxide molality, used in precursor synthesis, are tested and found to have no affect on the ability

to deposit high purity polycrystalline $BaTiO_3$ films. Given the experimental findings and the high $BaCo_3$ concentrations deposited on the films, it is proposed that the high purity polycrystalline $BaTiO_3$ did not form due to the inability to reach the final temperature of 380 ºC which is responsible for $BaTiO_3$ crystallinity.

4.2.4 Neodymium/Nickel

Solid oxide fuel cells (SOFCs) are electrochemical devices that can produce energy directly from the oxidation of a fuel with an efficiency of 60 %. Byproduct gases produced from this reaction can further be used to power gas turbines and increase the overall efficiency of the system to 85 %. The operating temperature for a SOFC is between 600 and 1000 ºC. It is of interest to reduce the operating temperature of SOFCs for the purpose of increased reliability and the option to use other materials for device fabrication, of which some are much cheaper. Unfortunately, electrochemical reactions are temperature driven and by reducing temperature, both power density and efficiency of the SOFC is reduced. Despite these drawbacks, it is still advantageous to move to reduced temperatures. In order to do this, optimization of the interface between electrodes and the electrolyte is necessary so that reduced energy losses are realized. Additionally, it is desirable to optimize the crystallinity, morphology and particle size for increased electrochemical performance.

One particular area of interest in developing reduced operating temperature SOFCs is the determination of high performance cathode materials. Doped lanthanum manganite perovskite is commonly used for SOFC cathodes, however, has shown to have poor performance at reduced temperatures. Recently, $Nd_2NiO_{4+\delta}$ was identified as a material that exhibits high ionic and electronic conductivity, high electrocatalytic activity towards oxygen reduction and good mechanical properties.[105, 106] These properties are ideal for a new cathode material.[107]

4.2.4.1 Experimental

4.2.4.1.1 Equipment

4.2.4.1.1.1 Reactor

The cold wall reactor used is previously described in detail in chapter 3.

4.2.4.1.2 Materials

Tris(2,2,6,6-tetramethyl-3,5-heptanedionato)neodymium (III), 99 % (99.9 % Nd), $Nd(tmhd)_3$, [15492-47-4], bis(2,2,6,6-tetramethyl-3,5-heptanedionato)nickel (II), 98 % (99.9 % Ni), $Ni(tmhd)_2$, [41749-92-2], tris(cyclopentadienyls)neodymium, 99 % (99.9 % Nd), $NdCp_3$, [1273-98-9], and bis(cyclopentadienyls)nickel, 99%, $NiCp_2$ or nickelocene, [1271-039-0] are used as received without any further purification (Strem Chemicals, Inc., Newburyport, MA), Figure 4.20. Coleman grade (99.99 %) carbon dioxide, ultra high purity (99.999 %) hydrogen and prepurified grade (99.998 %) nitrogen are used as received (Merriam Graves Corp, Charlestown, NH). A buna-N o-ring, size 2-236, is used for the high pressure and high temperature cold wall reactor seal (Marco Rubber and Plastic Products, Inc., North Andover, MA). Films are deposited on 2” silicon disks (crystal orientation <100>, native oxide, 1-100 micro-ohm centimeter) (Wafer World Inc., West Palm Beach, FL).

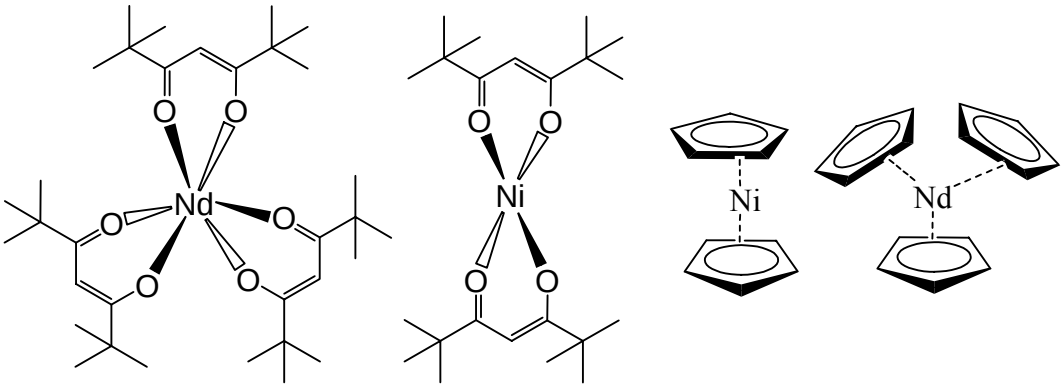

Figure 4.20: Chemical structure of tris(2,2,6,6-tetramethyl-3,5-heptanedionato)neodymium (III), $Nd(tmhd)_3$, bis(2,2,6,6-tetramethyl-3,5-heptanedionato)nickel (II), $Ni(tmhd)_2$, bis(cyclopentadienyls)nickel, $NiCp_2$ or nickelocene, and tris(cyclopentadienyls)neodymium, $NdCp_3$.

4.2.4.1.3 Procedure

For a typical reaction, a 2" <100> silicon wafer is mounted to the aluminum heated stage and secured with clips. A known amount of precursor is loaded into the vessel. The vessel is sealed and placed behind protective polycarbonate housing. Then, using a constant flow of nitrogen, the reaction vessel is purged continuously over a 30 minute period. Simultaneously, the reactor wall and stage are then heated to the desired preheating temperature. Carbon dioxide is introduced into the reactor using a computer-controlled syringe pump. The reactor is then heated and maintained at a higher temperature to induce quicker dissolution of precursor into the CO_2 (t = 60 min.). Next, hydrogen is loaded into the system using a manifold of known volume (70 mL). The aluminum stage is then quickly heated (~ 15 s.) to the desired reaction temperature and maintained for a set time. The heated stage is then allowed to cool down (~ 15 s.) while fresh CO_2 is used to flush multiple reactor volumes through the system to remove reaction byproducts and unreacted precursor. The effluent is passed through an activated carbon bed and silicon oil bubbler before being vented to the atmosphere.

The deposited films are characterized in order to obtain their purity, crystallinity and composition. Film purity and composition is determined by XPS (Nd[108], Ni[22, 25, 101, 109-112]). Crystallinity is determined by XRD.

4.2.4.2 Results and Discussion

The results and discussion for initial experimentation on the co-deposition of neodymium and nickel from $Ni(tmhd)_2$ and $Nd(tmhd)_3$ in supercritical carbon dioxide are presented. The precursors are chosen due to the temperatures at which they melt and decompose, Table 4.5. As seen with the ruthenium precursor presented in Chapter 2, dissolution rate increased with increasing temperature. This is because dissolution into CO_2 is quicker from a liquid than from a crystalline solid. Given the decomposition temperatures, the "sweet spot" for SFD reaction temperature is between 225 ºC and 270 ºC. The temperature range that was studied is between 265 ºC to 300 ºC in order to evaluate deposition at both optimum precursor conditions and reactor limits. The concentration range studied for both Nd and Ni is 0.1 wt. % to 0.2 wt. %. Hydrogen concentration is constant at 0.5 wt. %.

Deposition at both 265 ºC and 300 ºC yields high purity nickel films with trace amounts of neodymium. Figure 4.21 is an XPS survey scan of the Nd/Ni film deposited at 265 ºC. Ni 3p and 2p peaks are strong while Ni 3d peaks are relatively weak. Figure 4.22 shows the enlarged XPS survey scan for the Ni and Nd finger print regions, which show strong signals for their respective orbitals. Figure 4.23 is an XPS sputter depth profile showing the high purity nickel film with relatively little to no neodymium.

Table 4.5: Melting points and decomposition points for precursors used in Nd/Ni co-depositions experiments.

Precursor	T_m	T_d
$Ni(tmhd)_2$	223-225	300+
$Nd(tmhd)_3$	209-212	270

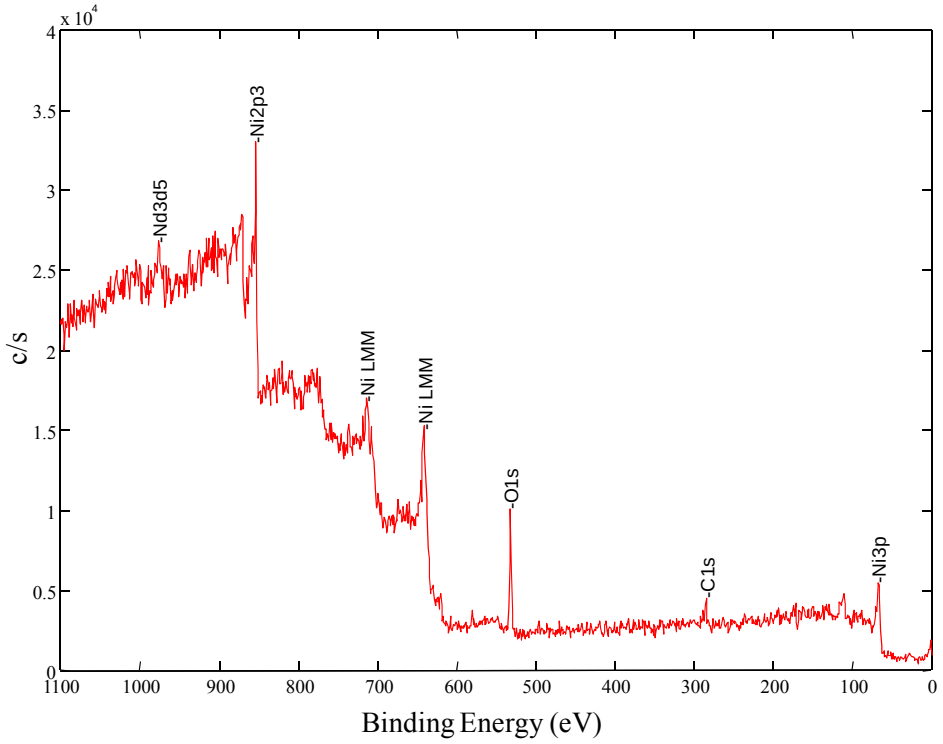

Figure 4.21: XPS survey scan of an Nd/Ni co-deposited film. Ni 3p and 2p peaks are strong while Ni 3d peaks are relatively weak. Reactions conditions: cold wall reactor, T = 265 ºC, 193 bar, 0.214 $Ni(tmhd)_2$ wt. %, 0.211 $Nd(tmhd)_3$ wt. %, 0.432 hydrogen wt. % and 30 min reaction time.

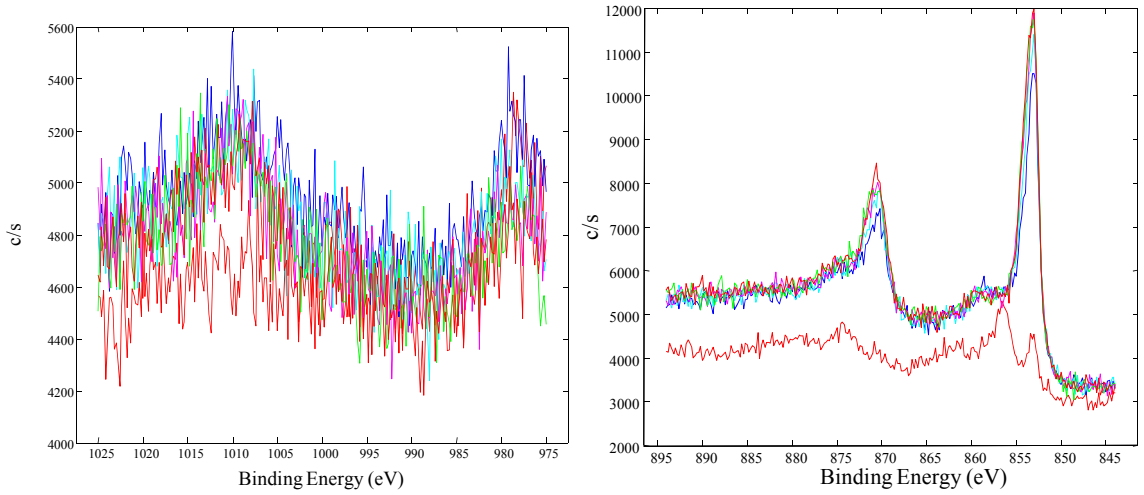

Figure 4.22: XPS spectra of Nd 3d (left) and Ni 2p (right) finger print regions for a Nd/Ni co-deposited sample. Reactions conditions: cold wall reactor, T = 300 ºC, 193 bar, 0.106 $Ni(tmhd)_2$ wt. %, 0.119 $Nd(tmhd)_3$ wt. %, 0.518 hydrogen wt. % and 30 min reaction time.

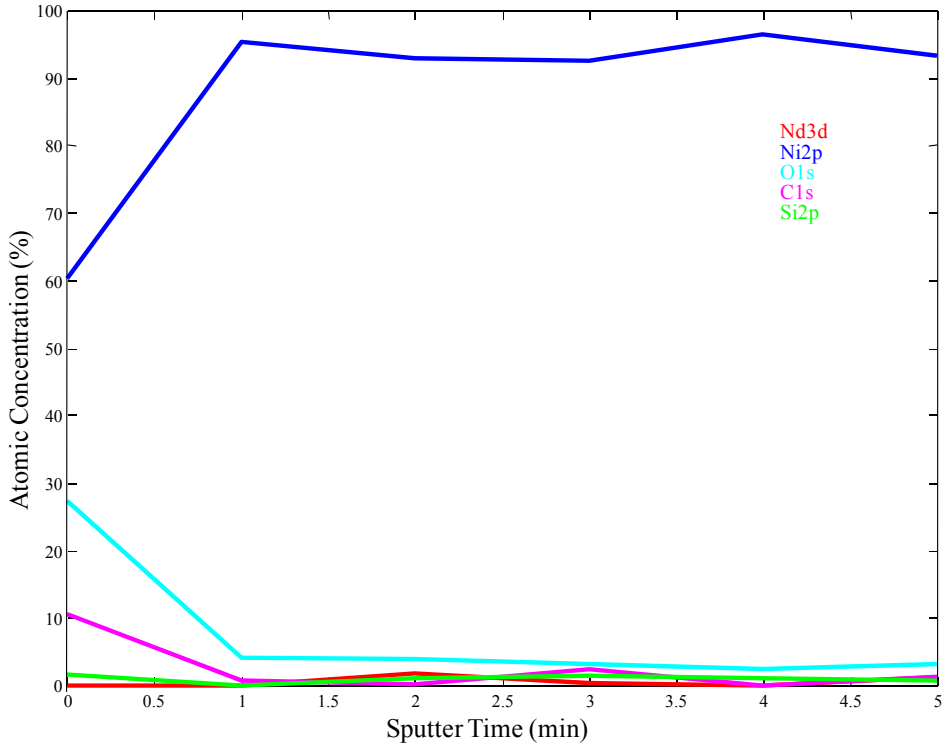

Figure 4.23: XPS sputter depth profile of an Nd/Ni co-deposited film. High purity nickel is deposited with trace amounts of neodymium. Reactions conditions: cold wall reactor, T = 265 ºC, 193 bar, 0.214 $Ni(tmhd)_2$ wt. %, 0.211 $Nd(tmhd)_3$ wt. %, 0.432 hydrogen wt. % and 30 min reaction time.

4.2.4.3 Conclusions

Simultaneous deposition of nickel and neodymium films (Nd in trace amounts) are deposited via the hydrogen assisted reduction of both precursors in supercritical carbon dioxide. An important aspect of the co-deposition of neodymium and nickel when using beta-diketonate organometallic precursors is the gas phase temperature. By causing the precursor to melt, dissolution rates are increased for the precursor into the supercritical carbon dioxide. Given that the precursors have a very tight range between melting and decomposition points, it is necessary to precisely control temperatures in the reactor. Given the monitored gas phase and reaction stage temperatures, the low neodymium concentration at 300 ºC, and likely at 265 ºC, is due to the near or surpassed decomposition temperature of the precursor. For nickel, the stage temperature of 265 ºC gives a max gas phase temperature of 215 ºC, which is not above the melting point of the nickel precursor. Regardless, high purity nickel is deposited and is attributed to a melting point depression from the interaction of the precursor with carbon dioxide.

4.3 Stacks via Layered Deposition

The deposition of films via SFD has been demonstrated. This section advances the utility of the technique by presenting the fabrication method of the first nano-sized electronic device structures made via SFD deposition. This is achieved by repeated SFD deposition to fabricate layers, or stacks, useful in creating electronic devices, specifically capacitors. Ru is used as the top and bottom electrode while TiO_2 and HfO_2 are used as the dielectric layer of the capacitors.

4.3.1 Experimental

4.3.1.1 Equipment

4.3.1.1.1 Reactors

The cold wall reactor used is previously described in detail in chapter 3.

4.3.1.2 Materials

Bis(2,2,6,6-tetramethyl-3,5-heptanedionato)(1,5-cyclooctadiene) ruthenium (II), 99 %, (99.9 % Ru), $Ru(tmhd)_2cod$, [329735-79-7] and di(isopropoxide)bis(2,2,6,6-tetramethyl-3,5-heptanedionato) titanium (IV), 98 %, $Ti(tmhd)_2(iPr)_2$, [144665-26-9] are obtained from Strem Chemicals, Inc. (Newburyport, MA), Figure 4.24. The ruthenium precursor is ground using a mortar and pestle and used without any further purification; the hafnium precursor is used as received. Tetra(2,2,6,6-tetramethyl-3,5-heptanedionato)hafnium, $Hf(tmhd)_4$ is used as received without any further purification (Gelest Inc., Morrisville, PA). Coleman grade (99.99 %) carbon dioxide, ultra high

purity (99.999 %) hydrogen and prepurified grade (99.998 %) nitrogen are used as received (Merriam Graves Corp, Charlestown, NH). A buna-N o-ring, size 2-236, is used for the high pressure and high temperature cold wall reactor seal (Marco Rubber and Plastic Products, Inc., North Andover, MA). Films are deposited on 2" silicon disks (crystal orientation <100>, native oxide, 1-100 micro-ohm centimeter) (Wafer World Inc., West Palm Beach, FL).

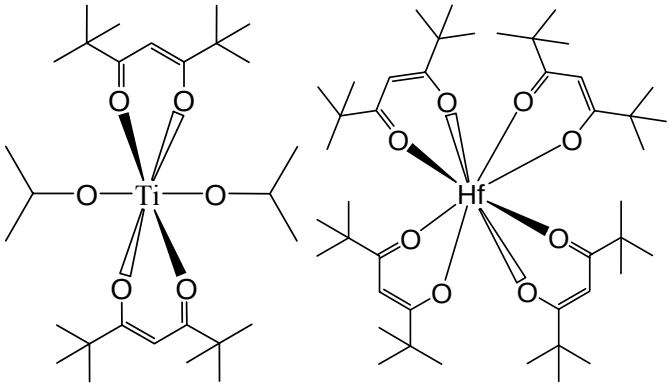

Figure 4.24: Chemical structure of di(isopropoxide)bis(2,2,6,6-tetramethyl-3,5-heptanedionato) titanium (IV), $Ti(tmhd)_2(iPr)_2$ and tetra(2,2,6,6-tetramethyl-3,5-heptanedionato)hafnium, $Hf(tmhd)_4$.

4.3.1.3 Procedure

For a typical reaction, a 2" <100> silicon wafer is mounted to the aluminum heated stage and secured with clips. A known amount of precursor is loaded into the vessel. A ceramic mask is placed over the wafer in order to set the deposition size of the layer. The vessel is sealed and placed behind protective polycarbonate housing. Then, using a constant flow of nitrogen, the reaction vessel is purged continuously over a 30 minute period. Simultaneously, the reactor wall and stage are then heated to the desired preheating temperature. Carbon dioxide is introduced into the reactor using a computer-controlled syringe pump. The reactor is then heated and maintained at a higher

temperature to induce quicker dissolution of precursor into the CO_2 (t = 60 min.). Next, hydrogen is loaded into the system using a manifold of known volume (70 mL). The aluminum stage is then quickly heated (~ 15 s.) to the desired reaction temperature and maintained for a set time. The heated stage is then allowed to cool down (~ 15 s.) while fresh CO_2 is used to flush multiple reactor volumes through the system to remove reaction byproducts and unreacted precursor. The effluent is passed through an activated carbon bed and silicon oil bubbler before being vented to the atmosphere.

The reaction sequence is repeated as many times as necessary to fabricate the subsequent device layers. A different ceramic mask is used in each deposition so that sequentially smaller concentric circles of deposited materials, Figure 4.25, are deposited until the desired stack is created.

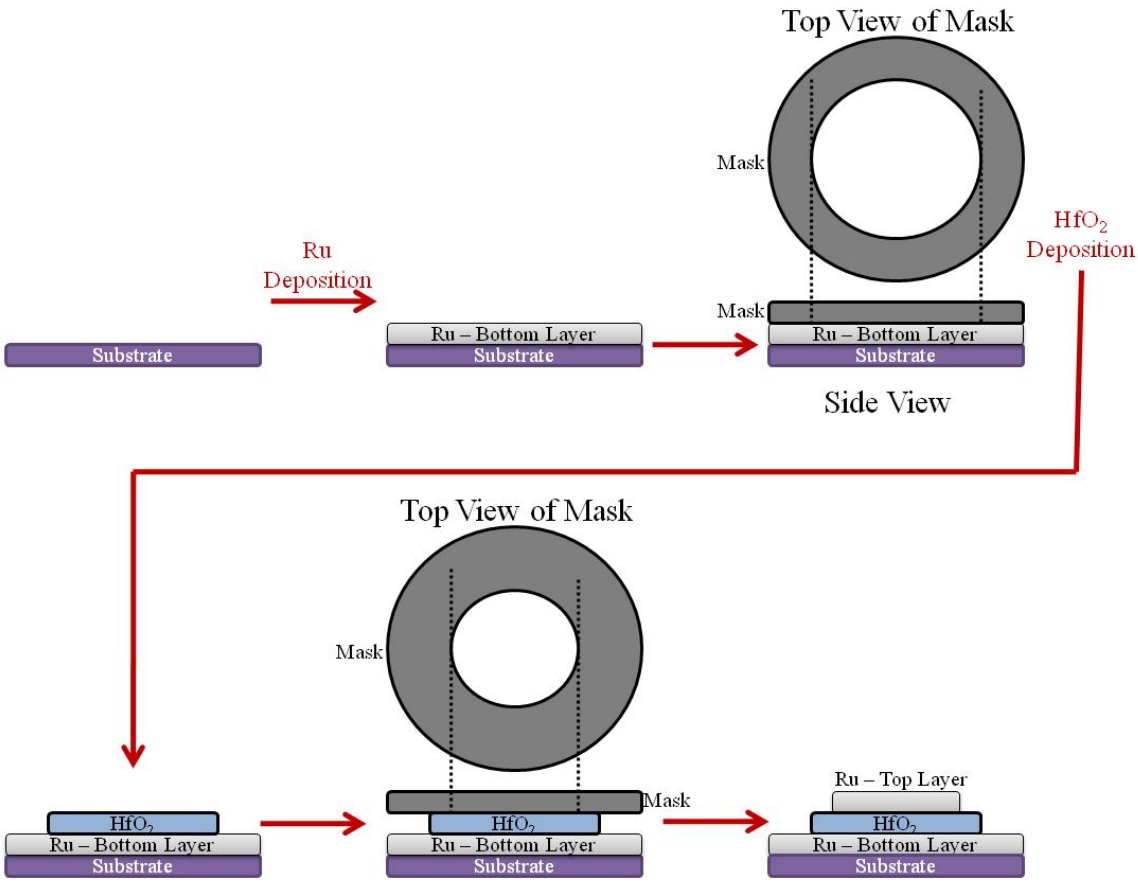

Figure 4.25: Procedure for creating mutli-layer sequentially smaller circular film stacks via SFD, specifically Ru/HfO_2/Ru.

4.3.2 Results and Discussion

The fabrication of mutli-layer stacks by SFD is reported. A three layer stack of Ru/TiO_2/Ru on silicon wafers is first reported. Then, the 3 layer multi-stack of Ru/HfO_2/Ru on silicon wafers is reported. The typical reaction conditions for each layer of the Ru/TiO_2/Ru multi-layer stack are reported in Table 4.6. The typical reaction conditions for each layer of the Ru/HfO_2/Ru multi-layer stack are reported in Table 4.7.

Table 4.6: Reaction conditions for Ru/TiO_2/Ru multi-layer stack fabrication.

Layer			Precursor	H_2	Deposition Temperature	Time
#	Compound	Precursor	wt. %	wt. %	ºC	min
1 - bottom	Ru	$Ru(tmhd)_2cod$	0.126	0.296	280	60
2 - middle	TiO_2	$Ti(tmhd)_2(iPr)_2$	0.184	0.246	300	30
3 - top	Ru	$Ru(tmhd)_2cod$	0.098	0.246	270	60

Table 4.7: Reaction conditions for Ru/ HfO_2/Ru multi-layer stack fabrication.

Layer			Precursor	H_2	Deposition Temperature	Time
#	Compound	Precursor	wt. %	wt. %	ºC	min
1 - bottom	Ru	$Ru(tmhd)_2cod$	0.117	0.443	270	5
2 - middle	HfO_2	$Hf(tmhd)_4$	0.344	0.000	300	30
3 - top	Ru	$Ru(tmhd)_2cod$	0.155	0.540	270	5

XPS sputter depth analysis of the Ru/TiO_2/Ru confirms all components of the stack, Figure 4.26. However, it also indicates that the interface between the each layer of the stack becomes less defined as you progress towards the substrate. This indicates that each deposited layer, during the next layers deposition reaction is undergoing a thermal cycle similar to annealing. This annealing is giving the previously deposited layers enough mobility such that the interface is eventually lost as indicated by the lower interface which went through two additional thermal cycles. FE-SEM, Figure 4.27 (right), also confirms the poor lower interface when compared to the upper interface. An interesting point to note is the non uniform growth of the TiO_2, Figure 4.27 (left). Typically, TiO_2 can be grown uniformly on many substrates. However, deposition is performed on ruthenium which is a known catalyst. It is proposed that the ruthenium is catalyzing the deposition of TiO_2 and is the reason why there are thicker films forming at closed corners on the substrate and not on open corners. However, since the goal of these depositions is to create nano-sized devices, both well defined interfaces as well as

conformal deposition across the entire film are necessary in order to eliminate component failure. For this reason, the titania dielectric layer for a nano-sized capacitor is no longer being pursued.

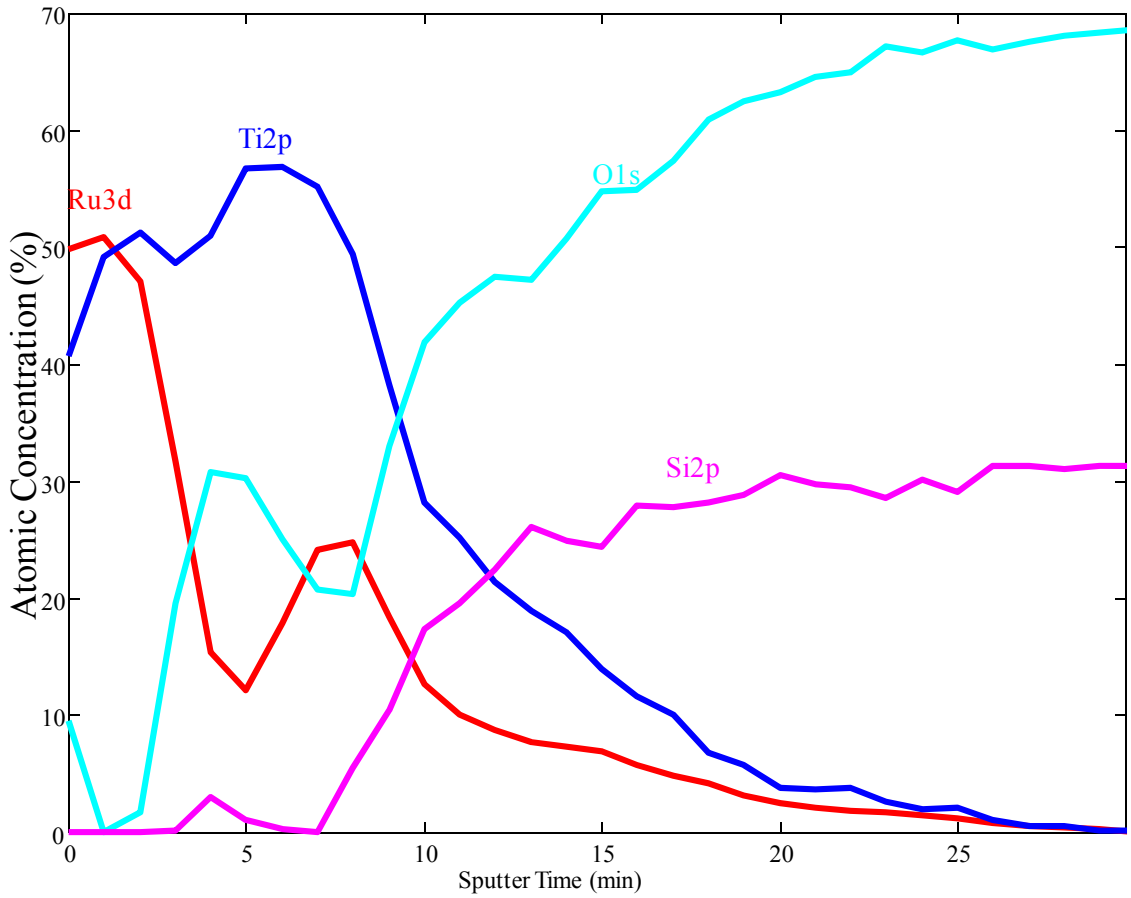

Figure 4.26: XPS sputter depth profile of a Ru/TiO_2/Ru stack confirming all components of the stack. However, layer definition is lost with increased sputter cycles (moving from top of the stack towards the substrate).

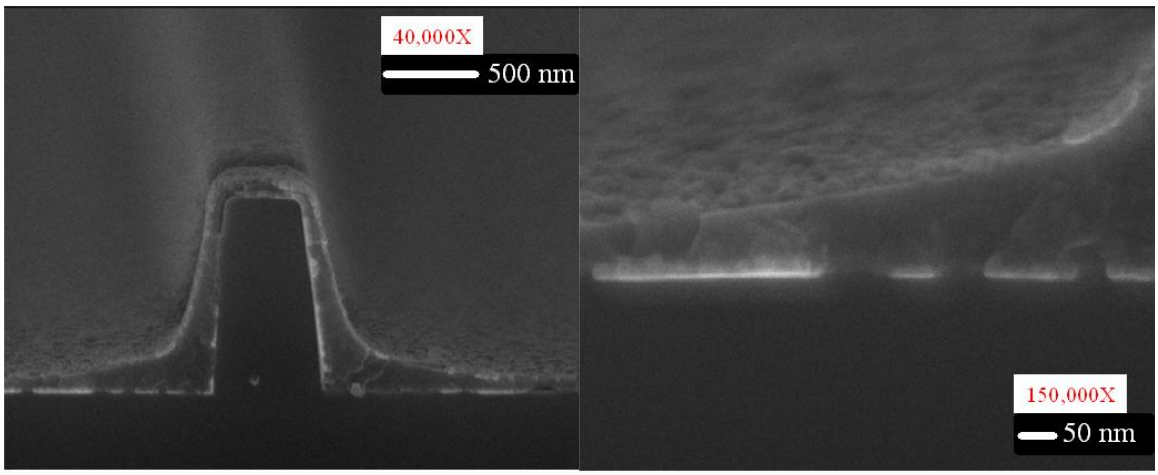

Figure 4.27: FE-SEM image of a Ru/TiO_2/Ru stack. Non uniform growth of TiO_2 is observed (left). The lower Ru and TiO_2 interface is less defined than the upper interface (right).

An alternative dielectric layer is hafnia, HfO_2. XPS sputter depth analysis of the Ru/HfO_2/Ru confirms all components of the stack, Figure 4.28. The interface between each layer of the stack is much more defined than the Ru/TiO_2/Ru stack. FE-SEM, Figure 4.29 (left), shows a zoomed in image of the stack deposited on the complex topography of a silicon substrate. Figure 4.29 (right), shows the conformal coverage of all three stacks on the silicon substrate. Figure 4.30 is a labeled top-down digital image of the Ru/HfO_2/Ru stack after all depositions are completed.

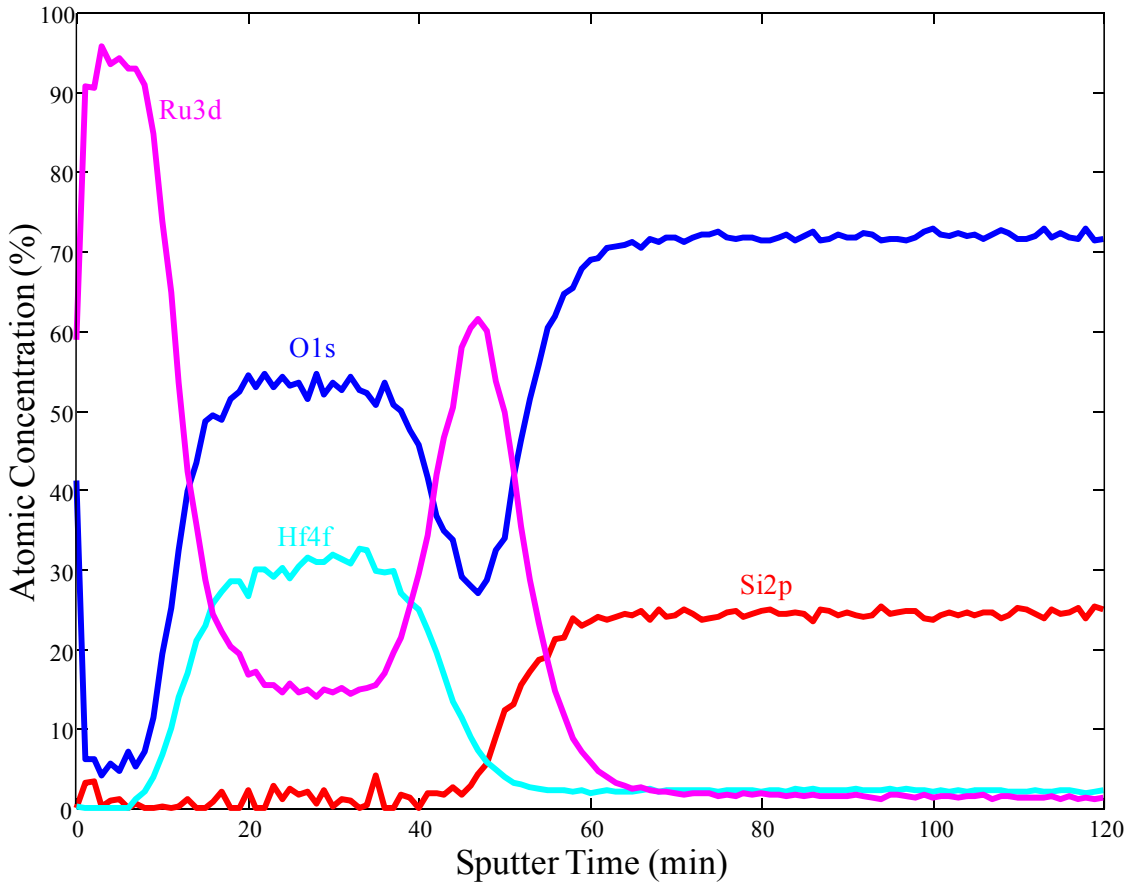

Figure 4.28: XPS sputter depth profile of a Ru/HfO_2/Ru stack confirming all components of the stack. Well defined stack layers are noted.

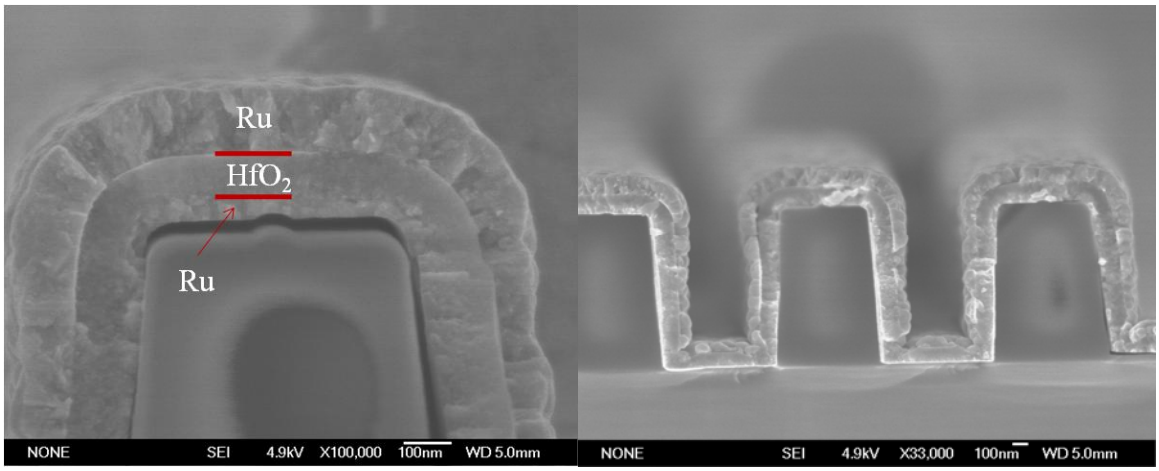

Figure 4.29: FE-SEM image of a Ru/HfO_2/Ru stack. Stack interfaces are visible and labeled (left). Image showing conformal deposition of the Ru/HfO_2/Ru across the complex substrate surface.

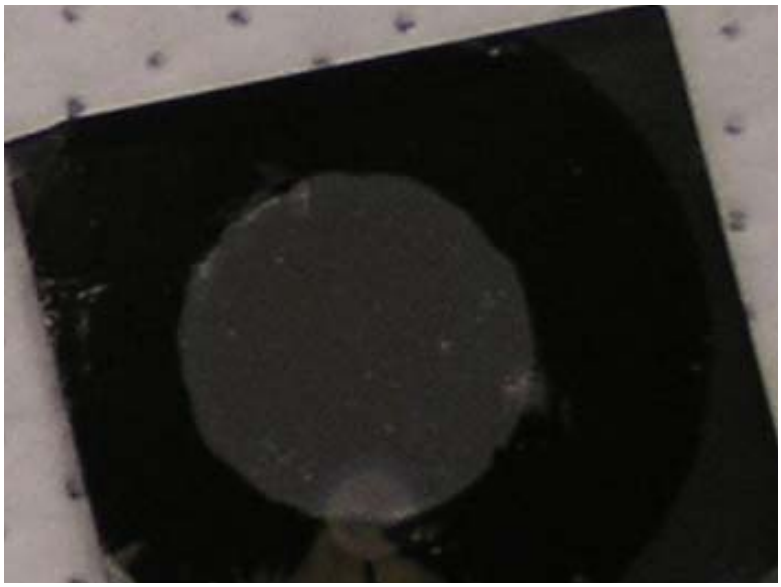

Figure 4.30: Top-down image of a Ru/HfO_2/Ru stack after all depositions are completed.

Ru/HfO_2/Ru sample stacks are tested for capacitance using a Fluke 112 multimeter. Thickness and capacitance measurements are reported in Table 4.8.

Table 4.8: Thickness and Capacitance Data for Ru/HfO_2/Ru Sample Stacks

	Top	Middle	Bottom		
	Ru	HfO_2	Ru		Capacitance
Sample	nm	nm	nm		μF
A	33	114	32		75
B	135	40	25		381
C	112	38	23		163

4.3.3 Conclusions

The fabrication of mutli-layer stacks of Ru/TiO_2/Ru and Ru/HfO_2/Ru on silicon substrates via SFD is reported. The Ru/TiO_2/Ru stack shows decreased definition at interfaces with each additional heat cycle. It is proposed that the ruthenium is catalyzing the deposition of titania and the increased amount of ruthenium on closed corners of the

substrate has yielded local increased growth rates thereby producing unconformal deposition. Ru/HfO_2/Ru stacks are also studied and are shown to have a much more defined interface regardless of the additional thermal cycles. Aditionally, all three stacks are observed to have deposited conformally across the high aspect ratio features of the substrate.

4.4 References

(1) P. David, in *Mechanical Engineering*, Vol. Masters, Louisiana State University, **2005**.

(2) D. Weller, H. Brandle, C. Chappert, *Journal of Magnetism and Magnetic Materials* **1993**, *121*, 461-470.

(3) Y. Yamada, W. P. Van Drent, E. N. Abarra, T. Suzuki, *Journal of Applied Physics* **1998**, *83*, 6527-6529.

(4) Y. Yamada, T. Suzuki, E. N. Abarra, *Ieee Transactions on Magnetics* **1998**, *34*, 343-345.

(5) I. Zana, G. Zangari, J. W. Park, M. G. Allen, *Journal of Magnetism and Magnetic Materials* **2004**, *272*, E1775-E1776.

(6) L. Favre, V. Dupuis, E. Bernstein, P. Melinon, A. Perez, *Physical Review B* **2006**, *74*.

(7) R. J. Feng, X. H. Xu, H. S. Wu, *Journal of Magnetism and Magnetic Materials* **2007**, *308*, 131-136.

(8) M. Maret, M. C. Cadeville, A. Herr, R. Poinsot, E. Beaurepaire, S. Lefebvre, M. Bessiere, *Journal of Magnetism and Magnetic Materials* **1999**, *191*, 61-71.

(9) J. I. Park, J. Cheon, *Journal of the American Chemical Society* **2001**, *123*, 5743-5746.

(10) C. Petit, S. Rusponi, H. Brune, *Journal of Applied Physics* **2004**, *95*, 4251-4260.

(11) C. W. Su, F. C. Chen, Y. E. Wu, C. S. Shern, *Surface Science* **2002**, *507*, 492-497.

(12) P. Hwang, B. H. Li, T. Yang, Z. H. Zhai, F. W. Zhu, *Journal of University of Science and Technology Beijing* **2004**, *11*, 319-323.

(13) P. Hwang, B. H. Li, T. Yang, Z. H. Zhai, F. W. Zhu, *Acta Physica Sinica* **2005**, *54*, 1841-1846.

(14) A. L. Shapiro, O. Vajk, F. Hellman, K. M. Ring, K. L. Kavanagh, *Applied Physics Letters* **1999**, *75*, 4177-4179.

(15) D. Niarchos, *Sensors and Actuators a-Physical* **2003**, *109*, 165-173.

(16) T. S. Chin, *Journal of Magnetism and Magnetic Materials* **2000**, *209*, 75-79.

(17) S. Jeong, Y. N. Hsu, D. E. Laughlin, M. E. McHenry, *Ieee Transactions on Magnetics* **2000**, *36*, 2336-2338.

(18) S. Jeong, Y. N. Hsu, D. E. Laughlin, M. E. McHenry, *Ieee Transactions on Magnetics* **2001**, *37*, 1299-1301.

(19) S. Jeong, Y. N. Hsu, M. E. McHenry, D. E. Laughlin, *Journal of Applied Physics* **2000**, *87*, 6950-6952.

(20) T. J. Chuang, C. R. Brundle, D. W. Rice, *Surface Science* **1976**, *59*, 413-429.

(21) K. S. Kim, *Physical Review B* **1975**, *11*, 2177-2185.

(22) A. Lebugle, U. Axelsson, R. Nyholm, N. Martensson, *Physica Scripta* **1981**, *23*, 825-827.

(23) V. I. Nefedov, M. N. Firsov, I. S. Shaplygin, *Journal of Electron Spectroscopy and Related Phenomena* **1982**, *26*, 65-78.

(24) V. I. Nefedov, D. Gati, B. F. Dzhurinskii, N. P. Sergushin, Y. V. Salyn, *Zhurnal Neorganicheskoi Khimii* **1975**, *20*, 2307-2314.

(25) C. D. Wagner, W. M. Riggs, L. E. Davis, J. F. Moulder, G. E. Mullenberg, *Handbook of X-ray Photoelectron Spectroscopy*, Perkin-Elmer, Physical Electronics Division, Eden Prairie MN 55344 **1979**.

(26) Y. Baer, P. F. Hedén, J. Hedman, M. Klasson, C. Nordling, K. Siegbahn, *Physica Scripta* **1970**, *1*, 55-65.

(27) G. M. Bancroft, I. Adams, L. L. Coatsworth, C. D. Bennewitz, J. D. Brown, W. D. Westwood, *Analytical Chemistry* **1975**, *47*, 586-588.

(28) D. Cahen, J. E. Lester, *Chemical Physics Letters* **1973**, *18*, 108-111.

(29) J. P. Contour, G. Mouvier, M. Hoogewys, C. Leclere, *Journal of Catalysis* **1977**, *48*, 217-228

(30) J. Escard, B. Pontvianne, M. T. Chenebaux, J. Cosyns, *Bulletin De La Societe Chimique De France Partie I-Physicochimie Des Systemes Liquides Electrochimie Catalyse Genie Chimique* **1975**, 2399-2402.

(31) J. S. Hammond, N. Winograd, *Journal of Electroanalytical Chemistry* **1977**, *78*, 55-69.

(32) G. Johansson, J. Hedman, A. Berndtsson, M. Klasson, R. Nilsson, *Journal of Electron Spectroscopy and Related Phenomena* **1973**, *2*, 295-317.

(33) K. S. Kim, N. Winograd, R. E. Davis, *Journal of the American Chemical Society* **1971**, *93*, 6296-&.

(34) V. I. Nefedov, Y. V. Salyn, *Inorganica Chimica Acta* **1978**, *28*, L135-L136.

(35) G. Schon, *Journal of Electron Spectroscopy and Related Phenomena* **1972-1973**, *1*, 377-387.

(36) C. D. Wagner, *Faraday Discussions of the Chemical Society* **1975**, *60*, 291 - 300.

(37) P. A. Christensen, A. Hamnett, J. Munk, G. L. Troughton, *Journal of Electroanalytical Chemistry* **1994**, *370*, 251-258.

(38) P. A. Christensen, A. Hamnett, G. L. Troughton, *Journal of Electroanalytical Chemistry* **1993**, *362*, 207-218.

(39) T. Schultz, S. Zhou, K. Sundmacher, *Chemical Engineering & Technology* **2001**, *24*, 1223-1233.

(40) Y. M. Zhu, H. Uchida, T. Yajima, M. Watanabe, *Langmuir* **2001**, *17*, 146-154.

(41) C. L. Perkins, M. A. Henderson, C. H. F. Peden, G. S. Herman, *Journal of Vacuum Science & Technology A* **2001**, *19*, 1942-1946.

(42) C. L. Campos, C. Roldan, M. Aponte, Y. Ishikawa, C. R. Cabrera, *Journal of Electroanalytical Chemistry* **2005**, *581*, 206-215.

(43) A. O'Neil, J. J. Watkins, *Chemistry of Materials* **2007**, *19*, 5460-5466.

(44) J. J. Watkins, J. M. Blackburn, T. J. McCarthy, *Chemistry of Materials* **1999**, *11*, 213-215.

(45) D. Barreca, A. Gasparotto, E. Tondello, C. Sada, S. Polizzi, A. Benedetti, *Chemical Vapor Deposition* **2003**, *9*, 199-206.

(46) J. P. Holgado, G. Munuera, J. P. Espinos, A. R. Gonzalez-Elipe, *Applied Surface Science* **2000**, *158*, 164-171.

(47) A. E. Hughes, J. D. Gorman, P. J. K. Patterson, R. Carter, *Surface and Interface Analysis* **1996**, *24*, 634-640.

(48) N. S. McIntyre, Ed. *Quantitative Surface Analysis of Materials*, **1977**.

(49) K. D. Pollard, H. A. Jenkins, R. J. Puddephatt, *Chemistry of Materials* **2000**, *12*, 701-710.

(50) W. D. Schneider, B. Delley, E. Wuilloud, J. M. Imer, Y. Baer, *Physical Review B* **1985**, *32*, 6819-6831.

(51) J. Z. Shyu, K. Otto, W. L. H. Watkins, G. W. Graham, R. K. Belitz, H. S. Gandhi, *Journal of Catalysis* **1988**, *114*, 23-33.

(52) M. L. Trudeau, A. Tschope, J. Y. Ying, *Surface and Interface Analysis* **1995**, *23*, 219-226.

(53) A. Q. Wang, P. Punchaipetch, R. M. Wallace, T. D. Golden, *Journal of Vacuum Science & Technology B* **2003**, *21*, 1169-1175.

(54) Z. L. Zhang, X. H. Du, W. D. Wang, *Journal of Vacuum Science & Technology A* **2000**, *18*, 2928-2931.

(55) Y. P. Zhang, R. J. Puddephatt, *Chemistry of Materials* **1999**, *11*, 148-153.

(56) D. R. Patil, S. A. Lokare, R. S. Devan, S. S. Chougule, C. M. Kanamadi, Y. Kolekar, B. K. Chougule, *Materials Chemistry and Physics* **2007**, *104*, 254-257.

(57) H. Reveron, C. Elissalde, C. Aymonier, O. Bidault, M. Maglione, F. Cansell, *Journal of Nanoscience and Nanotechnology* **2005**, *5*, 1741-1744.

(58) G. H. Haertling, *Journal of the American Ceramic Society* **1999**, *82*, 797-818.

(59) S. A. Bruno, D. K. Swanson, I. Burn, *Journal of the American Ceramic Society* **1993**, *76*, 1233-1241.

(60) H. V. Alexandru, C. Berbecaru, A. Ioachim, M. I. Toacsen, M. G. Banciu, L. Nedelcu, D. Ghetu, *Materials Science and Engineering B-Solid State Materials for Advanced Technology* **2004**, *109*, 152-159.

(61) V. V. Lemanov, E. P. Smirnova, P. P. Syrnikov, E. A. Tarakanov, *Physical Review B* **1996**, *54*, 3151-3157.

(62) V. S. Tiwari, N. Singh, D. Pandey, *Journal of Physics-Condensed Matter* **1995**, *7*, 1441-1460.

(63) M. C. Chiu, C. F. Cheng, W. T. Wu, F. S. Shieu, *Journal of the Electrochemical Society* **2005**, *152*, F66-F70.

(64) B. L. Gersten, M. M. Lencka, R. E. Riman, *Journal of the American Ceramic Society* **2004**, *87*, 2025-2032.

(65) X. F. Chen, W. Q. Lu, W. G. Zhu, S. Y. Lim, S. A. Akbar, *Surface & Coatings Technology* **2003**, *167*, 203-206.

(66) C. Shen, Q. F. Liu, Q. Liu, *Materials Letters* **2004**, *58*, 2302-2305.

(67) X. J. Yang, X. Yao, L. Y. Zhang, *Ceramics International* **2004**, *30*, 1525-1527.

(68) Y. B. Khollam, S. B. Deshpande, H. S. Potdar, S. V. Bhoraskar, S. R. Sainkar, S. K. Date, *Materials Characterization* **2005**, *54*, 63-74.

(69) J. Q. Qi, Y. Wang, W. P. Chen, L. T. Li, H. L. W. Chan, *Journal of Solid State Chemistry* **2005**, *178*, 279-284.

(70) I. P. Selvam, V. Kumar, *Materials Letters* **2002**, *56*, 1089-1092.

(71) S. B. Deshpande, Y. Khollam, Y. B. Bhoraskar, S. K. Date, S. R. Sainkara, H. S. Potdar, *Materials Letters* **2005**, *59*, 293-296.

(72) P. Pinceloup, C. Courtois, A. Leriche, B. Thierry, *Journal of the American Ceramic Society* **1999**, *82*, 3049-3056.

(73) R. K. Roeder, E. B. Slamovich, *Journal of the American Ceramic Society* **1999**, *82*, 1665-1675.

(74) X. Z. Wei, N. P. Padture, *Journal of Ceramic Processing Research* **2004**, *5*, 175-178.

(75) T. Hungria, M. Alguero, A. B. Hungria, A. Castro, *Chemistry of Materials* **2005**, *17*, 6205-6212.

(76) C. L. Fu, C. R. Yang, H. W. Chen, Y. X. Wang, L. Y. Hu, *Materials Science and Engineering B-Solid State Materials for Advanced Technology* **2005**, *119*, 185-188.

(77) C. F. Kao, W. D. Yang, *Applied Organometallic Chemistry* **1999**, *13*, 383-397.

(78) B. A. Wechsler, K. W. Kirby, *Journal of the American Ceramic Society* **1992**, *75*, 981-984.

(79) J. F. Bocquet, K. Chhor, C. Pommier, *Materials Chemistry and Physics* **1999**, *57*, 273-280.

(80) H. Reveron, C. Aymonier, A. Loppinet-Serani, C. Elissalde, M. Maglione, F. Cansell, *Nanotechnology* **2005**, *16*, 1137-1143.

(81) H. Reveron, C. Elissalde, C. Aymonier, C. Bousquet, M. Maglione, F. Cansell, *Nanotechnology* **2006**, *17*, 3527-3532.

(82) A. R. Bazaev, I. M. Abdulagatov, E. A. Bazaev, A. Abdurashidova, *International Journal of Thermophysics* **2007**, *28*, 194-219.

(83) H. E. Dillon, S. G. Penoncello, *International Journal of Thermophysics* **2004**, *25*, 321-335.

(84) N. G. Polikhronidi, I. M. Abdulagatov, G. V. Stepanov, R. G. Batyrova, *Journal of Supercritical Fluids* **2007**, *43*, 1-24.

(85) Y. Takiguchi, M. Uematsu, *Journal of Chemical Thermodynamics* **1996**, *28*, 7-16.

(86) Y. Zhang, J. C. Yang, Y. X. Yu, Y. G. Li, *Journal of Supercritical Fluids* **2005**, *36*, 145-153.

(87) A. A. Abduraslidova, A. R. Bazaev, E. A. Bazaev, I. M. Abdulagatov, *High Temperature* **2007**, *45*, 178-186.

(88) A. R. Bazaev, I. M. Abdulagatov, E. A. Bazaev, A. Abdurashidova, *Journal of Chemical Thermodynamics* **2007**, *39*, 385-411.

(89) G. K. Folas, J. Gabrielsen, M. L. Michelsen, E. H. Stenby, G. M. Kontogeorgis, *Industrial & Engineering Chemistry Research* **2005**, *44*, 3823-3833.

(90) Y. H. Fu, S. I. Sandler, H. Orbey, *Industrial & Engineering Chemistry Research* **1995**, *34*, 4351-4363.

(91) J. Griswold, J. D. Haney, V. A. Klein, *Industrial and Engineering Chemistry* **1943**, *35*, 701-704.

(92) O. Hernandez-Garduza, F. Garcia-Sanchez, E. Neau, M. Rogalski, *Chemical Engineering Journal* **2000**, *79*, 87-101.

(93) D. Pecar, V. Dolecek, *Fluid Phase Equilibria* **2005**, *230*, 36-44.

(94) C. Perakis, E. Voutsas, K. Magoulas, D. Tassios, *Fluid Phase Equilibria* **2006**, *243*, 142-150.

(95) N. G. Polikhronidi, I. M. Abdulagatov, G. V. Stepanov, R. G. Batyrova, *Fluid Phase Equilibria* **2007**, *252*, 33-46.

(96) D. T. Safarov, A. N. Shakhverdiev, *High Temperature* **2001**, *39*, 395-400.

(97) Y. Takiguchi, O. Osada, M. Uematsu, *Journal of Chemical Thermodynamics* **1996**, *28*, 1375-1385.

(98) Z. Y. Zhang, J. C. Yang, Y. G. Li, *Fluid Phase Equilibria* **2000**, *169*, 1-18.

(99) A. B. Christie, J. Lee, I. Sutherland, J. M. Walls, *Applied Surface Science* **1983**, *15*, 224-237.

(100) H. Vandoveren, J. A. T. Verhoeven, *Journal of Electron Spectroscopy and Related Phenomena* **1980**, *21*, 265-273.

(101) C. R. Anderson, R. N. Lee, J. F. Morar, R. L. Park, *Journal of Vacuum Science & Technology* **1982**, *20*, 617-621.

(102) M. Murata, K. Wakino, S. Ikeda, *Journal of Electron Spectroscopy and Related Phenomena* **1975**, *6*, 459-464.

(103) V. I. Nefedov, Y. V. Salyn, A. A. Chertkov, L. N. Padurets, *Zhurnal Neorganicheskoi Khimii* **1974**, *19*, 1443-1445.

(104) D. Simon, C. Perrin, J. Bardolle, *Journal De Microscopie Et De Spectroscopie Electroniques* **1976**, *1*, 175-186.

(105) E. Boehm, J. M. Bassat, P. Dordor, F. Mauvy, J. C. Grenier, P. Stevens, *Solid State Ionics* **2005**, *176*, 2717-2725.

(106) F. Mauvy, J. M. Bassat, E. Boehm, J. P. Manaud, P. Dordor, J. C. Grenier, *Solid State Ionics* **2003**, *158*, 17-28.

(107) D. Mesguich, J. M. Bassat, J. C. Grenier, F. Cansell, C. Aymonier, *Chemical Communications* **2008**, *Submitted*.

(108) D. D. Sarma, C. N. R. Rao, *Journal of Electron Spectroscopy and Related Phenomena* **1980**, *20*, 25-45.

(109) K. S. Kim, S. W. Gaarenstroom, N. Winograd, *Chemical Physics Letters* **1976**, *41*, 503-506.

(110) K. S. Kim, N. Winograd, *Journal of Catalysis* **1974**, *35*, 66-72.

(111) C. J. Powell, N. E. Erickson, T. Jach, *Journal of Vacuum Science & Technology* **1982**, *20*, 625-625.

(112) R. B. Shalvoy, P. J. Reucroft, *Journal of Vacuum Science & Technology* **1979**, *16*, 567-569.

CHAPTER 5

PLASMA ENHANCED RAPID EXPANSION OF SUPERCRITICAL SOLUTIONS

5.1 Introduction

Titanium dioxide, TiO_2 or titania, is an area of great interest due to its physiochemical properties and an increased demand for devices with enhanced properties and environmental friendliness. Currently, TiO_2 is the material of choice for environmental applications, such as air purifiers,[1] gas sensors,[2-4] water treatment[5, 6] and self cleaning and energy efficient windows[7] due to its photocatalytic properties, stability and low cost. It is also of interest in photoluminescent materials.[8, 9] Additionally, it has gained much attention in the areas of dye sensitized solar cells[10-14] because it provides a cost effective alternative to solar cells. Because TiO_2 has many favorable properties that are of particular interest in solar energy harvesting, it is desirable to find methods of creating high surface area coatings using both time and energy efficient methods to create durable and high efficiency solar cells.[15]

5.1.1 Motivation

The world consumption of energy per year is roughly 15 TW (1.5×10^{13} W). This number is rising each year with no foreseeable upper limit and no means of satisfying needs once natural reserves, such as coal, oil, natural gases, etc, are used. However, a potential solution has been identified. The average energy received by the Earth's surface from the sun is about 1.2×10^{17} W of solar power.[16] To put this in perspective, in less than one hour of time the Earth is supplied with more energy than is needed to meet all of the human population energy demands for an entire year. It is this energy that has

been stored over years that has made possible the current growth and way of life as we know it today. Harnessing this energy would help solve the world's energy crisis.[17]

Although this solution has been identified, solar power is only used to meet 0.04 % of the total yearly demand, with Japan, Germany and the USA at the forefront of solar power harvesting.[18] The solution, although seemingly perfect, is quite difficult in execution. The primary limitation is cost, with materials compromising 70 % of that cost, the remainder being assembly, installation and maintenance. Currently, the overall cost of solar power is roughly 5 to 10 times greater than electricity, which is currently a major drawback to worldwide adoption of this potential solution. Additional difficulties for this technology to be accepted include the low energy density of solar power, as the previously mentioned energy delivered to Earth is spread across the entire planet. This is compounded by the fact that the majority of the Earth is uninhabitable due to water and extreme climates. Current efficiency of solar cells is about 10 – 30 %, which again reduces the total amount of obtainable energy from solar power. Finally, the unpredictability of weather, which greatly reduces the percentage of obtainable energy from the sun, is an additional concern. Although these difficulties are great, advances in the technical side as well as a growing market to cater to the nontechnical economic challenges of this technology are quickly changing this into the solution it is meant to be.

5.1.1.1 Background

5.1.1.1.1 Solar Power

5.1.1.1.1.1 First Generation Solar Cells

Crystalline Si technology, known as first generation solar cells, dominates the photovoltaic (PV) market at 90 % of total cells. This is one of the best materials for first generation PV cells due to its band gap as well as being the most abundant material in the Earth's crust. However, given its brittle nature and optical properties, large volumes of high purity Si are needed in order to create PV cells. The amount of Si needed in conjunction with its high processing costs, to make high purity Si, make it very difficult to compete with electricity, even if the majority of the PV industry is using off grade poly-Si and scrap wafers from the microelectronics industry. It is because of this that newer technologies are emerging.

5.1.1.1.1.2 Second Generation Solar Cells

Thin film technology is identified as second generation solar cells. Thin film solar cells (TFSC) are about 100 times thinner then Si PV wafers. Low cost deposition over large areas at lower temperatures with materials that can tolerate much higher levels of impurities makes them a much more cost effective technology then first generation solar cells. However, the disadvantages of TFSC, such as lower efficiencies (currently) and smaller technology and knowledge bases, have kept first generation solar cells at 90 % of the market. Of the few potential TFSC materials that give efficiencies of over 10 %, $Cu(InGa)Se_2$ (CIGS) has emerged as the leader. It is reported to have efficiencies of 18.8 % on the lab scale[19] and efficiencies greater than 12 % on larger modules. 13.4 %

efficiency is recorded for a 3459 m^2 module.[17] Additional to its high efficiency, it shows excellent stability and radiation resistance.[20] Some minor disadvantages, primarily composition control during processing, are hindering its overall acceptance.

5.1.1.1.1.3 Third Generation Solar Cells

The third generation of solar cells is a general term coined to encompass all the new emerging technologies. Some of the popular emerging third generation solar cells in clued various semiconductor alloys, such as GaInP, quantum dots, dye-sensitized solar cells (DSSC) and organic photovoltaic cells implementing conducting polymers.[21-24]

Currently, the area of DSSC is gaining a majority of the attention due to its attractive efficiencies and ease of forming a working cell. The first DSSC photoelectrodes were made from Si, GaAs, InP, and CdS. When used with a redox electrolyte efficiencies of 10 % were realized. However, under irradiation, poor cell stability occurred due to photocorrosion of the electrode. This prompted new materials to be used as the photoelectrode material. Oxide semiconductors, such as TiO_2, SnO_2 and ZnO, are stable in solution during irradiation however, due to wide band gaps, cannot absorb light. This problem is quickly solved with the addition of a photosensitizer, typically an organic dye, which absorbs light and injects the electrons into the conduction band of the oxides. Efficiencies are increased by increasing the surface area of the oxide and by both increasing the amount of photosensitizer absorbed as well as the type of photosensitizer used based on the wavelength of light it will absorb.[25] Currently, the highest efficiency DSSC is the Gratzel cell. These cells obtain efficiencies of 7 to 10 % with TiO_2 photoelectrodes and Ru based organic dyes that can absorb light up to 900 nm

in the near-IR region.[10-14] These cells have a promising place in the near future, however, they are currently limited by their 10 % efficiency and expense in both time and cost to produce. For DSSC 3rd generation solar cells to become viable, efficiencies need to approach 15 % and processing times need to be reduced in order to become cost effective alternatives to first and second generation solar cells.

5.1.1.1.2 Plasma Spray Technology

5.1.1.1.2.1 History

First discovered by Sir William Crookes in 1879 and later identified by Sir Joseph John Thompson in 1897[1] in his cathode ray experiments. It was later named plasma by an American chemist and physicist Irving Langmuir in 1928.[26]

5.1.1.1.2.2 Plasma

Plasma is a 4th state of matter that composes approximately 99 % of the known universe. A plasma is an ionized gas, which is a collection of free moving electrons and ions that together carry a collective neutral charge. Because of this, they are electrically conductive and electromagnetic. Plasmas range in temperature from 0 K to 10^8 K.

5.1.1.1.2.3 Plasma Spray

Plasma spraying is one of many ways of performing a thermal spray. Thermal spraying is a technique that is used for line of sight coatings on objects. The material used for the coating is heated in a variety of methods, one of which is plasma. When a plasma jet, whose temperature is typically 10^5 K, is utilized for heating of the coating material, the technique is called plasma spraying. The coatings formed are on the order

of a few microns thick and are quite dense. Additionally, they have good adhesion and mechanical properties. Plasma spraying can be used to spray a variety of materials ranging from polymers, metals and even ceramics. One method used for feeding the coating material to the system is via solution. This method is called solution precursor plasma spray (SPSS). Recent studies to better understand the mechanism by which the coating is formed have been undertaken.[27-29] Some examples of deposited materials include TiO_2,[30] ZrO_2-Al_2O_3[31] and Y_2O_3-ZrO_2.[28, 29]

5.1.1.1.3 Rapid Expansion of Supercritical Solution Technology

5.1.1.1.3.1 History

The idea of precipitating a solid by the sudden reduction of pressure to form a crystal is outlines by Hannay and Hogarth in 1879.[32] In 1981,[33] Krukonis theorized on the use of this process to tailor the sizes of materials. He then followed this theory with a publication detailing some of the first work in really trying to understand and develop this technique in 1984.[34]

5.1.1.1.3.2 Rapid Expansion of Supercritical Solutions

Rapid expansion of supercritical solutions (RESS) utilizes the changing solvating power of the solvent to create nanometer sized particles. This technique uses the supercritical fluids ability to dissolve relatively large concentrations of material, as compared to a gas, to form a single homogeneous phase. The solution is then expanded across a nozzle, which in itself generates small particles. Additional particle size reduction occurs, due to the pressure drop across the nozzle, from the high pressure

supercritical state to atmospheric pressure which causes the dissolved material to precipitate out of solution via nucleation. The crystallized material encapsulates the supercritical solvent, which returns back to its STP state, in this case, a liquid. This causes the small crystal to break, from the inside out, which reduces particle size even further. Finally, additional particle size reduction occurs with the velocity and frequency at which the expanding particles collide with one another. The process typically generates particles on the nanometer scale.

5.1.1.2 Plasma Enhanced Rapid Expansion of Supercritical Solutions

The union of both RESS and plasma spray technology is used to create a powerful technique which is called plasma-enhanced rapid expansion of supercritical solution (PRESS). PRESS allows for the deposition of high surface area materials which are formed from highly dendritic metal oxides which in turn allow for fabrication of advanced material devices, such as photovoltaic cells. The new process linearly combines the RESS system which subsequently outputs into a plasma spray process. The individual advantage of each system coupled together in this new process enables the manipulation of materials in ways that have not been realized before.

The PRESS system is a serendipitous discovery whose original setup was designed for the economic and efficient deposition of thick, dense metal oxide films. However, upon initial experimentation, it was quickly realized that the resultant films are more suited for applications in photovoltaics, which benefit from thick and high surface area films of metal oxides.

The process has also evolved over time until it reached its current form. The initial apparatus is setup as detailed in Figure 5.1. Solid or liquid precursor is stored in a high pressure vessel which is plugged on both ends with glass wool and then sealed. The pressure vessel is heated with band heaters to the desired temperature and then the solvent, carbon dioxide, is introduced to the system. Then, a soaking period, which allows the precursor to dissolve into the solvent, occurs. The vessel is put in line with a high pressure ISCO pump before and a metering valve after which subsequently outputs to the plasma flame. The pressure of the system is maintained by the ISCO pump and the flow rate is controlled by the metering valve. As the solvent with dissolved precursor reaches the end of the system, it quickly expands at supersonic speeds and instantaneously vaporizes forming a fine mist, the essence of RESS. This mist then goes directly into the high temperature plasma flame where it quickly undergoes a decomposition of the precursor. The desired products are then quickly oxidized and/or crystallized, depending on the precursor, and deposited on a substrate in a pathway directly in front of the plasma spray. The resulting films in this process had no long or short range order and do not yield thick films.

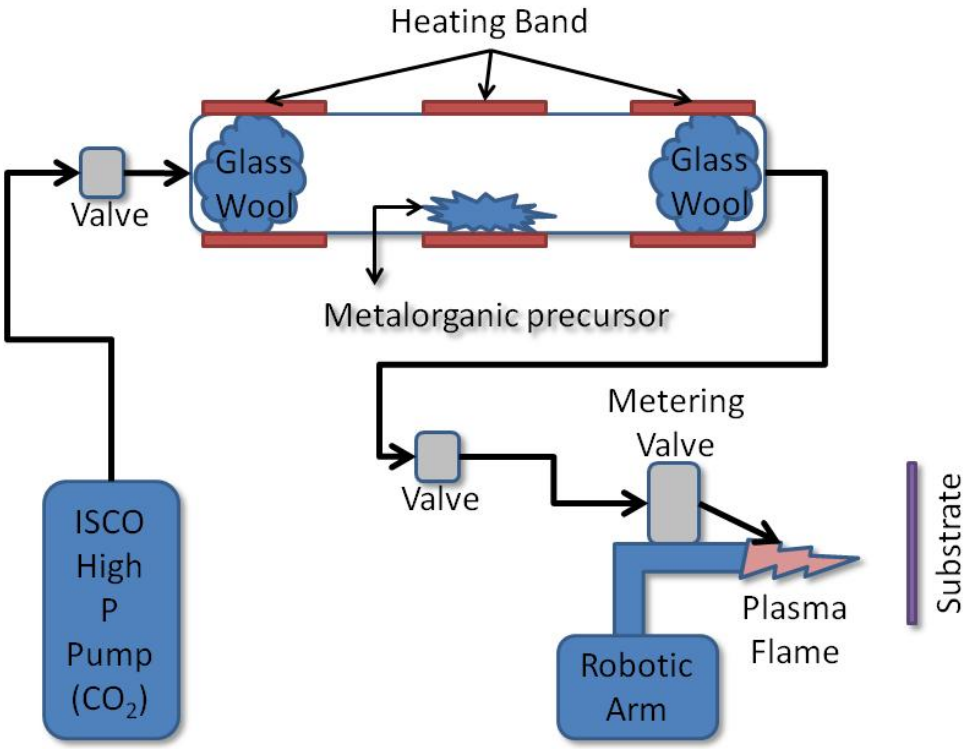

Figure 5.1: Schematic representation of the PRESS system – first design.

The next evolution of this process adds a piston to the pressure vessel, Figure 5.2. Precursors are limited to liquid precursors. In this process, precursor is loaded into the pressure vessel on the downstream side of the piston. Carbon dioxide is then loaded on to the upstream side of the piston in order to avoid carbon dioxide contact with the precursor and still maintain a constant pressure on the precursor. The carbon dioxide is maintained at pressure using a high pressure ISCO pump. The process is then run in a similar manor as the initial set up. The resultant films again have no long or short range order but films are much thicker as can be seen by the results later in this chapter.

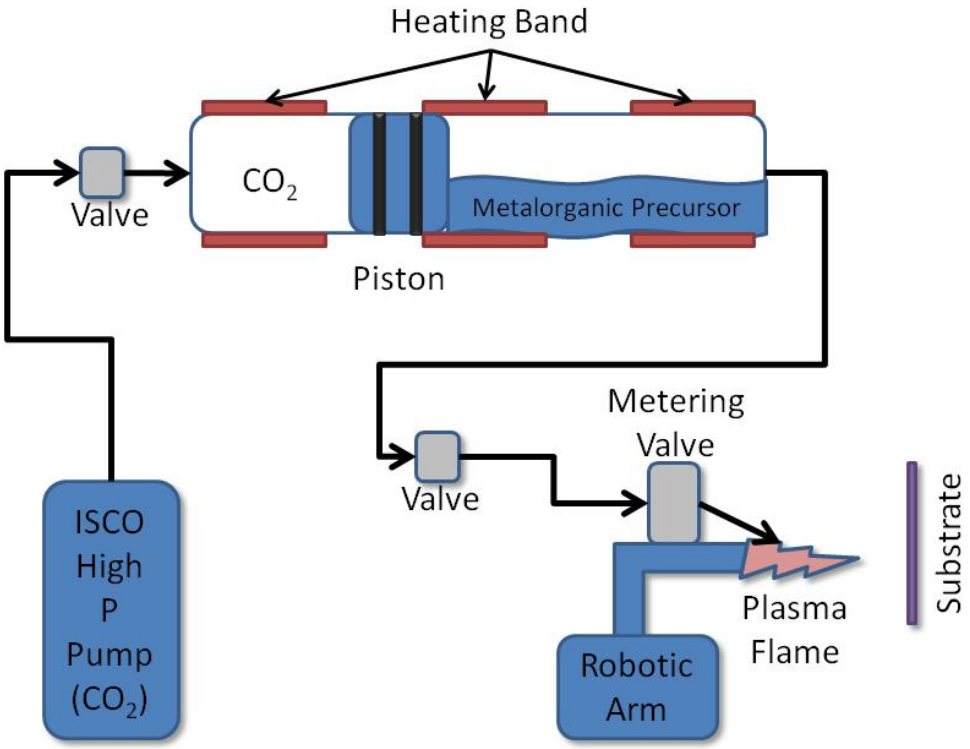

Figure 5.2: Schematic representation of the PRESS system – second design.

To this point, the results have not been the desired results. In an effort to increase the atomization of the precursor which decreases particle size and would help create denser films, liquid carbon dioxide is introduced to the liquid precursor side in order to allow the carbon dioxide to dissolve into the precursor, which makes a high concentration precursor mixture. This allows the high pressure carbon dioxide to rapidly expand across the nozzle and increase atomization of the precursor prior to entering the plasma flame. In order to keep the carbon dioxide in the liquid state, no heating is used, as it was for the previous iterations of this process, for the pressure vessel. Pressure is maintained via a high pressure ISCO pump across a piston in the pressure vessel. The pressure vessel is mixed so that a homogeneous mixture is obtained. From this point, the system, Figure 5.3, is operated in the same manner as the previous designs. This final form of the

process is now called the plasma-enhanced rapid expansion of supercritical solution which is used to fabricate films that are highly dendritic and consequently very porous with varying thicknesses of a few hundred nanometers to multiple microns simply by adjusting processing parameters.

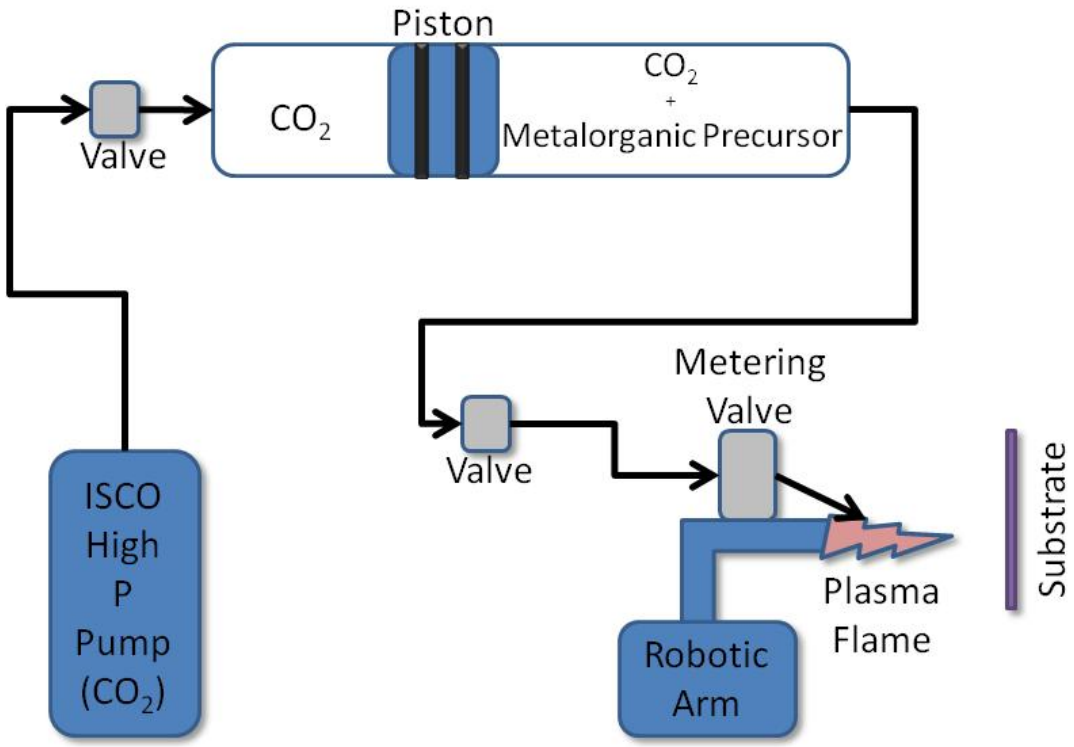

Figure 5.3: Schematic representation of the PRESS system – final design.

5.2 Experimental

5.2.1 Equipment

A direct current Metco 9 MB plasma torch (Sulzer Metco, Westbury, NY) attached to a six axis robotic arm is used as the plasma source. Argon and hydrogen gas are used as the primary and secondary plasma gases, respectively. Precursors are stored in metal on metal sealed medium pressure stainless steel tubing (ID =11/16”, OD = 1”, pressure rated to 689 bar) (High Pressure Equipment Company, Erie, PA) with custom

designed floating pistons utilizing two o-rings for sealing. The system is appropriately outfitted with 1/16” OD taper sealing stainless steel tubing and needle valves to deliver and control flow. A metering valve is used to control the system flow just prior to the nozzle. The nozzle is a 1/16” OD piece of stainless steel tubing. Two high power density cartridge heaters (Omega Engineering Inc, Stamford, CT) are used to heat the metering valve while temperature is controlled using a custom built temperature controller consisting of a solid state relay (Omega Engineering Inc, Stamford, CT) and microprocessor-based temperature controller, model CN76000 (Omega Engineering Inc, Stamford, CT) encased in an aluminum enclosure. A Flir ThermaCam SC 3000 (Flir Systems, Boston, MA) is used for infrared imaging of samples. The camera is interfaced with a computer running ThermaCAM Researcher Pro 2.7 (Flir Systems, Boston, MA) to collect and analyze data.

5.2.2 Materials

Titanium (di-isopropoxide) bis(acetylacetonate) (75 % in isopropanol) [17927-72-9], titanium (di-isopropoxide) bis[BREW], tris(2,2,6,6-tetramethyl-3-5-heptanedionato) aluminum, $Al(tmhd)_3$, [14319-08-5], titanium(IV) isopropoxide [546-68-9], titanium(IV) 2-ethylhexoxide [1070-10-6], zinc 2-ethylhexanoate [136-53-8] are used as received without any further purification (Strem Chemicals Inc, Newburyport, MA), Figure 5.4. Glacial acetic acid [64-19-7] (Fisher Scientific, Pittsburgh, PA) is used as received without any further purification. Coleman grade (99.99 %) carbon dioxide (Merriam Graves Corp, Charlestown, NH) is used as received. Films are deposited on silicon (crystal orientation <100>, 500 nm thermally grown oxide, 1-100 micro-ohm centimeter,

750 micron total thickness) (Novellus, San Jose, CA). Additionally, for electrical testing, films are deposited on square inch fluorinated tin oxide glass substrates called Tec 15 (Hartford Glass, Hartford City, IN).

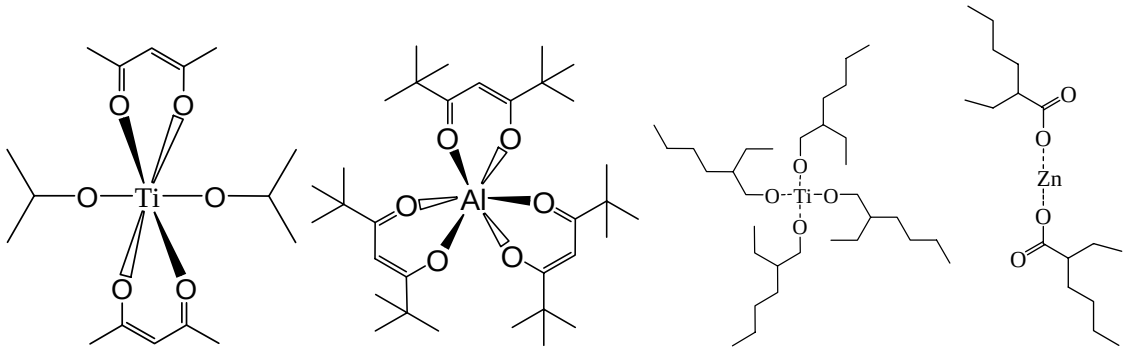

Figure 5.4: Chemical structure of titanium (di-isopropoxide) bis(acetylacetonate), tris(2,2,6,6-tetramethyl-3-5-heptanedionato) aluminum, $Al(tmhd)_3$, titanium(IV) 2-ethylhexoxide and zinc 2-ethylhexanoate.

5.2.3 Procedure

Silicon <100> with thermally grown (500 nm) silica and Tec 15, fluorinated tin oxide glass substrates, are mounted to a stainless steel support with copper wires or bolts. The support is a stainless steel I-beam cut in half and drilled with holes used to support the substrates for deposition. The support with substrates is clamped inside of a high throughput ventilation hood.

Liquid precursor and any additives are loaded into one side of a high pressure vessel with floating piston. This is done in a N_2 or Ar glove box if needed. Next, supercritical carbon dioxide (T = 60 ºC, P = 103 bar) is loaded from a high pressure ISCO pump into the precursor side of the high pressure vessel. The pressure vessel is not heated and the carbon dioxide returns to a liquid, although still at 103 bar. The vessel is mixed in order to create a homogeneous solution of liquid carbon dioxide dissolved into

the liquid precursor. The pressure vessel is then mounted to the six axis robot arm. The precursor side is connected to a metering valve which outputs to a 1/16" OD stainless steel nozzle. This nozzle sprays directly into the center of the plasma flame. The system is appropriately outfitted with nozzles. The metering valve is heated with two high power density cartridge heaters controlled with a custom built microprocessor controlled temperature controller. The temperature is maintained at 70 ºC. The side of the pressure vessel which does not contain the precursor, called the CO_2 side, is connected to the high pressure ISCO pump. The ISCO pump operates at constant pressure, P = 103 bar.

The plasma gun, argon primary and hydrogen secondary gases, is started. A standard movement routine is loaded into the robot arm that the plasma gun is directly attached to. A standard routine pass consists of seven left and seven right motions of the gun each at four mm below the previous motion. The overall vertical distance covered is 64 mm. The overall horizontal distance covered is 300 mm. Flow is controlled with the heated metering valve and read from the flow rate reading on the ISCO pump. For some runs, an IR camera is positioned so as to record temperature profiles of the substrates during deposition. After deposition, samples are allowed ample time to cool.

5.3 Results

Highly dendritic metal oxides are deposited via the PRESS system. A concentration study for both titanium oxide and zinc oxide is performed. The addition of acetic acid to titanium depositions is also studied in order to explore its effects on the crystalline nature of TiO_2. X-ray photoelectron spectroscopy (XPS), field emission

scanning electron microscopy (SEM), x-ray diffraction (XRD) and profilometry are used to determine composition, order, crystalline structure and thickness, respectively.

5.3.1 Titanium Dioxide

5.3.1.1 Concentration Study

A concentration study of titanium (IV) isopropoxide (Ttip) as the precursor in the PRESS system is performed in order to determine the range of concentration at which highly dendritic titania films can be created. The concentration range is 10 % by volume to 100 % by volume, with the remaining volume being liquid carbon dioxide (P = 103 bar, T = 60 ºC). 100 % by volume of precursor is used as the control experiment.

The experiments are performed at constant pressure, P = 103 bar and constant precursor concentration. The plasma torch is maintained at a constant 2” distance from the substrate surface. At low precursor concentration, 10 vol. % Ttip, no order is seen in the deposition, Figure 5.5.

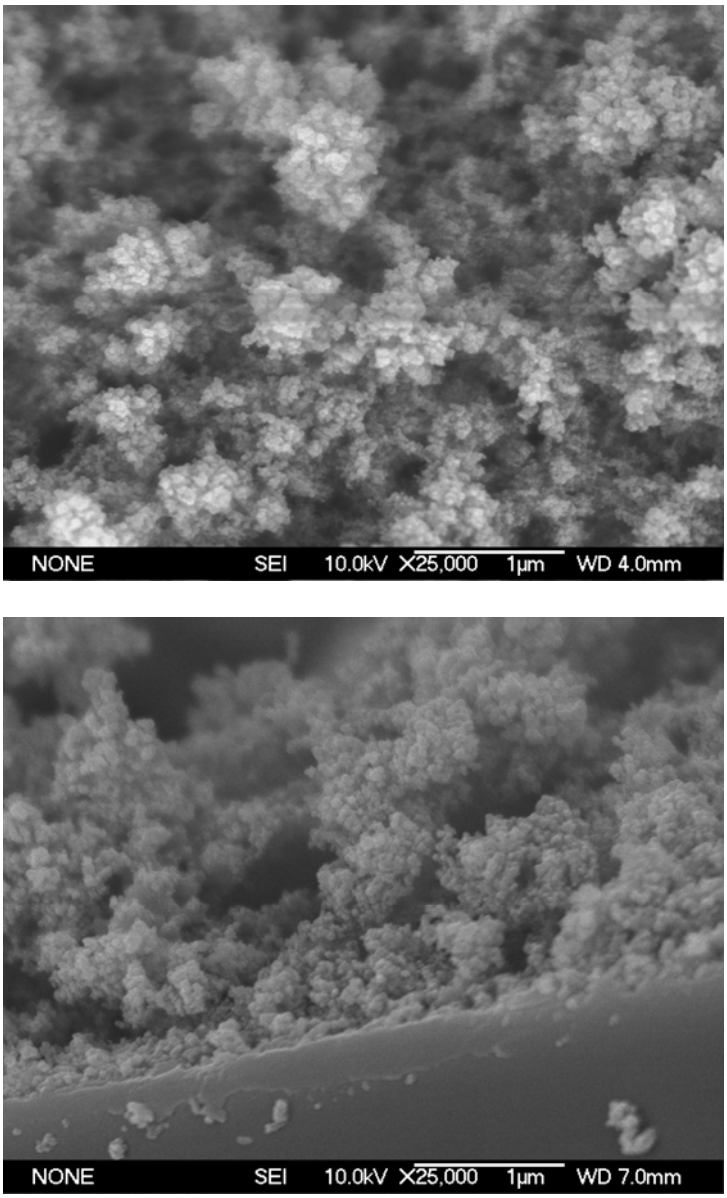

Figure 5.5: FE-SEM top-down (top) and cross sectional (bottom) of 10 vol. % Ttip PRESS sample. No order is observed.

As concentration is increased to 25 %, Figure 5.6, the cross sectional SEM reveals that a highly porous dendritic, with cylindrical macro scale, polycrystalline rutile titania film, consisting of agglomerated sub 100 nm titania crystals, is deposited.

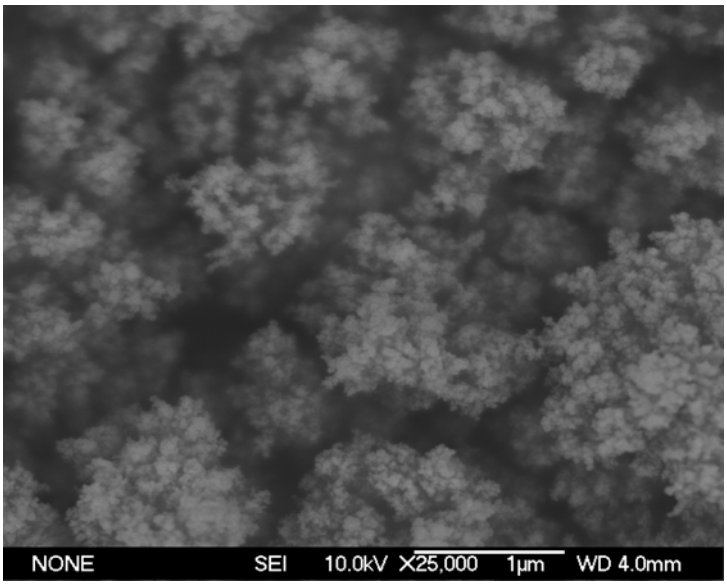

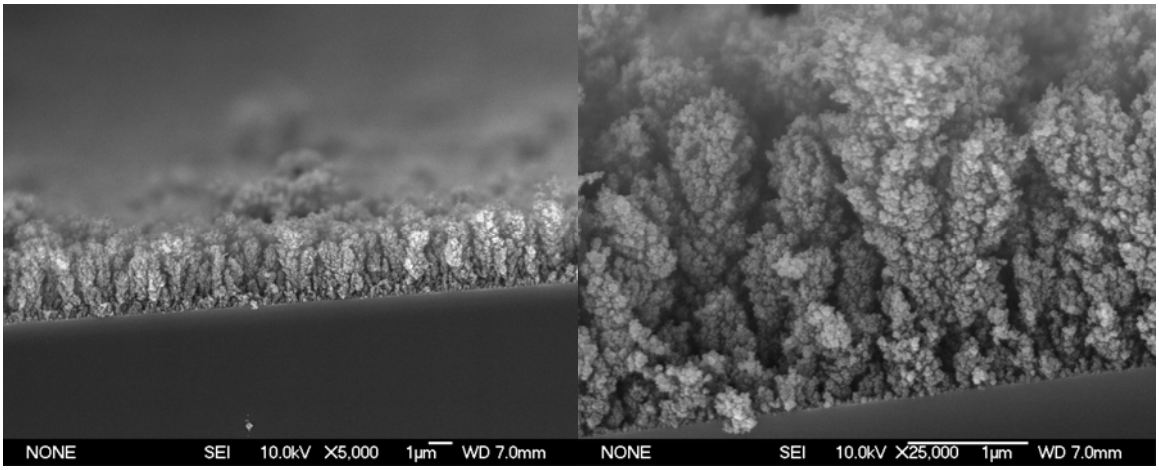

Figure 5.6: FE-SEM top-down (top) and cross sectional (bottom left and right) of 25 vol. % Ttip PRESS sample. A highly porous dendritic, with cylindrical macro scale, titania coating, consisting of agglomerated sub 100 nm titania crystals, is deposited.

The overall film thickness varied per sample due to the number of passes with the PRESS system. Overall, film thickness ranged between 1 and 10 microns, as measured by profilometry. At 75 % precursor concentration, SEM, Figure 5.7, continues to indicate that highly porous dendritic, with cylindrical macro scale, polycrystalline rutile titania film, consisting of agglomerated sub 100 nm titania crystals, is being deposited. Finally, the control experiment of 100% precursor results in a dense film, Figure 5.8.

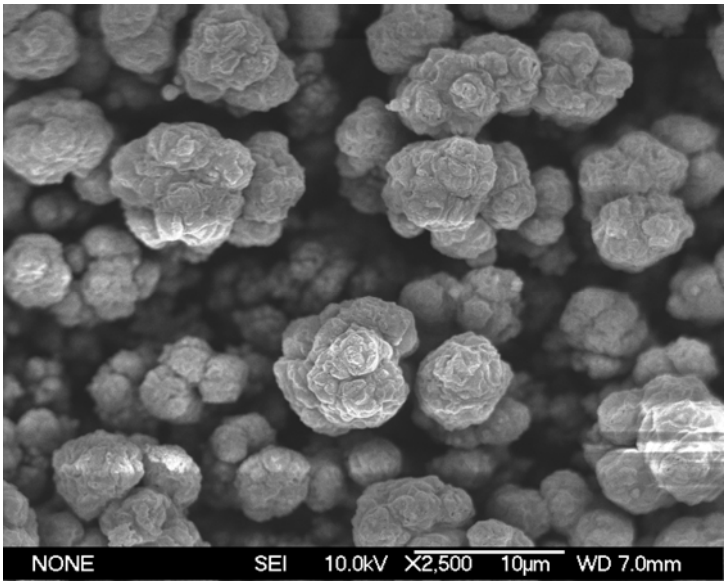

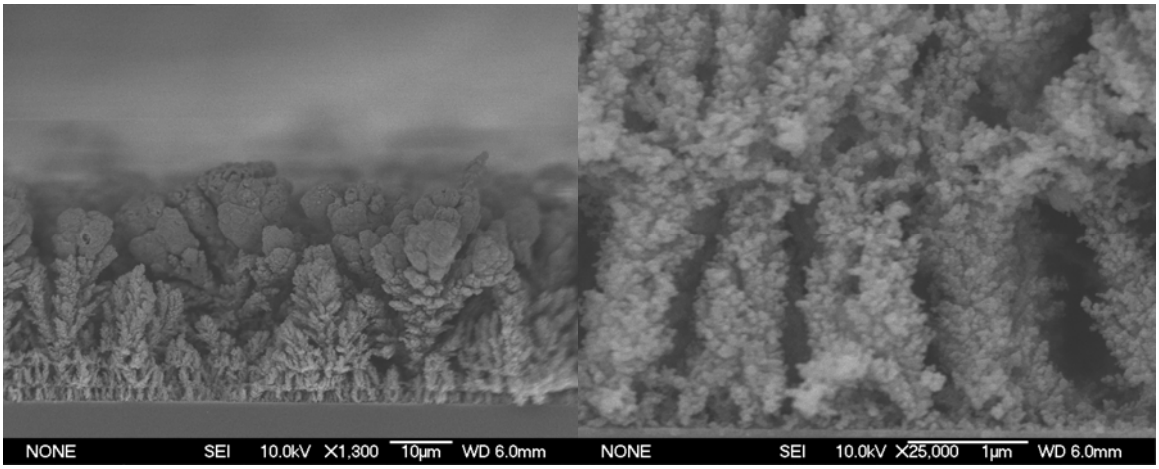

Figure 5.7: FE-SEM top-down (top) and cross sectional (bottom left and right) of 75 vol. % Ttip PRESS sample. A highly porous dendritic, with cylindrical macro scale, titania coating, consisting of agglomerated sub 100 nm titania crystals, is deposited.

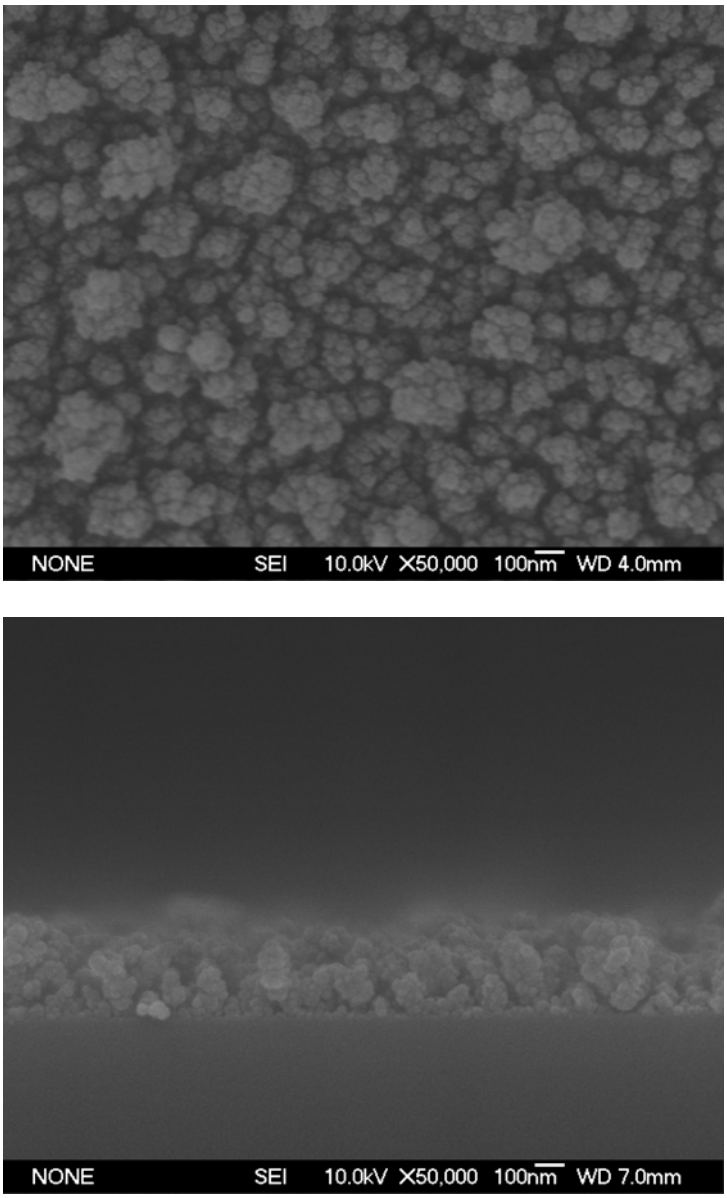

Figure 5.8: FE-SEM top-down (top) and cross sectional (bottom) of 100 vol. % Ttip (no CO_2) PRESS control sample. No order is observed.

XRD is used to reveal the rutile crystalline form of the titania film, Figure 5.9, which is consistent throughout all concentrations. XPS confirms the correct atomic concentration of Ti:O::1:2, with no carbon contamination in the bulk of the film, Figure 5.10, which is consistent throughout all concentrations.

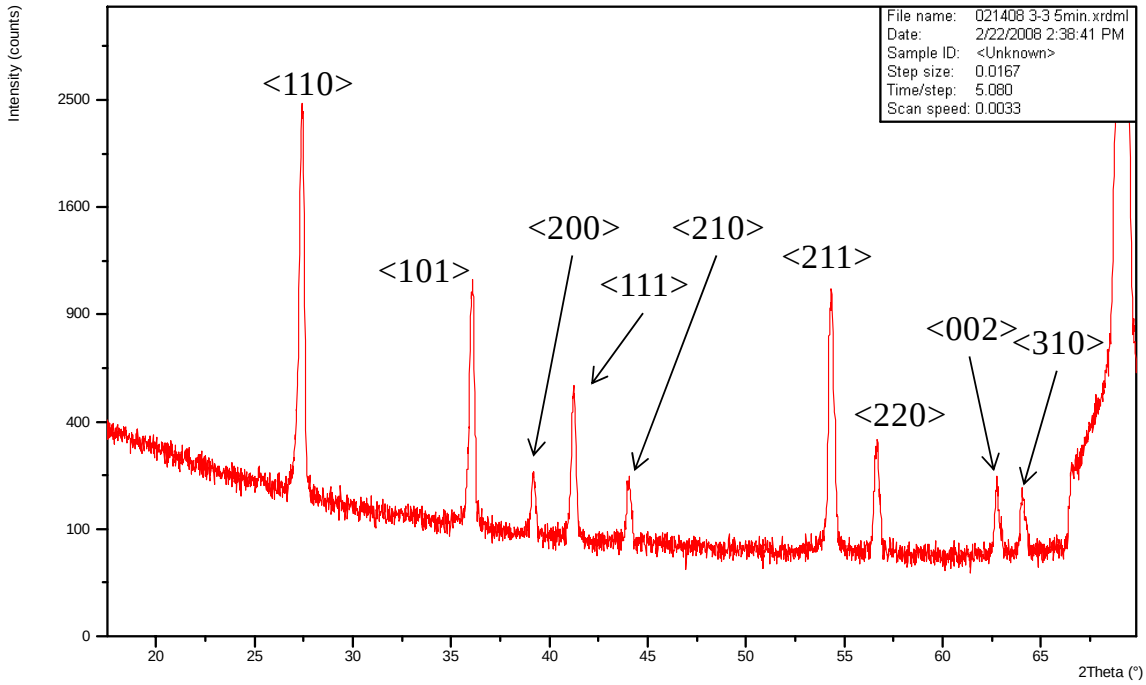

Figure 5.9: XRD of 75 vol. % Ttip PRESS sample. XRD indicates polycrystalline rutile titania is formed.

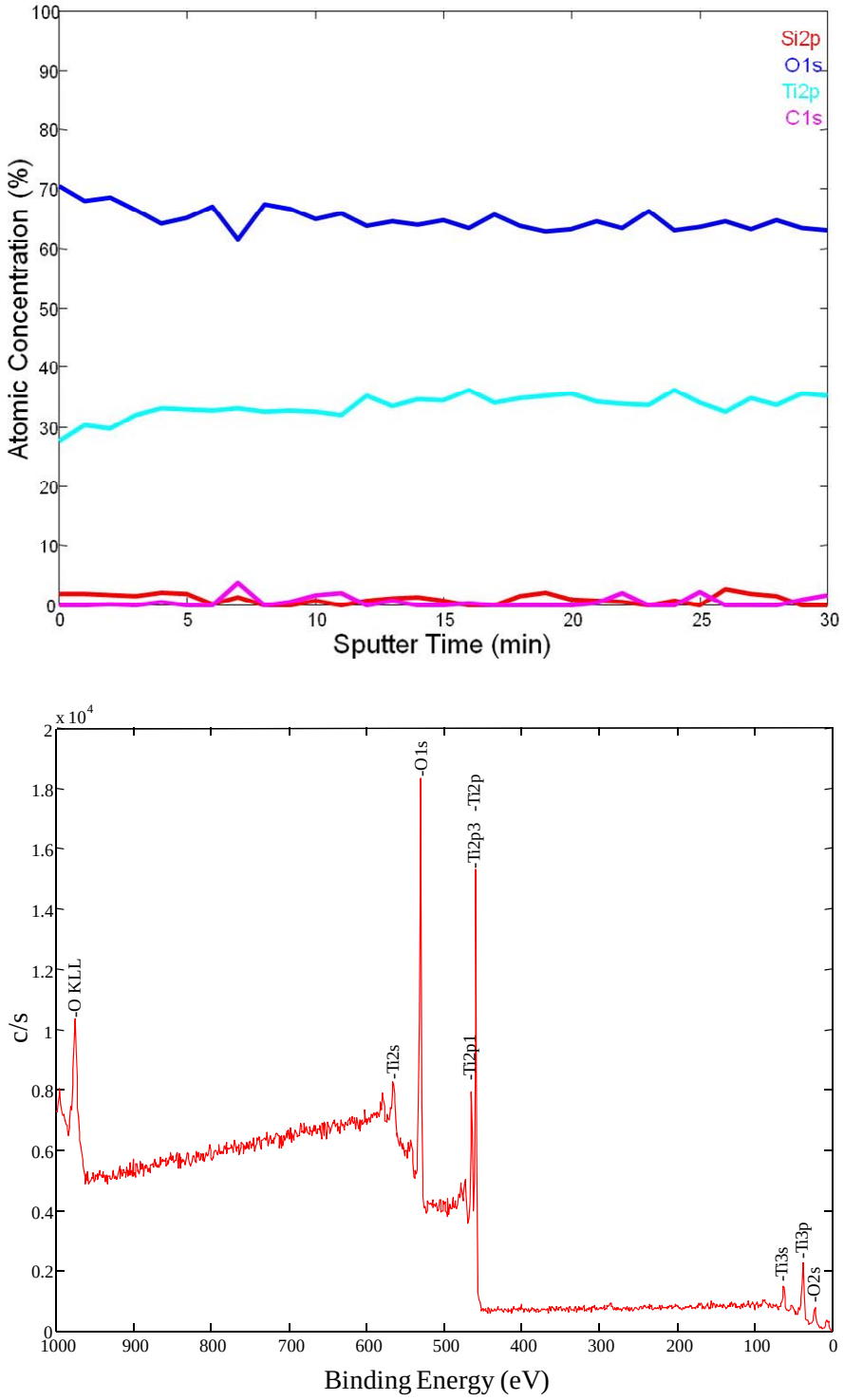

Figure 5.10: XPS sputter depth profile (top) and survey scan (bottom) of 75 vol. % Ttip PRESS sample. XPS confirms the correct atomic concentration of Ti:O::1:2, with no carbon contamination in the bulk of the film.

IR data are used to evaluate the temperature of the samples immediately after deposition, Figure 5.11. It is found that, typically, after 30 passes, the temperature of the substrate never exceeds 250 ºC.

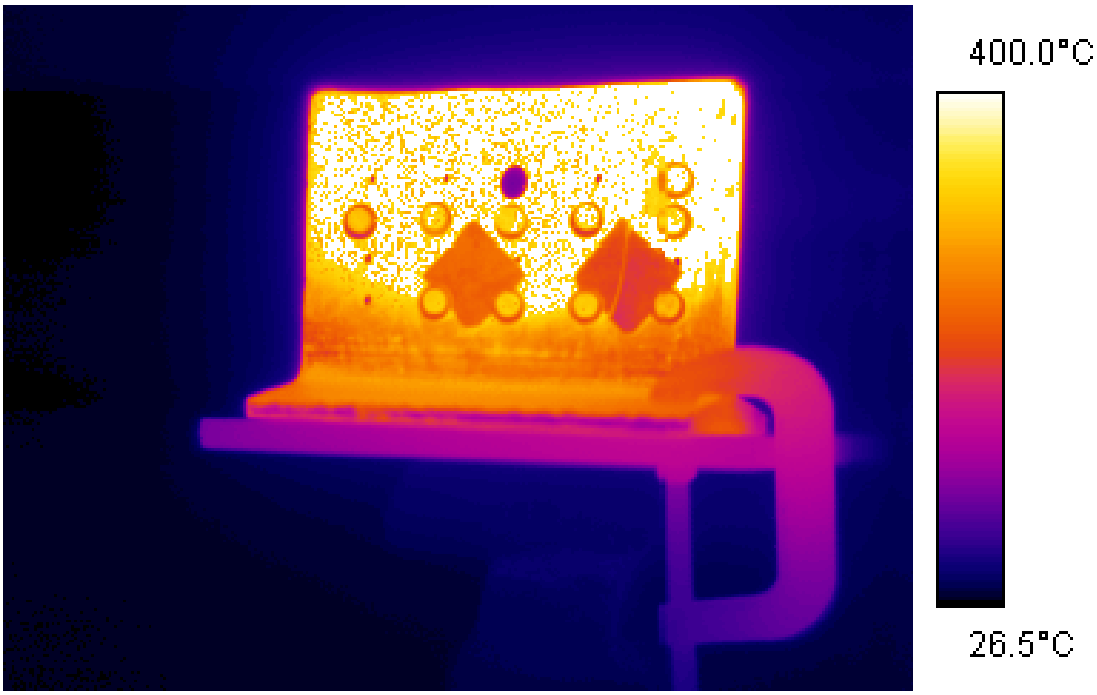

Figure 5.11: IR temperature profile of a typical Ttip PRESS deposition. Substrate temperature never exceeds 250 ºC

5.3.1.2 Acetic Acid Study

Acetic acids effect on the crystalline form of the deposited titania film is studied. The Ttip concentration is constant at 25 volume % for all the depositions. Additionally, the pressure is constant at 103 bar and the plasma torch is at a constant 2” from the substrate surface. The acetic acid is added in a molar ratio, with respect to titanium, from zero to three. At most, the total volume of the acetic acid is no more than 15 % total volume of the system.

It is observed that when no acetic acid is used, a polycrystalline titania film is deposited. Its main polymorph is rutile (Inorganic Crystal Structure Database, ICSD 01-089-4202) with traces of anatase (ICSD 00-021-1272) and brookite (ICSD 01-075-1582), Figure 5.12. It is found that the addition of acetic acid has no significant effect on changing the main polymorph of the deposited titania film.

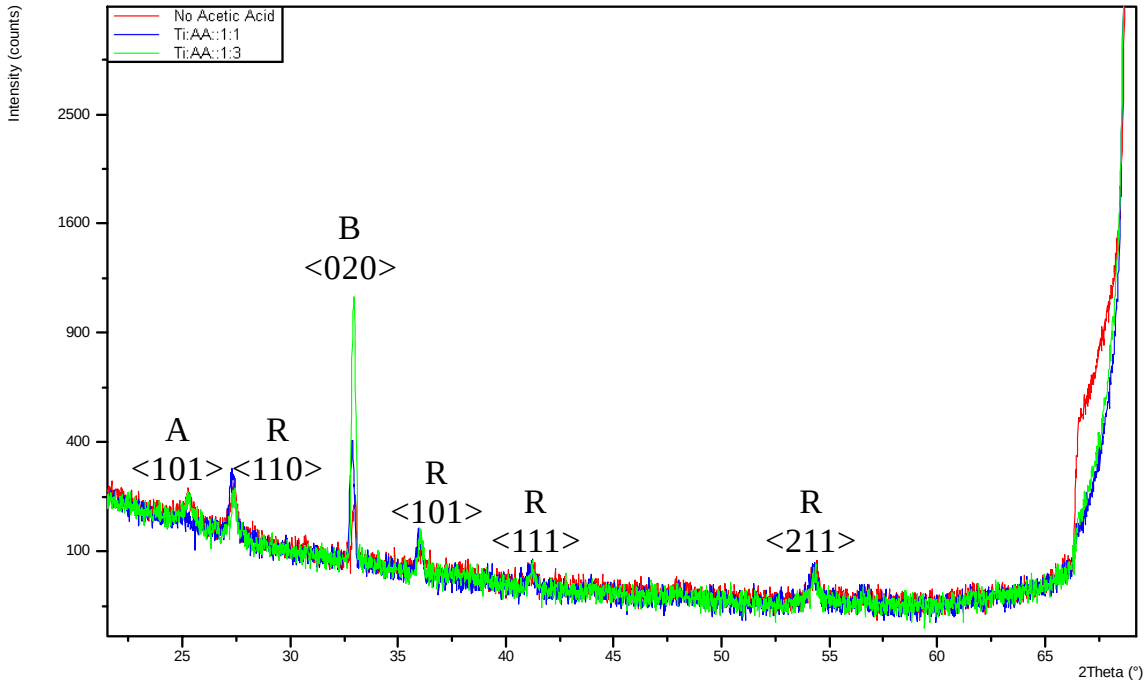

Figure 5.12: XRD comparison of samples in the acetic acid concentration study. The addition of acetic acid does not significantly alter the crystallinity of the titania film. XRD shows that the films main polymorph is rutile with traces of brookite and anatase titania.

5.3.2 Zinc Oxide

5.3.2.1 Concentration Study

A concentration study of zinc 2-ethylhexonate (ZnEO) as the precursor in the PRESS system is performed in order to determine the range of concentration at which highly dedritic Zn oxide films can be created. The concentration range is 25 % by

volume to 100 % by volume, with the remaining volume being liquid carbon dioxide (P = 103 bar, T = 60 ºC). 100 % by volume of precursor is used as the control experiment.

The experiments are performed at constant pressure, P = 103 bar and constant precursor concentration. The plasma torch is maintained at a constant 2" distance from the substrate surface. At low precursor concentration, 25 volume % ZnEO, no order is seen in the deposited film, Figure 5.13. As the concentration is increased to 50 volume %, Figure 5.14, the cross sectional SEM reveals that a highly porous dendritic zinc oxide nanostructure consisting of columnar assemblies of agglomerated zinc oxide particles of approximately 100 nm in size is deposited. It is observed that the cylindrical zinc oxide structures are topped with "boulders," most likely due to annealing of the film with subsequent plasma flame passes. The control experiment of 100% precursor results in a dense film, Figure 5.15.

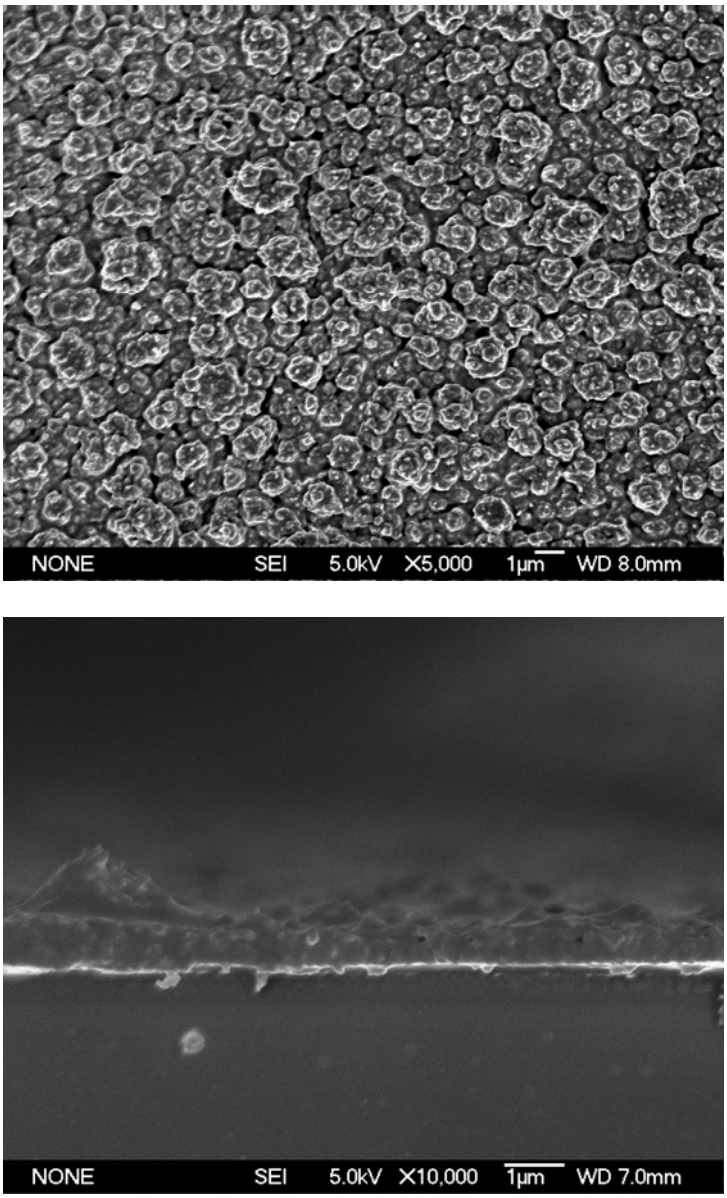

Figure 5.13: FE-SEM top-down (top) and cross sectional (bottom) of 25 vol. % ZnEO PRESS sample. No order is observed.

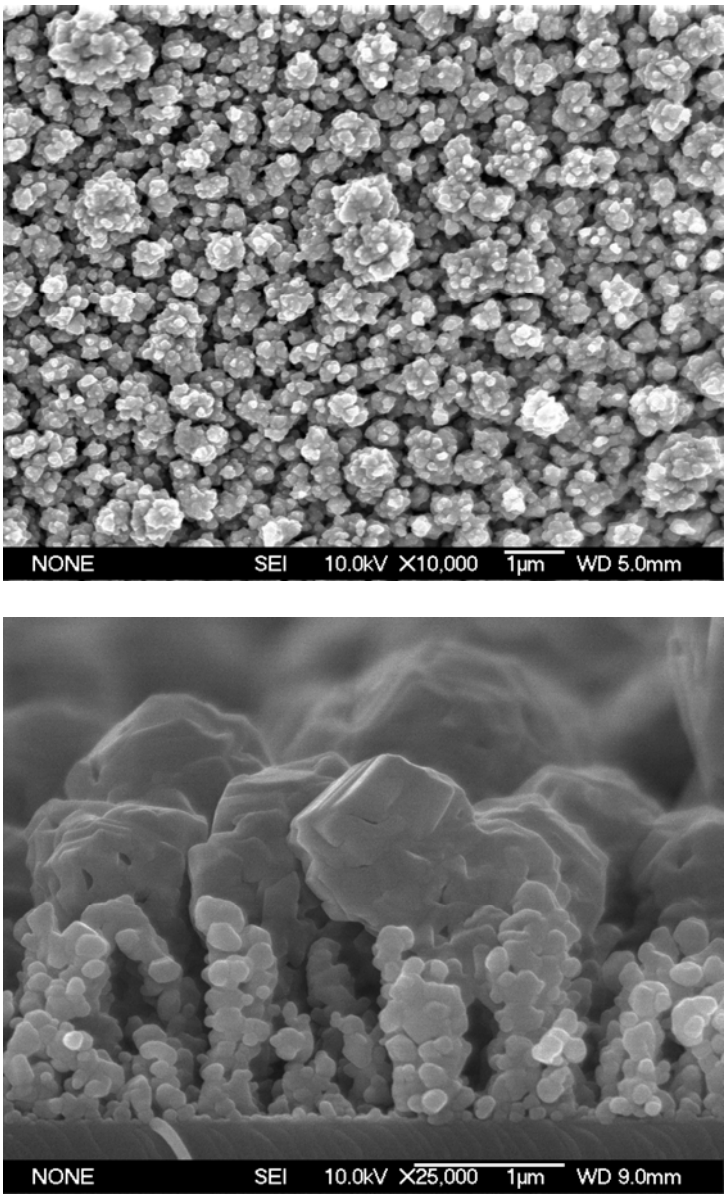

Figure 5.14: FE-SEM top-down (top) and cross sectional (bottom) of 50 vol. % Ttip ZnEO sample. A highly porous dendritic zinc oxide nanostructure consisting of columnar assemblies of agglomerated zinc oxide particles of approximately 100 nm in size is deposited.

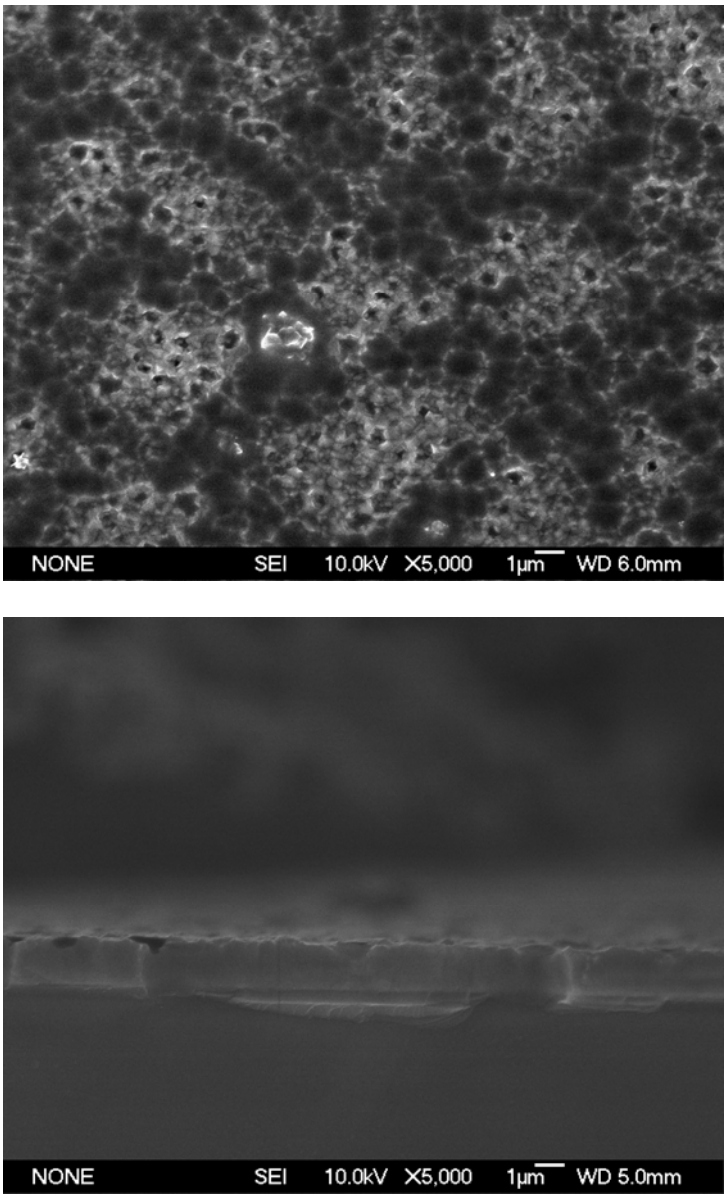

Figure 5.15: FE-SEM top-down (top) and cross sectional (bottom) of 100 vol. % ZnEO PRESS control sample. A dense film is observed.

XRD, Figure 5.16, indicates that the film consists of polycrystalline zincite (ZnO) and ZnO_2. XPS is used to determine the composition of the film. XPS, Figure 5.17, indicates an atomic ratio of Zn:O::1:1 at the surface and a different atomic ratio of Zn:O::2:3, with no carbon contamination, in the bulk of the film.

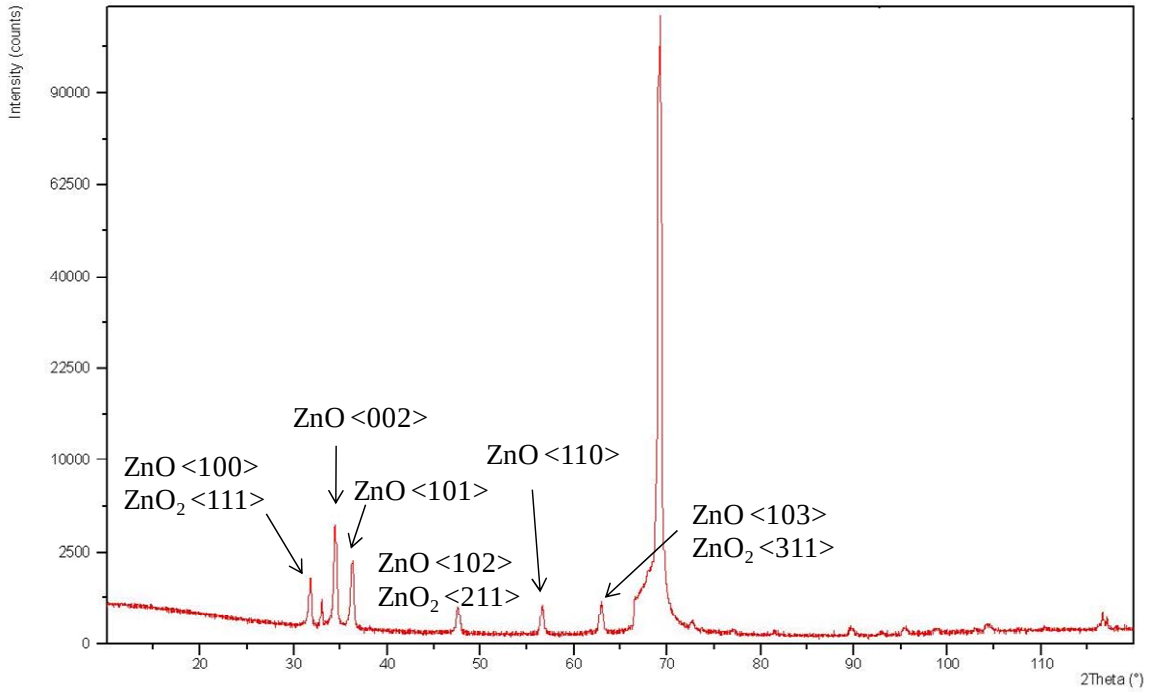

Figure 5.16: XRD of 50 vol. % ZnEO PRESS sample. XRD indicates polycrystalline zincite (ZnO) and ZnO_2 are formed.

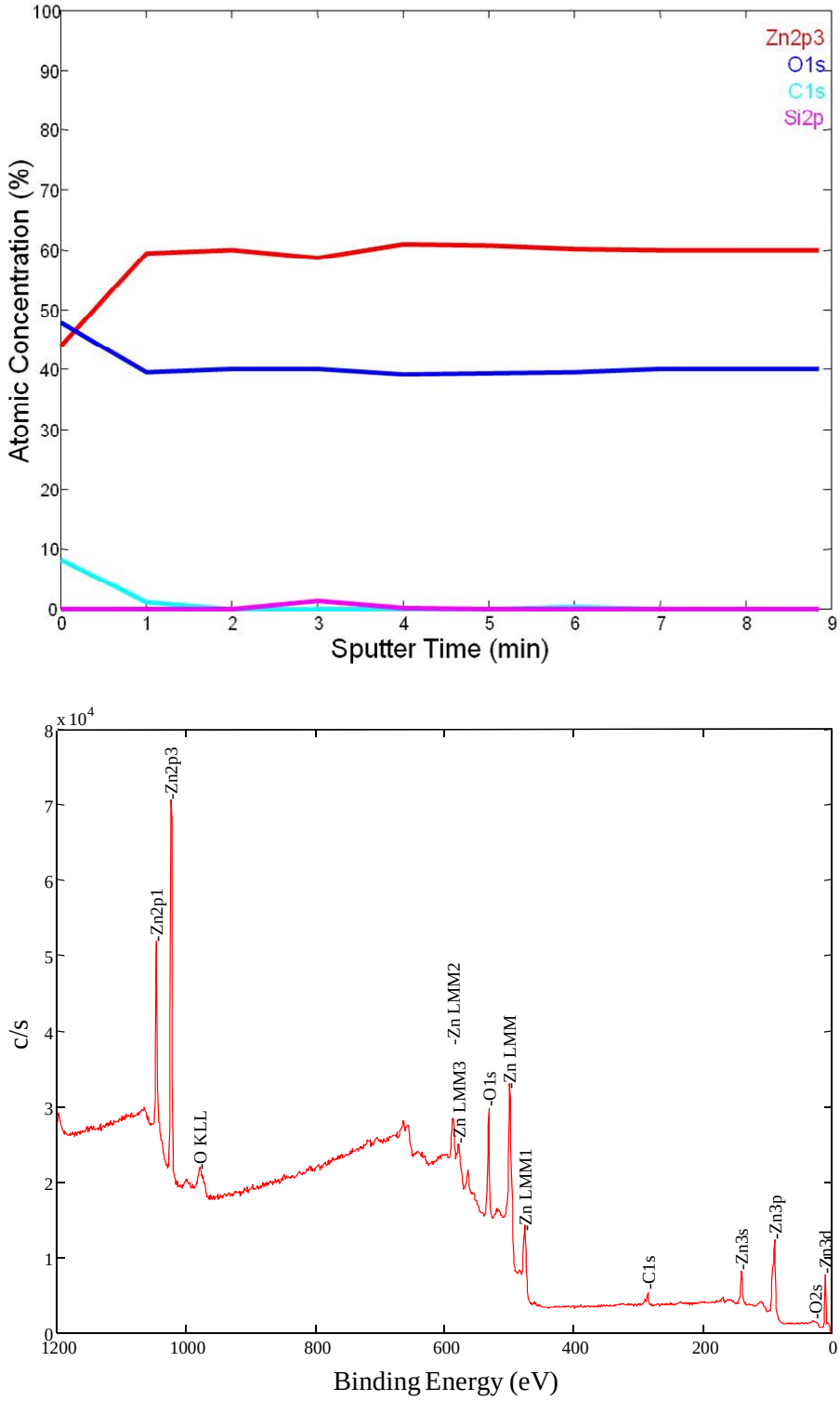

Figure 5.17: XPS sputter depth profile (top) and survey scan (bottom) of 50 vol. % ZnEO PRESS sample. XPS indicates an atomic ratio of Zn:O::1:1 at the surface and a different atomic ratio of Zn:O::2:3, with no carbon contamination, in the bulk of the film.

5.4 Discussion

The control experiments are used to validate that the PRESS process, through the use of high pressure carbon dioxide, is affecting the characteristics of the deposited metal oxide films. Dense films are observed at 100 volume % for either Ttip or ZnEO. This is also true at relatively low concentrations for both precursors. The highly dendritic structures occur in the middle of the concentrations range. This is likely due to the vapor-liquid (VL) equilibria of the two systems. Typically, when dealing with carbon dioxide and another component whose molecular size varies greatly, a "cigar" shaped VL envelope defines the phase of system in a P-x diagram.[35] At both extremes of composition of the heavy component, a single phase persists throughout the range of pressure. However, between these extremes, there exists a region of two phases. When the system is initially injected with CO_2 at high pressure, the system is forced into a single phase. As the solution expands across the nozzle, the two components are forced through this two phase region, resulting in increased atomization of the precursor. It is because of this quick phase change that highly dendritic films are deposited in the range of 25 to 75 volume %.

The acetic acid concentration study is performed at the 25 % Ttip concentration because the change in carbon dioxide concentration, from the addition of at most 15 volume % of acetic acid, is negligible between the range of 25 % and 75 % precursor concentration since the characteristics of the deposited film are not changed in this range. It is reported that the addition of acetic acid during the formation of titania nanoparticles via a modified sol-gel process with titanium isopropoxide is used to control the hydrolysis and condensation reactions in order to achieve the titania polymorph,

anatase.[36] The anatase phase of titania is the most favorable phase for photocatalysis and solar energy conversion due to its high photoactivity.[37, 38] It is hoped that the addition of acetic acid to Ttip PRESS deposited films would reduce the main polymorph, rutile, and yield anatase titania, however this was not observed. It is known that at temperatures above roughly 700 ºC, both anatase and brookite, another polymorph of titania, are converted to rutile. Since plasma flame temperatures are typically on the order of 1500 ºC, it is likely that any control over the crystallinity is quickly lost to the extreme temperature of the plasma flame thus giving rise to consistent rutile titania results.

The XPS data, Figure 5.17, for the ZnEO PRESS deposition indicate that a 1:1 ratio of Zn to O is at the surface. This is confirmed with XRD, Figure 5.16, which means that zincite (ICSD 00-036-1451) is the mineral form of the zinc oxide at the surface. It is less clear in determining the exact mineral structure of the bulk film. XPS indicates a Zn to O ratio of 2:3 in the bulk, however, Zn_2O_3 is a very uncommon form of zinc oxide. XRD also indicates the presence of polycrystalline ZnO_2. Given the XPS and XRD data, it is concluded that both ZnO and ZnO_2 are in a 1:1 ratio throughout the bulk of the film.

5.5 Conclusions

A new process that uses both plasma spray technology and the rapid expansion of supercritical solutions is combined to form a brand new process that is called plasma-enhanced rapid expansion of supercritical solutions, labeled PRESS. The PRESS process is used to deposit a variety of metal oxides, specifically, titanium oxide and zinc oxide. Ttip is used in the PRESS system to deposit highly porous dendritic, with cylindrical macro scale, polycrystalline rutile titania films, consisting of agglomerated sub 100 nm

titania crystals. ZnEO is used in the PRESS system to deposit highly porous dendritic zinc oxide nanostructure consisting of columnar assemblies of agglomerated zinc oxide particles of approximately 100 nm in size. These high surface area films are the first step towards making high efficiency inorganic solar cells that will be cost effective and have short fabrication times.

5.6 References

(1) S. J. J. Thompson, *Philosophical Magazine* **1897**, *44*, 293.

(2) C. Garzella, E. Comini, E. Tempesti, C. Frigeri, G. Sberveglieri, *Sensors and Actuators B-Chemical* **2000**, *68*, 189-196.

(3) I. D. Kim, A. Rothschild, B. H. Lee, D. Y. Kim, S. M. Jo, H. L. Tuller, *Nano Letters* **2006**, *6*, 2009-2013.

(4) A. M. Ruiz, G. Sakai, A. Cornet, K. Shimanoe, J. R. Morante, N. Yamazoe, *Sensors and Actuators B-Chemical* **2003**, *93*, 509-518.

(5) A. Fujishima, K. Honda, *Nature* **1972**, *238*, 37.

(6) S. N. Frank, A. J. Bard, *Journal of the American Chemical Society* **1977**, *99*, 303-304.

(7) A. Werner, A. Roos, *Solar Energy Materials and Solar Cells* **2007**, *91*, 609-615.

(8) Y. J. Liu, R. O. Claus, *Journal of the American Chemical Society* **1997**, *119*, 5273-5274.

(9) N. D. Abazovic, M. I. Comor, M. D. Dramicanin, D. J. Jovanovic, S. P. Ahrenkiel, J. M. Nedeljkovic, *Journal of Physical Chemistry B* **2006**, *110*, 25366-25370.

(10) C. J. Barbe, F. Arendse, P. Comte, M. Jirousek, F. Lenzmann, V. Shklover, M. Gratzel, *J. Am. Chem. Soc.* **1997**, *80*, 3157-3171.

(11) M. Gratzel, *Nature* **2001**, *414*, 338-344.

(12) M. K. Nazeeruddin, A. Kay, I. Rodicio, R. Humphry-Baker, E. Muller, P. Liska, N. Vlachopoulos, M. Gratzel, *J. Am. Chem. Soc.* **1993**, *115*, 6382-6390.

(13) B. O'Regan, M. Gratzel, *Nature* **1991**, *353*, 737-740.

(14) N. Vlachopoulos, P. Liska, J. Augustynski, M. Gratzel, *J. Am. Chem. Soc.* **1988**, *110*, 1216-1220.

(15) G. Smestad, *Solar Energy Materials and Solar Cells* **1998**, *55*, 157-178.

(16) T. Markvart, Ed. *Solar Electricity*, John Wiley and Sons, **2001**.

(17) A. Luque, S. Hegedus, Eds., *Handbook of Photovoltaic Science and Engineering*, John Wiley and Sons, **2007**.

(18) BP Statistical Review of World Energy Full Review 2008, www.bp.com, **2008**

(19) M. A. Conteras, B. Egaas, K. Ramanathan, J. Hiltner, A. Swatzlander, F. Hasoon, R. Noufi, *Progress in Photovoltaics* **1999**, *7*, 311-316.

(20) A. Jasenek, U. Rau, K. Weinert, I. M. Kotschau, G. Hanna, G. Voorwinden, M. Powalla, H. W. Schock, J. H. Werner, *Thin Solid Films* **2001**, *387*, 228-230.

(21) K. M. Coakley, Y. Liu, M. D. McGehee, K. L. Frindell, G. D. Stucky, *Advanced Functional Materials* **2003**, *13*, 301-306.

(22) K. M. Coakley, M. D. McGehee, *Applied Physics Letters* **2003**, *83*, 3380-3382.

(23) K. M. Coakley, M. D. McGehee, *Chemistry of Materials* **2004**, *16*, 4533-4542.

(24) H. Hoppe, N. Serdariciftci, *Journal of Materials Research* **2004**, *19*, 1924-1945.

(25) F. O. Lenzmann, J. M. Groon, *Advances in OptoElectronics* **2007**, *2007*, 1-10.

(26) I. Langmuir, *Proceedings of the National Academy of Sciences of the United States of America* **1928**, *14*, 627-637.

(27) M. Gell, L. Xie, X. Ma, E. Jordan, N. Padture, *Surface and Coating Technology* **2004**, *177-178*, 97-102.

(28) L. Xie, X. Ma, E. Jordan, N. Padture, D. Xiao, M. Gell, *Surface and Coating Technology* **2004**, *177-178*, 103-107.

(29) L. Xie, X. Ma, A. Ozturk, E. Jordan, N. Padture, B. Cetegen, D. Xiao, M. Gell, *Surface and Coating Technology* **2004**, *183*, 51-61.

(30) D. Chen, E. Jordan, M. Gell, X. Ma, *J. Am. Chem. Soc.* **2008**, *91*, 865-872.

(31) A. Vasiliev, N. Padture, X. Ma, *Acta Materialia* **2006**, *54*, 4913-4920.

(32) J. B. Hannay, J. Hogarth, *Proceedings of the Royal Society of London* **1879**, *29*, 324-326.

(33) W. Worthy, *Chemical and Engineering News* **1981**, *59*, 16-17.

(34) V. Krukonis, in *Annual Meeting AIChE* San Fransisco **1984**.

(35) M. A. McHugh, V. J. Krukonis, *Supercritical Fluid Extraction Practice and Principles*, Butterworth-Heinemann, **1994**.

(36) R. Parra, M. S. Goes, M. S. Castro, E. Longo, P. R. Bueno, J. A. Varela, *Chemistry of Materials* **2008**, *20*, 143-150.

(37) P. Hsiao, K. Wang, C. Cheng, H. Teng, *Journal of Photochemistry and Photobiology A-Chemistry* **2007**, *188*, 19-24.

(38) P. K. Khanna, N. Singh, S. Charan, *Materials Letters* **2007**, *61*, 4725-4730.

CHAPTER 6

CONCLUSIONS AND FUTURE WORK

6.1 Conclusions

The main goal of this work is take the supercritical fluid deposition technique from a demonstrated technology to a point where it is a viable option for the miniaturization of microelectronic devices in industry. Other technologies are identified to overcome certain aspects of the entire miniaturization challenge, from a top-down method, as a whole, however none can fully satisfy all the needs for industrial integration. From conformal coverage over large surface areas in complex geometries to industry scale cost-effective solutions for depositing thin films, supercritical fluid deposition technology can meet these challenges.

6.1.1 Kinetics

The challenge of industrial acceptance of SFD technology is first approached from the scale-up demands. An in depth study to understand the chemistry behind the deposition of thin films in supercritical fluid technology is undertaken.

The kinetics of ruthenium thin film deposition by supercritical fluids using bis(2,2,6,6-tetramethyl-heptane-3,5-dionato)(1,5-cyclooctadiene)ruthenium(II) as the precursor is studied. Reaction rate orders are determined and a Langmuir – Hinshelwood deposition mechanism is proposed. The apparent activation energy is found to be 45.3 kJ/mol over the temperature range of 240 °C to 280 °C. A study on the growth rate dependence of precursor concentration indicates a first order reaction rate order for concentrations less than 0.06 wt. % and zero order for concentrations higher than 0.06 wt.

%. The zero order deposition kinetics of SFD at high precursor concentration is the enabling feature of this technology that provides conformal film deposition in high aspect ratio and topographically complex features that overcomes the limitations of CVD technology to deposit conformal films. Next, reaction pressure is studied and is shown to have no effect on the growth rate over a large process window of 135 bar to 200 bar. Hydrogen concentration is also studied and has a second order effect on growth rate for concentrations less than 0.26 wt. % and a zero order effect on concentrations above that. The precursor decomposition products (tmhd, cod and cot) are studied to determine their affect on growth rate. Tmhd and cod have a negative first order effect on film growth which is attributed to their competition for surface active sites thereby decreasing the probability of a successful surface reaction. Cot shows negligible negative effects on growth rate which is attributed to cot having no affinity for the surface. The surface reaction is proposed to be rate determining.

6.1.2 Adhesion Enhancement and Mechanical Testing

The next challenge is that of performance and reliability of films for microelectronics after their deposition. A study to quantify the adhesion of metallization layers with and without the use of sacrificial interfacial adhesion promotion layers is performed.

A fivefold increase in adhesion strength is observed for PAA modified Cu/TaN interfaces in which the thin copper films are deposited by the hydrogen assisted reduction of bis(2,2,7-trimethyloctane-3,5-dionato) copper in supercritical carbon dioxide. PAA pretreatment is carried out via spin coating. The remaining 15 nm layer at the interface

becomes sacrificial at the reaction conditions used, leaving behind no trace of the PAA. The resulting average interfacial adhesion energy is just above 5 J/m^2, which meets adhesion standards in the semiconductor industry. The adhesion measurements are performed with a custom built four-point bend fracture mechanics testing system. Comparison of the copper film thickness to the measured adhesion energy indicated that there is no effect on the adhesion energy as the film thickness changes. Finally, it is observed that the growth rate of copper during deposition on surfaces pretreated with PAA is faster due to the higher number of available surface sites for the reduction reactions.

6.1.3 Applications

The final challenge sought out by this work is to both identify areas of development that would benefit from the SFD technology and then seek to demonstrate the ability of SFD to satisfy the difficulties associated with that technology. By doing this, the versatility of SFD technology is established and its ability to satisfy many industrial applications.

6.1.3.1 Cobalt/Platinum

The successful co-deposition of cobalt and platinum onto TaN capped silicon wafers using $CoCp_2$ as the cobalt source and $Pt(Me)_2cod$ as the platinum source in a hot wall reactor at both 60 ºC and 150 ºC is performed. The deposition of platinum itself or no deposition at all in the cold wall reactor is attributed to parasitic deposition to the heated sample stage. The tmhd ligand in $Co(tmhd)_3$ is etching the cobalt during deposition resulting in high purity platinum films being deposited. Finally, XRD is used

to analyze the crystal structure of the deposited film and the desirable alloying of cobalt and platinum is not observed.

6.1.3.2 Ceria/Platinum

The catalytically enhanced deposition of polycrystalline ceria ($^{+}3$ state) and polycrystalline platinum from $Ce(tmhd)_4$ and $Pt(Me)_2cod$, respectively, is discovered. This low temperature co-deposition is extended towards fuel cell applications, specifically, fabrication of methanol oxidation fuel cell electrodes. The resultant electrodes are shown to be catalytically active.

6.1.3.3 Barium Titanate

The deposition of barium titanate, $BaTiO_3$, as a high k dielectric material for high density energy storage applications is studied. Recently, a method for the single step synthesis of $BaTiO_3$ powders was identified. The method is modified and applied to the deposition of a thick dense film from a supercritical ethanol/water solution. Two important aspects of this reaction are studied in order to evaluate the ability to induce $BaTiO_3$ film formation in this new process. First, the water ratio, which controls $BaTiO_3$ crystallinity is tested and no film formation is detected. Next, the propoxide concentration, used in precursor synthesis, is evaluated and is found to have no affect on the ability to deposit high purity polycrystalline $BaTiO_3$ films. Given the experimental findings and the high $BaCo_3$ concentrations deposited on the films, it is proposed that the high purity polycrystalline $BaTiO_3$ did not form due to equipment limitations in reaching the desired reaction temperature of 380 ºC, which is responsible for $BaTiO_3$ crystallinity.

6.1.3.4 Neodymium/Nickel

In the area of solid oxide fuel cells, there exists a need to decrease the operating temperature. With this need comes the opportunity to find cheaper materials for electrode fabrication. Neodymium and nickel have been identified as candidates for high performance and low temperature solid oxide fuel cell cathodes

Simultaneous deposition of nickel and neodymium, in trace amounts, films are deposited by the hydrogen assisted reduction of both precursors via SFD. An important aspect of the co-deposition of neodymium and nickel when using beta-diketonate organometallic precursors is the gas phase temperature. By causing the precursor to melt, dissolution rates are increased for the precursor into the supercritical carbon dioxide. Given that the precursors have a very tight range between melting and decomposition points, it is necessary to precisely control temperatures in the reactor. Given the monitored gas phase and reaction stage temperatures, the low neodymium concentration is proposed to be a function of the near or surpassed decomposition temperature of the precursor. Additionally, the high purity nickel that is deposited is attributed to a melting point depression from the interaction of the precursor with the carbon dioxide.

6.1.3.5 Stacks via Layered Deposition

The ability to deposit conformal layers is being extended to the fabrication of devices by layer-by-layer deposition, which is no more complex than a simple deposition repeated numerous times to achieve the intended result. For demonstration of this technique, thin film capacitors are fabricated from three consecutive supercritical fluid depositions.

The fabrication of a mutli-layer stacks of Ru/TiO_2/Ru and Ru/HfO_2/Ru on silicon substrates via three consecutive SFD steps is reported. It is observed that the Ru/TiO_2/Ru stacks have decreased definition at the interfaces. This is a result of the heating, which is essentially an annealing step. Additionally, it is proposed that the ruthenium is catalyzing the deposition of titania and the increased amount of ruthenium on closed corners of the substrate yields local increased growth rates thereby producing unconformal deposition. Ru/HfO_2/Ru stacks are also studied and show much more defined interfaces regardless of the additional thermal cycles. Additionally, all three stacks are observed to have deposited conformally across the high aspect ratio features of the substrate.

6.1.4 Plasma Enhanced Rapid Expansion of Supercritical Solutions

A new process that uses both plasma spray technology and the rapid expansion of supercritical solutions is combined to form a brand new process that is called plasma-enhanced rapid expansion of supercritical solutions, labeled PRESS. The PRESS process is used to deposit a variety of metal oxides, specifically, titanium oxide and zinc oxide. Tiip is used in the PRESS system to deposit highly porous dendtritic, with cylindrical macro scale, polycrystalline rutile titania films, consisting of agglomerated sub 100 nm titania crystals. ZnEO is used in the PRESS system to deposit highly porous dendtritic zinc oxide nanostructure consisting of columnar assemblies of agglomerated zinc oxide particles of approximately 100 nm in size. These high surface area films are the first step towards making high efficiency inorganic solar cells that will be cost effective and have short fabrication times.

6.2 Future Work

6.2.1 Kinetics

The kinetics of SFD are now established for metal deposition via a copper SFD kinetics study and the ruthenium kinetics study detailed here. Further understanding of the deposition of metal oxides via hydrolysis reactions is currently under investigation. With the current level of understanding of the deposition kinetics for SFD reactions, many well educated guesses could be made about the variety of techniques that are discussed in Chapter 4. However, kinetic studies are essential to confirm them. Additional studies are needed to understand the interaction of multiple precursor systems during co-deposition reactions in supercritical fluids. Other works include understanding the kinetics of film formation from other supercritical solvents, such as the water/ethanol system studied for $BaTiO_3$ film formation. Finally, understanding more complex ligand systems for single precursor SFD reactions lends itself to better predicting the results of new systems without having to perform tedious kinetic studies.

6.2.2 Adhesion Enhancement and Mechanical Testing

The results of this study indicate that copper metallization layers have increased adhesion on TaN barrier layers. However, dependency on the metallization layer type and the substrate type are uncertain. In order to establish this important piece of information, an additional adhesion studies should be performed. First, a study on other barriers layers, such as TiN, should be performed. Next, a study using other metals should also be performed. This will establish whether or not there is a dependency on the

copper or TaN of the presented results. Further studies can be extended to metal oxide, alloy, co-deposited and layered films.

6.2.3 Applications

6.2.3.1 Ceria/Platinum

For DMFC electrodes, other oxygen buffer compounds can be used instead of the ceria. For instance, the use of ruthenium as an oxygen buffer is possible. Future work could be focused on the co-deposition of Pt and Ru matrices.

6.2.3.2 Barium Titanate

The equipment limitations prevent the ability of $BaTiO_3$ film formation from supercritical water/ethanol mixtures. Given the background that has been established for deposition from supercritical carbon dioxide, it would be advantageous to study the co-deposition of Ba and Ti from supercritical CO_2.

Additionally, if the water/ethanol solvent system is the desired route for Ba/Ti deposition, a new reactor system can be designed. To overcome the temperature limitations of the system, a metal on metal seal would have to be created since the o-ring seal is the limiting factor in the current reactor system.

6.2.3.3 Neodymium/Nickel

Further experimentation should be performed over a larger temperature range. The temperature of the reaction should be reduced to as low as 225 ºC, as long as nickel deposition still occurs. Additionally, experimentation should be extended to other precursor systems. The beta-diketonate, tmhd, ligand is known to etch surfaces during

deposition and may be preventing a higher neodymium concentration during co-deposition. The cyclopentadienyl ligand has proven to be a successful ligand for precursors in SFD previously and potential precursors have been identified for future studies. Both bis(cyclopentadienyls)nickel, nickelocene, $NiCp_2$ and tris(cyclopentadienyls)neodymium, $NdCp_3$ should be soluble and are liquids at room temperature.

6.2.3.4 Stacks via Layered Deposition

The first step towards future work for the capacitor fabrication is to electrically test the films deposited to ensure no leakage or short circuits were created. After determination of the capacitance, LCR measurements can be taken to determine the dielectric constant of the dielectric layer of the capacitor. A much higher resolution mask can be made and then used to replicate multiple capacitors on a substrate.

6.2.4 Plasma Enhanced Rapid Expansion of Supercritical Solutions

Mechanical testing of the deposited films to determine their ability to withstand future steps, such as spin coating, in the microelectronic fabrication process is critical. Building a working cell to determine the efficiency is also a large area of work that has been identified for the future given the large number of cells in which this type of structure could be integrated into.

APPENDICES

APPENDIX A

FOUR POINT BEND APPARATUS DESIGN

FOUR POINT BEND APPARATUS DESIGN
BASE COMPONENT (x2) – SCHEMATIC

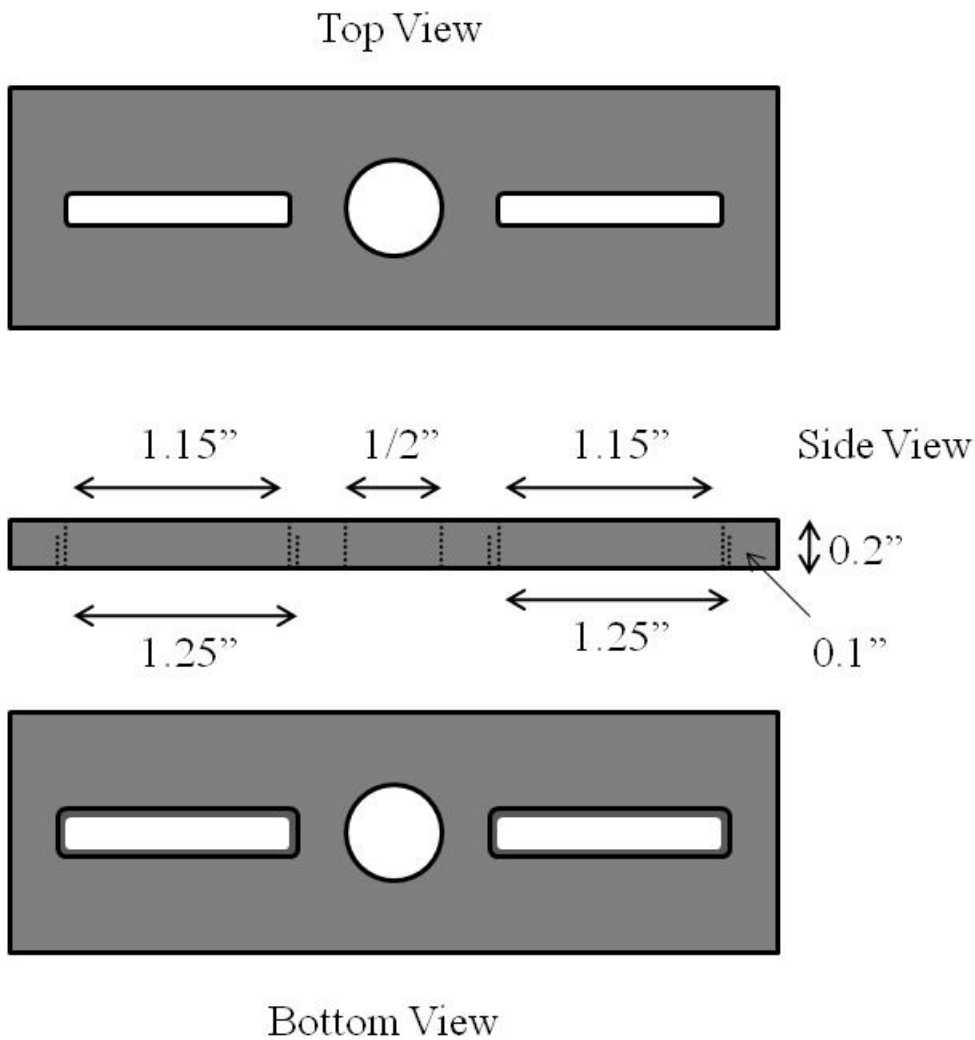

Figure A.1: Schematic of base plate for four point bend apparatus.

FOUR POINT BEND APPARATUS DESIGN
BASE COMPONENT (x2)

Figure A.2: Top view of base plate for four point bend apparatus.

Figure A.3: Side view of base plate for four point bend apparatus.

Figure A.4: Bottom view of base plate for four point bend apparatus.

FOUR POINT BEND APPARATUS DESIGN
SLIDER COMPONENT (x4) SCHEMATIC – TOP AND BOTTOM VIEW

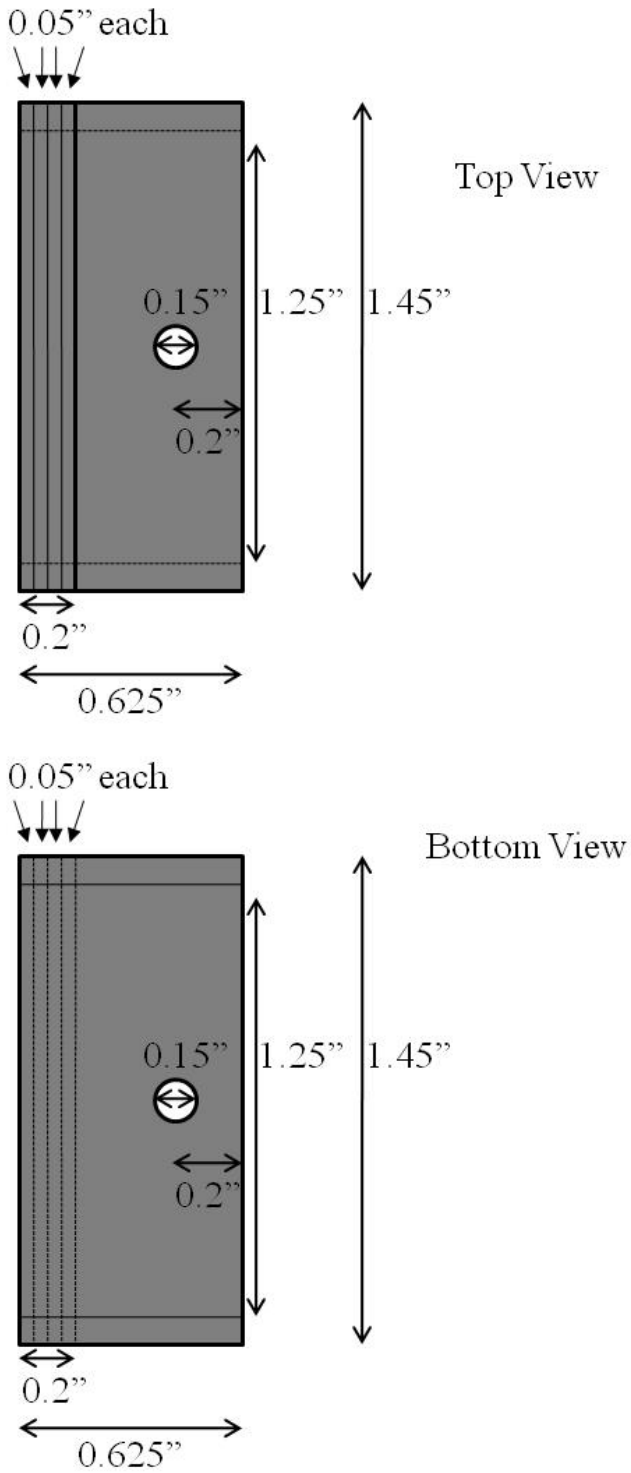

Figure A.5: Schematic (top and bottom view) of slider component for four point bend apparatus.

FOUR POINT BEND APPARATUS DESIGN
SLIDER COMPONENT (x4) – SIDE VIEW

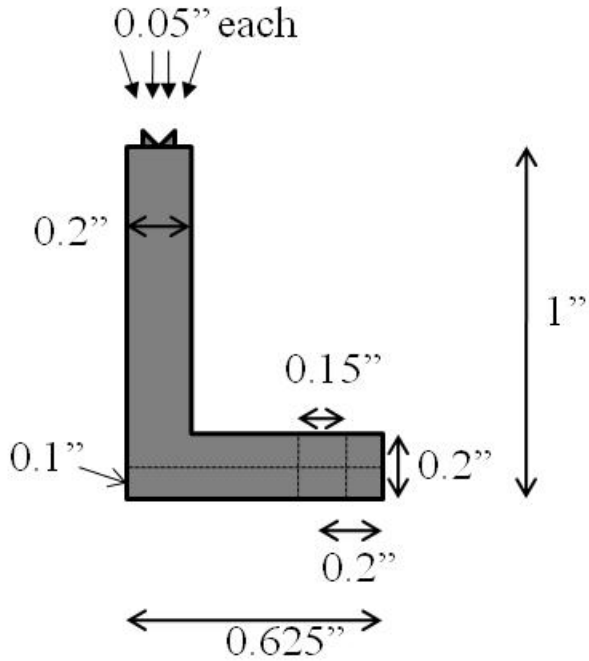

Figure A.6: Schematic (side view) of slider component for four point bend apparatus.

FOUR POINT BEND APPARATUS DESIGN
SLIDER COMPONENT (x4)

Figure A.7: Top view of slider component for four point bend apparatus.

Side View

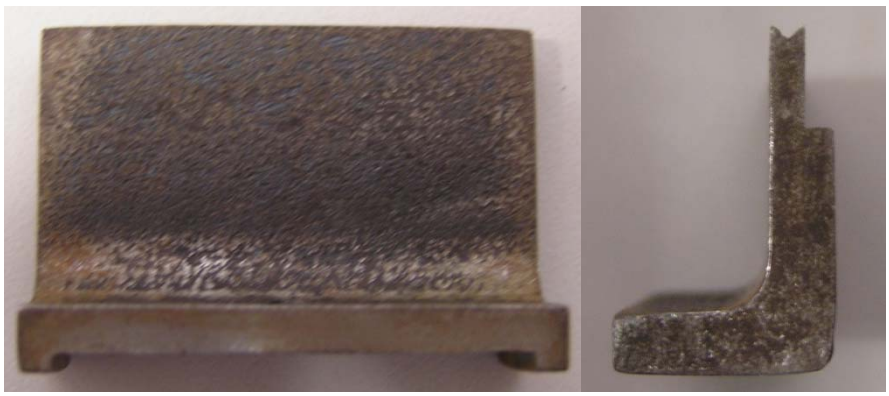

Figure A.8: Side view of slider component for four point bend apparatus.

Figure A.9: Bottom view of slider component for four point bend apparatus.

FOUR POINT BEND APPARATUS DESIGN
ASSEMBLED APPARATUS – DIGITAL IMAGE

Figure A.10: Top view of assemlbed four point bend apparatus.

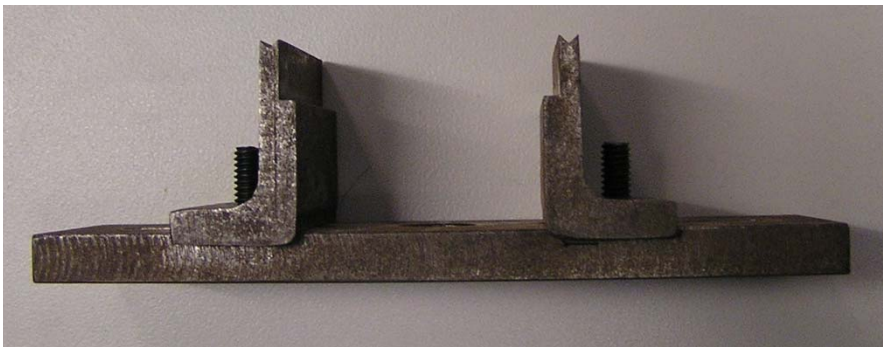

Figure A.11: Side view of assemlbed four point bend apparatus.

Figure A.12: Bottom view of assemlbed four point bend apparatus.

APPENDIX B

HEATED STAGE DESIGN FOR COLD WALL REACTOR

HEATED STAGE DESIGN FOR COLD WALL REACTOR
TOP COMPONENT

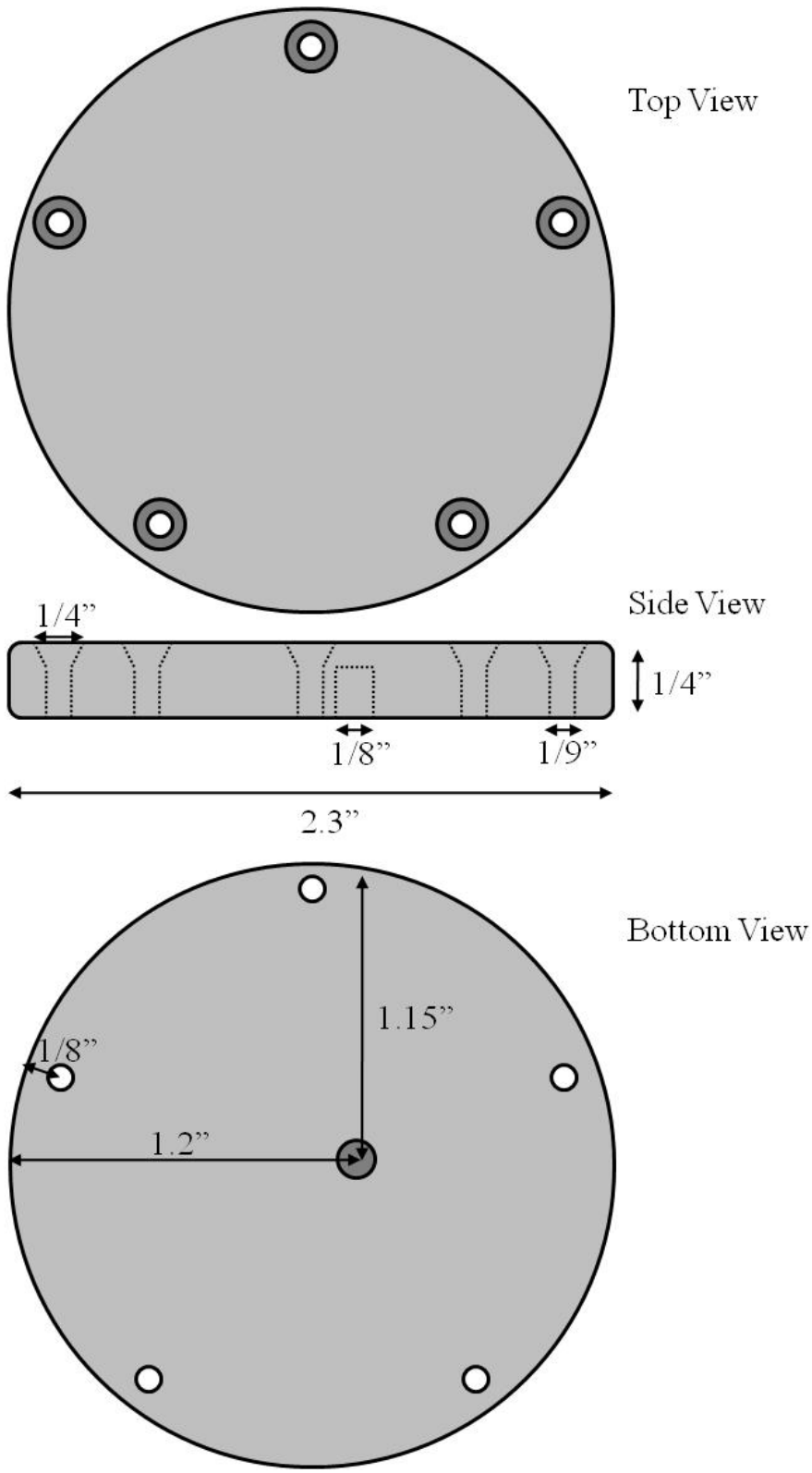

Figure B.1: Schematic of top plate of heated stage designed for the cold wall reactor.

HEATED STAGE DESIGN FOR COLD WALL REACTOR
BOTTOM COMPONENT

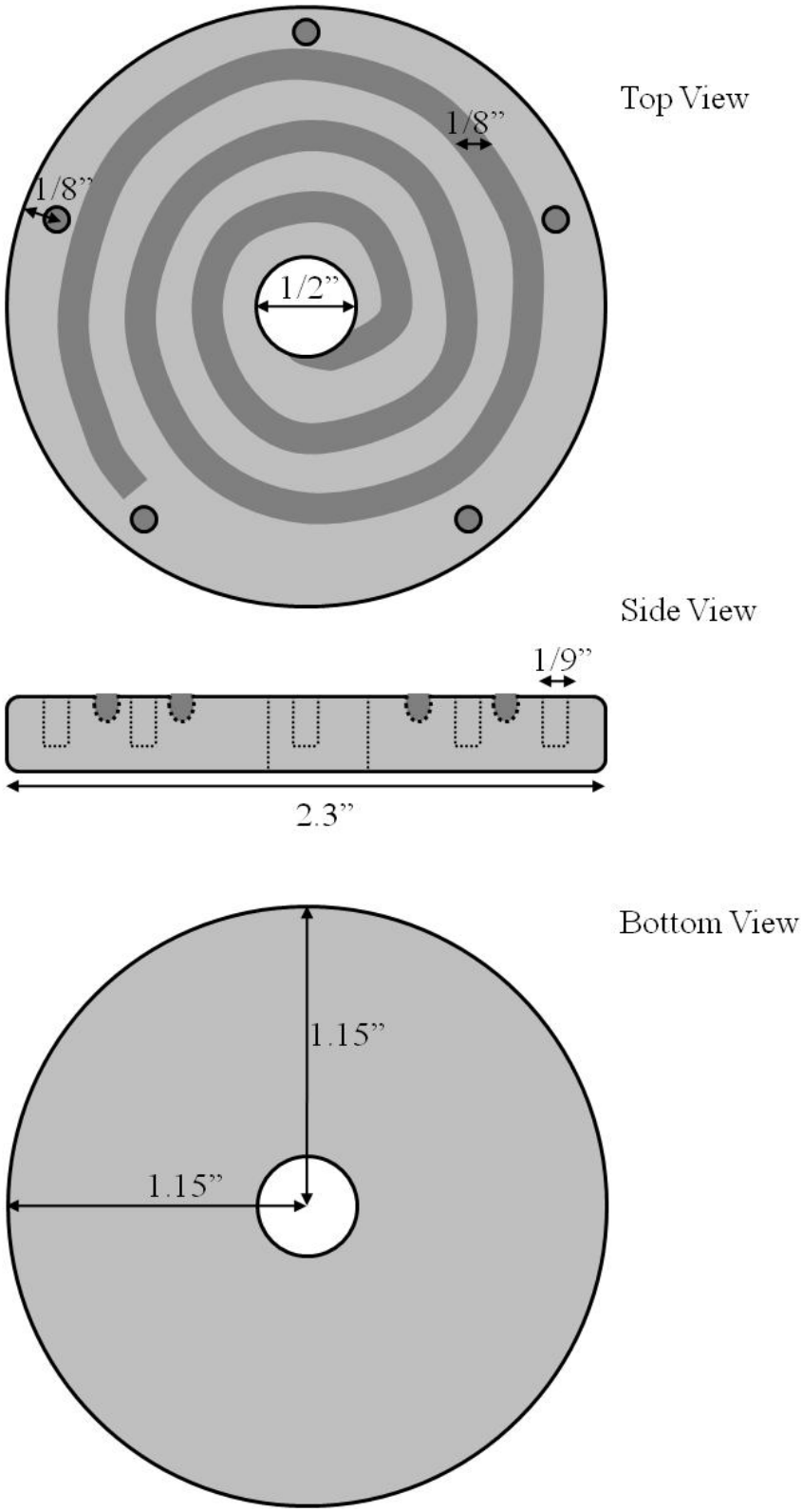

Figure B.2: Schematic of bottom plate of heated stage designed for the cold wall reactor.

BIBLIOGRAPHY

Abazovic, N. D., M. I. Comor, M. D. Dramicanin, D. J. Jovanovic, S. P. Ahrenkiel, J. M. Nedeljkovic, *Journal of Physical Chemistry B* **2006**, *110*, 25366-25370.

Abduraslidova, A. A., A. R. Bazaev, E. A. Bazaev, I. M. Abdulagatov, *High Temperature* **2007**, *45*, 178-186.

Alexandru, H. V., C. Berbecaru, A. Ioachim, M. I. Toacsen, M. G. Banciu, L. Nedelcu, D. Ghetu, *Materials Science and Engineering B-Solid State Materials for Advanced Technology* **2004**, *109*, 152-159.

Anderson, C. R., R. N. Lee, J. F. Morar, R. L. Park, *Journal of Vacuum Science & Technology* **1982**, *20*, 617-621.

Aoyama, T., K. Eguchi, *Japanease Journal of Applied Physics* **1999**, *38*, L1134-L1136.

Aoyama, T., M. Kiyotoshi, S. Yamazaki, K. Eguchi, *Japanease Journal of Applied Physics* **1999**, *38*, 2194-2199.

Aschenbrenner, O., S. Kemper, N. Dahmena, K. Schaber, E. Dinjus, *The Journal of Superciritcal Fluids* **2007**, *41*, 179-186.

ASTM Standard D3359 - 08, 2003, "Standard Test Methods for Measuring Adhesion by Tape Test," ASTM International, West Conshohocken, PA, www.astm.org.

Baer, Y., P. F. Hedén, J. Hedman, M. Klasson, C. Nordling, K. Siegbahn, *Physica Scripta* **1970**, *1*, 55-65.

Bancroft, G. M., I. Adams, L. L. Coatsworth, C. D. Bennewitz, J. D. Brown, W. D. Westwood, *Analytical Chemistry* **1975**, *47*, 586-588.

Barbe, C. J., F. Arendse, P. Comte, M. Jirousek, F. Lenzmann, V. Shklover, M. Gratzel, *J. Am. Chem. Soc.* **1997**, *80*, 3157-3171.

Barreca, D., A. Gasparotto, E. Tondello, C. Sada, S. Polizzi, A. Benedetti, *Chemical Vapor Deposition* **2003**, *9*, 199-206.

Bazaev, A. R., I. M. Abdulagatov, E. A. Bazaev, A. Abdurashidova, *Journal of Chemical Thermodynamics* **2007**, *39*, 385-411.

Bazaev, A. R., I. M. Abdulagatov, E. A. Bazaev, A. Abdurashidova, *International Journal of Thermophysics* **2007**, *28*, 194-219.

Berry, A. D., D. K. Brown, R. Kaplan, E. J. Cukauskas, *Journal of Vacuum Science and Technology A: Vacuum, Surfaces, and Films* **1986**, *4*, 215-218.

Blackburn, J. M., A. Cabanas, D. P. Long, J. J. Watkins, *Abstracts of Papers of the American Chemical Society* **2002**, *223*, U663-U664.

Blackburn, J. M., D. P. Long, A. Cabanas, J. J. Watkins, *Science* **2001**, *294*, 141-145.

Blackburn, J. M., D. P. Long, J. J. Watkins, *Chemistry of Materials* **2000**, *12*, 2625-2631.

Bocquet, J. F., K. Chhor, C. Pommier, *Materials Chemistry and Physics* **1999**, *57*, 273-280.

Boehm, E., J. M. Bassat, P. Dordor, F. Mauvy, J. C. Grenier, P. Stevens, *Solid State Ionics* **2005**, *176*, 2717-2725.

Boyd, E. P., D. R. Ketchum, B. Deng, S. G. Shore, *Chemistry of Materials* **1997**, *9*, 1154-1158.

BP Statistical Review of World Energy Full Review 2008, www.bp.com, **2008**

Bruno, S. A., D. K. Swanson, I. Burn, *Journal of the American Ceramic Society* **1993**, *76*, 1233-1241.

Cabanas, A., J. M. Blackburn, J. J. Watkins, *Microelectronic Engineering* **2002**, *64*, 53-61.

Cabanas, A., D. P. Long, J. J. Watkins, *Chemistry of Materials* **2004**, *16*, 2028-2033.

Cabanas, A., X. Shan, J. J. Watkins, *Chemistry of Materials* **2003**, *15*, 2910-2916.

Cahen, D., J. E. Lester, *Chemical Physics Letters* **1973**, *18*, 108-111.

Campos, C. L., C. Roldan, M. Aponte, Y. Ishikawa, C. R. Cabrera, *Journal of Electroanalytical Chemistry* **2005**, *581*, 206-215.

Carp, O., C. Huisman, A. Reller, *Progress in Solid State Chemistry* **2004**, *32*, 33-177.

Chalker, P. R., S. J. Bull, D. S. Rickerby, *Materials Science and Engineering a-Structural Materials Properties Microstructure and Processing* **1991**, *140*, 583-592.

Chan, R., T. N. Arunagiri, Y. Zhang, O. Chyan, R. M. Wallace, M. J. Kim, T. Q. Hurd, *Electrochemical and Solid-State Letters* **2004**, *7*, G154-G157.

Charalambides, P. G., J. Lund, A. G. Evans, R. M. McMeeking, *Journal of Applied Mechanics* **1989**, *56*, 77-82.

Chen, D., E. Jordan, M. Gell, X. Ma, *J. Am. Chem. Soc.* **2008**, *91*, 865-872.

Chen, L., J. A. Kelber, *Journal of Vacuum Science & Technology a-Vacuum Surfaces and Films* **1999**, *17*, 1968-1973.

Chen, L., N. Magtoto, B. Ekstrom, J. Kelber, *Thin Solid Films* **2000**, *376*, 115-123.

Chen, R.-s., Y.-s. Huang, Y.-l. Chen, Y. Chi, *Thin Solid Films* **2002**, *413*, 85-91.

Chen, X. F., W. Q. Lu, W. G. Zhu, S. Y. Lim, S. A. Akbar, *Surface & Coatings Technology* **2003**, *167*, 203-206.

Cheng, C., T. Arunagiri, O. Chyan, *American Journal of Undergraduate Research* **2003**, *2*, 11-18.

Chi, Y., F. J. Lee, C.-S. Liu, *USA Patent U.S. Patent 6,303,809*, **2001**.

Chin, T. S., *Journal of Magnetism and Magnetic Materials* **2000**, *209*, 75-79.

Chiu, M. C., C. F. Cheng, W. T. Wu, F. S. Shieu, *Journal of the Electrochemical Society* **2005**, *152*, F66-F70.

Christensen, P. A., A. Hamnett, J. Munk, G. L. Troughton, *Journal of Electroanalytical Chemistry* **1994**, *370*, 251-258.

Christensen, P. A., A. Hamnett, G. L. Troughton, *Journal of Electroanalytical Chemistry* **1993**, *362*, 207-218.

Christie, A. B., J. Lee, I. Sutherland, J. M. Walls, *Applied Surface Science* **1983**, *15*, 224-237.

Chuang, T. J., C. R. Brundle, D. W. Rice, *Surface Science* **1976**, *59*, 413-429.

Coakley, K. M., Y. Liu, M. D. McGehee, K. L. Frindell, G. D. Stucky, *Advanced Functional Materials* **2003**, *13*, 301-306.

Coakley, K. M., M. D. McGehee, *Chemistry of Materials* **2004**, *16*, 4533-4542.

Coakley, K. M., M. D. McGehee, *Applied Physics Letters* **2003**, *83*, 3380-3382.

Conteras, M. A., B. Egaas, K. Ramanathan, J. Hiltner, A. Swatzlander, F. Hasoon, R. Noufi, *Progress in Photovoltaics* **1999**, *7*, 311-316.

Contour, J. P., G. Mouvier, M. Hoogewys, C. Leclere, *Journal of Catalysis* **1977**, *48*, 217-228

Moore's Law, www.intel.com, **2008**

Crosby, J. N., R. S. Hanley, *United States Patent U.S. Patent 4,250,210*, **1981**.

Dauskardt, R. H., M. Lane, Q. Ma, N. Krishna, *Engineering Fracture Mechanics* **1998**, *61*, 141-162.

David, P., in *Mechanical Engineering*, Vol. Masters, Louisiana State University, **2005**.

de Felipe, T. S., S. P. Murarka, S. Bedell, W. A. Lanford, *Thin Solid Films* **1998**, *335*, 49-53.

Deshpande, S. B., Y. Khollam, Y. B. Bhoraskar, S. K. Date, S. R. Sainkara, H. S. Potdar, *Materials Letters* **2005**, *59*, 293-296.

Dey, S. K., J. Goswami, A. Das, W. Cao, M. Floyd, R. Carpenter, *Journal of Applied Physics* **2003**, *94*, 774-777.

Di-Serio, M., V. Valato, A. Dimiccoli, L. Maffucci, P. Iengo, E. Santacesaria, *Catalysis Today* **2001**, *66*, 403-410.

Dillon, H. E., S. G. Penoncello, *International Journal of Thermophysics* **2004**, *25*, 321-335.

Ding, P. J., W. A. Lanford, S. Hymes, S. P. Murarka, *Journal of Applied Physics* **1994**, *75*, 3627-3631.

Ding, P. J., W. A. Lanford, S. Hymes, S. P. Murarka, *Applied Physics Letters* **1994**, *64*, 2897-2899.

Escard, J., B. Pontvianne, M. T. Chenebaux, J. Cosyns, *Bulletin De La Societe Chimique De France Partie I-Physicochimie Des Systemes Liquides Electrochimie Catalyse Genie Chimique* **1975**, 2399-2402.

Favre, L., V. Dupuis, E. Bernstein, P. Melinon, A. Perez, *Physical Review B* **2006**, *74*.

Feng, R. J., X. H. Xu, H. S. Wu, *Journal of Magnetism and Magnetic Materials* **2007**, *308*, 131-136.

Ferguson, G. S., M. K. Chaudhury, G. B. Sigal, G. M. Whitesides, *Science* **1991**, *253*, 776-778.

Fernandes, N. E., S. M. Fisher, J. C. Poshusta, D. G. Vlachos, M. Tsapatsis, J. J. Watkins, *Chemistry of Materials* **2001**, *13*, 2023-2031.

Fisher, G. B., N. E. Erikson, T. E. Madey, J. John T. Yates, *Surface Sciences* **1977**, *65*, 210-228.

Fix, R., R. G. Gordon, D. M. Hoffman, *Chemistry of Materials* **1993**, *5*, 614-619.

Folas, G. K., J. Gabrielsen, M. L. Michelsen, E. H. Stenby, G. M. Kontogeorgis, *Industrial & Engineering Chemistry Research* **2005**, *44*, 3823-3833.

Folkesson, B., *Acta Chemica Scandinavica* **1973**, *27*, 287-302.

Frank, S. N., A. J. Bard, *Journal of the American Chemical Society* **1977**, *99*, 303-304.

Frohlich, F., D. Machajdik, V. Cambel, J. Fedor, A. Pisch, J. Lindner, *Journal of Physics IV France* **2001**, *11*, Pr3-325 - Pr323-332.

Fu, C. L., C. R. Yang, H. W. Chen, Y. X. Wang, L. Y. Hu, *Materials Science and Engineering B-Solid State Materials for Advanced Technology* **2005**, *119*, 185-188.

Fu, Y. H., S. I. Sandler, H. Orbey, *Industrial & Engineering Chemistry Research* **1995**, *34*, 4351-4363.

Fujishima, A., K. Honda, *Nature* **1972**, *238*, 37-+.

Furuya, A., M. Tagami, K. Shiba, K. Kikuta, Y. Hayashi, *Ieee Transactions on Electron Devices* **2002**, *49*, 733-738.

Gandhi, D. D., M. Lane, Y. Zhou, A. P. Singh, S. Nayak, U. Tisch, M. Eizenberg, G. Ramanath, *Nature* **2007**, *447*, 299-302.

Gandikota, S., S. Voss, R. Tao, A. Duboust, D. Cong, L. Y. Chen, S. Ramaswami, D. Carl, *Microelectronic Engineering* **2000**, *50*, 547-553.

Ganesan, P. G., J. Gamba, A. Ellis, R. S. Kane, G. Ramanath, *Applied Physics Letters* **2003**, *83*, 3302-3304.

Garzella, C., E. Comini, E. Tempesti, C. Frigeri, G. Sberveglieri, *Sensors and Actuators B-Chemical* **2000**, *68*, 189-196.

Gell, M., L. Xie, X. Ma, E. Jordan, N. Padture, *Surface and Coating Technology* **2004**, *177-178*, 97-102.

Gerberich, W. W., D. E. Kramer, N. I. Tymiak, A. A. Volinsky, D. F. Bahr, M. D. Kriese, *Acta Materialia* **1999**, *47*, 4115-4123.

Gersten, B. L., M. M. Lencka, R. E. Riman, *Journal of the American Ceramic Society* **2004**, *87*, 2025-2032.

Goswami, J., W. Noh, S. K. Dey, *Chemical Vapor Deposition* **2005**, *11*, 94-98.

Gratzel, M., *Nature* **2001**, *414*, 338-344.

Griswold, J., J. D. Haney, V. A. Klein, *Industrial and Engineering Chemistry* **1943**, *35*, 701-704.

Haas, T., J. Gaube, *Chemical Engineering and Technology* **1989**, *12*, 45-53.

Haertling, G. H., *Journal of the American Ceramic Society* **1999**, *82*, 797-818.

Hammond, J. S., N. Winograd, *Journal of Electroanalytical Chemistry* **1977**, *78*, 55-69.

Hampden-Smith, M. J., T. T. Kodas, *Chemical Vapor Deposition* **1995**, *1*, 8-23.

Hampden-Smith, M. J., T. T. Kodas, *Chemical Vapor Deposition* **1995**, *1*, 39-48.

Hannay, J. B., J. Hogarth, *Proceedings of the Royal Society of London* **1879**, *29*, 324-326.

Hernandez-Garduza, O., F. Garcia-Sanchez, E. Neau, M. Rogalski, *Chemical Engineering Journal* **2000**, *79*, 87-101.

Holgado, J. P., G. Munuera, J. P. Espinos, A. R. Gonzalez-Elipe, *Applied Surface Science* **2000**, *158*, 164-171.

Hones, P., F. Levy, T. Gerfin, M. Gratzel, *Chemical Vapor Deposition* **2000**, *6*, 193-198.

Hoppe, H., N. Serdariciftci, *Journal of Materials Research* **2004**, *19*, 1924-1945.

Howard, S. J., Y. C. Tsui, T. W. Clyne, *Acta Metallurgica et Materialia* **1994**, *42*, 2823-2836.

Hsiao, P., K. Wang, C. Cheng, H. Teng, *Journal of Photochemistry and Photobiology A-Chemistry* **2007**, *188*, 19-24.

Hughes, A. E., J. D. Gorman, P. J. K. Patterson, R. Carter, *Surface and Interface Analysis* **1996**, *24*, 634-640.

Hughey, M. P., D. J. Morris, R. F. Cook, S. P. Bozeman, B. L. Kelly, S. L. N. Chakravarty, D. P. Harkens, L. C. Stearns, *Engineering Fracture Mechanics* **2004**, *71*, 245-261.

Hunde, E. T., J. J. Watkins, *Chemistry of Materials* **2004**, *16*, 498-503.

Hungria, T., M. Alguero, A. B. Hungria, A. Castro, *Chemistry of Materials* **2005**, *17*, 6205-6212.

Hwang, P., B. H. Li, T. Yang, Z. H. Zhai, F. W. Zhu, *Acta Physica Sinica* **2005**, *54*, 1841-1846.

Hwang, P., B. H. Li, T. Yang, Z. H. Zhai, F. W. Zhu, *Journal of University of Science and Technology Beijing* **2004**, *11*, 319-323.

International Technology Roadmap for Semiconductors, http://www.itrs.net/, **2007**

Jasenek, A., U. Rau, K. Weinert, I. M. Kotschau, G. Hanna, G. Voorwinden, M. Powalla, H. W. Schock, J. H. Werner, *Thin Solid Films* **2001**, *387*, 228-230.

Jeong, S., Y. N. Hsu, D. E. Laughlin, M. E. McHenry, *Ieee Transactions on Magnetics* **2001**, *37*, 1299-1301.

Jeong, S., Y. N. Hsu, D. E. Laughlin, M. E. McHenry, *Ieee Transactions on Magnetics* **2000**, *36*, 2336-2338.

Jeong, S., Y. N. Hsu, M. E. McHenry, D. E. Laughlin, *Journal of Applied Physics* **2000**, *87*, 6950-6952.

Jin, X., C. P. Wade, X. Tao, E. Pao, Y. Wang, J. Zhao, *USA Patent U.S. Patent 6,479,100*, **2002**.

Johansson, G., J. Hedman, A. Berndtsson, M. Klasson, R. Nilsson, *Journal of Electron Spectroscopy and Related Phenomena* **1973**, *2*, 295-317.

Kadoshima, M., T. Nabatame, M. Hiratani, Y. Nakamura, *Japanease Journal of Applied Physics* **2002**, *41*, L347-L350.

Kao, C. F., W. D. Yang, *Applied Organometallic Chemistry* **1999**, *13*, 383-397.

Khanna, P. K., N. Singh, S. Charan, *Materials Letters* **2007**, *61*, 4725-4730.

Khollam, Y. B., S. B. Deshpande, H. S. Potdar, S. V. Bhoraskar, S. R. Sainkar, S. K. Date, *Materials Characterization* **2005**, *54*, 63-74.

Kim, D.-H., R. H. Wentorf, W. N. Gill, *Journal of the Electrochemical Society* **1993**, *140*, 3267-3272.

Kim, H., *Journal of Vacuum Science & Technology B* **2003**, *21*, 2231-2261.

Kim, I. D., A. Rothschild, B. H. Lee, D. Y. Kim, S. M. Jo, H. L. Tuller, *Nano Letters* **2006**, *6*, 2009-2013.

Kim, J. J., J. H. Jeong, K. R. Lee, D. Kwon, *Thin Solid Films* **2003**, *441*, 172-179.

Kim, J. J., D. H. Jung, M. S. Kim, S. H. Kim, D. Y. Yoon, *Thin Solid Films* **2002**, *409*, 28-32.

Kim, K. S., *Physical Review B* **1975**, *11*, 2177-2185.

Kim, K. S., S. W. Gaarenstroom, N. Winograd, *Chemical Physics Letters* **1976**, *41*, 503-506.

Kim, K. S., N. Winograd, *Journal of Catalysis* **1974**, *35*, 66-72.

Kim, K. S., N. Winograd, R. E. Davis, *Journal of the American Chemical Society* **1971**, *93*, 6296-&.

Kitamura, T., H. Hirakata, T. Itsuji, *Engineering Fracture Mechanics* **2003**, *70*, 2089-2101.

Kodas, T. T., *The Chemistry of Metal CVD*, John Wiley & Sons Ltd, **1994**.

Koelliker, R., G. Bor, *Inorganic Chemistry* **1991**, *30*, 2236-2237.

Kondoh, E., *Japanease Journal of Applied Physics* **2004**, *43*, 3928-3933.

Kondoh, E., *Japanease Journal of Applied Physics* **2005**, *44*, 5799-5802.

Kondoh, E., K. Shigama, *Thin Solid Films* **2005**, *491*, 228-234.

Kriese, M. D., W. W. Gerberich, N. R. Moody, *Journal of Materials Research* **1999**, *14*, 3007-3018.

Kriese, M. D., W. W. Gerberich, N. R. Moody, *Journal of Materials Research* **1999**, *14*, 3019-3026.

Krishnamoorthy, A., K. Chanda, S. P. Murarka, G. Ramanath, J. G. Ryan, *Applied Physics Letters* **2001**, *78*, 2467-2469.

Krukonis, V., in *Annual Meeting AIChE* San Fransisco **1984**.

Lagalante, A. F., B. N. Hansen, T. J. Bruno, R. E. Sievers, *Inorg. Chem.* **1995**, *34*, 5781-5785.

Lai, Y.-H., Y.-L. Chen, Y. Chi, C.-S. Liu, A. J. Carty, S.-M. Peng, G.-H. Lee, *Journal of Materials Chemistry* **2003**, *13*, 1999-2006.

Lanford, W. A., P. J. Ding, W. Wang, S. Hymes, S. P. Murarka, *Materials Chemistry and Physics* **1995**, *41*, 192-198.

Langmuir, I., *Proceedings of the National Academy of Sciences of the United States of America* **1928**, *14*, 627-637.

Lashdaf, M., T. Hatanpaa, A. O. I. Krause, J. Lahtinen, M. Lindblad, M. Tiitta, *Applied Catalysis A: General* **2003**, *241*, 51-63.

Lebugle, A., U. Axelsson, R. Nyholm, N. Martensson, *Physica Scripta* **1981**, *23*, 825-827.

Lee, D.-J., S.-W. Kang, S.-W. Rhee, *Thin Solid Films* **2002**, *413*, 237-242.

Lee, F.-J., Y. Chi, C.-S. Liu, P.-F. Hsu, T.-Y. Chou, S.-M. Peng, G.-H. Lee, *Chemical Vapor Deposition* **2001**, *7*, 99-101.

Lee, J.-H., J.-Y. Kim, S.-W. Rhee, D. Yang, D.-H. Kim, C.-H. Yang, Y.-K. Han, C.-J. Hwang, *Journal of Vacuum Science and Technology A: Vacuum, Surfaces, and Films* **2000**, *18*, 2400-2403.

Lee, J. M., J. C. Shin, C. S. Hwang, H. J. Kim, *Journal of Vacuum Science and Technology A: Vacuum, Surfaces, and Films* **1998**, *16*, 2768-2771.

Lee, S.-H., J.-K. Chun, J.-J. Hur, J.-S. Lee, G.-H. Rue, Y.-H. Bae, S.-H. Hahm, Y.-H. Lee, H.-H. Lee, *IEEE Electron Device Letters* **2000**, *21*, 261-263.

Lemanov, V. V., E. P. Smirnova, P. P. Syrnikov, E. A. Tarakanov, *Physical Review B* **1996**, *54*, 3151-3157.

Lenzmann, F. O., J. M. Groon, *Advances in OptoElectronics* **2007**, *2007*, 1-10.

Li, H., D. B. Farmer, R. G. Gordon, Y. Lin, J. Vlassak, *Journal of the Electrochemical Society* **2007**, *154*, D642-D647.

Li, Z., R. G. Gordon, D. B. Farmer, Y. Lin, J. J. Vlassak, *Electrochemical and Solid State Letters* **2005**, *8*, G182-G185.

Liu, Y. J., R. O. Claus, *Journal of the American Chemical Society* **1997**, *119*, 5273-5274.

Long, D. P., J. M. Blackburn, J. J. Watkins, *Advanced Materials* **2000**, *12*, 913-915.

Luque, A., S. Hegedus, Eds., *Handbook of Photovoltaic Science and Engineering*, John Wiley and Sons, **2007**.

Ma, Q., *Journal of Materials Research* **1997**, *12*, 840-845.

Magagnin, L., R. Maboudian, C. Carraro, *Thin Solid Films* **2003**, *434*, 100-105.

Maret, M., M. C. Cadeville, A. Herr, R. Poinsot, E. Beaurepaire, S. Lefebvre, M. Bessiere, *Journal of Magnetism and Magnetic Materials* **1999**, *191*, 61-71.

Markvart, T., Ed. *Solar Electricity*, John Wiley and Sons, **2001**.

Matsui, Y., M. Hiratani, T. Nabatame, Y. Shimamoto, S. Kimura, *Electrochemical and Solid-State Letters* **2002**, *5*, C18-C21.

Matsui, Y., M. Hiratani, T. Nabatame, Y. Shimamoto, S. Kimura, *Electrochemical and Solid-State Letters* **2001**, *4*, C9-C12.

Mauvy, F., J. M. Bassat, E. Boehm, J. P. Manaud, P. Dordor, J. C. Grenier, *Solid State Ionics* **2003**, *158*, 17-28.

McHugh, M. A., V. J. Krukonis, *Supercritical Fluid Extraction Practice and Principles*, Butterworth-Heinemann, **1994**.

McIntyre, N. S., Ed. *Quantitative Surface Analysis of Materials*, **1977**.

Mesguich, D., J. M. Bassat, J. C. Grenier, F. Cansell, C. Aymonier, *Chemical Communications* **2008**, *Submitted*.

Mittal, K. L., *Electrocomponent Science and Technology* **1976**, *3*, 21-42.

Moore, G. E., *Electronics* **1965**, *38*, 114-117.

Murata, M., K. Wakino, S. Ikeda, *Journal of Electron Spectroscopy and Related Phenomena* **1975**, *6*, 459-464.

Nabatame, T., M. Hiratani, M. Kadoshima, Y. Shimamoto, *Japanease Journal of Applied Physics* **2000**, *39*, L1188-L1190.

Nazeeruddin, M. K., A. Kay, I. Rodicio, R. Humphry-Baker, E. Muller, P. Liska, N. Vlachopoulos, M. Gratzel, *J. Am. Chem. Soc.* **1993**, *115*, 6382-6390.

Nefedov, V. I., M. N. Firsov, I. S. Shaplygin, *Journal of Electron Spectroscopy and Related Phenomena* **1982**, *26*, 65-78.

Nefedov, V. I., D. Gati, B. F. Dzhurinskii, N. P. Sergushin, Y. V. Salyn, *Zhurnal Neorganicheskoi Khimii* **1975**, *20*, 2307-2314.

Nefedov, V. I., Y. V. Salyn, *Inorganica Chimica Acta* **1978**, *28*, L135-L136.

Nefedov, V. I., Y. V. Salyn, A. A. Chertkov, L. N. Padurets, *Zhurnal Neorganicheskoi Khimii* **1974**, *19*, 1443-1445.

Niarchos, D., *Sensors and Actuators a-Physical* **2003**, *109*, 165-173.

Nist Chemistry Web Book, http://webbook.nist.gov/chemistry/, **2008**

Nyholm, R., N. Martensson, *Journal of Physics C: Solid State Physics* **1980**, *13*, L279-L284.

O'Neil, A., J. J. Watkins, *Green Chemistry* **2004**, *6*, 363-368.

O'Neil, A., J. J. Watkins, *Chemistry of Materials* **2007**, *19*, 5460-5466.

O'Neil, A., J. J. Watkins, *Chemistry of Materials* **2006**, *18*, 5652-5658.

O'Regan, B., M. Gratzel, *Nature* **1991**, *353*, 737-740.

Papadatos, F., S. Consiglio, S. Skordas, E. T. Eisenbraun, A. E. Kaloyeros, J. Peck, D. Thompson, C. Hoover, *Journal of Materials Research* **2004**, *19*, 2947-2955.

Papadatos, F., S. Skordas, Z. Patel, S. Consiglio, E. Eisenbraun, "Chemical Vapor Deposition of Ru and RuO2 for Gate Eelectrode Applications", presented at *Material Research Society*, **2002**.

Park, J. I., J. Cheon, *Journal of the American Chemical Society* **2001**, *123*, 5743-5746.

Park, J. S., M. J. Lee, C. S. Lee, S. W. Kang, *Electrochemical and Solid State Letters* **2001**, *4*, C17-C19.

Park, S.-E., H.-M. Kim, K.-B. Kim, S.-H. Min, *Journal of the Electrochemical Society* **2000**, *147*, 203-209.

Parra, R., M. S. Goes, M. S. Castro, E. Longo, P. R. Bueno, J. A. Varela, *Chemistry of Materials* **2008**, *20*, 143-150.

Patil, D. R., S. A. Lokare, R. S. Devan, S. S. Chougule, C. M. Kanamadi, Y. Kolekar, B. K. Chougule, *Materials Chemistry and Physics* **2007**, *104*, 254-257.

Pecar, D., V. Dolecek, *Fluid Phase Equilibria* **2005**, *230*, 36-44.

Perakis, C., E. Voutsas, K. Magoulas, D. Tassios, *Fluid Phase Equilibria* **2006**, *243*, 142-150.

Perkins, C. L., M. A. Henderson, C. H. F. Peden, G. S. Herman, *Journal of Vacuum Science & Technology A* **2001**, *19*, 1942-1946.

Petit, C., S. Rusponi, H. Brune, *Journal of Applied Physics* **2004**, *95*, 4251-4260.

Pinceloup, P., C. Courtois, A. Leriche, B. Thierry, *Journal of the American Ceramic Society* **1999**, *82*, 3049-3056.

Polikhronidi, N. G., I. M. Abdulagatov, G. V. Stepanov, R. G. Batyrova, *Fluid Phase Equilibria* **2007**, *252*, 33-46.

Polikhronidi, N. G., I. M. Abdulagatov, G. V. Stepanov, R. G. Batyrova, *Journal of Supercritical Fluids* **2007**, *43*, 1-24.

Pollard, K. D., H. A. Jenkins, R. J. Puddephatt, *Chemistry of Materials* **2000**, *12*, 701-710.

Powell, C. J., N. E. Erickson, T. Jach, *Journal of Vacuum Science & Technology* **1982**, *20*, 625-625.

Pulker, H. K., A. J. Perry, *Surface Technology* **1981**, *14*, 25-39.

Qi, J. Q., Y. Wang, W. P. Chen, L. T. Li, H. L. W. Chan, *Journal of Solid State Chemistry* **2005**, *178*, 279-284.

Ramanath, G., G. Cui, P. G. Ganesan, X. Guo, A. V. Ellis, M. Stukowski, K. Vijayamohanan, P. Doppelt, M. Lane, *Applied Physics Letters* **2003**, *83*, 383-385.

Reveron, H., C. Aymonier, A. Loppinet-Serani, C. Elissalde, M. Maglione, F. Cansell, *Nanotechnology* **2005**, *16*, 1137-1143.

Reveron, H., C. Elissalde, C. Aymonier, O. Bidault, M. Maglione, F. Cansell, *Journal of Nanoscience and Nanotechnology* **2005**, *5*, 1741-1744.

Reveron, H., C. Elissalde, C. Aymonier, C. Bousquet, M. Maglione, F. Cansell, *Nanotechnology* **2006**, *17*, 3527-3532.

Roeder, R. K., E. B. Slamovich, *Journal of the American Ceramic Society* **1999**, *82*, 1665-1675.

Roham, S., K. Hardikar, P. Woytowitz, *Journal of Materials Research* **2004**, *19*, 3019-3027.

Rossnagel, S. M., A. Sherman, F. Turner, *Journal of Vacuum Science & Technology B* **2000**, *18*, 2016-2020.

Ruiz, A. M., G. Sakai, A. Cornet, K. Shimanoe, J. R. Morante, N. Yamazoe, *Sensors and Actuators B-Chemical* **2003**, *93*, 509-518.

Safarov, D. T., A. N. Shakhverdiev, *High Temperature* **2001**, *39*, 395-400.

Sarma, D. D., C. N. R. Rao, *Journal of Electron Spectroscopy and Related Phenomena* **1980**, *20*, 25-45.

Scherban, T., B. Sun, J. Blaine, C. Block, B. Jin, E. Andideh, "Interfacial Adhesion of Copper-Low k Interconnects", presented at *Interconnect Technology Conference, 2001. Proceedings of the IEEE 2001 International*, Burlingame, CA, **2001**.

Schmidt, A., R. Schomacker, *Ind. Eng. Chem. Res.* **2007**, *46*, 1677-1681.

Schneider, A., N. Popovska, F. Holzmann, H. Gerhard, C. Topf, U. Zenneck, *Chemical Vapor Deposition* **2005**, *11*, 99-105.

Schneider, W. D., B. Delley, E. Wuilloud, J. M. Imer, Y. Baer, *Physical Review B* **1985**, *32*, 6819-6831.

Schon, G., *Journal of Electron Spectroscopy and Related Phenomena* **1972-1973**, *1*, 377-387.

Schultz, T., S. Zhou, K. Sundmacher, *Chemical Engineering & Technology* **2001**, *24*, 1223-1233.

Sekler, J., P. A. Steinmann, H. E. Hintermann, *Surface & Coatings Technology* **1988**, *36*, 519-529.

Selvam, I. P., V. Kumar, *Materials Letters* **2002**, *56*, 1089-1092.

Senzaki, Y., W. L. Gladfelter, F. B. McCormick, *Chemistry of Materials* **1993**, *5*, 1715-1721.

Senzaki, Y., F. B. McCormick, W. L. Gladfelter, *Chemistry of Materials* **1992**, *4*, 747-749.

Shalvoy, R. B., P. J. Reucroft, *Journal of Vacuum Science & Technology* **1979**, *16*, 567-569.

Shan, X., D. P. Schmidt, J. J. Watkins, *The Journal of Supercritical Fluids* **2007**, *40*, 84-92.

Shan, X., J. J. Watkins, *Thin Solid Films* **2006**, *496*, 412-416.

Shapiro, A. L., O. Vajk, F. Hellman, K. M. Ring, K. L. Kavanagh, *Applied Physics Letters* **1999**, *75*, 4177-4179.

Shen, C., Q. F. Liu, Q. Liu, *Materials Letters* **2004**, *58*, 2302-2305.

Shyu, J. Z., K. Otto, W. L. H. Watkins, G. W. Graham, R. K. Belitz, H. S. Gandhi, *Journal of Catalysis* **1988**, *114*, 23-33.

Simon, D., C. Perrin, J. Bardolle, *Journal De Microscopie Et De Spectroscopie Electroniques* **1976**, *1*, 175-186.

Smart, N. G., T. Carleson, T. Kast, A. A. Clifford, M. D. Burford, C. M. Wai, *Talanta* **1997**, *44*, 137-150.

Smestad, G., *Solar Energy Materials and Solar Cells* **1998**, *55*, 157-178.

Steinmann, P. A., H. E. Hintermann, *Journal of Vacuum Science & Technology a-Vacuum Surfaces and Films* **1989**, *7*, 2267-2272.

Steinmann, P. A., H. E. Hintermann, *Journal of the Electrochemical Society* **1988**, *135*, C358-C358.

Steinmann, P. A., Y. Tardy, H. E. Hintermann, *Thin Solid Films* **1987**, *154*, 333-349.

Su, C. W., F. C. Chen, Y. E. Wu, C. S. Shern, *Surface Science* **2002**, *507*, 492-497.

Takiguchi, Y., O. Osada, M. Uematsu, *Journal of Chemical Thermodynamics* **1996**, *28*, 1375-1385.

Takiguchi, Y., M. Uematsu, *Journal of Chemical Thermodynamics* **1996**, *28*, 7-16.

Thompson, S. J. J., *Philosophical Magazine* **1897**, *44*, 293.

Tiwari, V. S., N. Singh, D. Pandey, *Journal of Physics-Condensed Matter* **1995**, *7*, 1441-1460.

Tong, J., D. Martini, N. Magtoto, M. Pritchett, J. Kelber, *Applied Surface Science* **2002**, *187*, 253-260.

Toomey, J. J., S. Hymes, S. P. Murarka, *Applied Physics Letters* **1995**, *66*, 2074-2076.

Trent, D. E., B. Paris, H. H. Krause, *Inorganic Chemistry* **1964**, *3*, 1057-1058.

Trudeau, M. L., A. Tschope, J. Y. Ying, *Surface and Interface Analysis* **1995**, *23*, 219-226.

Tsui, T. Y., A. J. McKerrow, J. J. Vlassak, *Journal of Materials Research* **2005**, *20*, 2266-2273.

Tsui, Y. C., S. J. Howard, T. W. Clyne, *Acta Metallurgica et Materialia* **1994**, *42*, 2837-2844.

Vandoveren, H., J. A. T. Verhoeven, *Journal of Electron Spectroscopy and Related Phenomena* **1980**, *21*, 265-273.

Vasiliev, A., N. Padture, X. Ma, *Acta Materialia* **2006**, *54*, 4913-4920.

Vlachopoulos, N., P. Liska, J. Augustynski, M. Gratzel, *J. Am. Chem. Soc.* **1988**, *110*, 1216-1220.

Vlassak, J. J., Y. Lin, T. Y. Tsui, *Materials Science and Engineering A* **2005**, *391*, 159-174.

Voss, S., S. Gandikota, L. Y. Chen, R. Tao, D. Cong, A. Duboust, N. Yoshida, S. Ramaswami, *Microelectronic Engineering* **2000**, *50*, 501-508.

Wade, C. P., E. Pao, Y. Wang, J. Zhao, *USA Patent 6,440,495*, **2002**.

Wagner, C. D., *Faraday Discussions of the Chemical Society* **1975**, *60*, 291 - 300.

Wagner, C. D., W. M. Riggs, L. E. Davis, J. F. Moulder, G. E. Mullenberg, *Handbook of X-ray Photoelectron Spectroscopy*, Perkin-Elmer, Physical Electronics Division, Eden Prairie MN 55344 **1979**.

Wakayama, H., N. Setoyama, *Advanced Materials* **2003**, *15*, 742-745.

Wang, A. Q., P. Punchaipetch, R. M. Wallace, T. D. Golden, *Journal of Vacuum Science & Technology B* **2003**, *21*, 1169-1175.

Wang, Q., J. G. Ekerdt, D. Gay, Y.-M. Sun, J. M. White, *Applied Physics Letters* **2004**, *84*, 1380-1382.

Watkins, J. J., J. M. Blackburn, T. J. McCarthy, *Chemistry of Materials* **1999**, *11*, 213-215.

Wechsler, B. A., K. W. Kirby, *Journal of the American Ceramic Society* **1992**, *75*, 981-984.

Wei, X. Z., N. P. Padture, *Journal of Ceramic Processing Research* **2004**, *5*, 175-178.

Weller, D., H. Brandle, C. Chappert, *Journal of Magnetism and Magnetic Materials* **1993**, *121*, 461-470.

Werner, A., A. Roos, *Solar Energy Materials and Solar Cells* **2007**, *91*, 609-615.

Woo, T. G., I. S. Park, H. W. Lee, M. H. Lee, E. K. Park, Y. K. Hwang, K. W. Seol, *Journal of the Korean Institute of Metals and Materials* **2007**, *45*, 423-428.

Worthy, W., *Chemical and Engineering News* **1981**, *59*, 16-17.

Xie, L., X. Ma, E. Jordan, N. Padture, D. Xiao, M. Gell, *Surface and Coating Technology* **2004**, *177-178*, 103-107.

Xie, L., X. Ma, A. Ozturk, E. Jordan, N. Padture, B. Cetegen, D. Xiao, M. Gell, *Surface and Coating Technology* **2004**, *183*, 51-61.

Yamada, Y., T. Suzuki, E. N. Abarra, *Ieee Transactions on Magnetics* **1998**, *34*, 343-345.

Yamada, Y., W. P. Van Drent, E. N. Abarra, T. Suzuki, *Journal of Applied Physics* **1998**, *83*, 6527-6529.

Yang, X. J., X. Yao, L. Y. Zhang, *Ceramics International* **2004**, *30*, 1525-1527.

Yi, S. M., J. U. An, S. S. Hwang, J. R. Yim, Y. H. Huh, Y. B. Park, Y. C. Joo, *Thin Solid Films* **2008**, *516*, 2325-2330.

Yi, S. M., K. H. Jang, J. U. An, S. S. Hwang, Y. C. Joo, *Microelectronics Reliability* **2008**, *48*, 744-748.

Zana, I., G. Zangari, J. W. Park, M. G. Allen, *Journal of Magnetism and Magnetic Materials* **2004**, *272*, E1775-E1776.

Zhang, Y., D. Kang, M. Aindow, C. Erkey, *JOURNAL OF PHYSICAL CHEMISTRY B* **2005**, *109*, 2617-2624.

Zhang, Y., J. C. Yang, Y. X. Yu, Y. G. Li, *Journal of Supercritical Fluids* **2005**, *36*, 145-153.

Zhang, Y. P., R. J. Puddephatt, *Chemistry of Materials* **1999**, *11*, 148-153.

Zhang, Z. L., X. H. Du, W. D. Wang, *Journal of Vacuum Science & Technology A* **2000**, *18*, 2928-2931.

Zhang, Z. Y., J. C. Yang, Y. G. Li, *Fluid Phase Equilibria* **2000**, *169*, 1-18.

Zhu, Y. M., H. Uchida, T. Yajima, M. Watanabe, *Langmuir* **2001**, *17*, 146-154.

Zong, Y., in *Chemical Engineering*, Vol. Ph.D., University of Massachusetts - Amherst, **2004**.

Zong, Y., X. Shan, J. J. Watkins, *Langmuir* **2004**, *20*, 9210-9216.

Zong, Y., J. J. Watkins, *Chemistry of Materials* **2005**, *17*, 560-565.